Dynamics of open quantum systems: excitons, cavities and surface plasmons.

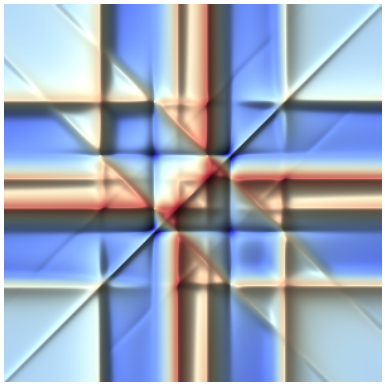

Alejandro Gonzalez-Tudela
Departamento de Fisica Teorica de la Materia Condensada
Universidad Autonoma de Madrid

Memoria presentada para optar al grado de
Doctor en Ciencias Físicas.

Madrid, Enero 2013

Acknowledgements

First of all, I would like to acknowledge my PhD advisor, Carlos, for having given the opportunity to work with complete freedom during the these years. The results of this Thesis have been results of many collaborations. Among them, I would like to thank Elena and Fabrice for all the things they have taught me during these years. In spite of the distance, we have been able to keep working together and the results of the first part of the Thesis have been directly resulted from this collaboration, which I hope to continue during the forthcoming years. Moreover, I have also enjoyed a lot their presence during conferences or my short stays in Münich,

The "plasmonic" part of the Thesis has also been possible thanks to the collaboration with the Nanophotonics group of the department, leaded by FJ. From this collaboration, I have been able to learn all I know about plasmons. Apart from FJ, I also enjoyed a lot the discussions with Esteban and Luis. However, among all I must specially thank Diego and Paloma. The results of Chapter 7 wouldn't have been possible without Diego's classical simulations. With Paloma, we have struggled (and we are still on it) to unravel the strong-coupling between quantum emitters and plasmons, which results are summarized in Chapter 7. Here, I would also like to acknowledge Diego Porras, with which I have developed the results of Chapter 8. I must thank him for his patiente and support on this topic, and for introducing me to the more formal theories of quantum optics.

During these years I have been able to travel a lot, and even make short stays in some institutes abroad. I would like to thank A. Imamoglu and Ignacio Cirac, and all the people from their group, for having given me the opportunity to visit them and learn a lot from the best experimental and theoretical physics respectively. They both made me feel at home, and I take many friends among which I want to highlight Thomas, Javier, Martin, "Lubi", ...

Regarding my colleagues at "Modulo 5", I must thank all of them for the nice atmosphere created. Among them, I would like to thank my office mates. Stefan is the person with which I have been sharing the office since the first time. Despite his initial shyness, he turned out a very funny guy, and especially helpful when something went wrong with the computer. With Emi I have not only shared the office but also lunch breaks, conferences,... It is always nice to have a good friend in the office and I have really missed his presence in the last year. Now I wish him the best of luck in his personal and professional career. I must also thank the rest of Semicuam: Guille, Carlos, Pepe, Luis, Andrei, Francesca, Maria, ... and especially our last incorporation, Carlos S, which I've had the pleasure to share

the office with. I've really enjoyed his passion for Physics and his dedication to every little detail. I just foresee a great future for him.

Out of the "Physics" I must also thank many friends that has kept me balanced during these years: Salva, Paco, Inma, Gelen, Agus, Mario, ... Obviously, among all of I must highlight Leo, who I have shared the last seven years of my life. Probably now the Thesis is over, she will be happy to recover her partner once for all. And last, but not least, I'm really thankful to my family for his support in every manner and and faith in me. Actually, without their constant support throughout all this years none of this would have been possible.

Abstract

English

This Thesis is devoted to the interplay between coherence and decoherence in open quantum optical systems. Coherence in these systems is given by the interaction of matter with different kind of electromagnetic modes. In particular, in this Thesis we focus on photonic modes in semiconductor microcavities and surface plasmons in metallic structures. Unfortunately, these systems have an unavoidable coupling with the environment that tends to destroy coherence. A deep understanding of this competition is needed to evaluate the possibilities of these systems in future quantum technologies.

The first part of the Thesis is focused on the so-called semiconductor cavity QED systems. They typically consists of a single quantum dot embedded inside a microcavity, where the exciton and cavity mode interact. Through the appropriate inclusion of a new Lindblad term in the Master Equation, we study how decoherence induced by the phonon modes of the solid-state matrix affects the observation of strong-coupling in the non-linear regime. Importantly, we are able to predict a new kind of spectral structures, namely triplets, due to the interplay between interaction and decoherence. These triplets have already been observed experimentally but attributed to different origins. Moreover, we are able to characterize the efficiency of these systems to generate identical and simultaneous photon pairs. Another important landmark developed within this Thesis is a new method to efficiently compute frequency and time resolved photon correlations. Our method overcomes the computational difficulties of the standard theory, being able to predict a new zoology of processes completely hidden in usual spectroscopy.

In the second part, metallic nanostructures are studied within an open quantum system formalism. Through this formalism we are able to characterize the strong-coupling between one or many quantum emitters interacting with surface plasmon modes of low dimensional structures. By tracing out the plasmonic degrees of freedom in one-dimensional systems, we find that they can induce a controllable coherent and incoherent coupling between emitters. Together with a continuous excitation, we show that this coupling can lead to entanglement generation between two or many quantum emitters.

Español

Esta Tesis se ocupa de la competición entre coherencia y decoherencia en sistemas de óptica cuántica abiertos. La coherencia de estos sistemas nace fundamentalmente de la interacción entre la materia y distintos modos electromagnéticos. En particular en esta Tesis nos centramos en los modos fotónicos de una cavidad o los plasmones superficiales en estructuras metálicas. El aislamiento de estos sistemas no es perfecto, y de la interacción con el ambiente surgen mecanismos que tienden a romper esa coherencia. El estudio de la competición de estos mecanismos es fundamental a la hora de determinar las posibilidades de estos sistemas para realizar tecnología basada en este tipo de sistemas.

La primera parte de la Tesis está centrada en la Electrodinámica Cuántica en cavidades semiconductoras. Estos sistemas están normalmente constituidos por un punto cuántico embebido dentro de una microcavidad, cuyo excitón interacciona con los modos de cavidad. A traves de la inclusión de terminos *Lindblad* adecuados en la ecuación maestra del sistema, vamos a estudiar como la decoherencia inducida por los fonones de la matrix semiconductora afecta a la observación del acoplo fuerte en el régimen no-lineal. La competición entre el acoplo fuerte y este tipo decoherencia específico de semiconductores muestra una tendencia robusta a emitir la luz con un espectro en forma de tripletes. Estos tripletes ya se han observado experimentalmente pero habían sido atribuidos a otros mecanismos. Dentro del mismo formalismo, pero incluyendo los grados de libertad de espín de los excitones, se estudia la capacidad de estos sistemas para generar parejas de fotones simultáneos e idénticos. Por último, desarrollamos un método para calcular correlaciones de fotones de distinta frecuencia. Esta medida es cada vez más accesibles y popular experimentalmente, sin embargo su desarrollo teórico estaba limitado por su complejidad computacional. Con ella, somos capaces de identificar procesos que pasan desapercibidos en otras medidas habituales de espectroscopía.

En la segunda parte, aplicamos el formalismo de sistemas cuánticos abiertos a estructuras metálicos de baja dimensionalidad con el objetivo de caracterizar las condiciones de acoplo fuerte entre uno (o muchos) emisores cuánticos y los plasmones. En el caso de sistemas uni-dimensionales, tracearemos los modos de plasmon obteniendo una interacción efectiva entre los emisores cuánticos. Al combinarla con un bombeo coherente, probamos que estos sistemas son capaces de generar estados entrelazados entre dos o más emisores.

Contents

List of Figures

Nomenclature

List of acronyms

This is a list of acronyms used in the text:

- **QD** Quantum dots.
- **SPP** Surface plasmon polariton.
- **QED** Quantum electro-dynamics.
- **cQED** Cavity quantum electro-dynamics.
- **EM** Electromagnetic.
- **QE** Quantum emitter.
- **WC** Weak Coupling.
- **SC** Strong Coupling.
- **PW** Plasmonic waveguide.
- **2LS** Two-level system.
- **c2LS** Coupled two-level system.
- **HO** Harmonic oscillator.
- **cHO** Coupled harmonic oscillator.
- **JC** Jaynes-Cummings.
- **1PS** One-photon spectrum.
- **2PS** Two-photon spectrum.

Notations

We set $\hbar = 1$ in most of the text. This removes the distinction between energy and frequency. The hat for the quantum operators is usually avoided for simplicity being clear by the context.

Chapter 1

Introduction

1.1 Motivation

During the centuries, Physics has constantly evolved trying to account for the experimental phenomenology which appeared at shorter and larger scales. As an example, in the beginning of the twentieth century Newton's laws of gravitation were overcome by Einstein's general relativity in 1916 [1], that accounted a unified description of gravity as a geometric property of space and time. Contemporarily, the foundations of strikingly new and fundamental theory to describe very small systems was being settled. Its birth is usually established with Planck's theory of the black body radiation. It was within this theory where the concept of *quanta* was first introduced, and after which this new revolutionary theory was named: *quantum mechanics*. It describes matter in its most basic level, and therefore can be arguably considered as the most fundamental physical theory ever developed by man.

Among all the characteristics of quantum mechanics emerges its inherent probabilistic nature. Its consequences were that all the predictions derived from this theory are of probabilistic character, that is, with no deterministic theory behind it. This statistical interpretation shocked a whole generation of physicists who were reluctant to accept a non-deterministic theory. This initial opposition, colloquially summarized in the well-known Einstein's statement: *God doesn't play dice*, was commonplace in the early years of quantum mechanics. Formally, Einstein's doubts were posed in a seminal paper of title: "Can Quantum Mechanical description of physical reality can be considered complete?" [2]. There, the authors were proposing that there should be some deterministic theory behind quantum mechanics. The debate over quantum mechanics foundations has extended still to our days [3], where still there is controversy about the completeness of theory.

Beyond these shaky beginnings, many of the physicists adopted the so-called *Copenhagen interpretation*, popularly stated as *"Shut up and calculate"*. It basically consisted of assuming the probabilistic nature of the theory and interpreting the results in a statistical way. From the technological point of view, its application to semiconductors leaded to breakthrough discoveries, such as the transistor [4] or the laser [5, 6]. The former is the essential building block of the current electronic technology which has made possible, for example, the exponential increase of the computing capabilities during the last decades.

However, the miniaturization of current electronics is reaching its limit. It has started probing the single atomic limit where quantum effects begin to be relevant. This physical

constrain forces to a change of paradigm if we want to keep increasing our computing capabilities. It is in this context where *quantum mechanics* may give a new twist, changing the classical paradigm of computing. The intuitive idea is to consider isolated single system behaving quantum mechanically as the building blocks for computation.

Quantum computation and quantum information [7] uses quantum mechanics, for instance, to develop new algorithms that outperform its classical counterpart. A paradigmatic example is the well-known Shor's algorithm to factorize prime numbers [7], which can be applied to develop more secure quantum cryptography protocols [8]. These applications in quantum cryptography are even commercial nowadays. Further practical applications envisioned for the future are the development of a whole new class of computers based on these computations. Besides, from the more fundamental point of view, quantum systems are expected to simulate physical systems which are otherwise intractable with a classical computer.

There are many possible candidates [9] of physical system to play the role of *hardware* for quantum computers. One of the first proposals relied in using trapped ions [10], whose degrees of freedom can be interfaced with a laser field. Up to our days, this scheme still appears as one of the most successful realizations, e.g. having been able to entangle controllably 14 quantum bits [11]. There are other proposals with atoms in optical lattices [12] or cavities [13]. Their main drawback for scalability is having to cool and trap the atoms in order to make them interact with the cavity. An alternative pathway to overcome this drawback are solid-state systems, where there is already a whole technology developed within semiconductors for current electronics. Among these systems, nitrogen vacancy centers [9] or semiconductor quantum dots (QDs) [14, 15] rank among the most promising platforms. As QDs are one of the topic of study of this Thesis, we make a more detailed introduction in Section 1.3.

The question of which is the optimal system to develop quantum scalable operations is still open. A good criterion was established by Loss and DiVincenzo [14] based on the following requirements:

- The system should posses two well-defined states, defining the qubits (*quantum bit*).
- Low decoherence.
- A way to reliable prepare/read the quantum state of your system.
- Accurate quantum gate operations.

These conditions, especially the last three, establish the link between this introduction and the title of this Thesis. Firstly, the aspect of decoherence is one of the fiercest problems from the technological point of view. Quantum computation considers single quantum levels isolated from the rest of the "universe". However, any realistic system has a non-negligible coupling with the environment that influences its properties. In fact, any quantum system must be regarded as a open one because, at least, it is interacting with the background of vacuum fluctuations. As a consequence, the *theory of open quantum systems* plays a major role in quantum computation in general, and in this Thesis in particular. We give a more detailed introduction to this theory in Section 1.2.

In this Thesis, we focus on quantum states connected by optical transitions. Thus, even isolated in the vacuum, they interact with the vacuum background of radiation modes [16]

yielding to the so-called spontaneous emission of photons. This emission is not only detrimental as it allows to extract information from the state of the system without altering it. In Chapter 2, we explain in detail how to do it just by post-processing the photons.

The coherent interaction between qubits and electromagnetic (EM) modes is also interesting for the preparing/reading requirement of the quantum state. A typical experimental approach is to make the qubits interact with cavity modes. This scheme is typically used as an interface between traveling qubits (photons) and localized qubits (QDs) [17]. The study of this interaction between light and matter in semiconductor systems is the topic of study in Chapters 3, 4 and 5. A further look to the experimental and theoretical state of art is contained in Section 1.3.

These qubit-photon interfaces require a clean and controlled interaction between the photons and the matter states. Semiconductor microcavities are good candidates but they are not suitable for miniaturization as they are diffraction-limited. In these cases, a promising alternative to photons is emerging in the last few years, the so-called: Surface Plasmon-Polaritons (SPPs). They are composite surface bound modes that appear in metal-dielectric interfaces, combining both EM fields and charge currents. They show both a subwavelength confinement and long propagation lengths [18, 19]. The former yields an enhancement of the EM field, increasing the interaction strength between qubits and SPPs. A detailed introduction to them will be made in Section 1.4. As they are the main system of stufy in Chapters 6,7 and 8, a more detailed introduction to SPPs will be given in Section 1.4.

Even though one of the goals of quantum computation is to fight against decoherence, it should be mentioned for completeness that it has emerged in the last years a new paradigm of quantum computation which turns dissipation into a useful resource [20]. This proposal combines all the fields that we have described throughout the introduction: quantum computation, quantum optics and open quantum systems. The intuitive idea is that if one is able to engineer the decoherent coupling with the reservoirs in a clever way, then this interaction can drive your system into a desired state [21, 22]. This new way of computation shows several advantages compared to the one relying in coherent unitary evolution: it does not suffer with decoherence and the initialization of the state is not necessary, as the desired state is the outcome of the evolution of the system. This approach has been proven to be useful to generate entanglement between atomic ensembles [23, 24] and one expects to implement it in solid state systems.

1.2 Introduction to open quantum systems.

Let us consider a closed quantum system described by a hamiltonian (H). Then, the evolution of a quantum state ($|\Phi(t)\rangle$) is completely governed by H following the Schrödinger equation:

$$i\frac{d\,|\Phi(t)\rangle}{dt} = H\,|\Phi(t)\rangle\ . \tag{1.1}$$

Its formal solution can be expressed in terms of a unitary evolution operator $U(t,t_0)$, that transforms the state as follows:

$$|\Phi(t)\rangle = U(t,t_0)\,|\Phi(t_0)\rangle\ . \tag{1.2}$$

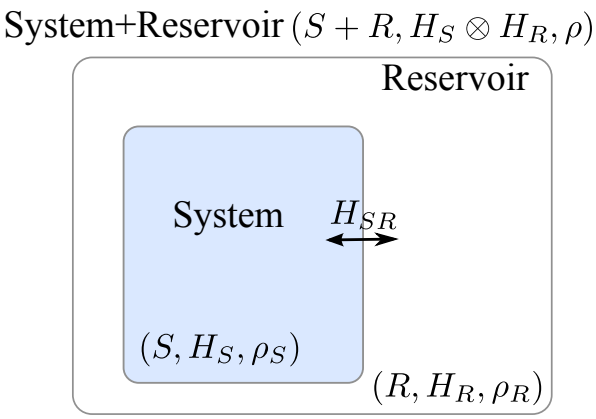

Figure 1.1: Schematic view of a open quantum system picture: the complete system or *universe* is described by the complete hamiltonian: $H = H_S \otimes H_R$. It can be divided in the system of interest, described by H_S and the reservoir, described by H_R. Both subsets interact through H_{SR}.

If the closed system hamiltonian is time-independent, then $U(t, t_0) = e^{-iH(t-t_0)}$. The inherent probabilistic nature of quantum mechanics makes that, in some situations, systems under consideration are in a mixed state of the corresponding quantum statistical ensemble. In these cases the introduction of the density matrix operator is defined as:

$$\rho(t_0) = \sum_i c_i \left|\Phi_i(t_0)\right\rangle \left\langle\Phi_i(t_0)\right| , \tag{1.3}$$

where c_i represents the probability to be in the state $|\Phi_i(t_0)\rangle$. Its time evolution can be obtained from Eq. 1.1:

$$\frac{d\rho(t)}{dt} = -i[H, \rho(t)] , \tag{1.4}$$

usually referred as the *Von Neumann* equation for the density matrix operator. This equation contains the whole description of the system dynamics. However, in practical terms this description is very limited as usually the number of degrees of freedom of a microscopic description is huge. Furthermore, most of the times one is only interested in a very small subset of the whole system. Therefore, the complete evolution extracted from Eq. 1.4 contains a great amount of information which is useless. For example, in the quantum computation context, one is basically interested in the evolution of the qubits, whereas the environment dynamics is irrelevant. It is in these situations where the *open quantum system* formalism emerges as a powerful tool. Several authoritative reviews on the topic can be found in [25–27].

The schematic view and notation for this formalism is settled in Fig. 1.1: the complete system or *universe*, described by $H = H_S \otimes H_R$, can be divided in two subsets: the *system* of interest, described by H_S, and its environment or *reservoir*, which free evolution is governed by H_R. Both subsets are connected through an interaction hamiltonian, H_{SR}, that links the evolution between the system and the reservoir. The evolution of the complete system-reservoir ensemble is given in terms of the total density matrix ρ. Typically, one is only interested in the *system* subset dynamics described by the reduced density matrix operator $\rho_S = \mathrm{Tr}_R(\rho)$, obtained by tracing out the the degrees of freedom of the bath. An interesting

situation arises when the interacting hamiltonian represents only a *small perturbation* to the evolution of the S. In this case, the evolution of the reduced system density matrix is governed by the following differential equation:

$$\frac{d\rho_S(t)}{dt} = i[\rho_S(t), H_S] + \mathcal{L}[\rho_S]\,, \tag{1.5}$$

usually referred to as *master equation*. It is divided in two terms: first, the coherent unitary evolution coming from the system hamiltonian H_S. The second term, $\mathcal{L}[\rho_S]$, represents the effective evolution induced in the system due to the interaction with the *reservoir* R. The latter is known as the *incoherent* part of the master equation as it leads to irreversible processes. The actual expression of $\mathcal{L}[\rho_S]$ depends on the type of coupling H_{SR}.

Due to the importance for this Thesis, we make a detailed derivation of Eq. 1.5 in Chapter 2. Special emphasis is made on the different type of incoherent processes that can emerge depending on the different reservoirs. After this general introduction to the open quantum system formalism, we introduce two specific examples of them that will be particularly relevant for this Thesis, namely semiconductor QDs embedded in photonic microcavities and quantum emitters coupled to surface plasmon polaritons.

1.3 Semiconductor cavity QED (cQED).

The study of interaction between quantum emitters (QEs), such as atoms, quantum dots, superconducting qubits, ... and EM modes has played a central role in the field of Quantum Optics. During this Thesis, we focus on physical systems where artificially designed atoms in solid-state setups, such as QDs or nitrogen vacancy center, are coupled deterministically to photonic cavities [28–30]. Due to the semiconductor environment, these systems are "dirtier" than their atomic counterpart. Nevertheless, solid-state systems show some advantages, such as the control in the fabrication process, possibility of placing them permanently at fixed positions at separations of the order of relevant wavelengths [31] or their prospect for scalability.

Even though some of results of this Thesis can be extrapolated to any QE, our main interest lies in the particular case of semiconductor QDs embedded in microcavities. Therefore, we proceed to review the experimental and theoretical state-of-art of these systems.

1.3.1 Semicondutor quantum dots.

Semiconductor QDs were highlighted in the introduction as one of the most promising systems for developing a scalable quantum computer architecture [14, 15]. They are small 0D semiconductor structures in which their excitations, such as electrons and/or holes, are confined in the three dimensions of space. Due to Coulomb interaction, these two semiconductor excitations can form a bound state, usually refereed as QD exciton. The energy levels of the exciton are discrete due to confinement, resembling the ones of the atoms. This has given them the name of "artificial atoms".

The confinement is achieved through semiconductor heterostructures, by growing layer by layer semiconductors with different bandgap, such as GaAs and AlAs. Due to this fabrication

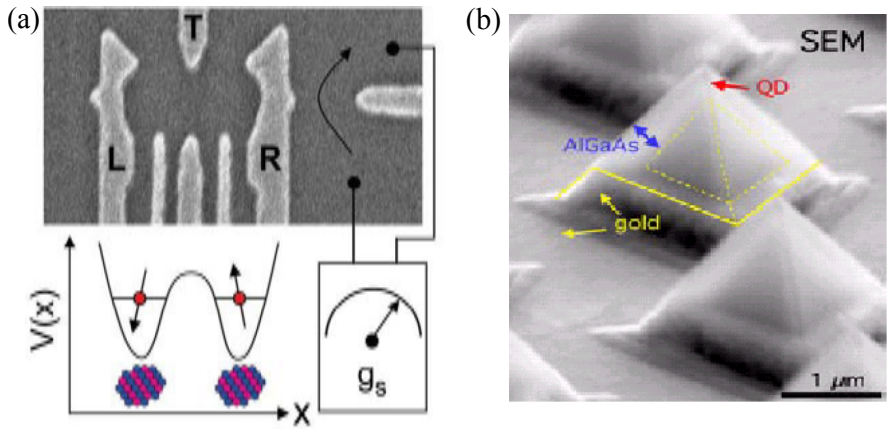

Figure 1.2: Panel (a): Image of electrostatically defined QDs [33]. Panel (b): Image of self-assembled AlGaAs quantum dots.

procedure, the confinement was first achieved in one dimension, in the so-called quantum wells, where the exciton was free to move in the other two-dimensions.

Further confinement is needed in order to define the 0D character of QDs that can be achieved in several ways. The initial proposal [14] was based on using electrostatic potentials, by applying gate voltages with lithographic defined contacts as shown in Fig. 1.2(a). These potentials allow to confine the electron spin and control its degrees of freedom. These type of QDs has been successful to meet great part of the requirement needed for scalable architecture: such as read-out [32] or two-qubit gate [33]. However, the small depth of their confinement potential and the short range of interactions limit their applicability to low temperatures and small distances. Moreover, it is difficult to confine electrons and holes in the same spatial region in order to get excitons.

Fortunately, electrostatic control is not the only way to achieve the necessary confinement. During the fabrication process of quantum wells, the lattice mismatch between the different materials induces some strain that ends up with the random creation of the so-called self-assembled QDs. A typical scheme of this strain-induced QDs is shown in Fig. 1.2(b). They are characterized by having a deeper confinement potential than electrostatic QDs. This allows to work at higher temperatures. Their main drawback is the randomness introduced by the fabrication process, which leads to certain randomness in positions and/or energies. However, technology is constantly evolving in this direction and a finer control of their attributes can be achieved now [31]. One of the advantages of these self-assembled QDs is that they are optically active. Thus, they can be naturally coupled to the photonic mode of a microcavity in order to realize the solid-state counterpart of atomic cavity QED (cQED) [34].

1.3.2 Semiconductor cavity QED.

The role of the cavity in cavity QED is to be an interface between traveling (photons) and localized qubits. In order for semiconductor cQED to be a serious candidate for quantum computation [15], a controllable and efficient coupling between the QDs and the cavity mode must be reached.

Microcavities are structures that confine the light field in micrometer size. Due to im-

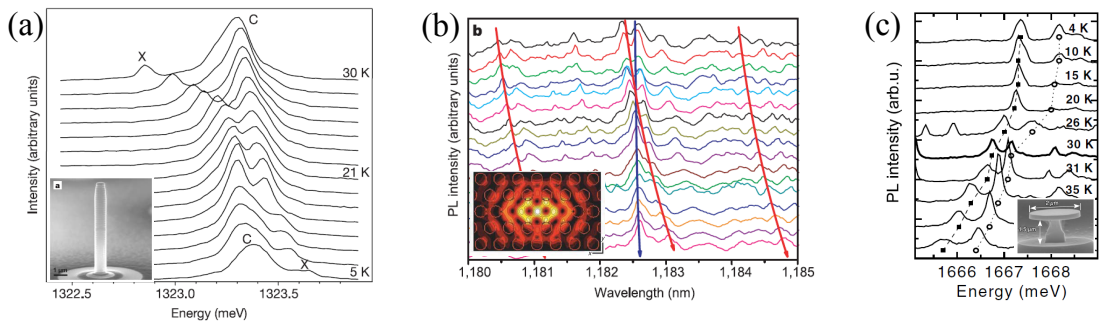

Figure 1.3: Seminal realizations of SC between semiconductor QDs with different type of microcavities: pillar [37] (a), photonic crystal cavity [46] (b) and microdisks [47] (c). All the experiments claimed the observation of SC reporting the avoided crossing of the exciton and cavity modes.

perfections in the fabrication the confinement is not perfect. Eventually photons leak out from the cavity at a certain rate, determining the so-called cavity losses. When a QD is embedded within a microcavity, the density of the EM modes into which it can decay is altered by the presence of the cavity. When the interaction with the cavity mode is smaller than the decay rate of photons leaking out the system, the main effect is a renormalization of the lifetime of the emitter according to the well-known Purcell effect [35]. This perturbative regime, named *weak-coupling* (WC) regime, can be calculated within an approach similar to the Fermi Golden Rule [36]. When the quality of the cavity is so good that the probability of reabsorbing the photon is bigger than the one to escape, this perturbative regime breaks down and strong-coupling (SC) regime takes place. SC is characterized by a reversible exchange of quanta between the QDs and a microcavity mode. The interest in this regime is two-fold: firstly, it is a requisite for many quantum information protocols. From the fundamental point of view [37], it gives rise to new quantum states of light-matter coupled systems, usually named *polaritons*. The manifestation of these new states is done through oscillations in mode populations in the temporal domain and with an avoided crossing of the exciton and cavity mode in the frequency domain.

The first report of SC of light and matter within the semiconductor context was achieved using quantum wells instead of QDs [38]. However, it is generally agreed that this normal mode coupling is basically classical effect [17], due to the high number of excitations taking part in the process. In fact, it can be qualitatively described in terms of Maxwell's equations coupled to excitonic susceptibility. The search for single quanta processes continued by putting efforts in reducing the dimensionality of the systems going to a QD picture [39, 40] and mastering the design of microcavities such as pillars [41], photonic crystal cavities [42–44] or microdisks [45].

All these efforts culminated with the –almost– simultaneous report of SC between QDs and pillar [37], photonic crystal [46] and microdisk [47] microcavities, shown in Fig. 1.3. The experimental signature of SC in all these reports is the avoided crossing between the exciton and the cavity mode. Since then, the field has witnessed many advances in the control of these systems. For instance, QDs can be precisely located inside the cavity [28, 29] and their state can be electrically controlled [48], paving the way towards on-chip control of cQED.

1.3.3 Semiconductor cQED in the context of open quantum systems.

Semiconductor cavity QED is a paradigmatic example where the theory of open quantum systems appears as an essential tool. Here, our system of interest is the composed QD-cavity system. However, there are many other elements that one must be taken into account. Firstly, as they are both optically active elements, the interaction with the vacuum radiative modes has to be considered. Besides, semiconductors underlying crystal structure supports the excitation of phonon modes that may couple to the QD. This mechanism can induce extra decoherence of the system different from the one coming from their finite linewidth. Finally, the excitation scheme typical in semiconductors is not done resonantly, but to higher levels of the QDs. This can be introduced as well in the master equation through the incoherent terms.

All these ingredients make the semiconductor cQED almost intractable from a first principles approach. Some successful attempts in this direction has been reported by using quantum many body theory [49] and methods such as clusters expansion [50]. Leading work in this direction has been also presented by [51], [52], [53] and [54].

Nonetheless, a more appealing approach for its simplicity and physical clarity is to treat all these ingredients in the semiconductor as reservoirs. Usually this can be done as they act simply perturbatively in the system dynamics. Then, we can include their effect through the incoherent terms of the master equation (Eq. 1.5. We leave the details of the discussion for Chapters 2 and 3, where it is shown how new incoherent elements appear in the master equation by tracing out the degrees of freedom of the different reservoirs. Though simpler, this approach succeeds capturing the basic effect of the different baths. In fact, this way of treating the problem has been able to achieve the best level of agreement with experimental data reported so far [48, 55].

1.4 Surface Plasmon Polaritons.

Photonic modes are not the only alternative to act as mediators of interaction between qubits. Surface Plasmon Polaritons (SPPs), an admixture of the collective charge excitation and the EM surface mode, have become increasingly popular in the last fer years since they were proven to be operating in the single quanta regime [56]. These new composited guided modes have emerged as candidates to enter in the miniaturization of quantum information devices were photonic modes are difraction-limited. In this Section, we just give a brief review of their properties in the classical regime together with a non-extensive review of the state of art within their quantum applications.

1.4.1 SPPs in the classical regime.

Maxwell equations tell us that the interaction between the light and the conduction electrons of the metal surface can lead to surface guided EM modes at the interface between a metal and a dielectric, the so-called SPPs. Their composite nature, schematically depicted in Fig. 1.4 (a), provides them most of their properties, e.g. the guided character.

The typical dispersion relationship of SPP, how their energy (ω) varies with their in-plane momentum (k), is plotted in Fig. 1.4(b). There, it can be observed that at small energies

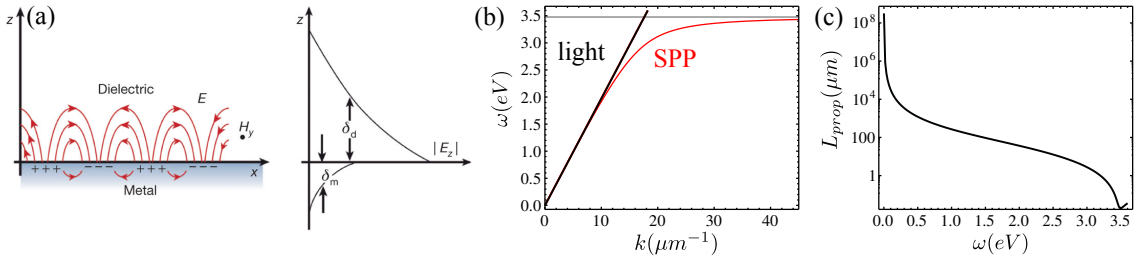

Figure 1.4: SPP properties: electric field distribution (a), dispersion relationship (b) and propagation length (c) for the SPPs supported in a silver-air interface.

the SPP energy lies close to the light-line being predominantly light-like. For THz-optical frequencies, the energy dispersion starts to bend until it reaches so-called cut-off frequency, where the SPP band becomes flat. Apart from this energy dispersion, there are three basic parameters determining the characteristics of SPPs:

- SPP wavelength, $\lambda_{spp} = 2\pi/k$: The interesting region for applications lies in the THz and optical regime, which corresponds to SPP wavelengths around $400nm - 1\mu m$.
- Decay length : The penetration length of the SPP field into the dielectric (denoted as δ_d in Fig. 1.4(a)). It measures the SPP capability to confine the field within the dielectric, i.e. for the optical regime it is around $100 - 300\,nm$.
- Propagation length, L_{prop}: It is the distance the SPP can travel before attenuating due to ohmic metallic losses. It is inversely proportional to the imaginary part of the parallel momentum k. It depends strongly on the metal properties and the frequency of operation. As an example, in Fig. 1.4(c) the propagation length for silver has been plotted as a function of the frequency. For the optical regime, which is the one we consider throughout this Thesis, is around $50\mu m$.

The last two magnitudes are closely related: longer propagation lengths are due to weakly localized SPP modes that extends widely in the dielectric and viceversa. This is the well-known trade-off between confinement and dissipation, which consequences in the light-matter coupling context are studied in Chapter 6. Remarkably, in the regions interesting for applications the interplay leads to subwavelength confinement and long propagation lengths [18, 19].

1.4.2 SPPs in the quantum regime.

The interest in using SPPs in a quantum optics and computation is two-fold. Due to their ability to confine EM field within a subwavelength scale, the possibility of reducing the size of the chips to the nanoscale is foreseen [57]. Secondly, the higher confinement also yields an enhancement of the light-matter coupling [58–60]. One of the main motivations to increase light-matter interaction is to achieve the so-called reversible or SC regime between the emitters and the SPP bath, which is useful for quantum information technologies.

The state-of-art theoretical and experimental investigations can be classified depending on the number of QEs that are interacting with the SPP field. A part of the experiments

is performed in the limit where only one QE is put in the presence of a metallic structure that supports the propagation of SPPs. The metal structures studied range from metallic nanowires [56, 61] to two-dimensional surfaces [62]. The generation of single SPPs, probing their quantum character, has been confirmed experimentally [56, 61, 62]. In all these experiments, the system is operating within the WC regime, as no back-action from the SPP is observed in the QE dynamics. Still interesting applications have been proposed within this regime, when few emitters are placed in front of these structures such as single-photon transistors [63] or mediation for qubit entanglement [64–66].

The opposite limit, where many QEs are placed in the surroundings of a metal-dielectric interface, has shown the emergence of SC in many experiments due to the collective enhancement ($\sqrt{N}$) of the coupling with the number of QEs. These experiments are similar to the normal mode coupling appearing quantum wells excitons [38]. Experiments have been done with different systems playing the role of QE ranging from organic molecules [67–70] to the excitons in QDs and quantum wells [71–73].

1.5 Summary of contents

The rest of the text is organized as follows:

- Chapter 2 introduces the basic formalism common to the rest of the Chapters. First, the different hamiltonian descriptions that we use to describe QEs and EM modes, namely the two-level system and harmonic oscillators respectively. A detailed derivation of the quantum optical master equation is given. We focus on the different incoherent terms that arise from the coupling of the different baths. Finally, we detail the different experimental tools available to characterize open quantum systems and their corresponding theoretical magnitude.

- In Chapter 3, we study the effect of the coupling to the bath of phonons in the observation of SC between a semiconductor QD and a microcavity. In the linear regime (low pumping), where there is still only one quanta of excitation involved, it only results in a broadening of the peaks in the luminescence spectrum. However, as the pumping increases and more excitations get involved, the system has a tendency to show robust triplet spectral shapes. We compare these spectral triplets to the ones recently reported in experiments [29, 74, 75].

- In Chapter 4, we present a new method to compute time and frequency resolved N-photon correlations. The basic idea is to study correlations between the different peaks of the spectra to learn about the dynamics of the system. Its formal definition in the standard theory is given in Chapter 2. However, in Chapter 4 we focus on our new approach to the problem that allows for computations otherwise unreachable. After having described the method, we show what kind of information one can get from this new kind of measurement by considering all possible combination of single and coupled quantum emitters. With a careful analysis we are able to identify a whole new zoology of processes, completely absent in other kind of measurements.

- In Chapter 5, we upgrade the two-level system description of the QD taking into account its spin degrees of freedom. Due to Coulomb interaction, when two excitons are present

in the system –*biexciton* state– its energy is decreased (or increased) due to attraction (repulsion) of the states. This energy shift, known as biexciton binding energy, allows to tune the cavity mode in resonance with the biexciton state and out of resonance of the single exciton resonance. We study the possibilities of this configuration to generate two-photon states in both an spontaneous emission and continuous (coherent and incoherent) pumping configuration.

- In Chapter 6, the focus is moved from semiconductor cQED systems to the interaction of QEs with SPPs. In this Chapter, we analyze in detail the possibilities of achieving the SC regime between single or many emitters and the SPPs present in a two-dimensional metallic system. In the single emitter situation, we upgrade our formalism in order to deal with the absorbing character of metals. We unravel the difficulties to achieve reversible dynamics in this limit. When many emitters are present, we develop an open quantum system description suitable to identify the optimal conditions for achieving SC and predict the possibility of observing quantum phenomena.

- Due to the difficulties to achieve the SC regime within the few QEs limit, in Chapter 7, we present a configuration where two QEs are interacting weakly with the SPPs modes of a one-dimensional plasmonic waveguide. By tracing out the SPPs degrees of freedom, an effective coherent and incoherent interaction between the QEs is obtained. Combined with two lasers, the steady-state of our two-qubit system can be controlled leading to entangled-stationary situations mediated by plasmons. The robustness of this proposal is analyzed by doing a systematic study in terms of the experimental parameters.

- In Chapter 8, we upgrade the previous configuration in several ways. We consider generic one-dimensional EM waveguides and consider many QEs instead of just two. We also consider different descriptions for the QEs, ranging from simple 2LS to more complex level schemes such as four-level configurations. By using coherent drivings, the steady-state of the system can be tuned. We show the possibility where pure entangled states of the ensemble of emitters can be found. Finally, a thorough discussion on the experimental feasibility is done to conclude the Chapter.

- Finally in Chapter 9, we provide a brief overview of the main results of this Thesis drawing some general conclusions.

Chapter 2

Theoretical background.

2.1 Introduction.

In this Chapter we introduce the formalism and tools that we use during the rest of the Thesis. We start describing the most basic systems, such as the two-level system and harmonic oscillators, that we use to model, e.g. the excitons of QDs, cavity modes, etc. After a brief introduction into the field quantization, we give a detailed derivation of a particular case of the master equation. We detail the different incoherent terms that arise from the kind of baths that are considered in this text. Finally, an extensive review on the experimental characterization of quantum optical systems is given, explaining the theoretical methods for computing them.

Most of the details of the Chapter can be found in many quantum optics textbooks [76], [34] or [77]. For a special emphasis in open quantum systems and decoherence there are specialized chapters in [25–27]. Other interesting works [78] or [79] are more focused on light-matter coupling in semiconductor environments.

2.2 Quantum emitters and electromagnetic fields.

2.2.1 Quantum emitters: two-level system approximation.

Quantum emitters (QEs) are the common link between all the Chapters of the Thesis. Their importance stems from the connection to the concept of qubit (*quantum bit*) introduced in the previous Chapter. Qubits are the central element of quantum information and computation schemes as it is where the information is encoded [7]. In general, any quantum system with two levels, "reasonably" isolated from the rest of world, can play the role of qubit.

We are basically interested in the possibility of developing quantum computation by optical means [15]. Thus, these two-levels are going to represent the ground ($|g\rangle$) and excited state ($|e\rangle$) of some QE with an optically active transition between them. Usually QEs, such as semiconductor QDs or molecules, are far more complicated than the simple two-level picture we use to describe them. However, most of the times the energy separation between other optically active levels is big enough to neglect their effect in the transition of interest. There are some situations, however, where interesting effects arise from a more complicated

picture as we show in Chapters 4 and 8, where we upgrade the description of QE to a more complicated scheme.

The intrinsic properties of the two-level system (2LS) approximation describing the QE are parametrized by two parameters: its transition frequency, ω_0, and the dipole moment strength of the optical transition, $\vec{\mu}$. Then, the description can be done in terms of σ-operators defined as:

$$\sigma^\dagger = |e\rangle\langle g| \,, \tag{2.1}$$

$$\sigma = |g\rangle\langle e| \,. \tag{2.2}$$

where $\sigma^\dagger$ (σ) are named as the creation (annihilation) operator of the QE. Their anti-commutation algebra:

$$[\sigma, \sigma^\dagger]_+ = 1 \,, \tag{2.3}$$

summarizes the fermionic properties of the σ-operator. Finally, the hamiltonian within the 2LS approximation can be written as:

$$H_0 = \omega_0 \sigma^\dagger \sigma \,. \tag{2.4}$$

Another ingredient needed for doing quantum computation is to have some mechanisms that allows for manipulation of the QE degrees of freedom. A first candidate can be monochromatic classical EM field, i.e. a laser field, which can be described through a time-dependent hamiltonian term [77]:

$$H_{\rm L}(t) = \Omega \sigma^\dagger e^{-i\omega_{\rm L} t} + \text{h.c.} \,, \tag{2.5}$$

where $\Omega \propto \vec{\mu} \cdot \vec{\mathcal{E}}$ (we assume it to be real), with $\vec{\mathcal{E}}$ representing the amplitude of the laser field. The dynamics of the combined QE-laser system can be obtained by solving Schrödinger equation (see Eq. 1.1). By using an ansatz: $|\phi(t)\rangle = c_g(t)|g\rangle + c_e(t)|e\rangle$, Eq. 1.1 yields a set of differential equation that can be solved analytically. For the particular case where the laser field is in resonance in the QE ($\omega_{\rm L} = \omega_0$) the solutions are:

$$c_g(t) = \cos(\Omega t) \,, \tag{2.6}$$

$$c_e(t) = i \sin(\Omega t) \,. \tag{2.7}$$

This solution tells us that one can switch the transition from $|g\rangle$ to $|e\rangle$ by choosing the time of interaction, t_0, with a (pulsed) laser field, e.g. $\Omega t_0 = n\pi/2$. In the language of quantum information the laser is "writing" or initializing the qubit. The possibility of solving the dynamics within a hamiltonian description relies on the assumption that the QE is a perfect isolated system. However, we already know that even if the QE is perfectly isolated in the vacuum, it is interacting with the background of radiative modes. In the next Section, we review how to consider this kind of irreversible processes.

2.2.2 Canonical quantization of the electromagnetic field.

Before studying the interaction between a QE and the radiation field from a quantum mechanical point of view, let us introduce the quantization of the EM field. To be concise we just review the basic steps of this quantization procedure, as it is extensively studied in all the quantum optics textbook. Quantization usually starts with Maxwell equations for the free field, in the absence of sources, that can be converted into wave equations:

$$\nabla^2 \vec{E} = \frac{1}{c^2}\frac{\partial^2 \vec{E}}{\partial^2 t}\,, \tag{2.8}$$

$$\nabla \times \vec{B} = \frac{1}{c^2}\frac{\partial^2 \vec{E}}{\partial^2 t}\,, \tag{2.9}$$

This choice is not causal, as the absence of sources allows us to deal implicitly only with transverse fields where $\nabla \cdot \vec{E} = 0$[1]. This is convenient because longitudinal fields do not satisfy a wave equation. For a deeper understanding on the consequences of this choice, one can look into Reference [80] where this problem is specifically addressed in detail.

The canonical quantization (in three dimensions) assumes a volume of quantization $V = L^3$ where the field is contained and solves the eigenvalue problem for Eqs. 2.8-2.9. The eigenmodes of such system are traveling waves ($e^{i\vec{k}\cdot\vec{r}}$) with allowed wavevectors $k_j L = 2\pi j_i$, where k_i represents the momentum in $i = x, y, z$ direction. Each $\vec{k}$ vector can have two polarization (denoted by the index λ) unit vectors such that:

$$\vec{k} \cdot \hat{e}_\lambda(\vec{k}) = 0\,, \tag{2.10}$$

$$\hat{e}_\lambda(\vec{k}) \cdot \hat{e}_{\lambda_1}(\vec{k}) = \delta_{\lambda,\lambda_1}\,, \tag{2.11}$$

$$\sum_\lambda \hat{e}^i_\lambda(\vec{k}) \cdot \hat{e}^j_\lambda(\vec{k}) = \delta_{ij} - \frac{k_i k_j}{k^2}\,. \tag{2.12}$$

With these normal modes, one constructs the quantum mechanical Hamiltonian corresponding to the classical energy of the EM field. It can be shown that this hamiltonian is formally equivalent to the one of a quantum harmonic oscillator. Thus, the quantization can be done along the same lines by defining the creation and annihilation operators of the EM field $a^\dagger_{\vec{k},\lambda}$ and $a_{\vec{k},\lambda}$. The final result of this process is the following free-energy hamiltonian for the field:

$$H_{\text{rad}} = \sum_{\vec{k},\lambda} \omega(\vec{k}) a^\dagger_{\vec{k},\lambda} a_{\vec{k},\lambda}\,, \tag{2.13}$$

where the electric field operator is given by:

$$\vec{E}(\vec{r}) = \sum_{\vec{k},\lambda} \sqrt{\frac{2\pi\omega(\vec{k})}{V}}\hat{e}_{\vec{k},\lambda}(a_{\vec{k},\lambda}e^{i\vec{k}\cdot\vec{r}} + \text{h.c.})\,, \tag{2.14}$$

[1] Another way of viewing it is as an implicit choice of the gauge where the $\phi = 0$ (scalar field) and $\nabla\cdot\vec{A} = 0$.

2.2.3 Quantum emitters interacting with a continuum of electromagnetic modes.

After having introduced the formalism to deal with quantized EM field, we address the effect of the interaction of a single QE interacting with a continuum of EM modes. A paradigmatic example of continuum is the one vacuum radiative modes. For simplicity, let us assume that only one polarization is relevant in order to drop the index λ of Eqs. 2.13, 2.14. Then, the interaction hamiltonian between the QE and the EM field is given by the product $\vec{d}\cdot\vec{E}$, where $\vec{d}$ is the dipole operator vector defined as follows: $\vec{d} = \vec{\mu}(\sigma + \sigma^\dagger)$. Combined with Eq. 2.14, one arrives to:

$$H_{\mathrm{I}} = \sum_{\vec{k}} g_{\vec{k}}(\sigma + \sigma^\dagger)a_{\vec{k}} + \mathrm{h.c}\,, \tag{2.15}$$

which contains two different kind of processes:

- Number of excitations conserving: $a\sigma^\dagger$ and $a^\dagger\sigma$.
- Number of excitations non-conserving: $a\sigma$ and $a^\dagger\sigma^\dagger$.

By writing H_{I} in the interaction picture:

$$H_{\mathrm{I}}(t) = \sum_{\vec{k}} g_{\vec{k}}(\sigma e^{-i\omega_0 t} + \sigma^\dagger e^{+i\omega_0 t})a_{\vec{k}}e^{-i\omega(\vec{k})t} + \mathrm{h.c}\,, \tag{2.16}$$

one realizes that the non-conserving processes are fast oscillating terms. Thus, they can be neglected as long as $|g_{\vec{k}}| \ll \omega_0 + \omega(\vec{k})$. This is the so-called *Rotating Wave Approximation*, under which the interaction hamiltonian can be finally written as:

$$H_{\mathrm{I}} \approx \sum_{\vec{k}} g_{\vec{k}}\sigma^\dagger a_{\vec{k}} + \mathrm{h.c}\,. \tag{2.17}$$

Once the hamiltonian has been determined, let us assume the QE is prepared in the excited state (i. e., with a laser field). As the interaction hamiltonian of Eq. 2.17 conserves the number of excitations, the Hilbert space of the problem can be restricted to: either the QE is in its initial excited state with no EM mode, $\left|e, 0_{\vec{k}}\right\rangle = \sigma^\dagger\left|0\right\rangle$, or it can be in the ground state after having decayed into one EM mode with a given $\vec{k}$, $\left|g, 1_{\vec{k}}\right\rangle = a^\dagger_{\vec{k}}\left|0\right\rangle$. Then, the evolution of the system can be expressed in terms of these two states:

$$\left|\Psi(t)\right\rangle = C_e(t)\left|e, 0_{\vec{k}}\right\rangle + C_{g,\vec{k}}(t)\left|g, 1_{\vec{k}}\right\rangle\,. \tag{2.18}$$

Schrödinger equation 1.1 yields a set of differential equations for $C_e(t)$ and $C_{g,\vec{k}}(t)$. By formally solving them, it is obtained an integro-differential equation for $C_e(t)$:

$$\dot{C}_e(t) = -\int_0^t K(t - t_1)C_e(t_1)dt_1\,. \tag{2.19}$$

The initial condition imposes $C_e(0) = 1$. The solution of this integro-differential equation is directly related with the excited state population through $n_\sigma(t) = |C_e(t)|^2$. The kernel of this integro-differential equation reads:

$$K(\tau) = \int_0^\infty d\omega J(\omega) e^{i(\omega_0-\omega)\tau}\,, \tag{2.20}$$

where $J(\omega)$ is the so-called *spectral density* of the bath. Its expression reads $J(\omega) = \sum_{\vec{k}} |g_{\vec{k}}|^2 = \rho(\omega)g(\omega)^2$, being directly proportional to the density of modes, $\rho(\omega)$, and the coupling to them, $g(\omega)^2$. From Eqs. 2.19-2.20 can be undestood that the *full* spectral density determines the QE-radiation dynamics. This is a good example to evidence that even the simplest problem leads to complicated time evolution within a hamiltonian description if no further simplifications are considered.

The coupling of a QE to a continuum is usually very weak, so further approximations can be made. Let us assume that the coupling to the bath is only a perturbation to the system and therefore $J(\omega)$ is *smooth* enough around ω_0. In this case, $J(\omega)$ can be extracted from the integral of Eq. 2.20 by approximating $J(\omega) \approx J(\omega_0)$. Then, it can be used that:

$$\int dt e^{iat} = \pi\delta(a) + i\text{P.V}\int dt e^{iat} \tag{2.21}$$

leading to:

$$K(\tau) \approx \frac{\Gamma(\omega_0)}{2}\delta(\tau) + i\text{P.V}\int_0^\infty d\omega J(\omega) e^{i(\omega_0-\omega)\tau}\,, \tag{2.22}$$

with $\Gamma(\omega_0) = 2\pi J(\omega_0)$. With this approximation of the kernel, the solution of the integro-differential equation is straightforward. It leads to an irreversible exponential decay of the excited state population of the QE $n_\sigma(t) = e^{-\Gamma(\omega_0)t}$, with rate of decay given by $\Gamma(\omega_0)$. It can be proven to be formally the same result than by using the Fermi Golden rule [36]. The principal value part gives the so-called *Lamb-shift* of the QE energy which is irrelevant for the purposes of the discussion. It yields a renormalization of the qubit energy ω_0 that is usually embedded in the definition of ω_0. Particularizing to the case of the vacuum radiation in three dimensions, it can be easily calculated that [58, 77] the spectral density is given by:

$$J_0(\omega) = \frac{\mu^2\omega^3}{6\pi^2\epsilon_0 c^3}\,. \tag{2.23}$$

This results proves that, even in vacuum, the QE decoheres at a rate:

$$\gamma_0 = \Gamma(\omega_0) = \frac{\mu^2\omega^3}{3\pi\epsilon_0 c^3}\,. \tag{2.24}$$

which is the so-called intrinsic decay rate of the QE. The intrinsic decay rate is proportional to the module of the dipole moment of the qubit ($\propto |\mu|^2$)). For this reason, in most of the Chapters we use γ_0 instead of the μ to parametrize the strength of the optical transition of the QE.

2.3 Open quantum systems: master equation formalism.

In the previous Section, it was shown how the hamiltonian description was very limited to calculate the dynamics of quantum systems having a lot of degrees of freedom. In these situations is where the open quantum system formalism becomes an essential tool to calculate the evolution of these systems. This formalism is especially suited for situation where one is solely interested in the dynamics of a small subset of a bigger system. The main result was summarized in the master equation described in Eq. 1.5. In this Section, we detail how to derive it and its application to particular cases of reservoirs that are considered throughout this Thesis.

2.3.1 General derivation of the master equation.

Let us continue the discussion where it was left it in the introductory Chapter. The starting point is the *Von Neumann* equation of the density matrix operator for the *total* system+reservoir system:

$$\frac{d\rho(t)}{dt} = -i[H, \rho(t)]\,, \tag{2.25}$$

where H describes the total hamiltonian: $H = H_S + H_R + H_{SR}$. It is convenient to re-write Eq. 2.25 in the interaction picture:

$$\frac{d\rho_{\mathrm{I}}(t)}{dt} = -i[H_{SR}(t), \rho_{\mathrm{I}}(t)]\,, \tag{2.26}$$

where $\rho_{\mathrm{I}}(t)$ and $H_{SR}(t)$ are operators in the interaction picture. Formally integrating it:

$$\rho_{\mathrm{I}}(t) = \rho_{\mathrm{I}}(0) - i\int_0^t ds[H_{SR}(s), \rho_{\mathrm{I}}(s)]\,. \tag{2.27}$$

Let us insert it again into Eq. 2.26 and trace over the degrees of freedom of the reservoir. Then, we get the evolution of the reduced density matrix of the system ($\rho_S = \mathrm{Tr}_R(\rho)$):

$$\frac{d\rho_{S,\mathrm{I}}(t)}{dt} = -\int_0^t ds \mathrm{Tr}_R\{[H_{SR}(t), [H_{SR}(s), \rho_{\mathrm{I}}(s)]]\}\,, \tag{2.28}$$

where we have neglected $Tr_R\{[H_{SR}(t), \rho_{S,\mathrm{I}}(0)]\}$. This process can be continuously iterated, however, two approximations are usually introduced at this point:

1. *Born approximation*: It is assumed that the coupling to the bath is so weak that the influence of the system on the reservoir is negligible. This justifies that the density matrix is separable at all times: $\rho(t) \approx \rho_S(t) \otimes \rho_R$. This does not mean that there are no excitations in the reservoir caused by the system, just that they decay in a time scale much faster than the one we are interested in to resolve.

2. *Markov approximation*: Connected to the previous approximation, it is also assumed that the dynamics of the reservoir is much faster than the dynamics of the system. Thus, any correlation induced in the reservoir is quickly lost. Mathematically it corresponds to replace $\rho_(s) \approx \rho(t)$ in Eq. 2.28 and extend the time integration to ∞.

With these two approximations, and going back to the Schrödinger picture, one arrives to the final *Born-Markov* master equation:

$$\frac{d\rho_S(t)}{dt} = -i[H_S(t), \rho_S(t)] - \int_0^\infty ds \mathrm{Tr}_R\{[H_{SR}(t), [H_{SR}(t-s), \rho_S(t) \otimes \rho_R]]\}\,, \tag{2.29}$$

which has the same functional expression as Eq. 1.5 presented in the introductory Chapter:

$$\frac{d\rho_S(t)}{dt} = -i[H_S, \rho_S(t)] + \mathcal{L}[\rho_S]\,. \tag{2.30}$$

The first part contains information about the coherent hamiltonian evolution of the system, whereas the second includes effectively the influence of the reservoir in the system dynamics. From now on, we drop the subindex S for the reduced density matrix and denote $\rho_S \to \rho$.

2.3.2 Reservoir induced coherent and incoherent processes in the master equation.

The functional form of $\mathcal{L}[\rho]$ depends basically on the nature of the reservoir and how it is coupled with the system through H_{SR}. In order to introduce the different terms that we use during the text, let us consider a system coupled to a reservoir through the following general interaction hamiltonian:

$$H_{SR}(t) = e^{i\omega_{\mathcal{O}} t}\mathcal{O}^\dagger E(t) + \mathrm{H.c.}, \tag{2.31}$$

where $\mathcal{O}$ represents any system operator and $E(t)$ is given by:

$$E(t) = \sum_{\vec{k}} g_{\vec{k}} a_{\vec{k}} e^{-i\omega_{\vec{k}} t} + \mathrm{h.c}\,. \tag{2.32}$$

For example, if $a_{\vec{k}}$ represents the vacuum radiative modes and $\mathcal{O} = \sigma$, then Eq. 2.31 recovers the typical QE-radiation dipolar interaction hamiltonian that we reviewed before. However, let us keep the discussion as general as possible and only particularize at the end. Computing the double commutator of Eq. 2.29 one arrives to the following master equation:

$$\begin{aligned}\frac{d\rho}{dt} = [\dots] &+ A(\mathcal{O}\rho\mathcal{O}^\dagger - \rho\mathcal{O}^\dagger\mathcal{O}) + B(\mathcal{O}^\dagger\rho\mathcal{O} - \rho\mathcal{O}\mathcal{O}^\dagger) \\ &+ C(\mathcal{O}\rho\mathcal{O}^\dagger - \mathcal{O}^\dagger\mathcal{O}\rho) + D(\mathcal{O}^\dagger\rho\mathcal{O}a - \mathcal{O}\mathcal{O}^\dagger\rho)\,,\end{aligned} \tag{2.33}$$

where $[\dots]$ represents other possible terms that are not directly related to the $H_{SR}(t)$ of Eq. 2.31. We have used the following properties:

- The cyclic properties of the trace $\mathrm{Tr}\{ABC\} = \mathrm{Tr}\{BCA\} = \mathrm{Tr}\{CAB\}$ to reorder the field operators that appear, i.e. $\mathrm{Tr}\{E^-(t)\rho_R E^+(t-s)\} = \mathrm{Tr}\{E^+(t-s)E^-(t)\rho_R\} = \langle E^+(t-s)E^-(t)\rangle$. This mean value is usually referred as the *field correlator of the bath.*

- The following commutation relationship for the bath operators:

$$\langle a_{\vec{k}} a_{\vec{q}} \rangle = \langle a^{\dagger}_{\vec{k}} a^{\dagger}_{\vec{q}} \rangle = 0\,, \tag{2.34}$$

$$\langle a^{\dagger}_{\vec{k}} a_{\vec{q}} \rangle = N(\omega_{\vec{q}})\delta_{\vec{k},\vec{q}}, \tag{2.35}$$

$$\langle a_{\vec{k}} a^{\dagger}_{\vec{q}} \rangle = (1 + N(\omega_{\vec{q}}))\delta_{\vec{k},\vec{q}}. \tag{2.36}$$

$$\tag{2.37}$$

The magnitudes A, B, C, D appearing in Eqs. 2.33 are calculated from the different bath correlators as follows:

$$A = C^* = \int_0^{\infty} ds e^{+i\omega_{\mathcal{O}} s} \langle E(t-s)E(t)\rangle =$$
$$\sum_{\vec{q}} |g_{\vec{q}}|^2 \big((1 + N(\omega_{\vec{q}})) \int_0^{\infty} ds (e^{-i(\omega_{\mathcal{O}} - \omega_{\vec{q}})s} + N(\omega_{\vec{q}}) \int_0^{\infty} ds e^{-i(\omega_{\mathcal{O}} + \omega_{\vec{q}})s}\big)\,, \tag{2.38}$$

$$B = D^* = \int_0^{\infty} ds e^{-i\omega_{\mathcal{O}} s} \langle E(t-s)E(t)\rangle =$$
$$\sum_{\vec{q}} |g_{\vec{q}}|^2 \big(N(\omega_{\vec{q}}) \int_0^{\infty} ds e^{i(\omega_{\mathcal{O}} - \omega_{\vec{q}})s} + (1 + N(\omega_{\vec{q}})) \int_0^{\infty} ds (e^{-i(\omega_{\mathcal{O}} + \omega_{\vec{q}})s}\big)\,, \tag{2.39}$$

The last step is to use the well-known relationship:

$$\int_0^{\infty} e^{\pm ias} = \pi\delta(a) \pm i\mathrm{P.V}\,. \tag{2.40}$$

With all this the master equation becomes:

$$\frac{\partial \rho}{\partial t} == [\dots] + i\Delta\omega[\rho, \mathcal{O}^{\dagger}\mathcal{O}] + \frac{\gamma(1 + N(\omega_{\mathcal{O}}))}{2}\mathcal{L}_{\mathcal{O}}[\rho] + \frac{\gamma N(\omega_{\mathcal{O}})}{2}\mathcal{L}_{\mathcal{O}^{\dagger}}[\rho]\,, \tag{2.41}$$

where we have adopted the following convention Lindblad super-operator:

$$\mathcal{L}_O(\rho) = (2O\rho O^{\dagger} - O^{\dagger}O\rho - \rho O^{\dagger}O)\,. \tag{2.42}$$

Let us now particularize for the case $\mathcal{O} = \sigma$ and explain the different terms that arise:

- The superoperator $\mathcal{L}_{\sigma}[\rho]$ represents an irreversible decay process due to the interaction with the reservoir. It is present even if $T = 0$ (which implies $N(\omega) = 0$). The parameter $\gamma = 2\pi J(\omega)$ is the modified lifetime due to the interaction with the bath. In the case $a_{\vec{k}}$ represents the vacuum radiative modes, the result from the Wigner-Weisskopf approach of the previous Section is recovered.

- When $T \neq 0$ ($N(\omega) \neq 0$) a new incoherent process appears described by the superoperator $\mathcal{L}_{\sigma^{\dagger}}[\rho]$. It represents the probability that the reservoir is returning some excitation back to the system incoherently due to its finite temperature. In Eq. 2.41 the rates of both processes are connected because we have implicitly assumed a bath in thermal

equilibrium in Eqs. 2.36-2.37. However, this is not always the case in real systems. For example, some incoherent pumping can emerge from out of equilibrium reservoirs, i.e. exciton reservoir in the wetting layer in QDs. Therefore, in the subsequent Chapters we use an independent pumping rate, $P_{\mathcal{O}}$, not directly connected to the decay rate.

- Together with the later incoherent processes, a new coherent term arises due to the interaction with the (virtual) modes of bath: the so-called *Lamb-shift*. Like in the Wigner-Weisskopf approach, it renormalizes the energy of the qubit. The explicit expression can be calculated from Eqs 2.38 2.39:

$$\Delta = \mathrm{P.V}\int_{-\infty}^{\infty} d\omega \frac{J(\omega)N(\omega)}{\omega_0 - \omega} + \mathrm{P.V}\int_{-\infty}^{\infty} d\omega \frac{J(\omega)(1+N(\omega))}{\omega_0 - \omega}\,. \tag{2.43}$$

  It is interesting to highlight here that in our initial interaction hamiltonian of Eq. 2.31 rotating and counter-rotating terms are preserved. If the latter were neglected, the incoherent terms would be the same, but the integral of Eq. 2.43 would extend only from 0 to ∞, leading to a wrong result. As the *Lamb-shift* is usually included in the definition of ω_0, the loss of the information is not so critical. Nonetheless, when more than one emitter is interacting through a common bath [81], special attention must be paid to the Cauchy principal value in order to accurately obtain the induced coherent couplings between the QEs.

Other common Lindblad term is the one originated from an interacting hamiltonian as in Eq. 2.31 with $\mathcal{O} = \sigma_z = [\sigma^\dagger, \sigma]$. This type of coupling typically arises from the coupling to vibrational baths [27], such as phonons or vibro-rotational degrees of freedom of molecules. By using that $\sigma_z^2 = 1$, the corresponding Lindblad superoperator reads [82]:

$$\frac{\gamma_x^\phi}{2}\mathcal{L}_{\sigma_z}[\rho] = \gamma_x^\phi\Big(\sigma_z\rho\sigma_z - \rho\Big)\,. \tag{2.44}$$

This mechanism is known as *pure dephasing* and its main effect is to erase the phase relationship between states (coherences) without altering directly the populations. With this mechanism, we have completed the description of single QE Lindblad terms that we use during this text. A generalization to many emitters for the particular case of one-dimensional reservoir is done in Appendix II, as it is needed for Chapters 7 and 8.

2.4 Experimental and theoretical characterization.

So far, we have introduced and explained in detail a simple way to deal with open quantum systems, including unitary and incoherent evolution on the same footing. The main prescription is to shift to a density matrix description of your system (ρ) rather than considering wavefunction ($|\Phi\rangle$). Then, Schrödinger equation is upgraded to a Born-Markov master equation:

$$\frac{d\rho}{dt} = -i[H,\rho] + \mathcal{L}[\rho]\,, \tag{2.45}$$

that includes the coherent evolution of the system (through H) and the incoherent processes due its open nature (through $\mathcal{L}[\rho]$). Once ρ is determined, all the information of the system can be calculated. The goal of this Section is to review the different magnitudes available for characterizing quantum systems and how to calculate them theoretically.

2.4.1 Mean values.

In general the quantum system of interest will be described by a set of operators a, b, etc., in a Hilbert space $\mathcal{H}$. In second quantization, these operators define annihilation operators in the Heisenberg picture. In some situations it is interesting to study the dynamics of the some of the modes of your system or its intensity of emission. These are related directly to single-time quantities that can be obtained from correlators of the type $\langle a^{\dagger\mu}a^{\nu}b^{\dagger\eta}b^{\theta}\ldots\rangle$ with μ, ν, η, θ, etc. being integer numbers. The dynamics of this general correlators can be calculated directly from ρ.

The straightforward approach consists of solving Eq. 2.45 to obtain $\rho(t)$ and then use $\langle\mathcal{C}\rangle = \mathrm{Tr}(\mathcal{C}\rho)$ to calculate its mean value. However, there is an alternative approach, namely the *correlator* approach, that most of the times is more efficient. Let us assume that we are interested in the dynamics of a particular single time quantity described by a particular operator $\mathcal{C} = a^{\dagger\mu}a^{\nu}b^{\dagger\eta}b^{\theta}\ldots$, then one can formally apply:

$$\frac{d\langle\mathcal{C}\rangle}{dt} = \mathrm{Tr}(\mathcal{C}\dot{\rho}) = \mathrm{Tr}\Big(\mathcal{C}(-i[H,\rho]+\mathcal{L}[\rho])\Big)\,, \tag{2.46}$$

and obtain the set of correlators which are linked to $\mathcal{C}$ through the equation of motion. This set of correlators can be grouped into a single vector $\mathbf{u}(t)$, whose dynamics is given by:

$$\frac{d\mathbf{u}}{dt} = M_0\mathbf{u}\,, \tag{2.47}$$

where M_0 is a matrix that can be formally obtained from Eq. 2.46. The solution is then straightforward: $\mathbf{u}(t) = e^{M_0 t}\mathbf{u}(0)$. In the case of a steady-state situation the problem can just be reduced to the inversion of a matrix.

2.4.2 First order correlation function and power spectrum.

In this Thesis, we are focused mainly on quantum optical systems. Most of the times, their open character comes from the leakage of radiation out from the system as depicted in Fig. 2.1. This represents not only a source of decoherence but also a way to extract information from it, i.e. to probe the inner structure of the system. This can be done by collecting all the photons coming from your system with a frequency sensitive single detector and doing statistics of the different frequencies detected. This measurement is usually referred as power spectrum or photoluminescence spectrum and we review now how to calculate it theoretically,

For the sake of illustration, let us assume that we are interested in observing the properties of the system through a given mode of the system, described by an operator a, which is leaking energy out of the system. The bridge between the quantum system and the observer can be made with the so-called input-output formalism: the photons *inside* the system, with operator a, are weakly coupled to an *outside* continuum of modes, with operators A_ω

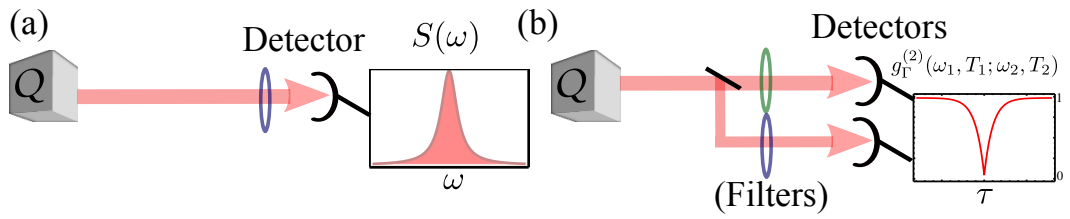

Figure 2.1: (a): Experimental scheme to measure one-photon spectrum: all the light of leaking out from the system is sent into a single detector that is able to resolve frequencies. This frequency sensitivity is schematically depicted as a filter before the detector. The filter determines the temporal and frequency response of the detector. (b): Experimental scheme to measure second order coherence function: the light leaking out from the system is divided into two beams and sent into two different detectors to study the correlation between them. If one is interested in frequency correlations, two filters should be included before the detector as depicted in the figure.

(corresponding to their frequency ω). In the Heisenberg picture, the output field allows to compute the time-dependent power spectrum of emission as the density of output photons with frequency ω_1 at time T_1:

$$S^{(1)}(\omega_1, T_1) = \langle A^\dagger_{\omega_1}(T_1) A_{\omega_1}(T_1) \rangle \,. \tag{2.48}$$

This quantity is physical (in the sense of being always positive and finite) only if the uncertainty of detection in both time and frequency are jointly taken into account [83]. Physically, this arrives from the fact that one is not directly looking to the *bare* fields, but it is always done through a detector which has both a frequency window and temporal response associated to it. In Fig. 2.1, this temporal and frequency uncertainty has been represented by filters. Mathematically, this amounts to adding two exponential decays in the Fourier transform of the time-autocorrelation:

$$S^{(1)}_{\Gamma_1}(\omega_1, T_1) = \frac{\Gamma_1}{2\pi} \iint_{-\infty}^{T_1} dt'_1 dt'_4 e^{-\frac{\Gamma_1}{2}(T_1 - t'_1)} e^{-\frac{\Gamma_1}{2}(T_1 - t'_4)} e^{i\omega_1 (t'_4 - t'_1)} \langle a^\dagger(t'_1) a(t'_4) \rangle \,, \tag{2.49}$$

where Γ_1 is interpreted as the frequency window of the detector. This translates through convolutions as uncertainties in the time of detection:

$$S^{(1)}_{\Gamma_1}(\omega_1, T_1) = \Gamma_1 \int_{-\infty}^{T_1} dt_1 e^{-\Gamma_1 (T_1 - t_1)} \Sigma^{(1)}_{\Gamma_1}(\omega_1, t_1) \,, \tag{2.50}$$

where:

$$\Sigma^{(1)}_{\Gamma_1}(\omega_1, t_1) = \frac{1}{\pi} \Re \int_0^\infty d\tau_1 e^{-\frac{\Gamma_1}{2}\tau_1} e^{-i\omega_1 \tau_1} \langle a^\dagger(t_1) a(t_1 - \tau_1) \rangle \,, \tag{2.51}$$

contains the uncertainty in the frequency of detection [84]:

$$\Sigma^{(1)}_{\Gamma_1}(\omega_1, t_1) = \int_{-\infty}^{\infty} d\omega'_1 \Sigma^{(1)}_0(\omega'_1, t_1) \frac{1}{\pi} \frac{\frac{\Gamma_1}{2}}{\left[(\frac{\Gamma_1}{2})^2 + (\omega'_1 - \omega_1)^2 \right]} \,. \tag{2.52}$$

The kernel of this expression corresponds to the case of a perfect detector, $\Gamma_1 = 0$, known as the Page–Lampard quasi-spectrum of emission $\Sigma_0^{(1)}(\omega_1, t_1)$ [85]. The results of Eberly and Wódkiewicz provide a time-dependent physical spectrum, which is:

- always positive, whereas $\Sigma_0^{(1)}(\omega_1, t_1)$ is not in general, and
- finite, even in the steady state $S_{\Gamma_1}^{(1)}(\omega_1, T_1 \to \infty) = \Sigma_{\Gamma_1}^{(1)}(\omega_1, t_1)$, whereas $S^{(1)}(\omega_1, T_1 \to \infty)$ diverges.

The Wiener–Khinchine theorem is recovered by the steady state physical spectrum in the limit $\Gamma_1 \to 0$, and in the places where there is no confusion we simplify the notation to:

$$S_{\Gamma_1=0}^{(1)}(\omega_1, T_1 \to \infty) = S(\omega_1) \tag{2.53}$$

2.4.2.1 Computing two-time averages: quantum regression theorem

We have shown that in order to calculate the spectrum of the system, one needs the following two-time correlator:

$$G^{(1)}(t, \tau) = \langle a^\dagger(t) a(t+\tau) \rangle \,, \tag{2.54}$$

usually known as the first order coherence function of the field. It can be computed from the one-time average correlators of Eq. 2.46 by recursing to the so-called *Quantum Regression Theorem* [86]. Here, we just enunciate it, but the curious reader can check very good demonstrations in the literature [27]. The theorem states that once a set of operators $C_{\{\eta\}}$, like the ones defined in the previous Section, satisfies:

$$\mathrm{Tr}(C_{\{\eta\}} \mathcal{L} \Omega_1) = \sum_{\{\lambda\}} M_{\{\eta\lambda\}} \mathrm{Tr}(C_{\{\lambda\}} \Omega_1) \,, \tag{2.55}$$

for a general operator Ω_1, and the corresponding matrix elements $M_{\{\alpha\beta\}}$ are found, then, the equations of motion for the two-time correlators have the same dynamics given by Ω_1 and $M_{\alpha\beta}$ as:

$$\frac{d}{d\tau} \langle \Omega_1(t) C_{\{\eta\}}(t+\tau) \rangle = \sum_{\eta\}} M_{\{\eta\lambda\}} \langle \Omega_1(t) C_{\{\lambda\}}(t+\tau) \rangle \,, \tag{2.56}$$

for $\tau \geq 0$. The initial conditions of Eq. 2.56 are the one-time averages that can be computed as explained in the previous Section from Eq. 2.46. Technical details of the calculation can be found in the literature [87]. Remarkably, once the set equations 2.55, 2.56 are solved, the structure of the spectrum has a transparent clear structure compared to other methods more based in numerics found in literature [88–90] which blind all the manifold information. For instance, for the case of the Wiener-Kintchine steady-state spectrum, the final shape of the spectra reads:

$$S(\omega) = \frac{1}{\pi} \sum_{p=1} \left[L_p \frac{\frac{\gamma_p}{2}}{\left(\frac{\gamma_p}{2}\right)^2 + (\omega - \omega_p)^2} - K_p \frac{\omega - \omega_p}{\left(\frac{\gamma_p}{2}\right)^2 + (\omega - \omega_p)^2} \right] \,, \tag{2.57}$$

where ω_p are the possible transitions in the system and γ_p their corresponding broadening, which are calculated from the diagonalization of the matrix M appearing in Eq. 2.56. The Lorentzian part corresponds to the decay of a dressed state whereas the dispersive part arises as an interference due to the overlap of energy of the dressed states. The factors L_p and K_p depend on factors like the dynamics of the initial state, channel of detection, etc.

2.4.3 Second order coherence function.

The first order coherence function or its Fourier transform (power spectrum) can only provide information on single particle events but no information at all about the statistics of the light emitted. In order to get this information, one must go further in the order of correlation function. The most popular one is the second-order coherence function of the system, $g^{(2)}(\tau)$. The experimental set-up, depicted in Fig. 2.1(b), uses a beam-splitter to divide the light in two beams that go into different detectors. Then, one studies the correlation between the different photon-clicks in the detector. Here, there are two-possible configurations:

- Before letting the beams into each detectors, one can put a filter, of frequency window Γ_i, to select a certain frequency ω_i and then study the correlations. This is the so-called time and frequency resolved correlations, which are the topic of study of Chapter 4.
- One can let all the light of the beams go through (no filter), obtaining the standard second order correlation function: $g^{(2)}(\tau)$. Even in the absence of filters, one should consider that the detection process has an intrinsic frequency window and temporal response that has to be taken into account properly to get meaningful results.

The two magnitudes are equivalent if one considers very broad filters ($\Gamma_i \to \infty$). Thus, we present the most general derivation –with filters included– and then particularize for colorblind detectors. Following the line of argumentation for the one-photon spectrum, we want to extend the results for the detection of two photons at given times and frequencies, ω_1 at T_1 and ω_2 at $T_2 = T_1 + \tau$. This is formally straightforward, simply by considering two detectors with their respective linewidths Γ_1 and Γ_2 [91]. The multiplicity of photons requires time ($\mathcal{T}$) and normal (:) ordering of the photon operators [92] and $\mathcal{T}\langle :A^\dagger_{\omega_1}(T_1)A_{\omega_1}(T_1)A^\dagger_{\omega_2}(T_2)A_{\omega_2}(T_2):\rangle$ upgrades to:

$$S^{(2)}_{\Gamma_1\Gamma_2}(\omega_1,T_1;\omega_2,T_2) = \frac{\Gamma_1\Gamma_2}{(2\pi)^2}\iint_{-\infty}^{T_1} dt'_1 dt'_4 e^{-\frac{\Gamma_1}{2}(T_1-t'_1)}e^{-\frac{\Gamma_1}{2}(T_1-t'_4)} \times$$
$$\iint_{-\infty}^{T_2} dt'_2 dt'_3 e^{-\frac{\Gamma_2}{2}(T_2-t'_2)}e^{-\frac{\Gamma_2}{2}(T_2-t'_3)}e^{i\omega_1(t'_4-t'_1)}e^{i\omega_2(t'_3-t'_2)}\mathcal{T}\langle a^\dagger(t'_1)a^\dagger(t'_2)a(t'_3)a(t'_4)\rangle. \quad (2.58)$$

Normalising this expression gives rise to the time- and frequency- resolved two-photon correlation function:

$$g^{(2)}_{\Gamma_1\Gamma_2}(\omega_1,T_1;\omega_2,T_2) = \frac{1}{S^{(1)}_{\Gamma_1}(\omega_1,T_1)S^{(1)}_{\Gamma_2}(\omega_2,T_2)}\Gamma_1\Gamma_2\int_{-\infty}^{T_1}dt_1\int_{-\infty}^{T_2}dt_2$$
$$\times\, e^{-\Gamma_1(T_1-t_1)}e^{-\Gamma_2(T_2-t_2)}\Sigma^{(2)}_{\Gamma_1\Gamma_2}(\omega_1,t_1;\omega_2,t_2)\,, \quad (2.59)$$

where we have also isolated the *two-photon quasi-distribution*:

$$\Sigma^{(2)}_{\Gamma_1\Gamma_2}(\omega_1,t_1;\omega_2,t_2)=\frac{2\Re}{(2\pi)^2}\iint_0^\infty d\tau_1 d\tau_2 e^{-\frac{\Gamma_1}{2}\tau_1}e^{-\frac{\Gamma_2}{2}\tau_2}$$
$$\times e^{-i\omega_2\tau_2}[e^{i\omega_1\tau_1}\mathcal{T}\langle a^\dagger(t_1-\tau_1)a^\dagger(t_2)a(t_2-\tau_2)a(t_1)\rangle+e^{-i\omega_1\tau_1}\mathcal{T}\langle a^\dagger(t_1)a^\dagger(t_2)a(t_2-\tau_2)a(t_1-\tau_1)\rangle]\,, \tag{2.60}$$

which, analogously to the one-photon quasi-spectrum, can be negative and is thus not a physical spectrum. The time-convoluted $g^{(2)}_{\Gamma_1\Gamma_2}$ is, on the other hand, positive, finite and qualifies to measure correlations. It takes into account that frequency and time of emission cannot be both measured with arbitrary precision, in accordance with Heisenberg uncertainty principle. In order to obtain it, one needs to calculate first the four-time averages: $\langle a^\dagger(t_1)a^\dagger(t_2)a(t_2-\tau_2)a(t_1-\tau_1)\rangle$ appearing inside the integrals, by using three-times (or two in steady-state situations) the Quantum Regression Theorem.

The limiting behaviors of $g^{(2)}_{\Gamma_1\Gamma_2}$ defined as in Eq. 2.59 are those expected on physical grounds: photons are uncorrelated at infinite delays,

$$\lim_{|T_2-T_1|\to\infty} g^{(2)}_{\Gamma_1\Gamma_2}(\omega_1,T_1;\omega_2,T_2)=1\,. \tag{2.61}$$

By assuming color-blind detectors, the standard two-time correlators is recovered:

$$\lim_{\Gamma_1,\Gamma_2\to\infty} g^{(2)}_{\Gamma_1\Gamma_2}(\omega_1,T_1;\omega_2,T_2)=g^{(2)}(T_1;T_2)\,. \tag{2.62}$$

In the steady-state, the notation is usually simplified to: $g^{(2)}(T_1;T_2)\to g^{(2)}(\tau)$. The most relevant information can be even obtained from its $\tau=0$ value:

- If $g^{(2)}(0)>1$, the photons coming out from the system are said to be *bunched* and is a typical signature of multiphoton processes.
- If $g^{(2)}(0)=1$, then the photons are said to be *coherent*. This is what one gets for example from a classical laser field.
- If $g^{(2)}(0)<1$, the photons are said to be *antibunched*, as for example in the case of single photon emitters. This is the smoking gun of the quantum character of the system, as it can never be obtained in a classical system.

2.4.4 Generalization to N-photon correlations.

Further generalizations of Eq. (2.59) to N-photon correlations, adding pairs of operators (with the corresponding integrals and detectors) [93] quickly become intractable and have proven to be already demanding for two photons only, even in the simplest case of zero time delay. The main reason for this difficulty is that all the possible time orderings of the $2N$-time correlator $\mathcal{T}\langle a^\dagger(t'_1)\dots a^\dagger(t'_N)a(t'_{N+1})\dots a(t'_{2N})\rangle$ result in $(2N-1)!!2^{N-1}$ independent regions of integration. Furthermore, each of these correlators requires the application of the quantum regression theorem $2N-1$ times. This growth of the complexity makes a direct computation hopeless for a quantity which is otherwise straightforward to measure experimentally, merely

by detecting photon clicks as function of time and energy. This technology can be provided for instance by a streak camera [94].

Despite the experimental importance of the general problem, the theoretical literature to date addressed only two-time correlators of simple systems such as resonance fluorescence, which allows strong approximations [91, 95], or in particular cases such as zero time delay [96]. In Chapter 4, we present a new approach to this problem beyond the standard theory that we have detailed here. It allows a much more efficient way of calculating all these magnitudes and calculate system hitherto intractable. As this is a recently developed method within this Thesis we have moved the discussion to a separate Chapter, where we include the details of the method and the results of its application to a wide variety of systems.

Chapter 3

Pure dephasing effects in the cavity QED non-linear regime.

3.1 Introduction.

The strong-coupling (SC) between the excitons in quantum dots (QDs) and a photonic cavity mode is now a commonplace in semiconductor cQED physics (see [29, 48, 97–100] for some recent reports). The best figures of merit, however, are still far from what has been obtained with atoms [13] or superconducting qubits [101]. However, when this quantum control will be ripe for technology, it is clear that semiconductors will play a primordial role for cheap and massive deployment. For this reason, it is important to evidence, understand and manipulate quantum interactions between photons and excitons in these systems.

The most appealing features of SC are at the quantum level, when a finite number of quanta of excitations are involved. A splitting at resonance is a tempting landmark of SC, but is in no essential way different from the normal mode coupling that is a classical feature of coupled oscillators [102]. To evidence the quantum character of the coupling, photon-counting experiments have been performed, that reported that only one quantum of excitation couples the modes [29, 97]. The next step is to probe nonlinearities and witness their sensitivity at the quantum level. Because the QD is a 2LS with saturable character, coupling it strongly with more than one photon yields a dressed-mode splitting that goes like $\sqrt{n}g$ when n quanta are involved (being the g the interaction strength). The transitions between these dressed states provide spectral lines at incommensurate energies $(\pm\sqrt{n} \pm \sqrt{n-1})g$. They provide a direct manifestation of full-field quantization, as predicted by one of the most important theoretical model of quantum physics, the Jaynes-Cummings (JC) Hamiltonian [103], that fully quantizes both the atomic and the optical fields. Evidencing these nonlinearities are one of the most important goal of quantum optics. This goal has been fulfilled with atoms [104] and more recently with superconducting circuits [105], but remains elusive for semiconductor quantum dots.

In this Chapter, we study the effects of a typical enemy of quantum control in semiconductors, namely *pure dephasing*. As explained in Chapter 2, it can appear due to the interaction with phonons at low temperatures [106]. Other possible mechanism inducing pure dephasing is the presence carriers outside the QD [107] at higher temperatures. In this text, the

microscopic nature will be overlooked. We do not pay attention to the specific mechanism causing it, just assume that it is non-negligible and treat it as a reservoir of the type described by Eq. 2.44. A careful experimental and theoretical analysis in these systems [48] has given compelling evidence that that a pure dephasing term is an important ingredient in semiconductor physics.

The structure of this Chapter is the following: first, in Section 3.2 we introduce and explain in detail all the ingredients needed to describe the dissipative JC model. This is the starting point many results of this Thesis, and in particular of this Chapter. Then, in Section 3.3 we describe the differences between the linear and non-linear regime. In Section 3.4, pure dephasing is introduced into the Master Equation of the system and study its effect in the spectral shapes, where as in Sections 3.5-3.6 a qualitative and quantitative comparison with reported experimental data is done. Finally, the main results are summarized in Section 3.7.

3.2 Dissipative Jaymes-Cummings model (cQED).

3.2.1 Coherent processes.

In this Section, we introduce the basic ingredients to describe the semiconductor cQED systems. Following the notation of open quantum systems, the system of interest is composed by the exciton of the QD, which interacts coherently with a cavity mode. The exciton in the QD is approximated within a two-level system (2LS) description as explained in Section 2.2, whereas the cavity mode is described as a quantum harmonic oscillator. The complete hamiltonian that describes the coupling between the two modes is the celebrated Jaynes-Cummings (JC) hamiltonian [103]:

$$H = \omega_a a^\dagger a + (\omega_a - \Delta)\sigma^\dagger\sigma + g(a^\dagger\sigma + a\sigma^\dagger)\,, \tag{3.1}$$

with a the photon annihilation operator (following Bose statistics) and σ the material excitation annihilation operator (following Fermi statistics). The parameter $\Delta = \omega_a - \omega_0$ is the detuning between the two modes and g the interaction strength. Notice that the hamiltonian in Eq. 3.1 involves a *Rotating Wave Approximation* that imposes the condition $g \ll \omega_a, \omega_0$. Thanks to this approximation, the hamiltonian is excitation-conserving which makes the quantum dynamics to be enclosed in 2×2 Hilbert subspaces for a fixed excitatiom number, admitting an analytical solution. These Hilbert subspaces of JC hamiltonian are usually named as *manifolds* of excitations or *rungs* of the JC ladder. Their eigenstates, called *polariton* or *dressed states*, are denoted by $|n, \pm\rangle$. They appear as a ladder structure, as depicted in Fig. 3.1(a), and diagonalize the hamiltonian as follows:

$$H = \sum_n (\omega_{L,n} |n,-\rangle \langle n,-| + \omega_{U,n} |n,+\rangle \langle n,+|)\,. \tag{3.2}$$

Their eigenenergies are n-dependent:

$$\Omega_{L(U),n} = \frac{n\omega_a + \omega_0}{2} \pm R_n^0\,. \tag{3.3}$$

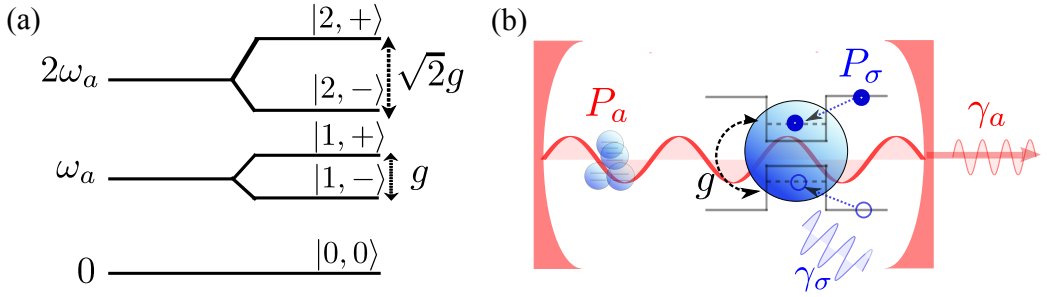

Figure 3.1: (a) Dissipative Jaynes-Cummings ladder up to the second rung or manifold. (b) General scheme of semiconductor cavity QED processes: QE-cavity coherent coupling, cavity losses, leaky modes and cavity and QE incoherent pumping.

R_n^0 gives the splitting between the states of the n-th rung:

$$R_n^0 = \sqrt{(\sqrt{n}g)^2 + \left(\frac{\Delta}{2}\right)^2}\,, \tag{3.4}$$

which contains the important $\sqrt{n}$ dependence of the splitting. This $\sqrt{n}$-dependence gives the non-linear behavior to the system dynamics. The most fundamental case corresponds to the case of the the first manifold $n = 1$, where only one quantum of excitation is being exchanged coherently between the QE and the cavity mode. At resonance, the eigenvectors are:

$$|1,\pm\rangle = \frac{1}{\sqrt{2}}(|1,0\rangle + \pm\,|0,1\rangle)\,. \tag{3.5}$$

This reversible exchange manifests as oscillations in the population dynamics of the *bare* states with frequency proportional to R_1^0. Another signature is an splitting, again proportional to R_1^0, in the frequency domain (i.e. in the spectrum) which yields a doublet shape known as *Rabi* doublet. As there is only one quantum of excitation being exchanged between the two fields R_1^0 this splitting is usually called *Vacuum Rabi splitting*.

3.2.1.1 Bosonization of the QD operators.

There are some situations in which one can consider a bosonic description for the QD operator σ:

- In large QDs, the excitation energy levels are very close to each other and one can neglect the Pauli effects coming from the fermionic nature of the components of the exciton QD.
- In situations where the exciton QD is very little occupied, $\langle\sigma^\dagger\sigma\rangle \ll 1$, only the first manifold of excitation is relevant for the description. In these cases, one can always *bosonize* or *linearize* the QD operator, inspired in the Holstein-Primakoff approximation [108]: $\sigma = \sqrt{1 - b^\dagger b}\,b$, with b satisfying $[b, b^\dagger] = 1$. To first order, it consists of substituting the fermionic operator, σ, by a bosonic one, b. One should be aware that this approximation is able to obtain accurate results only for "one-photon" properties, i.e. one-photon spectrum, but fails to capture properties like the statistics of the field.

In both cases, the 2LS operator σ is transformed into a bosonic operator b. This is what is usually called in the literature as the *linear model* [109, 110].

3.2.2 Incoherent processes.

It has been emphasized that the cavity-QD system is far from being a closed system. It is interacting with several reservoirs as it has been schematically depicted in Fig. 3.1(b). All of them should be taken into account in the density matrix description of the system:

- Even in the simplest picture, one should take into account that the exciton is also interacting with the vacuum radiative modes of the QD and emits radiation through them. In the notation of cQED these are the so-called *leaky modes* that emit at a rate γ_σ. They are described, following the prescriptions of Chapter 2, through a Lindblad superoperator: $(\gamma_\sigma/2)\mathcal{L}_\sigma[\rho]$.

- The cavity is intended to produce a perfect confinement of the light. However, due to imperfections in fabrication, there is always some escape of photons through the mirrors at a rate γ_a. Thus, it can be described through a Lindblad term: $(\gamma_a/2)\mathcal{L}_a[\rho]$. The quality of the cavity is usually characterized by the so-called Q-factor which is inversely proportional to the cavity decay rate: $Q = \omega_a/\gamma_a$.

- One essential ingredient distinguishing semiconductor cQED from their atomic counterpart is the excitation of the system. In Fig. 3.1(b), we have schematically depicted the most common way of exciting these systems: usually excitation is done, optically or by electric injection, to the electronic levels far above resonance. This excitation creates a reservoir of electron-hole pairs that relax incoherently into the QD of interest. There are indeed microscopic derivations of these mechanisms [111, 112], but for our purposes, we adopt an heuristic model to investigate the pumping at a fundamental level. As the nature of bath is inherently not in thermal equilibrium, it is described through a Lindblad operator, $(P_\sigma/2)\mathcal{L}_{\sigma^\dagger}[\rho]$, but with a pumping rate P_σ independent of γ_σ.

- For completeness, we also consider another type of pumping, which offers a counterpart for the cavity by injecting photons incoherently. As mentioned in the introductory Chapter, the self-assembled fabrication of QDs is a random process. Most of the times, together with the optically active QD that interacts strongly with the cavity, other randomly positioned QDs are also created in the neighborhood of the system. These *spectator* QDs interact very weakly with the cavity. As they are also excited by the reservoir of electron-hole pairs, they can leak some excitation into the cavity. In turn, this results in an effective cavity pumping [113, 114], which has to be described though a Lindblad term: $(P_a/2)\mathcal{L}_{a^\dagger}[\rho]$.

Taking into account all these processes, one finds that the evolution of the cavity-QD system is given by:

$$\frac{\partial \rho}{\partial t} = i[\rho, H] + \frac{\gamma_a}{2}\mathcal{L}_a[\rho] + \frac{\gamma_\sigma}{2}\mathcal{L}_\sigma[\rho] + \frac{P_a}{2}\mathcal{L}_{a^\dagger}[\rho] + \frac{\gamma_\sigma}{2}\mathcal{L}_\sigma[\rho]\,, \tag{3.6}$$

This is the so-called dissipative JC model. It has been throughly described in the literature and constitutes the starting point for our calculations. The incoherent processes renormalize the energy of the *polariton* states ($|n,\pm\rangle$) as follows:

$$E_{n,\pm} = n\omega_a - \frac{\Delta}{2} - i\frac{(2n-1)\Gamma_a + \Gamma_\sigma}{4} \pm \sqrt{(\sqrt{n}g)^2 - \left(\frac{\Gamma_a - \Gamma_\sigma}{4} + i\frac{\Delta}{2}\right)^2}. \tag{3.7}$$

The eigenenergies are now complex due to their dissipative part: the real part corresponds to the position of the energy, whereas the imaginary part reflects the broadening of the transition. The second part of Eq. 3.7 is the renormalized Rabi frequency for the dissipative JC model:

$$R_n = \sqrt{(\sqrt{n}g)^2 - \left(\frac{\Gamma_a - \Gamma_\sigma}{4} + i\frac{\Delta}{2}\right)^2}. \tag{3.8}$$

For the case corresponding the first rung, $n = 1$, we drop the subindex and just write $R_1 \equiv R$.

3.3 Linear vs non-linear regime.

Before studying in detail the effect of other kind of reservoirs, i.e. phonon bath, we review here some useful results that are relevant for our posterior discussion on the effect of pure dephasing. In particular, we study the differences between the linear and non-linear regime of the JC model. A special emphasis is made on the differences arising in the photoluminescence spectra.

The characterization of the different regimes appearing as a function of the incoherent pumping can be done through the study of the three following observables of the system:

- Cavity population: $n_a = \langle a^\dagger a\rangle$.
- QD population: $n_\sigma = \langle \sigma^\dagger \sigma\rangle$.
- Second order coherence of the light emitted by the cavity: $g_a^{(2)}(0) = \langle a^\dagger a^\dagger a a\rangle / n_a^2$.

In order to calculate them, we follow the procedure detailed in Section 2.4.1 (or here [87]). We define a general operator correlator $\langle (a^\dagger)^m a^n (\sigma^\dagger)^\mu \sigma^\eta\rangle$ and calculate the vector of correlators which are linked to it through the master equation. In Fig. 3.2 the evolution of these three observables as a function of P_σ is plotted for a situation with no dephasing (solid lines). The different colors indicate different cavity decay rates $\gamma_a/g = 0.2, 0.5, 1, 2$ (see the legend). In the case of the cavity population –n_a– the observable has been renormalized with the corresponding γ_a so that they all converge to a single line. In this figure, it is possible to identify four different regimes which are commonly named in the literature [115, 116] as:

1. *Linear regime*: when $P_\sigma \ll \gamma_\sigma$ the emitter is basically in the ground state, being only able to probe the first *rung* of the JC ladder. Here, the substitution of $\sigma \to b$ for a bosonic operator yields the same result.
2. *Non-linear quantum regime*: when $P_\sigma \approx \gamma_\sigma$, the emitter is able to probe a few rungs of the JC ladder, but without going so high that many photons effect dominates.

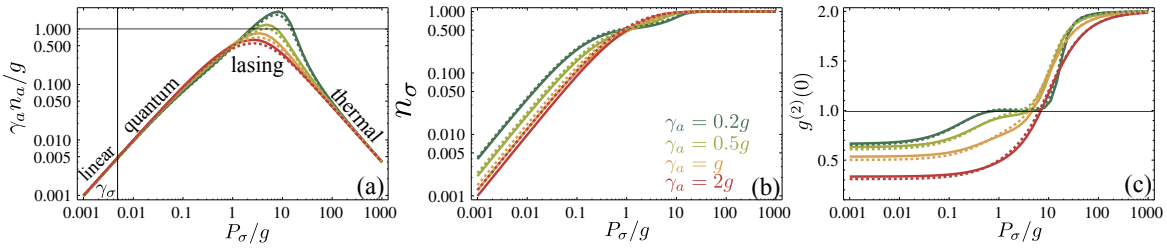

Figure 3.2: Evolution of the observables $\gamma_a n_a/g$ (a), n_σ (b) and $g_a^{(2)}(0)$) in the dissipative JC model as a function of P_σ for a system with $P_a = 0$, $\gamma_\sigma = 0.005g$ and $\gamma_\sigma^\phi = 0$ (solid) or $\gamma_\sigma^\phi = g$ (dashed). The different colors represent different values of γ_a indicated in the legend. In panel (a) are indicated the four different regions described in the main text: linear, quantum, lasing and thermal.

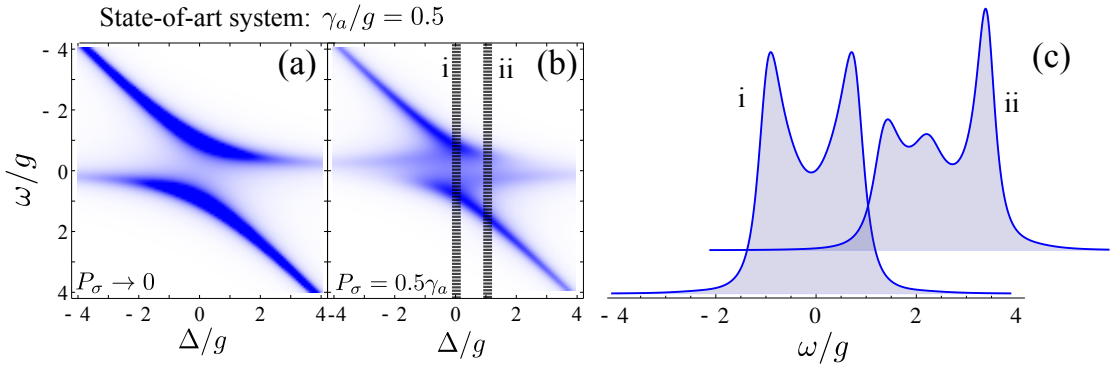

Figure 3.3: (a) Contour plot of the spectral shape, $S(\omega)$, of a cavity with $\gamma_a = 0.5g$ and $\gamma_\sigma = 0.001g$ as a function of detuning for a pumping in the linear regime ($P_\sigma \to 0$) with $P_a = 0$. (b) Same as in panel (a), but for a pumping in the non-linear regime $P_\sigma = 0.5g$. (c) Two cuts of the spectral shape on resonance (i) and out of resonance (ii) .

3. *Lasing or non-linear classical regime*: when $P_\sigma \gg \gamma_\sigma$, the emitter population is around $n_\sigma \approx 0.5$, and $g_a^{(2)}(0) \approx 1$ as in a classical field. This is where the cavity grows coherence emitting like a laser.

4. *Thermal regime*: when the pumping is so high than the emitter is mainly excited ($n_\sigma \approx 1$) and the dephasing induced by the pump disrupts the coherent coupling so that the number of photons is very low again and the field becomes thermal ($g_a^{(2)} \approx 2$). The intermediate region between the lasing and the thermal regime is called *self-quenching*.

For this Chapter, we focus only on the two first regions. Due to the incoherent nature of excitation in semiconductor systems, the access to the non-linear regime is not a trivial issue as one needs a high pumping to go up in the JC ladder, but the incoherent nature also disrupts SC. However, in the next Chapter we also explore the properties of the other regimes, i.e. lasing.

Here, we are interested in the spectral signatures in the emission of the cavity when the QD is pumped incoherently. This particular choice is the most common experimental configuration in semiconductor cQED. In Fig. 3.3, we study the cavity photoluminescence

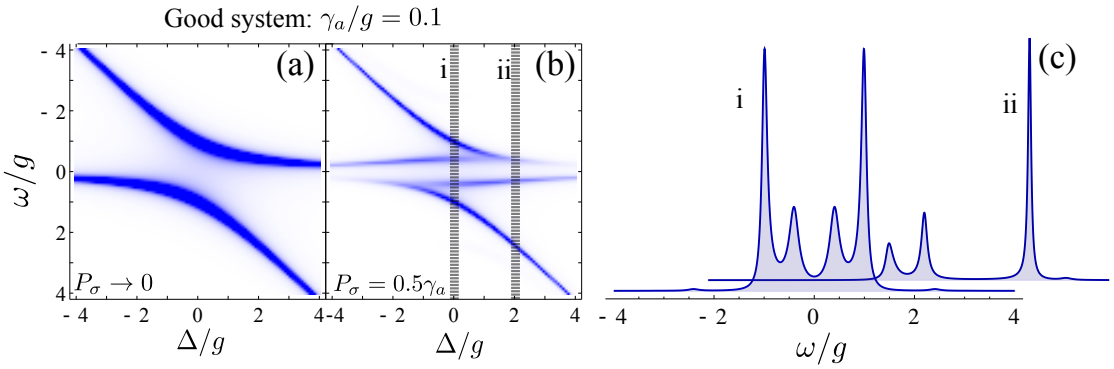

Figure 3.4: (a) Contour plot of the spectral shape, $S(\omega)$, of a cavity with $\gamma_a = 0.5g$ and $\gamma_\sigma = 0.001g$ as a function of detuning for a pumping in the linear regime ($P_\sigma \to 0$) with $P_a = 0$. (b) Same as in panel (a), but for a pumping in the non-linear regime $P_\sigma = 0.5g$. (c) Two cuts of the spectral shape on resonance (i) and out of resonance (ii)

spectrum, $S(\omega)$, as a function of the detuning of the QD in the linear and non-linear regime. The parameters considered for the cavity and exciton lifetime are $\gamma_a = 0.5g$ and $\gamma_\sigma = 0.001g$ respectively, which lie in the order of the state-of-art in semiconductor cQED [74, 117]. In the linear regime (Panel a, $P_\sigma \to 0$), one only observes the Vacuum Rabi splitting between the exciton and the cavity mode for all the possible detunings. In the case of a higher pump (Panel b,$P_\sigma = 0.5\gamma_a$), one still observes just a doublet in resonance in the cavity spectra. Only through a finite detuning, $\Delta \neq 0$, an asymmetric spectral triplet can be obtained. The extra peak comes from the transitions from the second rung of the ladder of Fig. 3.1(a). However, it practical terms it is difficult to resolve it and in fact no direct observation of the higher rungs of the ladder in semiconductor cQED has been reported by the time of writing. The only evidence of the higher rungs has been achieved through four-wave mixing experiments [118].

In Fig. 3.4, a cavity decay rate beyond the state-of-art of semiconductor parameters has been considered, $\gamma_a = 0.1g$ (and $\gamma_\sigma = 0.001g$). This value lies closer to the parameters of circuit QED [101]. In the linear regime (Panel a), only the Rabi doublet is resolved. Nonetheless, in the non-linear regime (Panel b) at resonance the system clearly shows a "fork" due to the four transitions involving the first two rungs of the ladder (clearly resolved in Fig. 3.4(c.i)). The symmetry is broken, when one considers an out of resonance situation, with a clearly asymmetric spectral triplet shape in Fig. 3.4(c.ii).

3.4 Effect of pure dephasing.

Now, we study the effect of *pure dephasing* in the observation of SC in the linear and non-linear regime. As detailed in Section 2.3.2, pure dephasing is described as an additional Lindblad term in the dissipate JC model [82]:

$$\frac{\partial \rho}{\partial t} = i[\rho, H] + \frac{\gamma_a}{2}\mathcal{L}_a[\rho] + \frac{\gamma_\sigma}{2}\mathcal{L}_\sigma[\rho] + \frac{P_a}{2}\mathcal{L}_{a^\dagger}[\rho] + \frac{\gamma_\sigma}{2}\mathcal{L}_\sigma[\rho] + \frac{\gamma_\sigma^\phi}{2}\mathcal{L}_{\sigma_z}[\rho]\,, \tag{3.9}$$

where $\sigma_z = [\sigma^\dagger, \sigma]$ [82]. When considering the general correlator $\langle (a^\dagger)^m a^n (\sigma^\dagger)^\mu \sigma^\eta \rangle$, one can

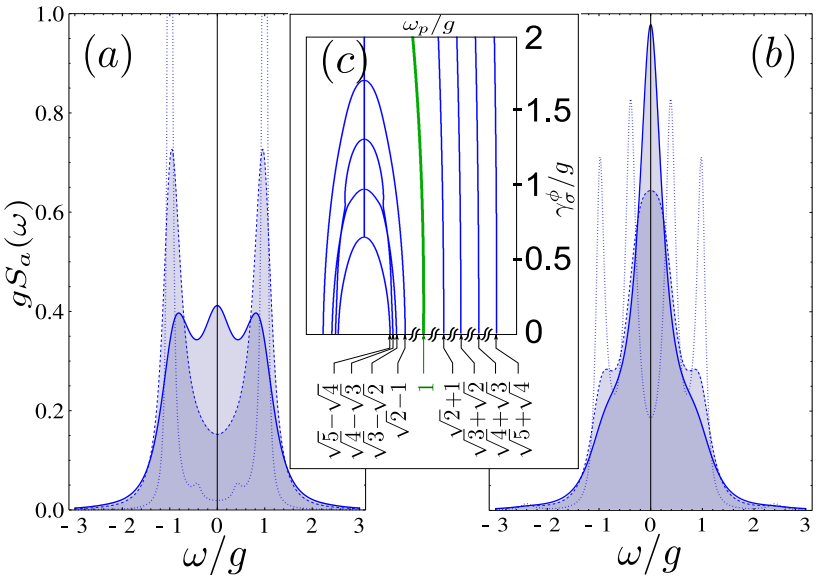

Figure 3.5: Loss of the Jaynes-Cummings quadruplet and emergence of a triplet with dephasing, for a system well into strong coupling ($\gamma_a/g = 1/10$ and $\gamma_\sigma/g = 1/1000$). Values of dephasing are $\gamma_\sigma^\phi/g = 0$ (dotted), 1/2 (dashed) and 3/2 (solid). Panel (a) is for $(P_a, P_\sigma)/g = (0.0011, 0.1)$ and (b) for $(0, 0.02)$. In inset (c), the dressed states resonances ω_p/g for the parameters of (a), showing the impact of dephasing on strong coupling: inner transitions are melted into a common one that results into lasing.

check that the addition of pure dephasing only affects diagonal elements of M and moreover, only when they belong to phase coherence (i.e. when $\mu \neq \nu$), where it is acting as an extra broadening:

$$M_{\substack{mn\mu\nu \\ mn\mu\nu}} = i\omega_a(m-n) + i\omega_\sigma(\mu-\nu) - \frac{\gamma_a - P_a}{2}(m+n) - \frac{\gamma_\sigma + P_\sigma}{2}(\mu+\nu) - \frac{\gamma_\sigma^\phi}{2}(\mu-\nu)^2 \,. \tag{3.10}$$

Other elements $M_{\substack{mn\mu\nu \\ pq\theta\vartheta}}$ are given in [87]. In the following, we study the effect of nonzero γ_σ^ϕ on the spectral shape of the cavity photoluminescence spectrum, under various cases of particular experimental relevance.

In Fig. 3.3, it was studied the effect of pure dephasing in the observables determining the different regimes of operation as a function of incoherent pumping. In dashed lines, we considered the same situation than for the solid lines but with a pure dephasing rate of $\gamma_\sigma^\phi = g$. One clearly sees that the differences between them are minimal in all the observables so that the distinction between the different regimes are still valid. Surprisingly, the same values of pure dephasing lead to interesting differences in the spectral shapes.

In the linear regime, dephasing only introduces an trivial extra broadening to the spectral lines: $\gamma_\sigma \to \gamma_\sigma + \gamma_\sigma^\phi$. Thus, its effect is quite trivial and predictable [48]. However, the interplay of this extra broadening and the observation of SC in the non-linear regime shows very interesting features. Figure 3.5 shows the impact of pure dephasing on the most striking landmark of the Jaynes-Cummings nonlinearities, namely, the multiplet structure that

corresponds to transitions between rungs of the Jaynes-Cummings ladder [119]. We consider a system as realistic as possible but still good enough to display multiplets unambiguously. i.e., such that transitions from states dressed by two (or more) photons are resolved in the photoluminescence spectrum. A system with $\gamma_a/g = 1/10$ and $\gamma_\sigma/g = 1/1000$, as the one considered in the previous Section, produces a Jaynes-Cummings fork (a quadruplet) at resonance, as shown in dotted lines. On Fig. 3.5(a), we have recoursed to a cavity pumping ($P_a/g = 0.0011$) as well as an electronic pumping ($P_b/g = 0.1$), so as to reveal the transition owing to the favorable effective quantum state realized in the system [109, 120]. Here the Rabi doublet neatly dominates.

On panel (b), only the electronic pumping is considered ($P_a = 0$) and a clear quadruplet is indeed produced, dominated by the transitions from states with two or more photons, over those with one photon that produce the Rabi doublet. With increasing pure dephasing, ($\gamma_\sigma^\phi/g = 1/2$ in dashed and $\gamma_\sigma^\phi/g = 3/2$ in solid lines), the spectra evolve in both cases into a triplet, with melting of the multiplet as well as the emergence of a central peak. The mechanism of this transition is revealed in the inset (c), where the dressed modes resonances ω_p (in units of g) are shown as a function of the dephasing for the parameters of panel (a).

These resonances correspond to transitions between the eigenstates of the system, which are the dressed states (polaritons) in the SC regime, and the bare states (exciton and photons) in the weak coupling regime. Dressed states up to five photons are excited for the chosen parameters, and the characteristic $\pm\sqrt{n}\pm\sqrt{n-1}$ frequencies of the transitions between rungs with a such a square root splitting is indicated at the bottom of the figure (where $\gamma_\sigma^\phi = 0$). Only inner peaks are displayed for clarity, outer peaks at frequencies $\sqrt{n}$.

The system remains in SC throughout, for all the states, as is evidenced from the permanence of the outer resonances $\pm(\sqrt{n} + \sqrt{n-1})$ for all $n \geq 2$. The case $n = 1$ (in green) corresponds to the vacuum Rabi splitting. Its position is only weakly perturbed by dephasing (as are outer peaks). Inner transitions—when the decay links identical rungs of the Jaynes-Cummings ladder (the two higher or the two lower rungs)—are more significantly affected. As shown on the figure, these inner resonances, at $\pm(\sqrt{n} - \sqrt{n-1})$ for $n \geq 2$, loose their splitting in succession with increasing dephasing, the sooner the higher the excited state (i.e., the larger the dressing). This loss of inner-splitting does not mean that the system goes to weak coupling, but instead that it crosses to lasing, as it would do without pure dephasing [120, 121].

Dephasing essentially accelerates this transition, by blurring the separation of the transitions and overlapping all of them into a common one, thereby indeed providing the system with a new common resonance, at the cavity mode. This transition is very strong from the accumulation of all the emissions of the system that were previously splitted from each others, and from Bose stimulation (dephasing here acts like a quantum eraser by providing an identical path to many previously distinguishable paths). Further increasing of the dephasing (or pumping) eventually brings the system into weak coupling, with collapse (not shown) of the outer resonances as well.

The effect on the spectral shape is to collapse the multiplet and grow a central peak that melts the inner, closely-spaced nonlinear Jaynes-Cummings features. At $\gamma_\sigma^\phi/g = 1/2$, all dressed states remain splitted, although less so, and the multiplet is qualitatively identical to the case without dephasing (only with a degraded resolution). At $\gamma_\sigma^\phi/g = 3/2$, however, almost all the excited states now have a common emission line, at the exception of the

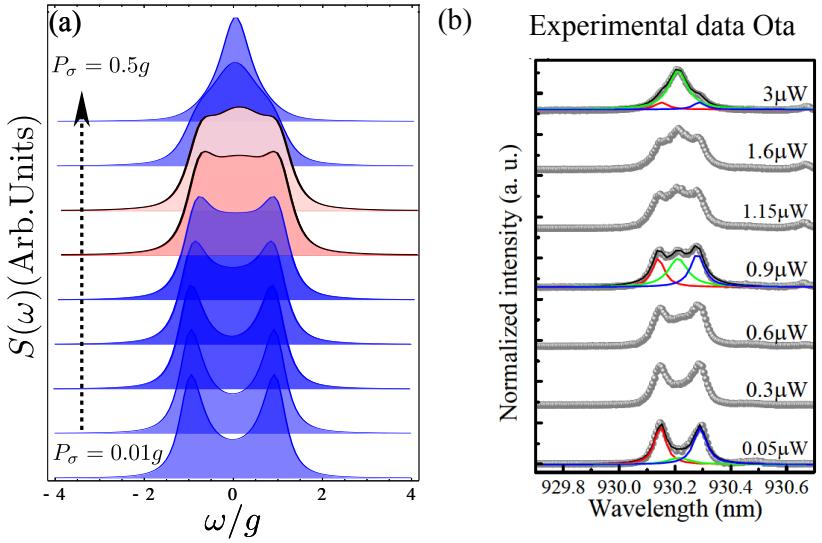

Figure 3.6: Evolution of Strong-coupling with increasing (electronic) pumping power. Parameters are $\gamma_a/g = 0.35$, $\gamma_\sigma/g = 0.001$, $\gamma_\sigma^\phi/g = 0.968$, $P_a = 0$ and P_σ/g varying as indicated in (a). The system evolves from the vacuum Rabi doublet into a triplet, much like the experiment of Ota *et al.* [74] (panel (b)). In red, it has been highlighted the cases where the triplet is clearly resolved.

first excited state, which splitting-to-broadening-ratio and intensity are however too small to remain observable in the spectrum. As a consequence, the emission features a dominating central peak. The same features are observed in panel (b), without cavity pumping and at lower electronic excitation. The quadruplet at small dephasing is much less apparent, but the triplet appears as a robust manifestation of nonlinear strong coupling with dephasing: overlapping an emerging lasing peak at the cavity emission with the vacuum Rabi doublet that produce satellite peaks.

In contrast with previously advanced suggestions [29, 74], our analysis shows that this spectral structure is not attributable to loss of strong coupling. It is also different from the triplet of Hughes and Yao [122] that is due to interferences, and, needless to say, it is not related to the Mollow triplet either [123]. Instead, our triplet appears as a new regime at the border of the quantum (Jaynes–Cummings) and classical (lasing) regimes, with dephasing acting as a smoothening agent (rather than a destructive one [124]).

3.5 Qualitative comparison with experimental data.

Dephasing is not a parameter that is easy to control directly. In order to probe the non-linearities of the system, a natural experimental attempt is to tune the pumping power, so as to populate predominantly the excited states. The evolution of the Rabi doublet with increasing electronic pumping is shown on Fig. 3.6(a), for a system with parameters closer to the current experimental reality (cf. caption). In this case, a triplet is also formed, but without any intermediate or direct manifestation of the Jaynes-Cumming spectral structure, owing to the poor splitting to broadening ratio with state of the art experimental figures. The observation of this trend has been recently reported by [74] (see panel (b) of Fig. 3.6).

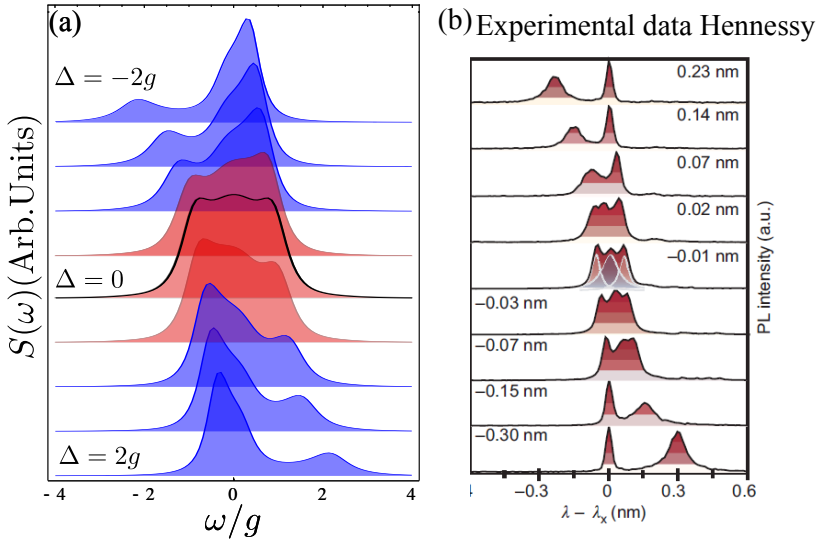

Figure 3.7: Strong-coupling in the nonlinear regime in presence of dephasing as detuning is varied. Parameters are $\gamma_\sigma/g = 0.001$ and $P_a/g = 0.011$ and $\gamma_\sigma^\phi/g = 1$], $\gamma_a/g = 0.35$ and $P_\sigma/g = 0.1$. Instead of the usual anticrossing, a triplet is grown as the dot enters in resonance, much like the experiment of [29] (shown in Panel (b)). In red, it has been highlighted the cases where the triplet is clearly resolved.

Incoherent pumping results in strong fluctuations of the particle numbers [120], so high pumping is not the ideal configuration to evidence the Jaynes-Cumming nonlinearity. Instead, high quality factor, long lifetime of the exciton and small dephasing should be a much better option.

Figs. 3.7 and 3.8 displays other manifestations of nonlinearities in the PL spectrum of a strongly-coupled quantum-dot/microcavity system. The intent is to show the wide range of phenomenologies that are accessible with different parameters, as well as the strong similarities with reported experiments that have so far eluded theoretical explanation. In the quest for strong-coupling in semiconductor, one typically performs an anticrossing experiment, where the dot and the cavity are brought to resonance to exhibit level-repulsion (maintaining their line splitting). Figure 3.7 shows a situation with detuning for a set of parameters (cf. caption). In this case case, well identified dot and cavity emission lines approach in the expected way but grow a central peak as they approach each other. This situation is very similar to the one reported by [29] which is compared in panel (b).

A second case is that of Fig. 3.8, where a doublet is now produced at resonance and a triplet is observed in its vicinity and only at negative detunings. This situation is very similar to the one reported by [75] (that has remained unexplained—and unpublished—so far).

In the case of Fig. 3.7, dephasing is constant, the cavity has a higher quality factor and electronic pumping is moderate. The triplet then arises for the same reasons as those explained for the phenomenology of Fig. 3.6. A slightly better system (either from system parameters or with less dephasing) would grow a quadruplet at resonance. These considerations match the experimental situation of a single QD detuned by a thin-film condensation technique.

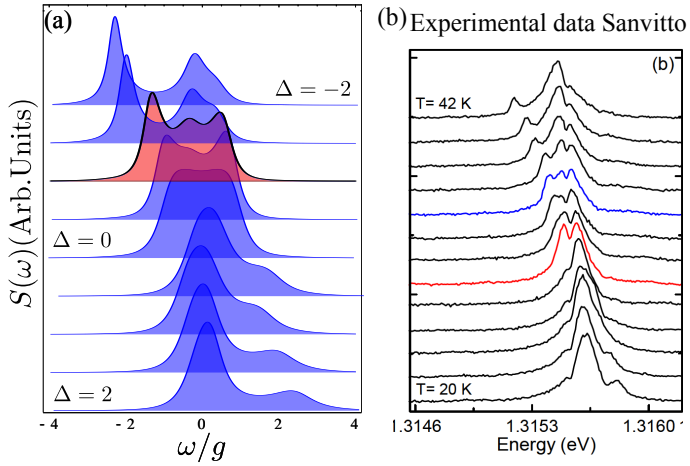

Figure 3.8: Strong-coupling in the nonlinear regime in presence of dephasing as detuning is varied. Parameters are $\gamma_\sigma/g = 0.001$, $P_a/g = 0.011$, γ_σ^ϕ/g sigmoid function of Δ, $\gamma_a/g = 0.5$ and $P_\sigma/g = 0.3$. Instead of the usual anticrossing, as detuning varies with temperature, a triplet is observed *out of resonance*, with an asymmetry with detuning caused by the temperature-dependent dephasing, much like the experiment of [75] (shown in Panel (b)). In red, it has been highlighted the cases where the triplet is clearly resolved.

However, in the second case of Fig. 3.8, the experimental situation varies in a few ways that would appear unimportant for the physics investigated, but that turn out to produce very different qualitative results: the dephasing has been correlated with the detuning (with a sigmoid function, to reflect that detuning is tuned with temperature), cavity photon has smaller lifetime and pumping is much stronger (as it was the case experimentally). This results in the emergence of a triplet outside of the resonance. In this later case, rather than superimposing a central peak, the noncommensurable transitions at $\pm(\sqrt{n}-\sqrt{n-1})$ produce the multiplet out of resonance owing to the virtue of transitions from excited states to be stationary with detuning [120]. The dephasing here serves the purpose of converting the quadruplet predicted for such a structure at nonzero detuning in Ref. [120] into a triplet.

3.6 Quantitative comparison with experimental data.

To conclude this Chapter, we include the first trial of confronting our theory with the experimental data, by means of a fitting of experimental results. The non-linear behavior is computationally far more complicated than the linear regime. As there are no closed expressions for the spectral lineshapes [125], one needs to compute spectra completely numerical. This requires the presence of many correlators in order to track the photons from the higher rungs of the ladder. This explains why the fittings so far have restricted to the linear regime [48, 109].

In order to do a global fitting, we have used genetic algorithm methods [126]. As we had no direct access to experimental results, a digitized extraction of the experimental data from [74] was done. In Fig. 3.9, we have overimposed the result of the fitting together with the experimental image. We find our proposition to be consistent with the supposed

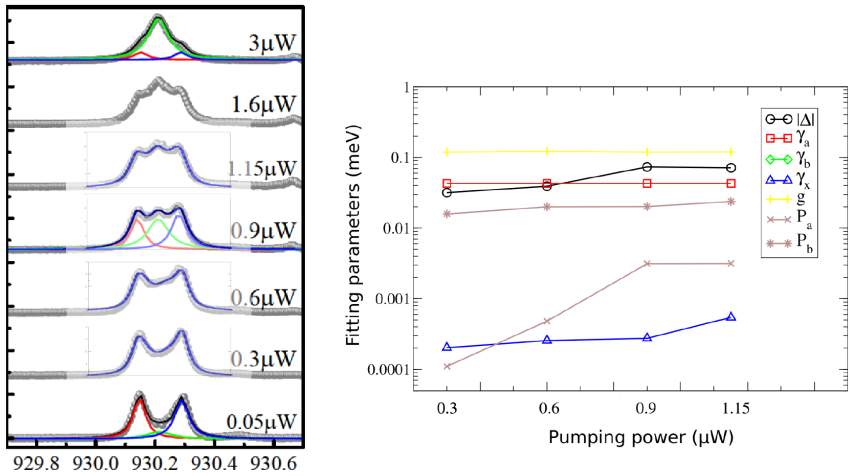

Figure 3.9: Fit in the nonlinear regime: data of [74] with. superimposed in blue for the four central panels, our global fitting (fitting parameters appear on the right side) with a fermion model [120] including dephasing [125].

parameters of this experiment, besides with a neat contribution due to a drift in detuning more than due to dephasing. Beyond supporting claims of quantum nonlinearities, our work also provides the first quantitative description of strong-coupling experimental data but now in the nonlinear and fermionic regime.

3.7 Conclusions.

In conclusion, we have shown that nonlinearities of the JC Hamiltonian–the pinnacle of full-field quantization in cavity Quantum Electrodynamics–have a robust tendency to manifest as triplet structures in presence of a non-negligible dephasing (such as is the case in semiconductors), rather than the expected JC multiplets of paired doublets with no emission at the cavity (central) mode.

We have also shown that various parameters (corresponding to slightly different experimental situations) result in strong qualitative differences, such as observation of a triplet at–or out of–resonance. We paid a particular attention to three experiments [29, 74, 75] that reported such triplet-like features, so far without a clear identification of the underlying physics. We can reproduce qualitatively all the experimental findings, and conjecture that in all these cases, nonlinear quantum physics is at work in a nontrivial way, being all variations of the same theme: rather than loosing strong coupling, as previously suggested, we show that dephasing acts as an smoothening agent in the quantum to classical (lasing) transition. This introduces a new type of triplet structure distinct in character from a Mollow triplet or a mere superposition of strong and weak coupling spectra.

The first global fitting within the non-linear regime is also presented, although further quantitative and qualitative analysis of the experimental data is in progress to substantiate our claims. Apart from a more compelling global fitting, other kind of measurements such as time and frequency resolved correlations (that we address in Chapter 4) can provide the definite test to discern the nature of the different spectral triplet.

Chapter 4

Theory of time and frequency resolved N-photon correlations.

4.1 Introduction

In Chapter 2, it was exposed how photons leaking out of the quantum system are the most straightforward way to extract information from them. For example, in semiconductor cavity QED systems where a QD is embedded inside a microcavity, one usually access to the information of the state of the QD from the photons leaking out of the cavity. This is why the field of *quantum optics*, which studies the concept of photon at the quantum level and its interaction with matter, lies at the heart of the characterization of cavity QED systems.

Regardless of the wave behavior of light in a variety of contexts, ultimately, every measurement is accounted for by clicks on a detector. Usually, even in the regime of a small number of quanta in the field, the experimental observables are obtained by averaging over a large enough repetition of the experiment. For instance, a luminescence spectrum is obtained by integrating the signal over long times, in order to obtain a continuous distribution that describes the probability of emission of each photon at a given energy.

With the advances in the generation, emission, transmission and detection of photons, quantum systems are increasingly addressed at the single photon level and there is a pressing need for generalizations as well as refinements of the theory of photo-detection. To access the dynamics of photons at a quantum level, with no counterpart from a classical theory involving a continuous field, it is necessary to invoke N-photon correlations. An average is still taken over a large number of single-detection events, but the latter now involves N correlated clicks in each shot.

Among this photon correlations measurements, the ones combining both their energy and time information are now routinely measured in the laboratory. These experiments have proven extremely powerful in characterising quantum systems such as a resonantly driven emitter [127–129] or the strong coupling of light and matter [29, 97, 130], to perform quantum state tomography [131] or to monitor heralded single photon sources [132]. At this level of fine control of the attributes of the quantum particles, one needs a theoretical description significantly more involved than general mathematical statements, such as the Wiener–Khinchine theorem which assumes abstract and unphysical properties of the light

field (like stationarity over infinite time durations). We already showed in Chapter 2, the more realistic and detailed one aims to characterize a quantum system in experiments, the more necessary it becomes to describe the measurement process accurately. However, it was shown how the consideration of the physics of detection into the standard photon correlation theory increases the computational complexity of the problem to the point of limiting the theoretical efforts so far to very specific and simple systems, i.e. resonance fluorescence [93, 96, 133–135], where some approximations can be done.

In this Chapter we explain our recently developed method which simplifies considerably the computational complexity by actually introducing the *sensors* into the dynamics. We mainly focus on the simplest case where $N = 2$ and no delay time between photons[1]. Some exception are made, i.e. for the paradignatic JC model, where we show time dynamics and higher order correlation in order to illustrate the power of our approach.

This Chapter is divided as follows: in Section 4.2, we give a brief overview of our method to compute these functions. Most of the details of the demonstration, which is rather technical and elaborate, are left for the Appendix I. In Section 4.3, we address the simplest case of a single mode: an harmonic oscillator (HO) or a two-level system (2LS). These serve as the first illustration of our theme that the 2PS reveals a considerably richer picture of the dynamics of emission for an otherwise identical 1PS lineshape, depending on both the mode statistics or the nature of its broadening (homogeneous or inhomogeneous). In 4.4, calculations for coupled quantum modes are shown. Here again, even though the low-pumping regime results in identical 1PS lineshapes, the coupling of two harmonic oscillators (cHOs), two two-level systems (c2LSs), or one harmonic oscillator to a two-level system (Jaynes-Cummings (JC) model), show distinct and peculiar features in the 2PS, unravelling the different nature of the three couplings. In the latter cases, of great importance in cavity-QED, we thereby identify an entire class of two-photon emission processes, to which one is completely oblivious through one-photon spectroscopy. In particular, Section 4.5 is devoted to the study of the high pumping regime for JC model, comparing it to its semi classical analogue (Mollow triplet). Finally, in Section 4.6, we summarize the main results obtained from this Chapter.

4.2 A new approach to N-photon correlations: "sensing" method.

In this Section, we briefly present our new theory of N-photon correlations, that allows for arbitrary time delays and frequencies, applicable to any open quantum system. It consists of the introduction of N *sensors* to the dynamics of the open quantum system (noted Q in Fig. 4.1(a)). Let us assume that one is interested in looking the dynamics of the system Q through a given mode, e.g. O, then, the approach consists of coupling very weakly the N sensors to this mode and study the correlation through the sensors and not through the O-mode itself.

Each sensor of the set $i = 1, \ldots, N$ is modeled by a two-level system with transition frequency ω_i, that is matched to the frequency to be probed in the system. Its lifetime $1/\Gamma_i$ corresponds to the detector's linewidth. The coupling or tunneling rate to each sensor ε_i is vanishingly small as compared to any other rate in the system Q, so that the system dynamics is unaltered by the presence of the detectors. Thanks to their vanishing coupling, the sensors

[1] The conjugate time information is still present through the linewidth of the frequency windows

remain in the linear regime, that is, they have a negligible population, $\langle n_i \rangle = \langle \sigma_i^\dagger \sigma_i \rangle \ll 1$. Furthermore, considering cross-correlations between sensors only, the result is independent of the nature of the sensors, that could be equally modeled by harmonic oscillators. Two-level systems are more convenient as their coupling to the original system adds very little computational complexity to the master equation.

Calling γ_Q any transition rate within Q (either with internal or external degrees of freedom) linked to the field of interest O, the tunnelling rates ε_i must fulfill two conditions: the losses into the sensors must be negligible, $4\varepsilon_i^2/\Gamma_i \ll \gamma_Q$ and so must be the back action of the sensors into the system, $4\varepsilon_i^2/\gamma_Q \ll \Gamma_i$. These conditions both lead to $\varepsilon_i \ll \sqrt{\Gamma_i \gamma_Q/2}$. Under these conditions, one can then solve the full quantum dynamics of the system supplemented with the N sensors. The latter play the role of the output fields $A_{\omega_i}(t)$, but instead of formally solving the Heisenberg equations and putting their correlations in terms of the system operators (as in the standard method exposed in Chapter 2), one computes directly intensity–intensity correlations between them, which is a considerably simpler task. The main result of this method is:

$$g^{(N)}_{\Gamma_1 \dots \Gamma_N}(\omega_1, T_1; \dots; \omega_N, T_N) = \lim_{\varepsilon_1, \dots, \varepsilon_N \to 0} \frac{\langle n_1(T_1) \dots n_N(T_N) \rangle}{\langle n_1(T_1) \rangle \dots \langle n_N(T_N) \rangle}\,, \tag{4.1}$$

where the left hand side is the time- and frequency-resolved N-photon correlation function as defined previously (Eqs. 2.59 and 2.60) for $N = 2$). The proof, detailed in the Appendix I, hinges on the result that, to leading order in the couplings $\varepsilon_1^2 \dots \varepsilon_N^2$, the correlator $\langle n_1(T_1) \dots n_N(T_N) \rangle$ is linked to the integrals of Chapter 2 as:

$$\langle n_1(T_1) \dots n_N(T_N) \rangle = \frac{\varepsilon_1^2 \dots \varepsilon_N^2}{\Gamma_1 \dots \Gamma_N} (2\pi)^N S^{(N)}_{\Gamma_1 \dots \Gamma_N}(\omega_1, T_1; \dots; \omega_N, T_N)\,. \tag{4.2}$$

With this result, the complexity of computing $g^{(N)}_{\Gamma_1 \dots \Gamma_N}(\omega_1, T_1; \dots \omega_N, T_N)$ is reduced to applying the quantum regression theorem only $N - 1$ times in addition to getting rid of all the integrals. For the important case of zero delay, $g^{(N)}_{\Gamma_1 \dots \Gamma_N}(\omega_1; \dots; \omega_N)$ reduces to a single-time average quantity.

Most of the results of this Chapter are obtained in the limit of zero delay between the photons and for $N = 2$ only. In this situation, the normalised correlation function, that we name *two-photon spectrum* (2PS), is therefore obtained simply in terms of the population operators of the sensors n_1 and n_2, as:

$$g^{(2)}_{\Gamma_1, \Gamma_2}(\omega_1, \omega_2) = \lim_{\varepsilon \to 0} \frac{\langle n_1 n_2 \rangle}{\langle n_1 \rangle \langle n_2 \rangle}\,, \tag{4.3}$$

where ε represents the coupling to the sensors, small enough not to disturb the system, and Γ_1, Γ_2 are the sensors decay rates that provide the detectors linewidths or, in other terms, the respective width of the frequency windows. The case of equal frequencies $g^{(2)}_{\Gamma}(\omega, \omega)$ corresponds to measuring the photon-statistics of photons passing through a frequency window of Lorentzian shape of linewidth Γ. This corresponds to applying a single filter or to the effect of the detectors resolution, and is thus also of interest.

In practical terms, the calculation can be performed in two alternative ways. The first method relies in the actual inclusion of the sensors in the dynamics of the system, supplementing the Hamiltonian and the master equation with the corresponding terms. The main

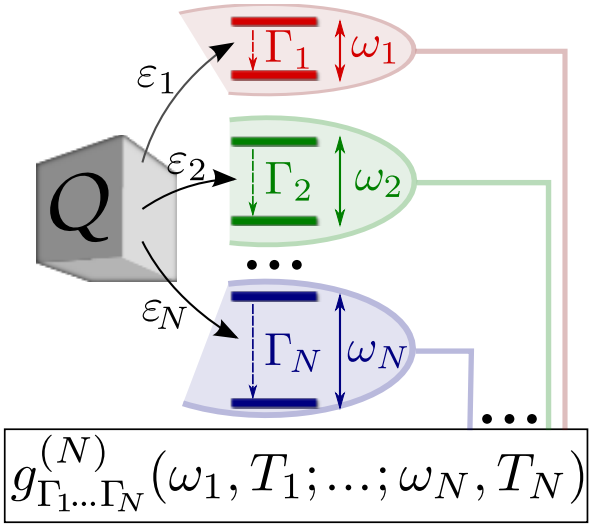

Figure 4.1: Scheme of our proposal to compute N-photon correlations between photons emitted at different times and frequencies from an open quantum open system Q. N two-level systems of ascribed frequencies are weakly coupled to Q and serve as correlation sensors at these frequencies, with their decay rate providing the detector linewidth.

drawback is that the size of the Hilbert space is increased by a factor 2^2 (and the density matrix by a factor 4^2). However, the computational operations are simple. In one of the possible approaches to the problem, one merely needs to solve the steady state of the full system (a set of homogeneous linear equations), which only requires the inversion of a matrix [120].

An alternative method, presented in detail in the Appendix I, consists in obtaining formally the populations and cross correlations between the sensors to leading order in the couplings, ε^2 and ε^4 respectively. Then, the relevant quantities $\langle n_1\rangle$, $\langle n_2\rangle$ and $\langle n_1 n_2\rangle$ can be obtained through the master equation of the system only with no increase in the numerical complexity.

In order to implement this method, one first needs to determine a vector of the system operators whose average are needed to compute the coupling to the sensors. Calling O the annihilation operator of the mode of interest, which correlations one wishes to compute, such a vector can be written in the form $\mathbf{v} = (1, O, O^\dagger, O^\dagger O \ldots)$ (with subsequent terms depending on the systems and its dynamics). The observables of interest for the sensors cross-correlations are specified by the mean values of this vector: $\langle \mathbf{v}\rangle = (1, \langle O\rangle, \langle O^\dagger\rangle, \langle O^\dagger O\rangle, \ldots)$. A regression matrix $\mathbf{M}$ can be obtained from the master equation of the system [120] which rules the dynamics of these correlators according to $\partial_t\langle \mathbf{v}\rangle = \mathbf{M}\langle \mathbf{v}\rangle$. The steady state (if it exists) is obtained in the limit of infinite times: $\langle \mathbf{v}^{\rm ss}\rangle = \lim_{t\to\infty} e^{\mathbf{M}t}\langle \mathbf{v}(0)\rangle$, for any initial state $\mathbf{v}(0)$. Next, one builds two re-ordering matrices, $\mathbf{T}_\pm$, which, when acting on the vector $\langle \mathbf{v}\rangle$, introduce in all correlators an extra operator $O^\dagger$ for $\mathbf{T}_+$ and an extra operator O for $\mathbf{T}_-$, keeping normal order in each case. That is, $\mathbf{T}_+\langle \mathbf{v}\rangle = (\langle O^\dagger\rangle, \langle O^\dagger O\rangle, \langle (O^\dagger)^2\rangle, \langle (O^\dagger)^2 O\rangle, \ldots)$ and $\mathbf{T}_-\langle \mathbf{v}\rangle = (\langle O\rangle, \langle O^2\rangle, \langle O^\dagger O\rangle, \langle O^\dagger O^2\rangle, \ldots)$, respectively. With these matrices, one obtains

the populations of the sensors to leading order in ε, as the first element $[\dots]_1$ of the vector:

$$\langle n_j\rangle = \frac{2\varepsilon^2}{\Gamma_j}\Re\Big[\mathbf{T}_+\frac{-1}{\mathbf{M}+[-i\omega_j-\frac{\Gamma_j}{2}]\mathbf{1}}\mathbf{T}_-\langle\mathbf{v}^{\rm ss}\rangle\Big]_1\,,\quad j=1,\,2\,. \tag{4.4}$$

Regarded as a function of the frequency ω_j, this produces the 1PS as measured by a detector of linewidth Γ_j. Similarly, the cross-correlations that provide the 2PS is given by:

$$\begin{aligned}\langle n_1 n_2\rangle = \frac{2\varepsilon^4}{\Gamma_1+\Gamma_2}\Re\Big[\mathbf{T}_+\frac{-1}{\mathbf{M}+(-i\omega_2-\Gamma_1-\frac{\Gamma_2}{2})\mathbf{1}}\times\\ \Big\{\mathbf{T}_-\frac{-1}{\mathbf{M}-\Gamma_1\mathbf{1}}\Big(\mathbf{T}_+\frac{-1}{\mathbf{M}+(-i\omega_1-\frac{\Gamma_1}{2})\mathbf{1}}\mathbf{T}_-+\mathbf{T}_-\frac{-1}{\mathbf{M}+(i\omega_1-\frac{\Gamma_1}{2})\mathbf{1}}\mathbf{T}_+\Big)\\ +\mathbf{T}_-\frac{-1}{\mathbf{M}+(i\omega_1-i\omega_2-\frac{\Gamma_1+\Gamma_2}{2})\mathbf{1}}\Big(\mathbf{T}_-\frac{-1}{\mathbf{M}+(i\omega_1-\frac{\Gamma_1}{2})\mathbf{1}}\mathbf{T}_++\mathbf{T}_+\frac{-1}{\mathbf{M}+(-i\omega_2-\frac{\Gamma_2}{2})\mathbf{1}}\mathbf{T}_-\Big)\\ +\mathbf{T}_+\frac{-1}{\mathbf{M}+(-i\omega_1-i\omega_2-\frac{\Gamma_1+\Gamma_2}{2})\mathbf{1}}\mathbf{T}_-\Big(\frac{-1}{\mathbf{M}+(-i\omega_2-\frac{\Gamma_2}{2})\mathbf{1}}+\frac{-1}{\mathbf{M}+(-i\omega_1-\frac{\Gamma_1}{2})\mathbf{1}}\Big)\mathbf{T}_-\Big\}\mathbf{v}^{\rm ss}\Big]_1\\ +[1\leftrightarrow 2]\,,\end{aligned}$$

where $[1\leftrightarrow 2]$ means the interchange of sensors 1 and 2, that is, permuting $\omega_1\leftrightarrow\omega_2$ and $\Gamma_1\leftrightarrow\Gamma_2$ everywhere.

The advantage of this second method is twofold. First, it is very useful when the Hilbert space is small as it can lead to closed-form analytical expressions. We see some exampled of this in the next Section. Second, it may also be numerically advantageous as the matrices involved correspond to the original (smaller) Hilbert space of the bare system, in the absence of sensors. The computational price to pay is in a higher number of matrix operations (eleven different matrix inversions and numerous multiplications for $\langle n_1 n_2\rangle$). In some situations, the advantage of a smaller Hilbert space dominate. In others, it is more convenient and straightforward to explicitly include the sensors and solve for the enlarged system, with a similar overall numerical efficiency. For the calculations in this Chapter we use both methods indistinctly.

Throughout the rest of the Chapter, the linewidths of the detectors will be taken equal, $\Gamma_1=\Gamma_2=\Gamma$, for the sake of simplicity. Thus, we simply write $g^{(2)}_\Gamma(\omega_1,\omega_2)$. The width Γ of the frequency windows is a fundamental parameter that cannot be dispensed with, unlike the 1PS case where an ideal detector is usually assumed in theoretical works. In the 2PS, Γ provides the uncertainty in the frequency (Γ) and time of detection ($1/\Gamma$) [83], as required by the Heisenberg principle. In the limit of very broad filters ($\Gamma\to\infty$) the standard second order coherence function at zero delay is recovered: $\lim_{\Gamma\to\infty} g^{(2)}_\Gamma(\omega_1,\omega_2)=g^{(2)}$. The opposite limit of very narrow filters ($\Gamma\to 0$), results in a systematic tendency regardless of the underlying system, namely uncorrelated photons of different frequencies and bunching of photons with the same frequencies. This can be understood on physical grounds: in order for the detectors to provide high precision in frequency ($\Gamma\to 0$), their interaction time with the system has to be long ($1/\Gamma\to\infty$), so that the collected photons correspond to all the possible times in the dynamics. This leads to an apparent uncorrelated statistics: $\lim_{\Gamma\to 0} g^{(2)}_\Gamma(\omega_1,\omega_2)=1$ provided

that $\omega_1 \neq \omega_2$. The limiting value becomes $\lim_{\Gamma\to 0} g^{(2)}_\Gamma(\omega,\omega) = 2$ in the case of detection at equal frequencies as there are 2! ways that two indistinguishable photons can be collected by two different detectors. This tendency to bunch when $\omega_1 \approx \omega_2$ and Γ is small (as compared to the relevant linewidths in the system) will be a common feature that appears independently of the system. For that reason, we name it as *indistinguishability bunching*. This effect has been observed experimentally in the filtering of a single mode laser [136].

4.3 Single mode emitters.

Two-photon frequency-resolved spectroscopy is such a nascent field of optical characterization that even the trivial systems need to be investigated. Namely, our starting point is the free mode (or, in the quantum optics terminology, "single mode"), which Hamiltonian simply reads:

$$H_O = \omega_O O^\dagger O\,. \tag{4.5}$$

There are two fundamental possibilities for the operator O, namely, it can be the annihilation operator of an harmonic oscillator (HO), in which case we denote it $O = a$, or it can be that of a two-level system (2LS), in which case we denote it $O = \sigma$. Their respective quantum algebra is given by the bosonic commutation rule ($aa^\dagger - a^\dagger a = 1$) and the fermionic anticommutation rule ($\sigma\sigma^\dagger + \sigma^\dagger\sigma = 1$). The dynamics of the density matrix ρ of the emitter—including decay (required to bridge with the external world where the measurement is performed) and a continuous incoherent pump (to populate the system)—is given by the master equation:

$$\partial_t\rho = i[\rho, H_O] + \frac{\gamma_O}{2}\mathcal{L}_O(\rho) + \frac{P_O}{2}\mathcal{L}_{O^\dagger}(\rho) \tag{4.6}$$

with the Lindblad super-operator as defined in Chapter 2. The 1PS, provided by Eq. (12), is the same for both systems $O = a, \sigma$. It is plotted in Fig. 4.2(a). It is a Lorentzian lineshape with linewidth Γ_O (inverse mode lifetime) given by $\Gamma_a = \gamma_a - P_a$ for the HO and $\Gamma_\sigma = \gamma_\sigma + P_\sigma$ for the 2LS [87].

The two-photon correlations, however, are dramatically different, since the HO displays bunching, $g^{(2)}[a] = 2$, while the 2LS displays the exact opposite behaviour of antibunching, $g^{(2)}[\sigma] = 0$ (the mode which statistics is measured is here denoted explicitly in square brackets to avoid confusion). The 2PS also exhibits structures in the frequency correlations that are qualitatively different. For such simple cases, Eq. (43) can be solved exactly and analytical formulas for the 2PS obtained:

$$g^{(2)}_\Gamma[O](\omega_1,\omega_2) = \frac{\Gamma_O}{(\Gamma+\Gamma_O)^2}\left[\Gamma_O + \frac{\Gamma^2(2\Gamma+\Gamma_O)}{\Gamma^2 + (\omega_1-\omega_2)^2} + \tilde{g}^{(2)}_\Gamma[O](\omega_1,\omega_2)\right], \tag{4.7}$$

with a common expression regardless of the mode $O = a, \sigma$ spelled out above, and a term $\tilde{g}^{(2)}_\Gamma[O]$ specific to each case,given by:

$$\tilde{g}^{(2)}_\Gamma[a] = 2\Gamma\left(1 + \frac{\Gamma}{\Gamma_a}\right), \tag{4.8}$$

for the HO (note that it is frequency independent), and by

$$\tilde{g}^{(2)}_\Gamma[\sigma](\omega_1,\omega_2) = 4\Gamma - 2\Gamma(2\Gamma+\Gamma_\sigma)\left(\frac{\frac{3\Gamma+\Gamma_\sigma}{2}}{(\frac{3\Gamma+\Gamma_\sigma}{2})^2+\omega_1^2} + \frac{\frac{3\Gamma+\Gamma_\sigma}{2}}{(\frac{3\Gamma+\Gamma_\sigma}{2})^2+\omega_2^2}\right),$$

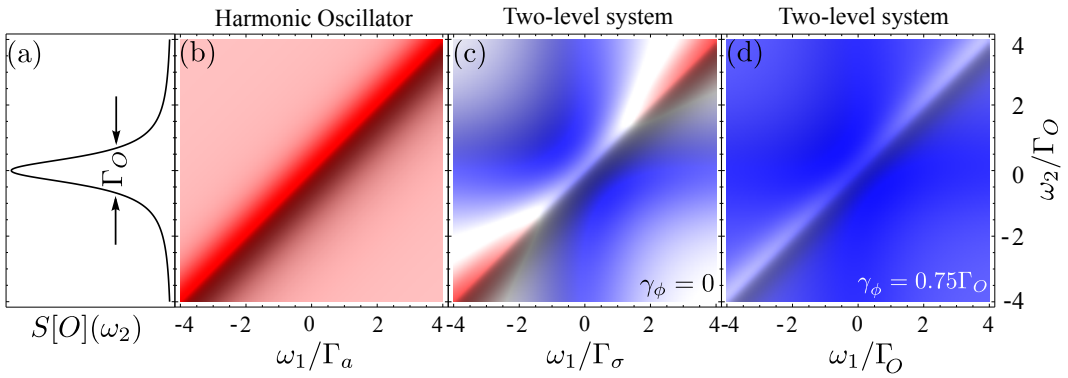

Figure 4.2: (a) The one-photon spectrum (1PS) common to a single harmonic oscillator (HO) and a two-level system (2LS), and the corresponding two-photon spectra (2PS), $g^{(2)}_{\Gamma_O}[O](\omega_1,\omega_2)$, for (b) an HO and (c)–(d) a two-level system, in units of the total broadening Γ_O. In (d), the emitter is subject to pure dephasing, $\gamma_\phi = 0.75\Gamma_\sigma$, with Γ_σ such that the 1PS remains the one shown in (a). Beyond the bunching on the diagonal, common to all 2PS, clear deviations are observed depending on the type of emitter: the harmonic oscillator is structureless while the two-level system concentrates its antibunching in a butterfly-shaped region of non-overlapping frequencies. Dephasing favours antibunching. The color code is: 0 blue; 1 white; 2 red.

for the 2LS. The single filter case $g^{(2)}_\Gamma(\omega,\omega)$ shows that for the 2LS, correlations are maximum when filtering the peak itself, $\omega = 0$, and that a large overlap of the peak is needed to recover a good antibunching of the 2LS (the ideal result is recovered in the limit of broadband detection: $\lim_{\Gamma\to\infty} g^{(2)}_\Gamma[\sigma](\omega_1,\omega_2) = g^{(2)}[\sigma] = 0$). The photon-counting correlation of the filtered peak indeed reads $g^{(2)}_\Gamma[\sigma](0,0) = 2(\Gamma_\sigma/\Gamma)/\big(3 + (\Gamma_\sigma/\Gamma)\big)$, e.g., the filter linewidth must be over sixty-six times that of the emitter to reach the 1% level of accuracy, an awkward requirement in practice. This is an effect of the indeterminacy in the photon arrival time due to a better knowledge of its frequency. For this reason, post-processing of the coincidences through deconvolution of the spectral response is important to characterise fairly a quantum emitter.

For the HO, on the other hand, $g^{(2)}_\Gamma[a](\omega,\omega) = 2$ regardless of the filtering window Γ and of which part of the peak is detected (maximum or any point in the tail). This is a manifestation of the classical character of the HO: it has no local information, any part behaves like the whole and one cannot tell apart from a filtered window whether the information is of a microscopic or macroscopic nature. In contrast, the 2LS has an energy scale and the information is localized in the energy window proper to the dynamics of the emitter.

The full 2PS of these systems further reveals such fundamental aspects of these emitters, the 2LS and the HO. In Fig. 4.2, we plot Eq. (4.7) in the case where the detector linewidth matches that of the 1PS peak, $\Gamma = \Gamma_O$. In this and all subsequent density plots of the 2PS, we use a color code where red corresponds to bunching ($g^{(2)} \gtrsim 2$), blue to antibunching ($g^{(2)} \approx 0$) and white to non-correlated emission ($g^{(2)} = 1$). In this Chapter, we are more concerned with the qualitative patterns that emerge in two-photon spectroscopy than quantitative results.

The common characteristic between the HO and the 2LS is the indistinguishability bunching line, for frequencies that are indeed indistinguishable within the detector linewidth $|\omega_1 - \omega_2| < \Gamma$. This accounts for the diagonal feature on all plots. Apart from that, the HO correlations lack any structure and are always above one, corresponding to the expected

bunching, whereas the 2LS correlations mainly assume values below one, the expected antibunching, furthermore in a nontrivial configuration of detection $\mathcal{C}$ with different frequencies that attempt to maximise the overlap with the 1PS without entering the indistinguishability bunching region:

$$\mathcal{C} = \Big((|\omega_1 - \omega_\sigma| < \Gamma_\sigma) \vee (|\omega_2 - \omega_\sigma| < \Gamma_\sigma) \Big) \wedge (|\omega_1 - \omega_2| > \Gamma) \,. \tag{4.9}$$

The highest antibunching is thus obtained on the antidiagonal. In practical terms, for a given detector linewidth, it is therefore better to perform photon coincidences between the left and right elbows of the 1PS, with a slight shift of both windows away from the center, rather than between photons both coming from the central peak. One can easily compute where exactly to place the filters by evaluating $g^{(2)}_\Gamma[\sigma](\omega, -\omega)$ with Eqs. (4.7) and (4.9). For instance, in the case $\Gamma = \Gamma_\sigma$, the minimum goes down to $2(\sqrt{2}-1)/5 \approx 0.16$, for $\omega_1 = -\omega_2 = \sqrt{(15\sqrt{2}-4)/31}\,\Gamma_\sigma \approx 0.75\,\Gamma_\sigma$. This is the closest that the frequencies can get to the central one without suffering from the indistinguishability bunching. It is a considerable improvement, at the small cost of a reduced signal, on measuring the correlations from the central peak with a detector of the same linewidth, that provides an antibunching of 0.5 only. When both detection windows are far from the peak, the emitter looses its quantum character and behaves like its classical counterpart, exhibiting bunching of its photons on the diagonal and uncorrelated emission otherwise.

In order to complete the study of the correlations of a single 2LS emitter by characterizing the effect of inhomogeneous broadening. This is relevant, for instance, in semiconductor systems (quantum dots) where the solid state environment induces fluctuations and pure dephasing on the levels. In this context, filtered two-photon correlations have already shed light on the timescales and origin of fluctuation in quantum dots [137]. Theoretically, inhomogeneous broadening is introduced in the dynamics through another Lindblad term of the form $\frac{\gamma_\phi}{2}\mathcal{L}_{\sigma_z}(\rho)$ [138, 139] as thoroughly studied in the previous Chapter. Pure dephasing occurs at the rate γ_ϕ, diminishing coherence in the system without affecting directly the populations. Its effect on the 1PS is merely to increase the linewidth of the peak, $\Gamma_\sigma = \gamma_\sigma + P_\sigma + \gamma_\phi$. For this reason, it is typically difficult to measure a radiative lifetime from spectroscopy and time-resolved measurements are usually invoked for that purpose. For a given 1PS, however, the 2PS changes quantitatively, which allows radiative and non-radiative contributions to be measured directly from spectroscopy measurements. The 2PS spectra without (c), and with (d), pure dephasing are compared in Fig. 4.2. While the statistics of the 2LS as a whole is not affected by γ_ϕ, its 2PS structure is. Namely, pure dephasing extends the condition of antibunching (4.9) to a wider range of frequencies and enhances the anticorrelations. This counter-intuitive result is a manifestation in 2PS of the profitable effect of dephasing for some quantum correlations [124, 140].

4.4 Coupled single mode emitters.

After having characterized single mode systems according to their statistics, We analyse the dipolar coupling of different combinations of HOs and 2LSs. We consider three paradigmatic examples, subject of intense both theoretical [87] and experimental study: two coupled harmonic oscillators (cHOs) [37, 141], two coupled two-level systems (c2LSs) [142–145] and the

Jaynes-Cummings model (JC) [29, 121, 146–148] where one HO is coupled to a 2LS. All of them can be described by the following Hamiltonian:

$$H_C = \omega_{O_1} O_1^\dagger O_1 + \omega_{O_2} O_2^\dagger O_2 + g(O_1^\dagger O_2 + O_2^\dagger O_1) \tag{4.10}$$

As in the previous section, $O_{1,2}$ can describe two different kind of modes, either HO or 2LS. The dynamics of the system is completed with the inclusion of the decay and pumping in the following master equation:

$$\partial_t \rho = i[\rho, H_C] + [\frac{\gamma_{O_1}}{2}\mathcal{L}_{O_1} + \frac{\gamma_{O_2}}{2}\mathcal{L}_{O_2} + \frac{P_{O_1}}{2}\mathcal{L}_{O_1^\dagger} + \frac{P_{O_2}}{2}\mathcal{L}_{O_2^\dagger}](\rho)\,. \tag{4.11}$$

In the rest of the Section we investigate an asymmetric situation where the second mode O_2 is pumped ($P_{O_1} = 0$) while the other one is detected, O_1. With this, we reduce the number of parameters and remain close to the experimental situation in cavity-QED where typically the emitter is incoherently pumped and the system is analysed through the cavity emission.

In Fig. 4.3, we explore the 2PS of the O_1-mode for different values of $\Gamma = \gamma_{O_1}$, from $0.1g$ to $4g$ and fixing the lifetime of the second mode to a small value $\gamma_{O_2} = 0.001g$. In the linear regime, where $P_{O_2} \to 0$, all the models converge to the same 1PS (first row), whereas their 2PS exhibit very different structures depending on the statistics of the fields. When the losses of the modes overcome the coupling, namely in the WC regime, the 1PS converges to that of the bare mode O_1. Also, the 2PS maintains the form of the single mode for cHOs and c2LSs, as in Fig. 4.2(a) and (b) respectively. However, in the case of the JC model, the saturation features of the 2LS remain present even in WC. As the quality of the coupling increases ($\gamma_{O_1} \to 0.1g$), the system enters in the so-called SC regime, where the coherent exchange overcomes the losses. As a result, new dressed states or polaritons are formed, $p_\pm$. The 1PS, still identical for the three coupling models, becomes the so called "Rabi doublet" with splitting by $2R = 2\sqrt{g^2 - [(\gamma_{O_1} - \gamma_{O_2})/4]^2}$. The 2PS, however, present different features that we discuss in turns.

4.4.1 Coupled Harmonic Oscillators (cHOs).

The cHOs, that we denote a and b, are characterised by bunched correlations between any two frequencies, as expected due to the bosonic character of both modes. Similarly to the case of a single harmonic oscillator, the color-blind statistics always remains thermal, for both the bare and dressed modes: $g^{(2)}[a] = g^{(2)}[b] = g^{(2)}[p_+] = g^{(2)}[p_-] = 2$. The cross correlations, however, depend on the system parameters:

$$g^{(2)}[a;b] \equiv \frac{\langle a^\dagger a b^\dagger b\rangle}{\langle n_a\rangle\langle n_b\rangle} = 2 - \frac{P_a/\langle n_a\rangle + P_b/\langle n_b\rangle}{\Gamma_a + \Gamma_b}\,, \tag{4.12}$$

(at resonance) and is always between 1 and 2. In the strong-coupling regime, $g^{(2)}[a;b] \to 1$, i.e., the two modes become uncorrelated. The correlations between polaritons, $g^{(2)}[p_+;p_-]$, are also close to 1 as long as polaritons are well defined (well separated spectrally), due to the formation of an independent polaritonic dynamics.

Coming back to frequency-resolved correlations, the 2PS of the mode a (2nd row in Fig. 4.3) presents, in strong-coupling, two hyperbolic dips where $g^{(2)}_\Gamma(\omega_1, \omega_2)$ drops to its

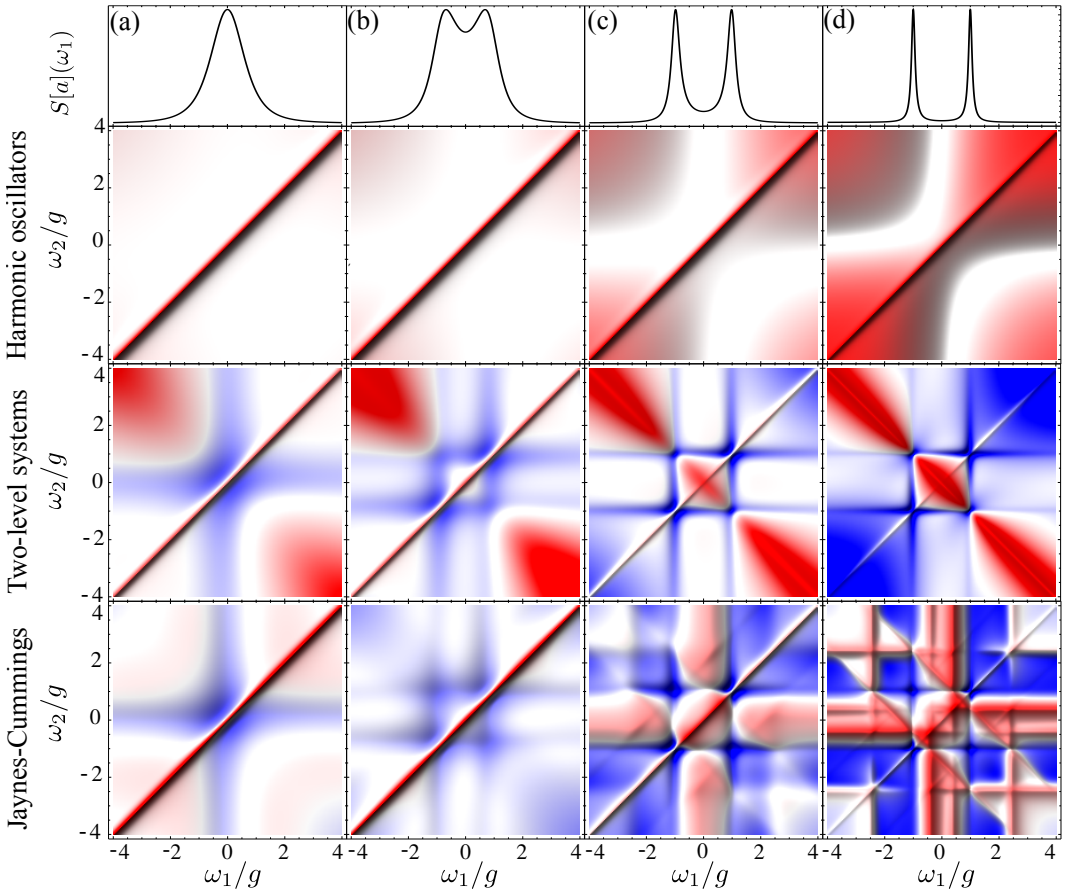

Figure 4.3: First row: 1PS in the linear regime, identical for cHOs, c2LSs and the JC model. Second/third/fourth rows: 2PS for the cHOs/c2LSs/JC model. In the c2LS and JC model a logarithmic scale has been used to improve the visibility of the features. Columns (a)-(e) correspond to increasing the quality of the coupling as $\gamma_{O_1}/g = 4, 2, 1, 0.5, 0.1$. In all cases, $\Gamma = 0.1g$, $P_{O_1} = 0$ and $\gamma_{O_2} = 0.001g$.

minimum value of 1. The hyperbolas, given by the equation

$$\omega_1\omega_2 = -g^2\,, \tag{4.13}$$

corresponds to the detected frequencies (ω_1, ω_2) hitting the polariton branches which, as a function of detuning Δ, read $\omega_\pm(\Delta) = \Delta/2 \pm \sqrt{g^2 + (\Delta/2)^2}$. When one detects a photon at ω_1, the classical system does not provide information on whether this photon comes from the main peak itself (where the dressed state is located and the mode emits predominantly) or from any other point on its tail. This photon is detected as if emitted by the polariton being at precisely this energy. It has thus the fitting correlation of the coupled oscillators with another photon detected at the energy of the other polariton with the same detuning as the would-be polariton accounting for the first photon. The 2PS thus evidence the existence of the full polariton dispersion via a change in the statistics, even though the modes are at resonance in the 1PS. This shows again the richer discriminative power of two-photon spectroscopy. The 2PS anticrossing is wider than the 1PS one given that the distance between vertices $(\pm g, \mp g)$

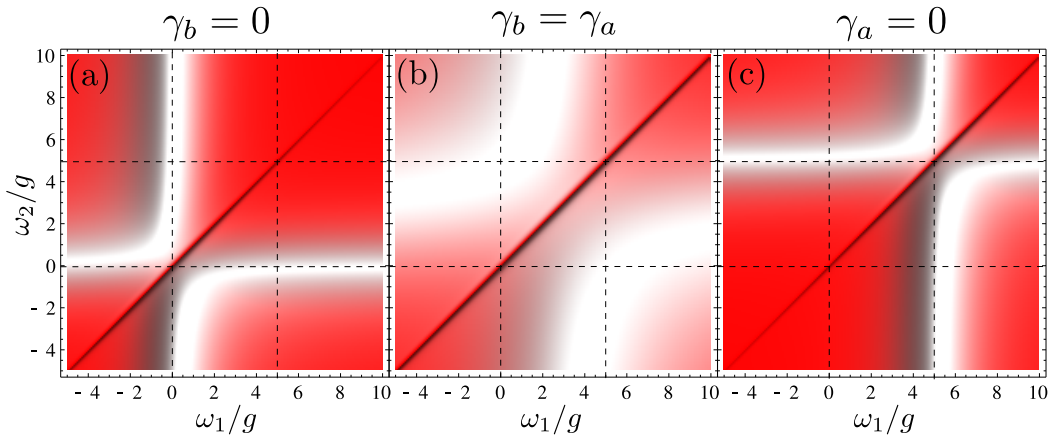

Figure 4.4: 2PS for coupled and detuned harmonic oscillators. The bare states are at frequencies $\omega_a = 0$ and $\omega_b = 5g$ (dashed lines). The total decay in the system is kept fixed to $\gamma_a + \gamma_b = 0.1g$ while γ_a and γ_b vary as indicated above each plot. Other parameters: $P_a = 0$, $P_b \ll \gamma_{a,b}$ and $\Gamma = 0.1g$.

is $2\sqrt{2}g$ instead of $2g$. The renormalisation by $\sqrt{2}$ is due to the fact that the information is carried at the two-photon level instead of one in the photoluminescence.

When the modes are detuned, the polariton correlation interferences still form an hyperbola,

$$\Big(\omega_1 - \omega_{\rm hyp}\Big)\Big(\omega_2 - \omega_{\rm hyp}\Big) = -V_{\rm hyp}^2\,, \tag{4.14}$$

but its center, $\omega_{\rm hyp}$, and vertex, $V_{\rm hyp}$, depend on the set of relevant parameters of the system, namely $\{P_a, P_b, \gamma_a, \gamma_b, \omega_a, \omega_b\}$, as shown in Fig. 4.4. In order to gain further insight into this dependence, let us assume that polaritons are well defined and, therefore, the 1PS is essentially the sum of two Lorentzian peaks associated with each polariton, $S[a](\omega) \approx L_-^a(\omega) + L_+^a(\omega)$. We can neglect the dispersive contributions to the spectrum [110] thanks to the negligible overlap between these peaks and assume complete uncorrelation between the polaritons, $g^{(2)}[p_+; p_-] \approx 1$. In a single particle picture, one can define a frequency dependent operator for mode a, $\alpha(\omega) = \sqrt{L_-^a(\omega)}p_- + \sqrt{L_+^a(\omega)}p_+$, using the relative spectral weights,

$$L_\pm^a(\omega) = \frac{l_\pm^a}{\pi}\frac{\gamma_\pm/2}{(\gamma_\pm/2)^2 + (\omega - \omega_\pm)^2}\,, \tag{4.15}$$

that take into account the quantum state of the system through the coefficients $l_\pm^a$ [110]. The parameters $\gamma_\pm$ and $\omega_\pm$ are the full-width half-maximum and positions of the polariton modes, $p_\pm$. The 1PS is well approximated by $\langle\alpha^\dagger(\omega)\alpha(\omega)\rangle$. In a similar way, $\langle\alpha^\dagger(\omega_1)\alpha^\dagger(\omega_2)\alpha(\omega_2)\alpha(\omega_1)\rangle$, captures some of the features of the exact results in Fig. 4.4. The correlations computed in this way are less well reproduced than the 1PS as this approach neglects the multi-photon dynamics. However, due to the linear nature of the system, they produce interferences between the well defined polaritons with the same hyperbola, Eq. (4.14), specified by:

$$\omega_{\rm hyp} \approx \frac{l_-^a}{l_-^a + l_+^a}\omega_+ + \frac{l_+^a}{l_-^a + l_+^a}\omega_-\,, \tag{4.16}$$

$$V_{\rm hyp} \approx \Re\sqrt{g^2 - \Big(\frac{4l_-^a l_+^a}{(l_-^a + l_+^a)^2}\Big)^2\Big(\frac{\Gamma_a - \Gamma_b}{4} + i\frac{\omega_a - \omega_b}{2}\Big)^2}\,. \tag{4.17}$$

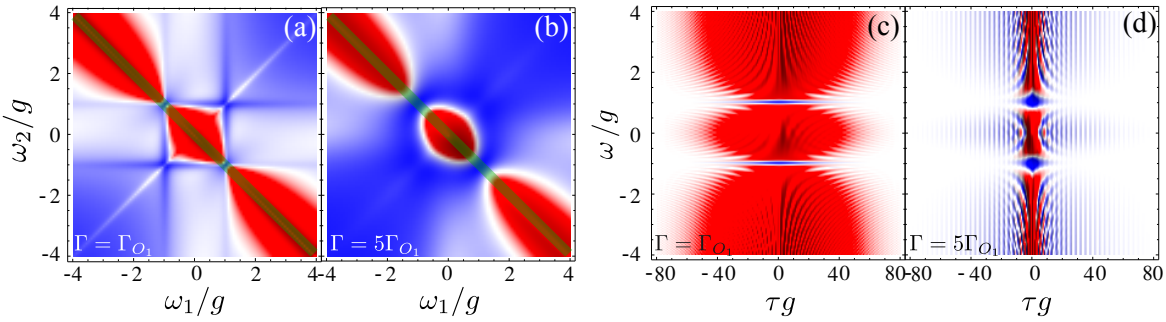

Figure 4.5: (a)–(b) Two-photon spectra (2PS), $g^{(2)}_{\Gamma}[\sigma](\omega_1, \omega_2)$, for the coupled two-level systems (c2LSs) for the parameters of Fig. 4.3 and $\Gamma = \Gamma_{O_1}$ and $\Gamma = 5\Gamma_{O_2}$.(c)–(d) Two-photon spectra dynamics (2PS), $g^{(2)}_{\Gamma}[\sigma](\omega, -\omega; \tau)$ for the c2LSs for pair of frequencies which follows the green anti-diagonal line in the 2PS of panels (a)–(b).

In Fig. 4.4, we exemplify how the quantum state affects the anticrossing of the 2PS for a detuned situation, where $\omega_- \approx \omega_a = 0$ and $\omega_+ \approx \omega_b = 5g$. For simplicity, only one mode is pumped in the linear regime ($P_a = 0$, $P_b \ll \gamma_b$). The total decay of the system is fixed ($\gamma_a + \gamma_b = 0.1g$) whereas the relative value of the two rates is varied to alter the quantum state of the system. In the asymmetric case where $\gamma_b = 0$, Fig. 4.4(a), the normalized weight is $l^a_+ \approx 0$ and, in accordance with Eq. (4.16), the center of the anticrossing $\omega_{\rm hyp} \approx \omega_a$ with a vertex $V_{\rm hyp} \approx g$. In the symmetric situation where $\gamma_a = \gamma_b$, Fig. 4.4(b), both weights are equal, $l^a_+ \approx l^a_-$, yielding a balanced position of the anticrossing between the two modes, $\omega_{\rm hyp} \approx \frac{\omega_a+\omega_b}{2}$, and a larger splitting given by the same Rabi splitting as the 1PS, $V_{\rm hyp} \approx \sqrt{g^2 + (\omega_a - \omega_b)^2/4}$. Finally, in Fig. 4.4(c) where $\gamma_a = 0$, the quantum state with $l^a_- \approx 0$, yields $\omega_{\rm hyp} \approx \omega_b$ and the same vertex as in the case of Fig. 4.4(a), $V_{\rm hyp} \approx g$.

4.4.2 Coupled Two-Level Systems (c2Ls).

The c2LSs inherit the possibility to display antibunching from its components. When the system enters in SC marked subpoissonian regions appear in the 2PS in stark contrast with the cHOs. First, four vertical and horizontal lines, with stronger suppression at their crossing, appear when ω_1 or $\omega_2 = \pm R$, the polaritonic energies. At low pumping, the first rung of excitation dominates and, therefore, two polaritons are rarely detected simultaneously. The second feature that jumps to the eye is the superpoissonian antidiagonal, $\omega_1 + \omega_2 = 2\omega_\sigma = 0$. Such correlations correspond to fast two-photon relaxation from the doubly occupied state $|1,1\rangle \rightarrow\rightarrow |0,0\rangle$, through a virtual (off-resonant) intermediate state. Only thanks to the coupling, can the same 2LS effectively emits two excitations at the same time (within the detector time window $1/\Gamma$). We use the term *leapfrog* for this new type of processes, as the first rung is not actually populated. This is a fundamental process that is common to all quantum non-linear systems. It becomes more prominent as the detector width, Γ, decreases and the time uncertainty of measurement increases. This supports the idea that the emission of two identical photons can be enhanced (and selected) by placing the system in a high-Q cavity [149–151].

In order to get further understanding in the impact of the detector linewidth in the

observation of these new type of processes, in Fig. 4.5, the 2PS and time-dynamics of the c2LS system for two different Γ's have been plotted. In panels (a)–(b), we show the 2PS for $\Gamma = \Gamma_{0_1} = 0.1g$ and $\Gamma = 5\Gamma_{0_1}$. As expected for the case of a bigger filter, all the features are smoother than for the thinner case. Remarkably, the four points of antibunching appearing at $(\pm g, \pm g)$ and $(\mp g, \pm g)$ are smeared out transforming into a circle of antibunching. In order to explore the τ-dynamics of the real and virtual processes, we choose the set of points corresponding to the antidiagonal line depicted in green in panels (a)–(b) of Fig. 4.5. This set of frequencies is significant as it sweeps the main line of leapfrog processes together with two points, $(\pm g, \mp g)$, of interference of the polariton lines. In panel (c), the τ-dynamics for the thinner detector, $\Gamma = \Gamma_{0_1}$, is plotted. One can observe that the leapgrogs are dominated by a bunching dynamics, whereas in the case of $(\pm g, \mp g)$ two lines of antibunching dynamics appear. Here as the timescale induced by the detector and the system is of the same order, both types of processes lead to the same timescale dynamics. In panel (d), however, we consider a case with $\Gamma = 5\Gamma_{O_1}$. Thus, the time dynamics induced by the detection process is 5 times faster than the one of the system. It is noteworthy how this fast detection timescale affects strongly to the the leapfrogs, by diminishing their importance. However it does not have much effect in the antibunching points, corresponding to real processes, which are even enhanced by a bigger filter linewidth. This proves that these new kind of leapfrog processes emerging in quantum non-linear systems are directly connected to the uncertainty introduced by the detection.

4.4.3 Jaynes-Cummings model (JC).

In the remainder of the text, we focus on the paradigmatic JC model, the coupling of a single HO (a) and 2LS (σ), as the different nature of the modes provides a richer dynamics. The ladder-type level structure that arises in SC, as shown in Fig. 4.6, is formed by the non-linear splittings (with the number of excitations n): $2E_n = 2\sqrt{(\sqrt{n}g)^2 - [(\gamma_a - \gamma_\sigma)/4]^2}$ [87]. The broadening of the transitions are also dependent on the manifold of excitation and they are given by: $\gamma_n = 2(n-1)\gamma_a + \gamma_b$ [120]. As with the c2LSs, at the same coupling strength that the Rabi doublet appears in the 1PS, Fig. 4.3(b), four antibunching dips appear in the 2PS at ω_1 or $\omega_2 = \pm R$, corresponding to the situation depicted in Fig. 4.6(i).

Stronger coupling, in Fig. 4.3(c)-(e), provides a distinct separation of transitions between different rungs, $R_n^{\pm} = E_n \pm E_{n-1}$, following their non-linear splitting. Two-photon cascade processes resonant with the ladder transitions, such as that in Fig. 4.6(ii), are isolated from each other and manifest in a clear enhancement of correlations. Similarly, non-consecutive transition frequencies appear as anticorrelated, such as $(-R_2^-, R)$. A grid of the corresponding horizontal and vertical lines emerges, as plotted in Fig. 4.6 with black solid lines, with enhancement/suppression of correlations at every crossing point depending if the frequency combination corresponds to consecutive/non-consecutive processes [152]. This grid structure corresponding to the system "real transitions" is better resolved in the best systems, Fig. 4.3(d)–(e), Fig. 4.7(c).

We now turn to the "virtual processes" which involve transitions into virtual states during the short interaction time with the detector, $\sim 1/\Gamma$. Two antidiagonal lines at $\omega_1 + \omega_2 = 2\omega_a \pm E_2 \approx \pm\sqrt{2}g$ (dashed green lines in Fig. 4.6), present superpoissonian enhancement with the same origin as the antidiagonal line in the c2LSs: leapfrog two-photon transitions

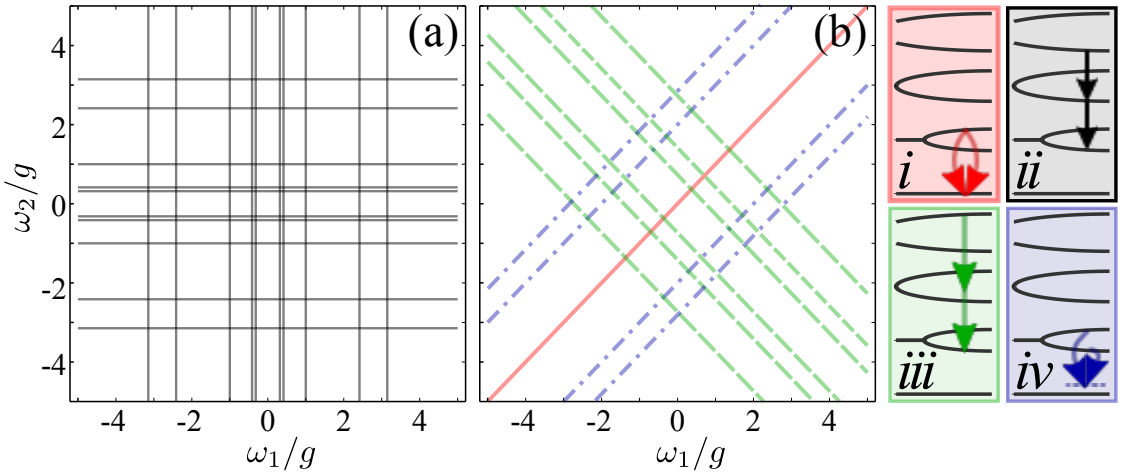

Figure 4.6: Patterns of two-photon correlations in the Jaynes–Cummings model up to the third rung of excitation (low pumping regime). (a) The grid of horizontal and vertical lines (solid black) corresponds to correlations between real states, when one frequency is pinned at a transition in the ladder that is correlated with emission anywhere else in the system resulting in resonances when matching with a cascade (bunching) or an incompatible process like emission from the other type of polariton (antibunching). (b) The grid of antidiagonal lines (dashed green) corresponds to leapfrog processes where two-photon transitions take place from one rung of the ladder to another one two steps below, jumping over the intermediate rung. The grid of diagonal lines (except the central one, dashed-dot blue) correspond to polariton-to-virtual-state antibunching. The "indistinguishability bunching" (diagonal red line) is common to all 2PS. These two panels overlapping emerge clearly in the best systems, cf. Fig. 4.3(c)–(e), up to the second rung, and Fig. 4.7(c), (d). Panels *i*–*iv* on the right are sketches of the underlying processes responsible for these correlations (with the same color code).

from the second rung dressed states to the ground state, through virtual intermediate states, as depicted in Fig. 4.6(iii). Increasing the excitation power, four satellite antidiagonal lines appear corresponding to leapfrogs from the third rung, satisfying: $\omega_1 + \omega_2 = 2\omega_a \pm (E_3 - E_1)$ or $\pm(E_3 + E_1)$, as one can identify in Fig. 4.7(d). In general, leapfrogs are present in any nonlinear system, as simple as the c2LSs or an anharmonic oscillator.

We discuss next new unexpected features that emerge in the JC case, namely the secondary diagonal lines at $\omega_1 - \omega_2 = \pm 2R$ (dotted-dashed blue lines in Fig. 4.6). The 2PS here is typically reduced as compared to the surrounding region, melting into the two antibunching dips at the first rung resonances $\omega_1 = -\omega_2 = \pm R$. They correspond to the anticorrelated emission from both polaritons of the first rung into the same virtual final state, as shown in Fig. 4.6(iv). The lines become more pronounced when only the mode under observation is pumped, meaning that the interference between relaxations from $|1+\rangle$ and $|1-\rangle$ is playing a role. In such pumping configuration, strong polariton-to-virtual-state correlations appear in the c2LSs as well (not shown). They are not peculiar to the JC model but to any strongly coupled, nonlinear system. Higher excitation, makes higher order diagonal lines appear, corresponding to higher rung dressed states, such as $\omega_1 - \omega_2 = \pm 2E_n$. Second rung diagonals are visible in Fig. 4.7(d).

This Section provides one of the main conclusions of the Chapter: The dynamics of "real processes", involving photon by photon de-excitations, are related to the system parameters

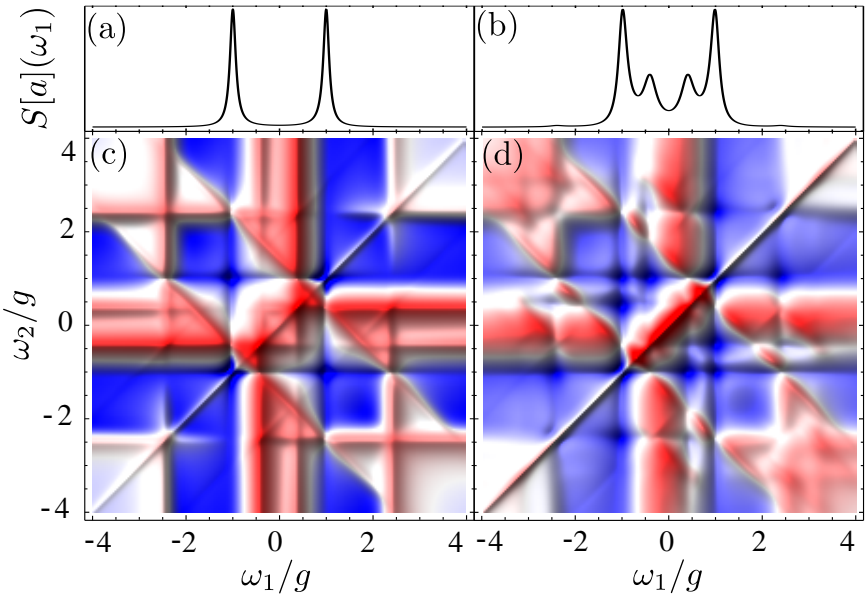

Figure 4.7: 1PS (first row) and 2PS (second row) for JC, going from vanishing pumping in (a), (c), to the nonlinear regime in (b), (d), $P_\sigma = 0.05g$. Second rung transitions appear in the 1PS inside the Rabi doublet and new features involving the third rung of excitation appear in the 2PS.

and less influenced by detection. The corresponding correlations are best resolved when the related peaks are separated and fully filtered. On the other hand, "virtual processes", involving virtual states such as the leapfrogs and polariton-to-virtual state interferences, happen within the time of interaction with the detector $1/\Gamma$ and conserving energy within its width Γ. Therefore, their correlations become more prominent using narrow filters.

Apart from making a comprehensive analysis of $g^{(2)}_\Gamma[a]$ specifics, we now turn to investigate higher order correlation functions which are exceedingly hard to compute with previous methods, such as the simultaneous three-photon correlations, $g^{(3)}_\Gamma[a](\omega_1;\omega_2;\omega_3)$. First, we fix two frequencies of detection at $\omega_2 = R_2^-$ and $\omega_3 = R$ (solid arrows on the right of Fig. 4.8(a)) and again let ω_1 vary. A strong enhancement is also observed for all systems, now at $\omega_1 = R_3^-$ which monitors the cascade $|3+\rangle \to |2+\rangle \to |1+\rangle \to |\text{vac}\rangle$ depicted in Fig. 4.2(a) and at $\omega_1 = -R_3^+$ which starts it with $|3-\rangle \to |2+\rangle$. Other transitions show dips that are also clearly understood. This hints at the possible characterization of the level structure of an open quantum system. In general, however, one cannot draw conclusions from the zero-delay case only, in particular for small features, such as the small enhancement at $\omega_1 = -R_2^+$ in $g^{(3)}_\Gamma[a]$ (for the dashed line only) which is not necessarily a bunching peak and reveals itself in the τ-dynamics to be antibunched, as discussed later.

In Fig. 4.9(a), we explore the next important aspect of $g^{(N)}_\Gamma[a]$, namely the dependence of correlations on the sensors' linewidths, which is related to the complementary uncertainties in time and frequency. In the case $\Gamma \to 0$ of perfect detectors, $g^{(N)}_0[a] = 1$ for all N, since all the frequencies are different [1]. The other limit $\Gamma \to \infty$ corresponds to the opposite situation

[1]This limit has been misunderstood in the literature. In Ref. [96], only the frequency convolution is performed and, in the absence of time convolution, photon counting diverges in the steady state. A generalized

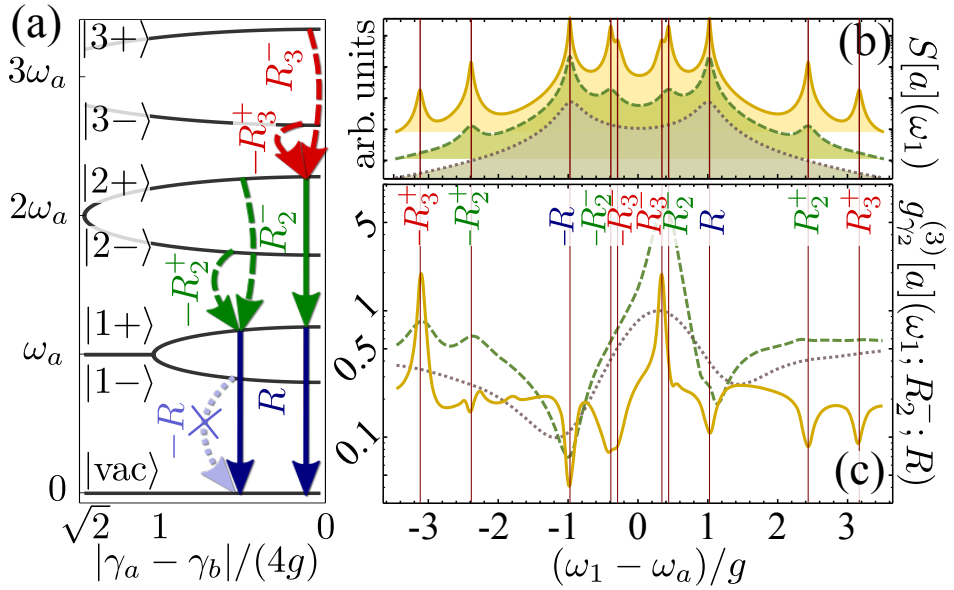

Figure 4.8: (a) Dissipative Jaynes-Cummings ladder up to the first three rungs with two of the cascades probed in panels (c) [with three photons]. Solid arrows show the fixed frequencies. Curved arrows show the scanning frequency ω_1, at the transitions where the joint emission is strongly enhanced (dashed) or, on the other hand, suppressed (dotted). (b) Cavity 1PS, $S[a](\omega)$, probed by weak incoherent excitation ($P_b = \gamma_b = 0.01g$) for three cavities of decreasing quality $\gamma_a = 0.01$ (solid), 0.1 (dashed) and $0.5g$ (dotted).(c) Three-photon correlations, $g^{(3)}_\Gamma(\omega_1;\omega_2;\omega_3)$, at zero delay for the three cavities, with sensor linewidths $\Gamma = \gamma_2$ (solid) and $\gamma_2/2$ (dashed and dotted).

of exact τ-delay between photons of completely indeterminate frequencies. This is of more interest, in particular at zero time delay, which is the case of Fig. 4.9(a). For instance, for the Jaynes-Cummings system at low pumping, this recovers results derived by other approaches for colorblind detectors [115, 153]:

$$g^{(N)}[a] = Ng^{(N-1)}[a](4g^2/\gamma_a+\gamma_b)(\gamma_b+\gamma_a)/\left[(4g^2/\gamma_a+\gamma_b+(n-1)\gamma_a)(\gamma_b+(n-1)\gamma_a)\right] \quad (4.18)$$

The intermediate case of finite linewidth of the sensors is the most interesting. Features are most marked when linewidths are of the order of those of the transitions involved, since this is when the peaks of the spectrum are best filtered. Smaller linewidths (longer times) are to be favoured for bunching and larger linewidths (smaller time) for antibunching. One sees for instance in Fig. 4.9(a) that consecutive transitions—such as those sketched in panel i (with three photons) or ii (with two photons)—show an enhancement as a result of detecting photons in the order of their emission in the cascade. Conversely, the simultaneous emission from both Rabi peaks, in the configuration sketched as iv, is substantially suppressed, leading to a strong antibunching. This observation with a microcavity containing a single quantum

Mandel Q parameter $\sqrt{S^{(1)}_\Gamma(\omega_1)S^{(1)}_\Gamma(\omega_2)}\left(g^{(2)}_\Gamma(\omega_1,\omega_2)-1\right)$ (in our notations) is used to bypass this difficulty, but for the smallest Γ considered, the filtering of the peaks is too narrow and the structures obtained are those of the prefactor only (uncorrelated photons).

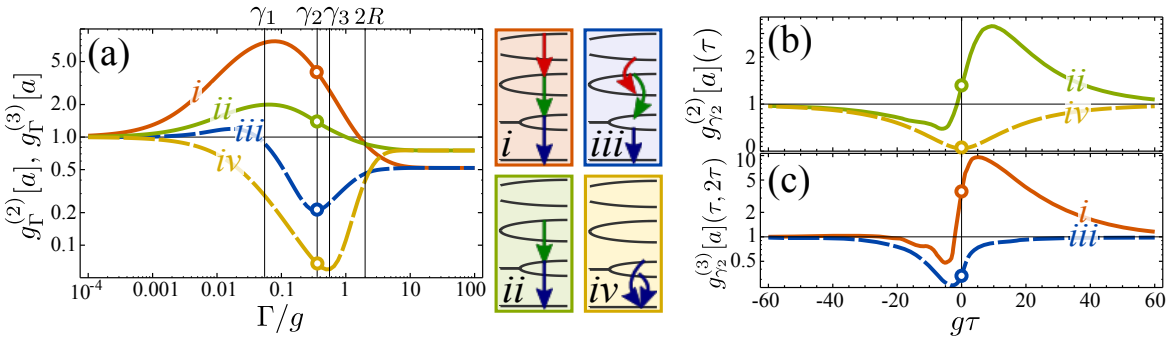

Figure 4.9: (a) Two- and three-photon correlations at zero delay as a function of the sensor linewidth Γ, with frequencies of detection as shown in the insets *i*–*iv*. (b-c) τ-dynamics of the correlation functions with $\Gamma = \gamma_2$ for, (b), two photons in the configurations of insets *ii* and *iv* and, (c), three photons in the configurations *i* and *iii*. Positive τ corresponds to detection in the order from top to bottom of the ladder. Parameters: $P_b = \gamma_b = 0.01g$, $\gamma_a = 0.1g$.

dot has been used to demonstrate the quantum nature of strong light-matter coupling [29] (with detuning to better separate the peaks). Further theoretical investigations with this formalism (to be discussed elsewhere) would allow to elucidate the nature of spectral triplets also observed in such experiments [29, 74, 139].

Figures 4.9(b-c) show an example of the τ-dependence of the correlations, for the case $\Gamma = \gamma_2$, both at positive and negative delays. The configuration *ii* has the typical shape of a cascade between consecutive levels, with antibunching for $\tau < 0$, a step at $\tau = 0$ and bunching for $\tau > 0$. This behaviour is well known, for instance from the biexciton-exciton cascade [132]. It is also observed for two-photon transitions higher in the ladder (not shown) or N-photon in any consecutive transitions, such as is shown in *i* for three photons starting from the third rung. In contrast, the filtering of peaks which do not belong to the same cascade, exhibit antibunching, as seen in *iv* for the two Rabi peaks or *iii* for one of its three-photon counterparts. In such a case, the order of the transition does not matter anyway and the $\pm\tau$ show qualitatively the same behaviour. These results are, to the best of our knowledge, the first computations of three-time frequency-resolved correlation functions. Thanks to the ease of our method, they could be easily extended to higher order correlations.

4.5 Lasing and the Mollow triplet.

We have already described the effect on the JC model 2PS of increasing the excitation power and entering the non-linear regime. Higher rungs are populated and in Fig. 4.7(d), one can distinguish correlations between transitions involving up to the third rung. Increasing P_σ further brings the HO (typically a cavity mode) into the lasing regime [88, 115] where the field becomes coherent and $g^{(2)}[a] \to 1$ as already shown in Chapter 3. There, the cavity 1PS reduces to a single line that narrows with its population as $\gamma_L \approx g^2/(2\gamma_a\langle n_a\rangle^2)$ [116], where $\langle n_a\rangle \approx P_\sigma/(2\gamma_a)$. The inverse quantity, $1/\gamma_L$, corresponds to the coherence time of the laser. More interesting is the 1PS of the 2LS (or quantum emitter), which converges to the so-called *Mollow triplet* [123], with some specificity of its own due to the incoherent nature of the excitation [154]. Therefore, in this discussion we analyse the emission directly from the

2LS, by connecting the sensors to it.

The classical Mollow triplet is obtained when a 2LS is driven by intense laser light. A standard way to describe the laser excitation is through the semiclassical Hamiltonian term $H_{\mathrm{L}} = \Omega_{\mathrm{L}}(\sigma + \sigma^{\dagger})$ which relies on the approximation of an infinite laser coherence time ($\gamma_{\mathrm{L}} = 0$). In this model, the laser dresses the 2LS levels arriving to the following dressed states,

$$|-\rangle = c\,|0\rangle - s\,|1\rangle\ , \tag{4.19}$$

$$|+\rangle = s\,|0\rangle + c\,|1\rangle\ , \tag{4.20}$$

with $|0\rangle$ the ground state and $|1\rangle$ the excited state of the 2LS. The parameters c and s determine the proportion of bare states that contains each of the dressed states and are depend on both the laser intensity, Ω_L, and detuning, $\Delta = \omega_0 - \omega_L$, as follows:

$$c = \sqrt{\frac{\sqrt{(2\Omega_L)^2 + \Delta^2} + \Delta}{2\sqrt{(2\Omega_L)^2 + \Delta^2}}}\,, \tag{4.21}$$

$$s = \sqrt{\frac{\sqrt{(2\Omega_L)^2 + \Delta^2} - \Delta}{2\sqrt{(2\Omega_L)^2 + \Delta^2}}}\,. \tag{4.22}$$

The ladder operator can then be decomposed into the four possible transitions, $\sigma = |0\rangle\langle 1| = |0\rangle\langle 1| = c^2\,|+\rangle\langle -| + cs\,|+\rangle\langle +| - cs\,|-\rangle\langle -| - s^2\,|+\rangle\langle -|$. The first and last terms give rise to sidebands in the 1PS at positions $\Omega_{\pm} = \pm\sqrt{(2\Omega_L)^2 + \Delta^2}$, whereas the two in the middle are responsible of the central peak, as showed schematically in Fig. 4.10(c).

In the case of the quantized model of laser described by the JC ladder, the splitting from very high rungs of the JC ladder becomes homogeneous giving rise to similar dressed states, $|n\pm\rangle \approx |n\pm\rangle$ as in the classical Mollow triplet. The intensity of the effective cavity laser acting on the 2LS depends directly on the population of the cavity $\langle n_a\rangle = \Omega_{\mathrm{L}}^2/g^2$.

The 1PS between the conventional Mollow triplet and the fully quantized picture are compared in Fig. 4.10(a) and Fig. 4.10(b) respectively. Parameters were chosen so that $\langle n_a\rangle = 9.5$ in both cases and the three peaks match in position and broadening, with $P_\sigma = 2g$ for the JC. A fundamental difference between the lineshapes, is that the finite laser linewidth, γ_{L}, in the JC model produces a Rayleigh scattering peak of the same width on top of the 2LS incoherent triplet, while it is a Dirac δ function in the conventional Mollow triplet theory due to the infinite coherence time of the laser. We show that, although this is a rather innocent departure in the 1PS, it has dramatic consequences for the photon statistics.

Correlation between full, well separated peaks of the Mollow triplet has been subject of experimental [127–129] and theoretical [91, 93, 95, 96, 133–135, 155, 156] studies, always within the semiclassical model. Recently, the 2PS (more specifically a closely related generalised Mandel Q parameter) of resonance fluorescence was obtained [96] within the generating function formalism, via single-molecule photon counting statistics with spectral resolution. One can understand these correlations again through the decomposition into two-photon dressed state transitions:

$$\sigma\sigma = s^3 c\,|-\rangle\Big(\langle +|+\rangle - \langle -|-\rangle\Big)\langle +| - c^2 s^2\,|+\rangle\Big(\langle -|-\rangle - \langle +|+\rangle\Big)\langle +| \tag{4.23}$$

$$+c^3 s\,|+\rangle\Big(\langle +|+\rangle - \langle -|-\rangle\Big)\langle -| - c^2 s^2\,|-\rangle\Big(\langle +|+\rangle - \langle -|-\rangle\Big)\langle -|\ . \tag{4.24}$$

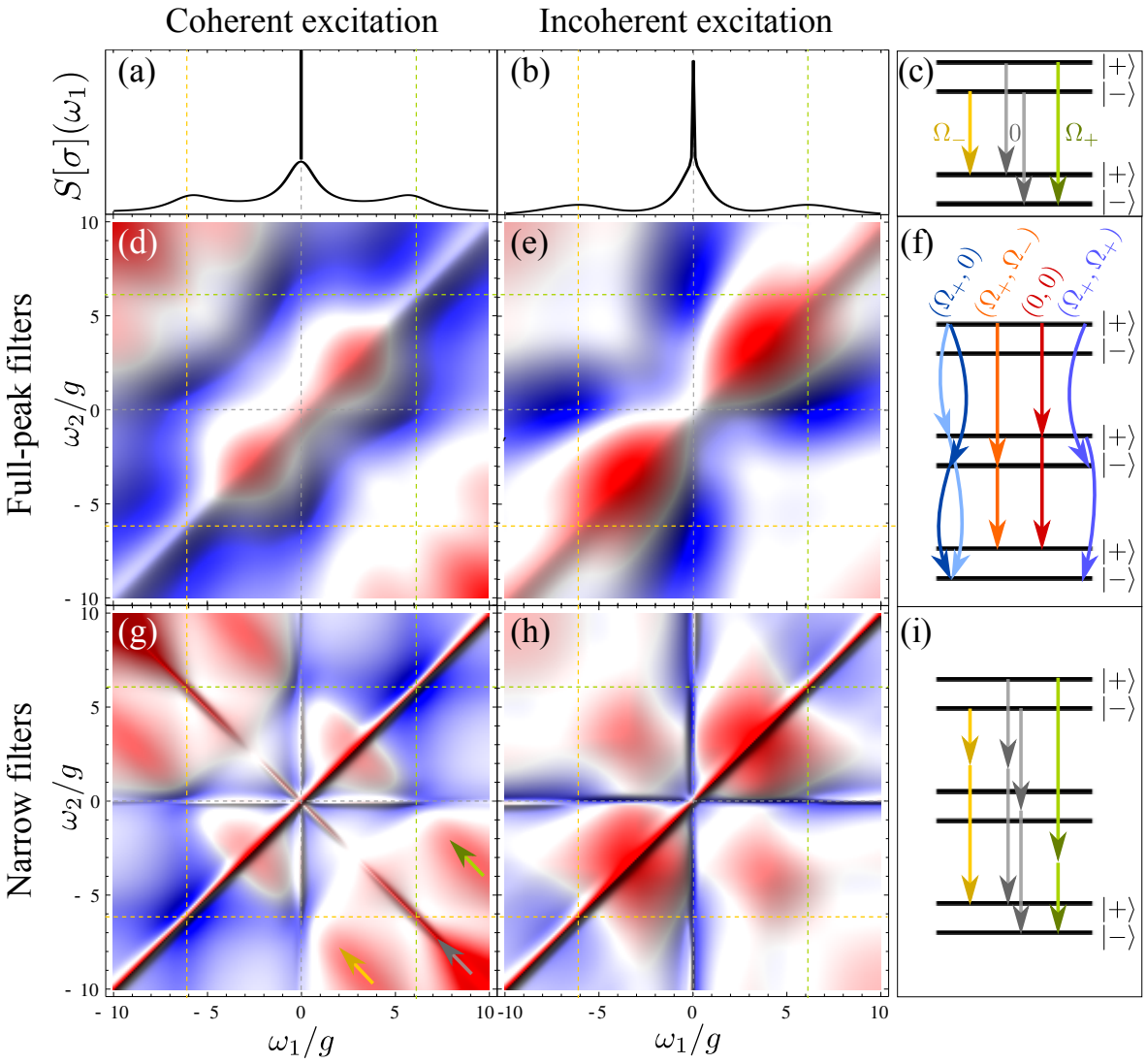

Figure 4.10: Normalised 1PS (first row) and 2PS (second and third rows) for the Mollow triplet under coherent (left) and incoherent excitation (right). Parameters are chosen so that the sidebands are at the same positions $\Omega_\pm = \pm 6.16g$ and have the same broadening with $P_\sigma = 2g$ and $\langle n_a \rangle = 9.5$. Vertical/horizontal gridlines mark the positions of the upper (green), lower (orange) and central black (peaks), arising from the transitions between dressed states depicted in (c). In (d) and (e) the detector width, $\Gamma = 3P_\sigma/2$, is wide enough to filter full spectral peaks. Clear correlations appear for the pairs of transitions in (f). In (g) and (h) the detector width, $\Gamma = P_\sigma/2$, is smaller than the spectral peaks. In this case, the dominant feature is the *leapfrog* triplet of antidiagonal lines, corresponding the to two-photon de-excitation processes sketched in (i).

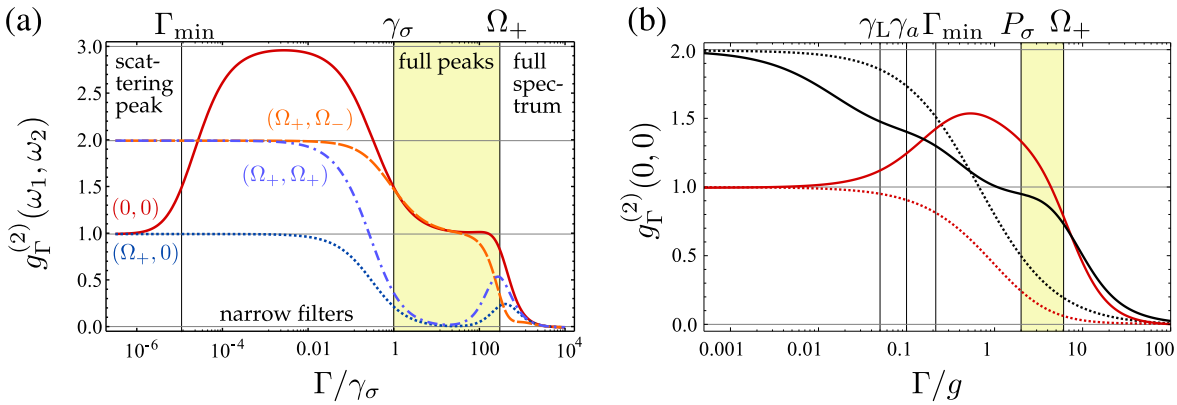

Figure 4.11: Two-photon correlators for frequencies of interest of the Mollow triplets as a function of the detector linewidth, Γ. (a) Correlations of a two-level system driven by a large coherent pump ($\Omega_L = 150\gamma_\sigma$) for the four most relevant (ω_1,ω_2) configurations: $(0,0)$ in a solid red line, (Ω_+,Ω_-) in dashed orange, (Ω_+,Ω_+) in dotted-dashed blue and $(\Omega_+,0)$ in dotted blue. Four regions of detection can be defined (separated by vertical gridlines). Correlations from the central peak (solid red) exhibit a bunching region of $g^{(2)}_\Gamma[\sigma](0,0) \approx 3$ at small Γ when the coherent scattering is a significant fraction of the filtered light. Vanishing Γ yields the statistics of the classical laser since the semiclassical zero linewidth cannot display indinstinguishability bunching. (b) Comparison of the central peak correlations, $(0,0)$ (solid red), in the case of an incoherently pumped two-level system in free space (dotted black) and in a cavity (solid black). The laser intensity here is lower: $\Omega_\pm = \pm 6.16g$ as in Fig. 4.10. The linear regime, $\Omega_L \ll \gamma_\sigma$, is plotted with a dotted red line as a reference in units of $\gamma_\sigma = g$. When the photon field is quantized, the correct limit $g^{(2)}_\Gamma[\sigma](0,0) = 2$ when $\Gamma \to 0$ is recovered.

Each of the 2^3 terms represents a possible deexcitation path and all together, they interfere destructively to give rise to the expected total antibunching as $\sigma\sigma = 0$. The first line corresponds to the cascade transitions depicted in Fig. 4.10(f), starting from $|+\rangle$:

- $(\Omega_+,0)$: One would expect this combination to produce bunched photons but, as it corresponds to two different paths with amplitudes of probability with opposite signs (first two terms in Eq. (4.23)), destructive interference leads to $g^{(2)}_\Gamma[\sigma](\Omega_+,0) = 0$. Such *debunching* effect occurs within the detector timescale $1/\Gamma$ [128, 157].
- (Ω_+,Ω_-): Their cascade configuration produces a strong bunching, with a well defined time order that depends on the detuning with the laser [134]. However, at resonance, destructive interference debunches again the statistics to $g^{(2)}_\Gamma[\sigma](\Omega_+,\Omega_-) = 1$.
- $(0,0)$: A similar situation of bunching and interference leads to $g^{(2)}_\Gamma[\sigma](0,0) = 1$.
- (Ω_+,Ω_+): photons from the same sideband do not form a cascade so their simultaneous emission is suppressed (despite the indistinguishability bunching): $g^{(2)}_\Gamma[\sigma](\Omega_+,\Omega_+) = 0$.

These ideal correlations are shown in Fig. 4.11(a) in the full peak detection region (in yellow), where $\Omega_L \gg \Gamma_\sigma$. With a less intense laser such as than in Fig. 4.10, the features are still visible but slightly tempered due to the overlap between peaks, as is the case in experiments [129].

Thanks to the ease of use of our general solution, we are able to compare the semiclassical, in Fig. 4.10(d), model for the laser to the JC model, Fig. 4.10(e), which requires a high cavity photon number, providing the one-atom laser 2PS for the first time. In these qualitatively similar plots, the interference effect described above is even more evident as it extends beyond the four points $(\Omega_\pm, 0)$, forming two blue rings of antibunched statistics. These interference rings are more clear in the strongly driven situation depicted in Fig. 4.12. Their origin, as for the leapfrogs, stems from the uncertainty introduced by including the detector physics, which extends the interference appearing at the points $(\Omega_\pm, 0)$ and $(\Omega_\pm, \Omega_\pm)$ to two circles. At the center of these interference rings, $(\Omega_\pm/2, \Omega_\pm/2)$, two red spots of enhanced emission appear from the concentration of leapfrog outer lines in the Jaynes-Cummings model. With a narrower detector, leapfrogs are enhanced due to the longer uncertainty in the time of two-photon emission, as shown in Fig. 4.10(g) and (h). In the same way that the JC multiplets from high rungs of excitation converge to the Mollow triplet in the 1PS, the antidiagonal leapfrog lines in the 2PS converge to a *leapfrog triplet* at:

$$\omega_1 + \omega_2 \approx 0\,, \quad \omega_1 + \omega_2 \approx \Omega_\pm\,, \tag{4.25}$$

as schematically depicted in Fig. 4.10(i). They are more pronounced in Fig. 4.10(g), as the perfect laser approximation, H_L, generates dressed states homogeneously split for all intensities $\Omega_{\rm L}$.

If the detectors are narrower than the peaks, $\Gamma < \Gamma_\sigma$, the interference effect described above disappears (see Fig. 4.11). Furthermore, as we previously discussed, when Γ is smaller than any peak width, photons are detected from any point of the dynamics and appear as uncorrelated. For different frequencies this means $\lim_{\Gamma\to 0} g^{(2)}_\Gamma[\sigma](\omega_1,\omega_2) = 1$ while for equal frecuencies, $\lim_{\Gamma\to 0} g^{(2)}_\Gamma[\sigma](\omega,\omega) = 2$ due to the indistinguishability of the photons. In this limit, the statistics observed can no longer be attributed to the system, but to the detection process. The 2LS excited incoherently (with or without the cavity) always recovers this limit correctly as, in the JC model, the smallest width, $\gamma_{\rm L}$ is still finite and sets a clear lower boundary (see Fig. 4.11(b)). In contrast, one has a totally different result under coherent excitation of a perfect laser whenever $\omega_1 + \omega_2 = 2\omega_{\rm L} = 0$: $\lim_{\Gamma\to 0} g^{(2)}_\Gamma[\sigma](0,0) = 1$ and $\lim_{\Gamma\to 0} g^{(2)}_\Gamma[\sigma](\Omega_+,\Omega_-) = 2$. Due to the implicit assumption of zero-linewidth for the laser field, it is not possible in these cases for the detector linewidth to be thinner and reach the uncorrelated limit. Instead, the limit $\Gamma \to 0$ isolates completely the Rayleigh peak so correlations become exactly 1, those of the laser. This occurs with a detector linewidth below $\Gamma_{\rm min}$, defined as that at which the coherent part of the filtered 1PS is as large as the incoherent part,

$$S^{\rm coh}_{\Gamma_{\rm min}}[\sigma](0) = S^{\rm incoh}_{\Gamma_{\rm min}}[\sigma](0)\,, \tag{4.26}$$

where $S_\Gamma[\sigma](\omega) = S^{\rm coh}_\Gamma[\sigma](\omega) + S^{\rm incoh}_\Gamma[\sigma](\omega)$. In the limit of intense lasing, $\Gamma_{\rm min} \approx \Gamma^3_\sigma/(4\Omega^2_{\rm L})$. In the intermediate region, $\Gamma_{\rm min} < \Gamma < \Gamma_\sigma$, correlations from the central peak are bunched (and equal to 3 in the ideal case), due to the mixture of scattered and emitted light.

In real lasers, $\gamma_{\rm L} \neq 0$ due to phase fluctuations. Non-monochromatic theoretical models, where the phase varies stochastically [158, 159], take into account both the amplitude and speed of fluctuations, recovering not only a finite $\gamma_{\rm L}$ for the laser mode [158, 160] but also physical correlations at all limits [161]. The JC model or one-atom laser is free from this pathology as fluctuations are intrinsic to the dynamics, provided by the interplay between

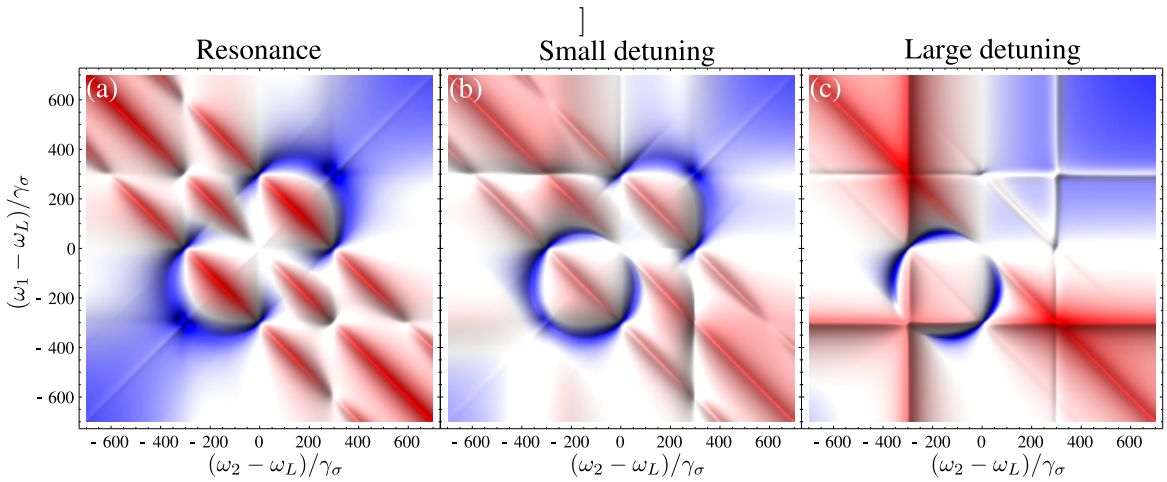

Figure 4.12: 2PS for the 2LS under coherent excitation deep in the Mollow triplet regime ($\Omega_+ = \sqrt{(2\Omega_\mathrm{L})^2 + (\omega_\sigma - \omega_\mathrm{L})^2} = 300\gamma_\sigma$) in the cases where (a) the laser is on resonance with the 2LS ($\Omega_\mathrm{L} = 150\gamma_\sigma$, as in Fig. 4.11(a)), (b) there is some detuning ($\Omega_\mathrm{L} = 100\gamma_\sigma$), (c) detuning dominates ($\Omega_\mathrm{L} = 10\gamma_\sigma$). In contrast with the 1PS, detuning turns the 2PS assymetric.

coherent exchange, incoherent pump and decay. However, not being perfectly coherent, it is harder to isolate completely the cavity laser field and recover the laser correlations. One requires a very good system ($\gamma_a \ll g$) in a very intense and well defined lasing regime, where $\gamma_\mathrm{L} \ll \gamma_a, \Gamma_\mathrm{min}$, that is $P_\sigma \gg \sqrt{2}g$.

Very broad filters $\Gamma \gg \Omega_+$, overlapping in frequency, recover the full antinbunching of the 2LS, $\lim_{\Gamma\to\infty} g^{(2)}_\Gamma(0,0) = g^{(2)}_\sigma = 0$. This is independent of the type of excitation. Under very low coherent excitation (dotted red line in Fig. 4.11(b)), where the 1PS is dominated by the coherent part, correlations monotonously go from 1 to 0 as

$$\lim_{\Omega_\mathrm{L}\to 0} g^{(2)}_\Gamma(0,0) = \left(\frac{\gamma_\sigma}{\gamma_\sigma + \Gamma}\right)^2. \tag{4.27}$$

This regime has been exploited to create an ultra-coherent, i.e. indistinguishable in frequency thanks to the inherited long laser coherence time, single photon source [162–166]. It is interesting to note that filtering the coherent peak, $\Gamma < \gamma_\sigma$, leads to the laser statistics and the destruction of the antibunching even if the coherent part strongly dominates the 1PS. Only the full emission has the property of interfering destructively and provide photons one by one.

Finally, the impact of detuning from the laser (in the semiclassical approximation) is shown in Fig. 4.12. In the absence of pure dephasing, the 1PS remains symmetric around the laser frequency (here $\omega_\mathrm{L} = 0$). Interestingly, the 2PS does not, even if detuning is small as compared to the driving, as shown in (b). The asymmetry in the 2PS consists in the disappearance of the ring of interferences nearer to the two-level system frequency (in this case $\omega_\sigma > \omega_\mathrm{L}$). When detuning dominates and $\Omega_+ \approx \omega_\sigma$, as in (c), the region around this peak becomes more antibunched, as it correspond to a real transition in a two-level system. On the other hand, the region around the other sideband, (Ω_-, Ω_-), becomes more bunched, as it corresponds to a virtual laser transition [133, 134]. Two red lines cross at (Ω_-, Ω_-),

only interrupted by the blue interference ring. A strong bunching point emerges at (Ω_+, Ω_-), accompanied by the typical cascade τ-dynamics, making the system suitable for heralded single photon emission [129].

One can understand the asymmetry in the 2PS with detuning, $g^{(2)}_\Gamma[\sigma](\Omega_+, \Omega_+) \neq g^{(2)}_\Gamma[\sigma](\Omega_-, \Omega_-)$, as a manifestation of the dissimilar two-photon dynamics of the dressed states, namely, the τ-dynamics of the colour-blind correlations corresponding to each transition: $g^{(2)}[|-\rangle\langle+|](\tau)$ and $g^{(2)}[|+\rangle\langle-|](\tau)$. These two functions are identical in the limiting τ-values, equal to 0 at $\tau = 0$ and to 1 at $\tau \to \infty$, but evolve differently at intermediate τ. In the limit of high excitation and full filtering of each peak, such dressed state two-photon dynamics is overall well mapped by the frequency-resolved correlations, $g^{(2)}_\Gamma[\sigma](\Omega_+, \Omega_+, \tau)$ and $g^{(2)}_\Gamma[\sigma](\Omega_-, \Omega_-, \tau)$, as long as $\tau > 1/\Gamma$. However, as we have shown, the $\tau = 0$ value is not well mapped, being larger than zero when the detection is included (spoiling perfect antibunching). The frequency-resolved functions at $\tau = 0$, include an average over the short-time dressed-state dynamics, within the detector time-scale, $1/\Gamma$. Therefore, the interaction with the filter/detector can be considered a dephasing mechanism of the dressed-state dynamics, which breaks the symmetry of the 2PS even at $\tau = 0$. This view is confirmed by the behaviour of the physical time-dependent 1PS [83], in the absence of pure dephasing, which is also asymmetric in general before reaching its symmetric steady state lineshape (not shown).

4.6 Conclusions.

In conclusion, we have performed the first systematic investigation of the two-photon spectra (2PS) of a variety of quantum optical systems, using our recently developed formalism to compute frequency and time resolved N-photon correlations [152, 167]. We have focused here on the case $N = 2$ of two-photon correlations at zero time delay. Thanks to our formalism, such investigations can be generalised to higher photon number and/or arbitrary time delays. We studied systems of increasing complexity, starting from the simplest possible case that is the quantum harmonic oscillator and proceeding with the two-level system and then all their possible combinations, namely, two coupled harmonic oscillators, two two-level systems and a mixture of both that amounts to the celebrated Jaynes-Cummings model. The latter, in contrast with our starting point, is an extremely rich and complicated system that stands as the pillar of cavity quantum electrodynamics. We have outlined what are the common features shared by all these systems and what are those specific to their underlying structure and dynamics. These results constitute the backbone for two-photon spectroscopy. The main finding can be summarised as follows:

- There is a universal bunching of photons when filtering an emission line below its linewidth, regardless of its inherent statistics, due to the indistinguishable and uncorrelated arrival of photons (*indistinguishability bunching*). This manifests as a diagonal on all 2PS.

- An antibunching arises for a two-level system with a characteristic butterfly-shape that is reproduced by any two-level transition that can be resolved in isolation from a more complex level structure (see Ref. [168] for an example within a four-level system).

- The 2PS of various types of coupled systems differ greatly from each other even when their 1PS are identical, and within the same system, some symmetries of the 1PS are lifted in 2PS. This shows the much higher degree of characterization accessible via two-photon spectroscopy.

- The 2PS of coupled harmonic oscillators features an anticrossing (two hyperbolas) of uncorrelated emission corresponding to the independent and classical polaritons dynamics. Coupled two-level systems or the Jaynes–Cummings model on the other hand give rise to rich patterns of correlations permitting to investigate the underlying physical picture in terms of relaxation between quantum states.

- Such correlations are due to fundamental processes that can be identified through simple equations that locate them in the 2PS. They are *i*) *leapfrog processes*, i.e., two-photon emission jumping over an intermediate rung of the level structure through a virtual state of indeterminate frequency and *ii*) *polariton-to-virtual-state* anticorrelations, where the emission does not correspond to dressed states transitions but take into account the dynamical nature of the system, with the final state provided by a virtual state or fluctuation of the system.

- Leapfrog processes are particularly noteworthy for applications in quantum information processing. They are present in any nonlinear quantum system, as simple as an anharmonic oscillator. N-photon leapfrogs with $N > 2$ also take place, though the higher the N, the weaker the process. In the Jaynes–Cummings system, they are evidenced by higher order correlations, $g_\Gamma^{(N)}(\omega_1, \ldots, \omega_N)$, at the frequencies

$$\sum_{i=1}^{N} \omega_i = N\omega_a \pm (E_n - E_{n-N}) \quad \text{or} \tag{4.28}$$

$$= N\omega_a \pm (E_n + E_{n-N})\,, \tag{4.29}$$

  but their further characterization is out of scope of this text.

- The intricate pattern of N-photon correlations that is formed by the combination of all the above processes in the Jaynes–Cummings model, that is neatly resolved in a system well into the strong-coupling regime, evolves when brought in the lasing regime into the qualitatively different 2PS of the Mollow triplet, that features new types of patterns such as circles rather than simply straight lines. For high rungs of excitation, $n \gg 1$, the lines in Eq. (4.28) converge to the central antidiagonal, $\sum_i \omega_i \approx 0$, while the lines in Eq. (4.29) agglomerate at the outer positions, $\sum_i \omega_i \approx \pm 2\sqrt{n}g$. This formation of the Mollow triplet in the 1PS gives rise to *leapfrog triplet* in the 2PS, with the same origin as in the linear regime in terms of two-photon transitions between dressed states.

Beyond spelling out the dynamics of emission at the quantum level, the theory of two-photon spectroscopy also allows to address fundamental theoretical issues of the quantum formalism and illustrates the deep link between the quantum dynamics and the detection process. For instance, in the limit of an ideal detector, the semiclassical description of the Mollow triplet fails to recover the fundamental indistinguishability bunching. This is due to the artificial δ line of the scattering peak produced by the semiclassical approximation.

This shortcoming can be solved by turning to a fully quantized theory or upgrading the semiclassical theory to get rid of the artifacts caused by a fixed phase.

Another conclusion from our study is that the dynamics of "real processes", involving photon by photon de-excitations, are related to the system parameters and less influenced by detection. The corresponding correlations are best resolved when the related peaks are separated and fully filtered. On the other hand, "virtual processes", involving virtual states such as the leapfrogs and polariton-to-virtual state interferences, happen within the time of interaction with the detector, $1/\Gamma$, and conserving energy within its linewidth, Γ. Therefore, their correlations become more prominent using narrow filters.

We have thus amply demonstrated that two-photon spectroscopy unravels a rich two-photon dynamics and interference effects in open quantum systems by a precise disposition of filters of given resolutions. Such correlations can be further taken advantage of by considering finite time delays and/or optimising the frequency windows. Further interesting systems to apply two-photon spectroscopy are ultra strong coupling systems [169], closely spaced atoms in optical lattice [170], the biexciton two-photon emission in a quantum dot [150, 168] or the dynamics of Bose-Einstein condensation [171].

Chapter 5

Photon pair emission in cavity QED systems

5.1 Introduction

Photon pairs can be used as fundamental building blocks for an extended range of Quantum Information Processing protocols, with applications in quantum metrology [172], quantum communication and cryptography [173–175], linear-optics quantum computation [176–180], and even for fundamental tests of quantum mechanics like hidden variables interpretations [181, 182]. A number of devices have been proposed and experimentally demonstrated with atomic gases [183–185] or nonlinear crystals [172, 186, 187]. The realization of such devices, however, is a highly nontrivial task since, in order to be useful, the generated photons need to be almost identical, narrow-band and generated with a high repetition rate. Useful quantum states made from two photons include pairs of identical photons, that are however not necessarily superimposed in space and/or in time, and the two-photon (2P) Fock states $|2\rangle$ where the two photons share the same attributes in their energy, space and time profile, encoding the information in their polarization. Standard protocols for quantum computation may rely on not-superimposed photons pairs [173] but 2P states can be used for more efficient quantum computation [178].

In this Chapter, we show how a semiconductor cavity QED system appears to be a suitable platform where two-photons states can be created at will with the promising advantages of semiconductor systems for optical access, on-chip integration, output-collection and scalable technological implementations [131, 188–190]. As explained in Chapters 1 and 2, a semiconductor quantum dot (QD) has a discrete spectrum that supports a series of optical transitions that can be coupled to one or more cavity modes. Apart from a few localized state in the neutral QD, this nanostructure can accomodate several carriers in several states, which combined with Coulomb interaction, makes the electronic configurations to form a very rich N-exciton optical spectrum [130, 191, 192]. However, in most of the cases a "minimal" description can be made: in Chapter 3, a two-level system approximation was used, which is suitable for systems where only one excitonic transition is relevant for the physics described. However, here we use an upgraded configuration where the QD is composed by four levels as the ones shown in panel (b) of 5.1: ground state, exciton and a biexciton state. Our proposal [149, 150] relies

on the fact that the biexciton (the occupation of the quantum dot by two excitons of opposite spins) energy allows to tune the cavity in resonance with twice the cavity photon energy (see panel (b) Fig. 5.1). As the biexciton binding energy can be large, single-photon processes are detuned and therefore effectively suppressed, while simultaneous two-photon emission is Purcell enhanced [149]. This effect has been recently demonstrated experimentally [151]. In the experiment, following our proposal, the signature for the two-photon emission is a strong emission enhancement of the cavity mode when hitting the biexciton two-photon resonance. Because of incoherent excitation used in both the theoretical proposal and its experimental realization, the quantum character of the two-photon emission is not directly demonstrated nor quantified [1].

This Chapter is divided as follows: first, in Section 5.2 we describe the system, introducing the Hamiltonian and Lindblad terms needed to account for the dissipative and pumping mechanisms. Next, in Section 5.3 we introduce the configuration, that is nowadays experimentally accessible, to achieve a two-photon state by starting with a quantum dot which is initially prepared in a pure biexciton state, and analyze in detail the underlying microscopic mechanisms, demonstrating the perfect two-photon character of the emission beyond a mere enhancement at the expected energy. we show how the two-photon state is created by the system in a chain of virtual processes that cannot be broken apart in physical one-photon states. The understanding we develop is analytical and allows for optimisation of a practical setup, enabling the realization of a practical source of two simultaneous and indistinguishable photons in a monolithic semiconductor device. Then, in Section **??** we study thoroughly the effect of continuous excitation with coherent and incoherent character respectively in the limit of low pumping, which we see is the optimal configuration to achieve the desired two-photon state. In both cases, we develop an analytical approach at the two-photon resonance that yields to analytical formulas for the optimal pumping in both configurations. Finally, in Section 5.5 we make a summary of the main points and give an outlook on the possibilities of the system.

5.2 Description of the system

So far we have described exciton in QD systems in a simplified two-level system picture. However, if one takes into account the spin-degree of freedom of the exciton, one realizes it is possible for the QD to accommodate two different excitons, with spin-up and spin down and even both of them at the same time forming the so-called biexciton state. Taking into account these degrees of freedom the complete QD picture should be described with the following hamiltonian:

$$H_{\mathrm{QD}} = \sum_{i=\uparrow,\downarrow} \omega_{\mathrm{X}} \sigma_i^\dagger \sigma_i - \chi \sigma_\uparrow^\dagger \sigma_\uparrow \sigma_\downarrow^\dagger \sigma_\downarrow \,, \tag{5.1}$$

where we have included $i = \uparrow, \downarrow$ the spin-up and spin-down degrees of freedom for the excitonic states σ_i (fermions) with common frequency ω_{X}. The biexciton binding energy χ allows to

[1] The Authors of Ref. [151] also realize this limitation and speculate on the scheme that we analyze here in details.

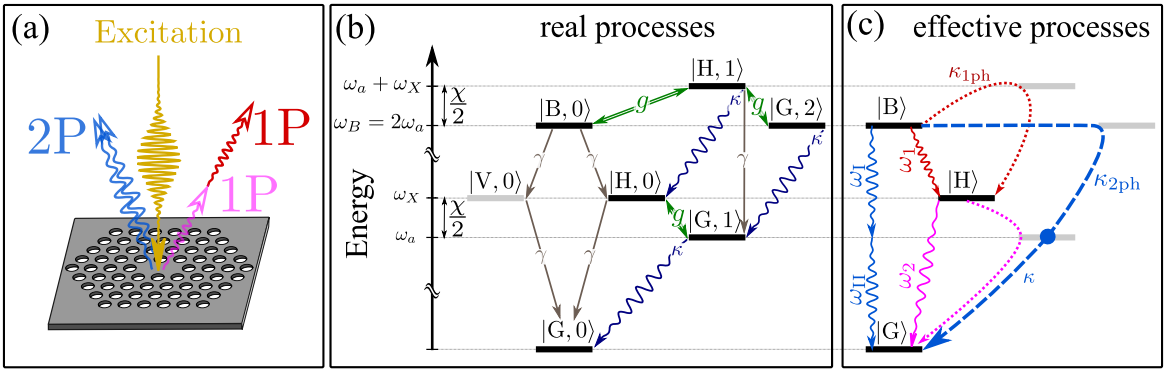

Figure 5.1: Panel(a): Possible experimental configuration for two-photon emission. Panel (b) & (c): Level scheme of a quantum dot coupled to a cavity mode with linear polarization H at the 2PR. In (b), the microscopic configuration and in (b) the effective processes taking place in the de-excitation of the biexciton. Those involving the cavity are, on the one hand, through the emission of two real and distinguishable photons ω_1 and ω_2 (in dotted red and pink), and, on the other hand, through the simultaneous emission of one two-photon state at ω_a (in dashed blue), labeled $\omega_{\mathrm{I,II}}$.

bring the biexciton energy ω_{B} in resonance with the two-photon energy while detuning all other excitonic emissions from the cavity mode. It is red (blue) shifted if the biexciton is "bound" ("antibound"), giving rise to a positive $\chi > 0$ (negative $\chi < 0$) binding energy $\chi = 2\omega_{\mathrm{X}} - \omega_{\mathrm{B}}$. Our scheme works with both the bound and antibound biexciton. Without loss of generality, we assume $\chi > 0$, with the added advantage of being less affected by pure dephasing and coupling to phonons [193], that will be neglected in this Chapter. This binding energy is typically large ($\chi \gtrapprox 400\mu eV$) as compared to the possible splittings between excitonic states ($\approx 10\mu eV$) [151], which is ideal for our purpose.

The complete system consists of a QD embedded in a microcavity. The description of the cavity can also be upgraded by considering the two-possible polarizations. However, for the purposes of the proposal it is convenient that the QD is coupled only to one of its modes, polarised along a direction that we call horizontal (H). In principle, the full Hamiltonian of the system without making any explicit assumption, is given by [149]:

$$H = H_{\mathrm{QD}} + \omega_a a^\dagger a + \sum_{i=\uparrow,\downarrow} \left[g_i (a^\dagger \sigma_i + a \sigma_i^\dagger) \right]. \tag{5.2}$$

The cavity mode should have a strong polarization, say linearly polarized in the horizontal direction for a photonic crystal, a case we shall assume in the following. The first requirement of the proposal is the following: we assume an equal coupling of both excitons to the linearly polarized mode of the cavity, $g_\uparrow = g_\downarrow = g/\sqrt{2}$, and take g as the unit in the remaining of the Chapter.

The Hilbert space of the quantum dot is spanned, in its natural basis of circular polarisation, by the ground $|\mathrm{G}\rangle$, spin-up $|\uparrow\rangle$, spin-down $|\downarrow\rangle$ and biexciton $|\mathrm{B}\rangle$ states. In the linearly polarised basis, the excitonic states are $|\mathrm{H}\rangle = (|\uparrow\rangle + |\downarrow\rangle)/\sqrt{2}$ and $|\mathrm{V}\rangle = (|\uparrow\rangle - |\downarrow\rangle)/\sqrt{2}$. The dot-cavity joint Hilbert space includes the photonic number n: $|j, n\rangle$, where $j = \mathrm{G}$, V, H and B, with $n \in \mathbb{N}$. With the previous considerations, the Hamiltonian in the basis of linearly

polarized states reads:

$$H = \omega_a a^\dagger a + \omega_{\rm X}(|{\rm H}\rangle\langle{\rm H}| + |{\rm V}\rangle\langle{\rm V}|) + (2\omega_{\rm X} - \chi)|{\rm B}\rangle\langle{\rm B}| + g\Big[a^\dagger(|{\rm G}\rangle\langle{\rm H}| + |{\rm H}\rangle\langle{\rm B}|) + {\rm h.c.}\Big], \tag{5.3}$$

The dynamics is completed then by including the dissipative terms which affects the bare states, i.e., in the spin-up/spin-down basis, yielding a master equation:

$$\partial_t\rho = i[\rho, H] + \frac{\kappa}{2}\mathcal{L}_a(\rho) + \frac{\gamma}{2}\sum_{i=\uparrow,\downarrow}\Big[\mathcal{L}_{|{\rm G}\rangle\langle i|} + \mathcal{L}_{|i\rangle\langle{\rm B}|}\Big](\rho)\,, \tag{5.4}$$

where $\mathcal{L}_c(\rho)$ is following the notation introduced in Chapter 2, with κ the cavity losses and γ the exciton relaxation rates. Another assumption is that $\gamma \ll \kappa$, which is the typical experimental situation. Panel (b) of Fig. 5.1 shows the self-consistently truncated configuration of levels involved in the biexciton de-excitation. The coherent coupling (g) is represented by bidirectional (green) arrows, spontaneous decay (γ) by straight (gray) arrows and cavity decay (κ) by curly (blue) arrows, each of them linking in a reversible (g) or irreversible (γ, κ) way the different levels.

A *one-photon resonance* (1PR) is realized when the cavity is set at resonance with one of the excitonic transitions: $|{\rm B},0\rangle \to |{\rm H},0\rangle$ with frequency $\omega_1 \approx \omega_{\rm B} - \omega_{\rm X}$ or $|{\rm H},0\rangle \to |{\rm G},0\rangle$ with frequency $\omega_2 \approx \omega_{\rm X}$. The resonant single-photon emission is then enhanced into the cavity mode according to the conventional scenario [194], with a Purcell decay rate:

$$\gamma_{\rm P} = 4g^2/\kappa\,. \tag{5.5}$$

A *two-photon resonance* (2PR) is realized when the transition $|{\rm B},0\rangle \to |{\rm G},0\rangle$ matches energetically the emission of two cavity photons [149]:

$$\omega_a \approx \omega_{\rm X} - \chi/2 \quad \text{with} \quad \chi \gg g\,, \kappa\,, \gamma\,. \tag{5.6}$$

This process also benefits from Purcell enhancement. In fact, if the decay rates κ and γ are small enough, two-photon Rabi oscillations between states $|{\rm B},0\rangle$ and $|{\rm G},2\rangle$ are even realized, with a characteristic frequency $g_{\rm 2P} \approx 4g^2/(\sqrt{2}\chi)$ [149]. Note that in Eq. (5.6), we have neglected the small Stark shifts $\sim g_{\rm 2P}$, which should be taken into account to achieve maximum Rabi amplitude. Here, to remain within experimentally achievable configurations, we consider systems which figures of merit are such that the system is in strong coupling at the 1PR, $4g \gtrapprox \kappa$. However the coupling needs not be so large that the system is in strong-coupling also at the 2PR. In other words, the system remains within the 2P weakly coupled regime, $4g_{\rm 2P} \ll \kappa$, where two-photon oscillations do not actually take place. In these conditions, at the 2PR, the one-photon Rabi oscillations (e.g., $|{\rm B},0\rangle \leftrightarrow |{\rm H},1\rangle$) still take place at the frequency g but, as they are largely detuned, the coupling strength effectively reduces to $g_{\rm 1P} \approx g/\sqrt{1 + [\chi/(\gamma+\kappa)]^2} \approx g\kappa/\chi$ [110].

Now, in order to study the 2P emission character of the described system we propose three different experimental configurations regarding the pumping conditions. In Section 5.3 we consider that the system is initially prepared in the biexciton state by a pulsed orthogonal laser and study its desexcitation properties. In Section 5.4, we introduce continuous excitation of coherent and incoherent nature and study its impact on 2P emission efficiency.

5.3 Spontaneous emission configuration

5.3.1 Initialization in the biexciton state

In this Section, we assume that the QD is in the biexciton state in an empty cavity, $|\mathrm{B}, 0\rangle$, as the initial state and then leave the system free to relax. This is what is known as *spontaneous emission configuration*. Remarkably, it can be easily proven that a small spurious population of excitonic states does not directly affects the results either, but merely decreases the efficiency of the proposal. The fine structure splitting between $|H\rangle$ and $|V\rangle$ is not important as the latter is not directly coupled to the cavity, thus not entering in the desexcitation process. This recourse to one polarization is an additional advantage of our scheme as compared to others that rely on the biexciton decay through both of the excitonic paths, such as the generation of entangled photon pairs [195, 196].

There are several ways to initialize the system in the biexciton state. We can assume that the QD is excited by a laser of amplitude $\Omega_i(t)$ and frequency ω_{L}, described in the coherent part of the master equation 5.4 by an extra Hamiltonian:

$$H_{\mathrm{las}}(t) = \sum_{i=\uparrow,\downarrow} \Omega_i(t)(\sigma_i + \sigma_i^\dagger)\,, \tag{5.7}$$

The laser, which should be set to match the two-photon resonance,$\omega_{\mathrm{L}} = \omega_{\mathrm{B}}/2 = \omega_{\mathrm{X}} - \chi/2$, brings it in the biexciton state through two-photon absorption. This can be realized via two appropriate colored pulses [197, 198] or, more efficiently by a single pulse spectrally matching the direct 2P absorption [199]. The laser polarization should be taken orthogonal to that of the cavity, $\Omega_\uparrow(t) = -\Omega_\downarrow(t) = \Omega(t)/\sqrt{2}$, so that the latter is not affected by the excitation process. Such an inversion of the system has been demonstrated both theoretically and experimentally [199]. In the case of a single excitonic transition under pulsed excitation, it is well known that the population inversion follows single-photon Rabi oscillations as a function of the pulse total intensity $\theta = \int \Omega(t)dt$ only, according to the pulse area theorem, as $\sin^2(\theta/2)$. In the case of 2P resonant excitation of the biexciton, the oscillations depend also on the pulse shape, duration τ_p and binding energy χ. Only when the pulse becomes very strong, $\theta \gg \chi\tau_p$, one finds simple relation $\sin^2(\theta/(2\sqrt{2}))$ independent of the pulse characteristics. This pulse should be intense enough to fully invert the population into the biexciton state, short (at most of a few picoseconds) in order to minimize the effect of pure dephasing, and spectrally much narrower than the binding energy in order to minimize the transfer of population to the intermediate excitonic states. Another promising possibility is the *rapid adiabatic passage* from the ground to the biexciton state via frequency-sweeping pulse as proposed in [200]. This has been recently experimentally demonstrated for single exciton [201, 202] and has the advantage of being largely unaffected by variation in the dipole coupling or in the optical field, typical of quantum dots. To summarize, coherent control of excitonic states has made significant progresses in the last years [203] and successful manipulation of the biexciton has been reported in several works [195, 196, 204–206].

Nonetheless, for the purposes of this Section we do not worry about the particular mechanism chosen, but just assume the biexciton state as the initial state of the dynamics. For the rest of the Chapter, we use the following state-of-art parameters for the calculations: $\chi = 20g$, $\kappa = g$, $\gamma = 5 \times 10^{-4} g$, unless stated otherwise.

5.3.2 Demonstration of the two-photon emission at the two-photon resonance

To characterize and analyze the main output of the system, shown in Fig. 5.2, we study the time-resolved power spectrum $S(t,\omega) \propto \Re \int_0^t dT \int_0^{t-T} d\tau e^{i\omega\tau} \langle a^\dagger(T) a(T+\tau)\rangle$ [83] introduced in Chapter 2 and which calculation can be done in two ways. One can make use of our recently developed method explained in Chapter 4, and calculate the time-dependent spectra by coupling one "sensor" two the system and calculating its time-dependent population as a function of its transition frequency. Alternatively, due to the small size of the Hilbert space in this case the explicit computation can be done by making use of the Quantum Regression Theorem and doing the formal integration obtaining the following expression:

$$S(t,\omega) = \frac{1}{\pi} \sum_{\alpha\in\{1,2,\mathrm{I},\mathrm{II},\dots\}} \left(\tilde{L}_\alpha(t,\omega) \frac{\frac{\gamma_\alpha}{2}}{(\frac{\gamma_\alpha}{2})^2 + (\omega-\omega_\alpha)^2} - \tilde{K}_\alpha(t,\omega) \frac{\omega-\omega_\alpha}{(\frac{\gamma_\alpha}{2})^2 + (\omega-\omega_\alpha)^2} \right) , \quad (5.8)$$

where we emphasised in the sum four dominant processes labeled 1, 2, I and II (results below include all processes). In this Chapter we prefer the latter method to calculate $S(t,\omega)$ as one obtains separate information from the different decay channels. Each α corresponds to a transition in the system, characterised by its frequency (ω_α) and broadening (γ_α), which allow us to identify its microscopic origin, as discussed below. The quantities $\tilde{L}_\alpha$ and $\tilde{K}_\alpha$ are real-valued functions of time and frequency, that correspond, respectively, to the time-integrated signal and its interference with other transitions, up to time t. They tend at infinite time to frequency-independent quantities that we label without tilde, L_α and K_α, corresponding to their full time-integrated values. Therefore, L_α quantifies the total intensity emitted through a given transition α. The characteristic spectral profile of the cavity-assisted two-photon emission is shown in Fig. 5.2, with a central peak that is strongly enhanced at the two-photon resonance, corroborating its two-photon character, and surrounded by standard (single-photon) de-excitation [149, 151]. The 2P peak is spectrally narrow and isolated from the other events, that can never be completely avoided, so the source is appealing on practical grounds. As such, this is one of the principal quantities of interest in this text, that is experimentally measured by conventional photoluminescence measurements. The time dependent spectra of emission, on the other hand, can be obtained with a streak camera [94].

The system decays via the cavity mode (through the annihilation of a photon a) or via spontaneous emission into the leaky modes (related to the four excitonic lowering operators). With the biexciton state in an empty cavity, $|\mathrm{B},0\rangle$, as the initial condition, we identify three main de-excitation mechanisms of the system. We now describe them in turns.

i) The first decay route is a cascade of two spontaneous emissions, from $|B\rangle$ to $|H\rangle$ (or $|V\rangle$) in a first time, and then from $|H\rangle$ (or $|V\rangle$) to $|G\rangle$ in a second time, as shown in straight (gray) lines in Fig. **??** (b). This decay into leaky modes is at the excitonic energies, ω_1, ω_2, and is a direct process with a straightforward microscopic origin as a real transition between two states. Each process happens at the rate γ, so that, as far as the biexciton is concerned, its total rate of de-excitation through this channel is 2γ. The effect of this channel is to reduce the efficiency of de-excitation through the cavity mode, which is the one of interest. This can be kept small by choosing a system with a small γ.

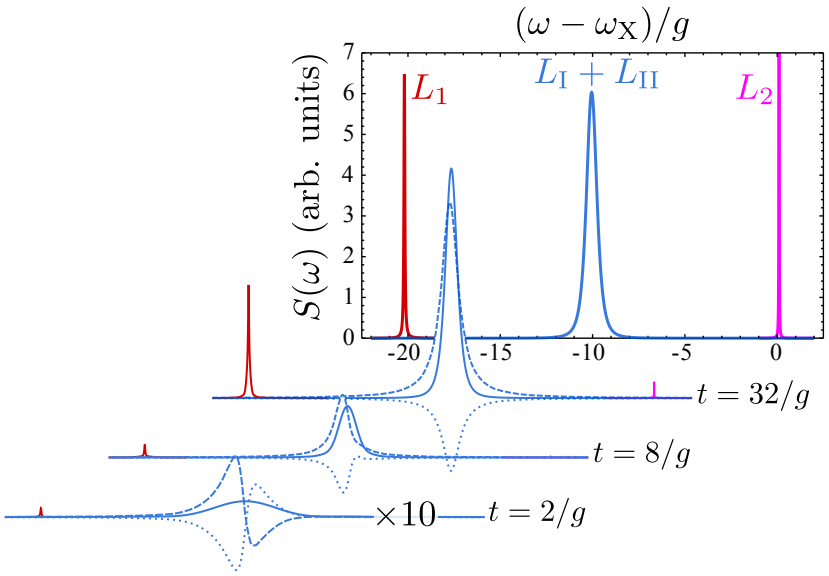

Figure 5.2: Cavity spectra of emission $S(t, \omega)$ at the two-photon resonance for different times (unframed) and integrated over all times (framed). They feature the 2P peak at $\omega_a \approx -\chi/2$ (central, blue) and the two 1P peaks at $\omega_1 \approx -\chi$ (left, red) and $\omega_2 \approx 0$ (right, pink). The 2P peak cannot be decomposed into two physical processes. Parameters: $\chi = 20g$, $\kappa = g$, $\gamma = 5 \times 10^{-4} g$.

ii) The second decay route is another cascade of one-photon emissions, but now through the cavity mode, namely from $|B\rangle$ to $|G\rangle$ passing by $|H\rangle$. It is shown in dotted lines in Fig. 5.1(b). It effectively amounts to two consecutive photons into the cavity mode at the excitonic energies ω_1 and ω_2, also shown (with the same color code) in Fig. 5.1 (b), but the microscopic origin is now more complex, as it involves virtual intermediate states. The first photon, 1, is emitted through the process $|\mathrm{B}, 0\rangle \xrightarrow{|\mathrm{H},1\rangle} |\mathrm{H}, 0\rangle$, via the off-resonant ("virtual") state $|\mathrm{H}, 1\rangle$ and the second, 2, similarly through the process $|\mathrm{H}, 0\rangle \xrightarrow{|\mathrm{G},1\rangle} |\mathrm{G}, 0\rangle$. Due to the dispersive coupling, the initial state in each of these processes (which has no photon) acquires a small component, $C_{1\mathrm{P}} = 2g/\chi$, from the corresponding virtual state (which has one photon). It is through this component that it can effectively emit a cavity photon, at rate κ. The effective total decay rate can be understood as the probability to transit to the virtual state, times the photon decay rate: $\kappa_{1\mathrm{P}} = C_{1\mathrm{P}}^2 \kappa$. This derivation leads to the same result as directly computing the Purcell decay rate in the dispersive regime, $\kappa_{1\mathrm{P}} = 4g_{1\mathrm{P}}^2/\kappa$. we estimate the positions and broadenings of the two resulting spectral peaks ($\alpha = 1$, 2 in Eq. (5.8)), by applying the quantum regression theorem within an effective Hilbert space [120] excluding V-polarised and two-photon states (none of them being an initial or a final state of the aforementioned processes). The minimal regression matrix to reproduce the main spectral features, including the two transitions under discussion, is 4×4. With this prescription, $\omega_1 \approx -\chi - 2g^2/\chi$, $\omega_2 \approx 2g^2/\chi$ and $\gamma_1 \approx 3\gamma$, $\gamma_2 \approx \gamma$. The broadenings of the transitions correspond, as expected on physical grounds, to the sum of the decay rates that affect the initial and the final states, without any influence from the virtual ones.

iii) Finally, the central event in our proposal is formed by the third channel of de-excitation of the biexciton, namely, the emission into the cavity mode of two simultaneous and indistinguishable photons with a frequency very close to that of the cavity $\omega_{\rm I} \approx \omega_{\rm II} \approx \omega_a$. This process is sketched by the single dashed (blue) line in Fig. 5.1(b), with an intermediate step marked by a point at $|{\rm G},1\rangle$. Effectively, this amounts to the generation of a two-photon state, represented by the two curly transitions $\omega_{\rm I,II}$ in Fig. 5.1(b). The two indices I and II strictly correspond to transitions that arise in the spectral decomposition (5.8), namely, $|{\rm B},0\rangle \xrightarrow{|{\rm G},2\rangle} |{\rm G},1\rangle$ for the first sequence of events, I, and the closing of the path, $|{\rm G},1\rangle \to |{\rm G},0\rangle$, for the second transition, II. Although I and II are used in Fig. 5.1 to label the two photons for the sake of illustration, these two photons are indistinguishable and cannot be interpreted as real events taken in isolation in association with the above sequences of transitions. Indeed, each event gives rise to an unphysical spectrum (involving negative values) and only when both processes are taken together, they interfere to sum to a physical spectrum which can be interpreted as a probability of (two-photon) detection. This decomposition of the two-photon (central) peak is shown in Fig. 5.2 in the time-dependent spectra, with the process I shown in a dotted line and II in dashed line. They sum to the physical (observable) peak, in solid line. Both peaks grow together in time and develop an asymmetry, one being completely positive, I, the other completely negative, II. None, not even the fully positive peak, can be observed in isolation. In contrast, the single-photon peaks on both sides (red and pink), are formed by single, isolated transitions, showing their real (as opposed to virtual) nature. The Purcell rate of the two-photon emission is again related to the small component of $|{\rm G},2\rangle$ that the initial state $|{\rm B},0\rangle$ grows due to the weak two-photon coupling, $C_{\rm 2P} = 2\sqrt{2}g^2/(\chi\kappa)$. Given that the rate of photon emission of state $|{\rm G},2\rangle$ is 2κ, in this case we have $\kappa_{\rm 2P} = C_{\rm 2P}^2 2\kappa$, equivalent to $\kappa_{\rm 2P} = 4g_{\rm 2P}^2/(2\kappa)$. Following our analytical approach, one finds $\omega_{\rm I} \approx -\chi/2 + 2g^2/\chi$ with broadening $\gamma_{\rm I} \approx \kappa + 2\gamma$ (this is the sum of the decay that initial and final states, $|{\rm B},0\rangle$ and $|{\rm G},1\rangle$, suffer). The second transition (II) stems from the direct process $|{\rm G},1\rangle \to |{\rm G},0\rangle$. This transition appears at $\omega_{\rm II} \approx -\chi/2 - 2g^2/\chi$ with broadening $\gamma_{\rm II} \approx \kappa$.

A compelling proof of the two-photon character of the central peak is given by the time-dependent spectrum, Fig. 5.2. Whereas the single-photon events grow in succession—first the L_1 peak, that populates the state $|{\rm H}\rangle$, which subsequently decays to $|{\rm G}\rangle$, forming the L_2 peak—the two photon peak arises from the joint and simultaneous contribution of the I and II processes. In fact, one can show that at the 2PR, $L_{\rm I} + L_{\rm II} \approx 2\int_0^\infty dt \langle a^{\dagger 2} a^2\rangle(t)$, linking directly the intensity of the peak with the two-photon emission probability.

This can be brought to the experimental test by resolving the photon statistics in time, $g^{(2)}(t,\tau) = \langle a^\dagger(t)a^\dagger(t+\tau)a(t+\tau)a(t)\rangle/[n_a(t)n_a(t+\tau)]$. the Mandel Q-parameter is used to illustrate this, $Q(t,\tau) = n_a(t)(g^{(2)}(t,\tau) - 1)$, since it changes sign with the nature of the correlations (negative for anticorrelations). This is shown in Fig. 5.3, with a strong and sharp bunching of the emission when the cavity hits the two-photon resonance (meaning that photons come together, and in our case, in pairs), while it is antibunched in other cases (photons coming separately). What is remarkable of the two photon emission is that it is consistently bunched at all times: while the system can emit at any time, when it does, it emits the two photons together. In contrast, the 1PR emission is mostly antibunched, as expected, but it also has the possibility to be bunched by fortuitous joint emission of two photons. This is the case when $\omega_a = \omega_2$, the cavity is then in resonance with the lower transition, that can start only as a successor of the upper transition resulting in high probability for

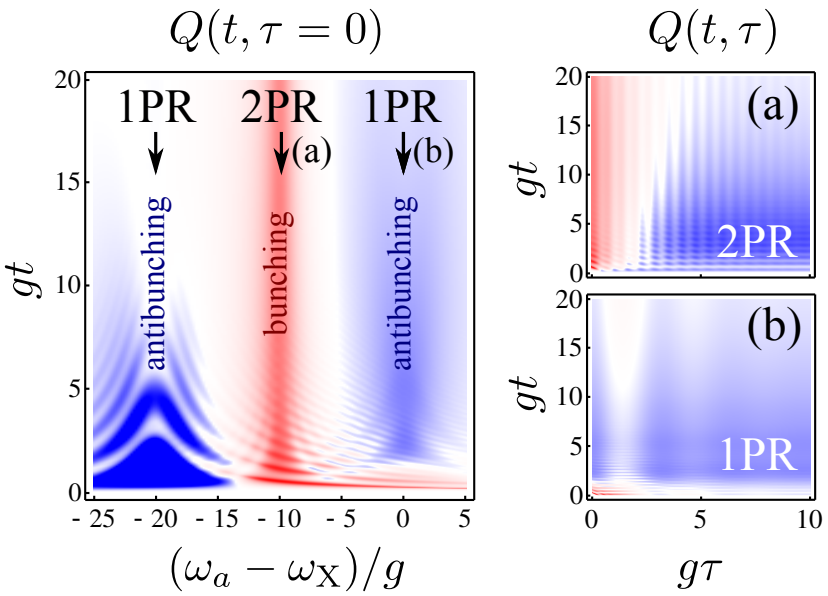

Figure 5.3: Mandel parameter $Q(t,\tau=0)$ as a function of the cavity frequency ω_a, for a set of typical parameters ($\chi=20g$, $\kappa=g$ and $\gamma=5\times10^{-2}g$). $Q(t,\tau)$ is shown on the right panels at the two relevant resonances: (a) two-photon and (b) one-photon. There is a change in the statistics from antibunching <0 (1PR), colored in blue, to bunching >0 (2PR), colored in red.

two photons detection, but only at very early times, since one photon is a precursor of the other one in a cascade of two otherwise distinguishable events. The proof is complete with the autocorrelation time τ, shown in panels (a) and (b), further demonstrating that in the 2PR emission, the two photons arrive at zero time delay (the emission being less likely again at nonzero delay). Cross-correlations measurements between the three filtered peaks would also show strong features, namely anticorrelations at all delays between all the peaks, with the exception of the positive cross-correlation between 1 and 2 (in this order and with some delay) and positive autocorrelation of the central peak (at zero delay).

5.3.3 Efficiency of the two-photon emission

Now that we have demonstrated from various points of view the two-photon character of the central peak, we aim to maximise it as compared to all other de-excitation channels.

Although we present and plot numerical results of the full master equation (5.4) throughout the manuscript, we also provide analytical expressions for the magnitudes of interest. In order to compute intensities of emission, L_α, we need to obtain the full density matrix. As in the case of solving the QRT, we can exclude in the derivation the V polarised states. Note, however, that $|\mathrm{G},2\rangle$ plays a central role in the one-time dynamics and must be included in the estimation of the density matrix elements. There are three key parameters to enhance the 2P emission: κ, γ and χ. The case $\gamma=0$ is the ideal configuration, where all the emission goes through the cavity:

$$I_a=\int_0^\infty \langle a^\dagger a\rangle(t)\,dt=2/\kappa\,, \tag{5.9}$$

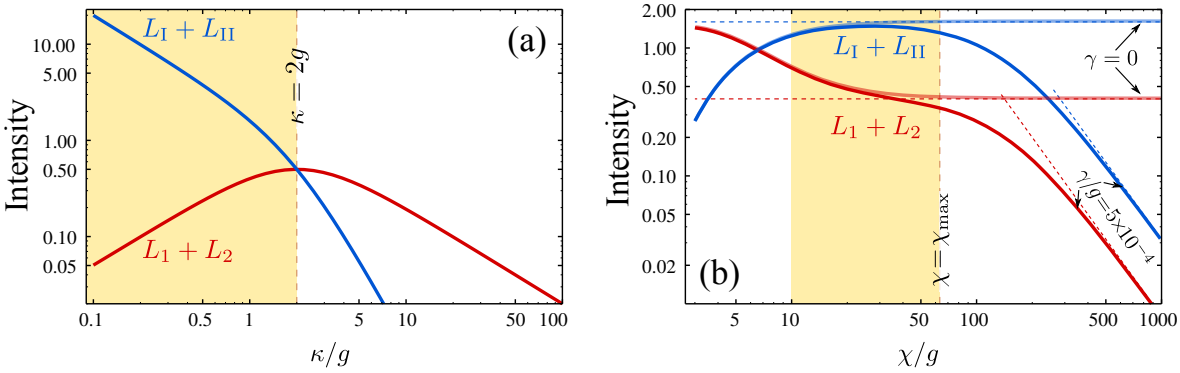

Figure 5.4: (a) Intensity $L_{\rm I}+L_{\rm II}$ of emission in the 2P channel (blue) and L_1+L_2 in the two 1P channels (red) as a function of κ, for $\chi\to\infty$ in the most efficient case $\gamma=0$. The shaded (yellow) area $\kappa<2g$ shows the region where the 2P emission dominates. (b) Same as before for $\kappa=g$ as a function of χ, that must be large enough so that 1P are suppressed and small enough to maintain a high cavity emission efficiency in the realistic case of nonzero γ.

which, in the limit $\chi\to\infty$, is redistributed between the two possible decay paths as:

$$L_1+L_2\approx\tfrac{\kappa_{\rm 1P}}{\kappa_{\rm 1P}+\kappa_{\rm 2P}}I_a\approx\tfrac{2}{\gamma_{\rm P}+\kappa}\,, \tag{5.10}$$

$$L_{\rm I}+L_{\rm II}\approx\tfrac{\kappa_{\rm 2P}}{\kappa_{\rm 1P}+\kappa_{\rm 2P}}I_a\approx\tfrac{2\gamma_{\rm P}/\kappa}{\gamma_{\rm P}+\kappa}\,. \tag{5.11}$$

This is shown in Fig. 5.4(a), where we see that the 2P emission dominates over the 1P when $\kappa<2g$ (shaded in yellow in Fig. 5.4(a)), since in this case $\kappa_{\rm 2P}>\kappa_{\rm 1P}$. For cavities with high enough quality factor (small κ), the 2P emission is over four orders of magnitude higher than the 1P, showing that the device is extremely efficient for good technological systems [98].

When γ is nonzero, the situation of experimental interest, but still is the smallest parameter ($\gamma\ll\kappa,g\ll\chi$), the channel of decay that it opens, leads to:

$$I_a=\int_0^\infty n_a(t)\,dt=\frac{\gamma_{\rm P}(\gamma_{\rm P}+\kappa)}{\gamma\chi^2}\,, \tag{5.12}$$

which is now redistributed between the two cavity decay paths as an increasing function of χ^{-2}:

$$L_1+L_2\approx\tfrac{\kappa_{\rm 1P}}{\kappa_{\rm 1P}+\kappa_{\rm 2P}+2\gamma}I_a\approx\tfrac{\gamma_{\rm P}\kappa}{\gamma\chi^2}\,, \tag{5.13}$$

$$L_{\rm I}+L_{\rm II}\approx\tfrac{\kappa_{\rm 2P}}{\kappa_{\rm 1P}+\kappa_{\rm 2P}+2\gamma}I_a\approx\tfrac{\gamma_{\rm P}^2}{\gamma\chi^2}\,. \tag{5.14}$$

This nonzero γ case is shown in Fig. 5.4(b), where the most efficient situation can be recovered in a region of χ bounded by above by:

$$\chi_{\rm max}=\min(2g\sqrt{\kappa/(2\gamma)}\,,4g^2/\sqrt{2\kappa\gamma})\,, \tag{5.15}$$

that follows from $2\gamma=\min(\kappa_{\rm 1P},\kappa_{\rm 2P})$. Above $\chi_{\rm max}$, the 2P emission still dominates over 1P emission but efficiency is spoiled, according to Eqs. (5.13), that are shown in dashed tilted lines.

5.4 Continous excitation configuration

5.4.1 Theoretical desciption.

In the previous configuration, the dynamics was always time-dependent: the final state was always $|G\rangle$ and system needed to be initialized each time in the biexciton state, $|B\rangle$ to get the 2P state out from the cavity.

Now, we study a different configuration where some source of continuous excitation is plugged into the system, arriving to a stationary situation where the 2P state is being continuously emitted.

As introduced in Chapter 2, semiconductor QDs are usually excited via a continuous excitation of the wetting layer which results in an incoherent population of the dot levels, named as *Incoherent excitation*. This kind of excitation can have a substantial and undesired impact on the quantum properties, namely, an increase of decoherence and dephasing in the dynamics as we described in Chapter 3. It enters in the incoherent part of the master equation with the following Lindblad term:

$$\frac{P}{2}\sum_{i=\mathrm{V,H}}\left[\mathcal{L}_{|\mathrm{i}\rangle\langle\mathrm{G}|}+\mathcal{L}_{|\mathrm{B}\rangle\langle\mathrm{i}|}\right](\rho)\,. \tag{5.16a}$$

Coherent excitation, close to resonance to the quantum dot levels, provides a second possibility to probe the system. To this intent, one can for instance apply a laser whose polarization is orthogonal to that of the cavity mode, in order not to excite cavity photons (directly or indirectly though the state with the cavity polarization). Coherent excitation may seem like a better choice because it does not introduce extra decoherence in the dynamics. Moreover, if the laser is also tuned to the two-photon resonance, it excites the biexciton directly with high probability [199]. However, one must remain in the linear regime as well in order not to dress the system [207], adding excitation-induced features. It is theoretically described by an extra hamiltonian, already defined in 5.7 that enters in the coherent part of the master equation.

In this Section, the two-photon emission under a low continuous excitation of both types is considered, as it appears to be the optimal regime. An analytical approach at the two-photon resonance is derived, consisting in solving the effective dot dynamics and deriving the cavity properties from physical arguments. The comparison between the numerical and analytical results provides the limiting excitation before the two-photon emission is hindered by decoherence or dressed states. This analytical understanding provides optimal pumping strength and information on the differences between the two types of excitation and the limiting excitation before the two-photon emission is hindered by decoherence (incoherent excitation) or dressed (coherent excitation).

5.4.2 Numerical results

The steady state of a given density matrix ρ is obtained by setting $\partial_t\rho = 0$. As we are interested in the low excitation regime, this is done numerically with a sufficient truncation in the number of photons. The characteristic experimental values are similar to the ones considered in the previous Section. Taking the exciton relaxation rate, γ, as the smallest

parameter in the system and the biexciton binding energy, χ, as the largest, which is the typical experimental situation [151]. In order to increase efficiency of the two photon emission, the system is in the regime of strong coupling, that is, we assume parameters in the range [150] $\gamma \ll \kappa \lessapprox g \ll \chi$.

As in the previous Section, in a continuously pumped the main quantities of interest—characterising the cavity emission—are the steady state mean cavity photon number $n_a = \langle a^\dagger a \rangle$ and the Q Mandel factor at zero delay. The Q factor quantifies bunching ($Q > 0$) and antibunching ($Q < 0$) in the emission, taking into account the available signal n_a. In Fig. 5.5, Q and n_a is plotted under weak incoherent (a) and coherent (b) excitation.

As a first step, the cavity frequency is tuned through the system, probing the different resonances. Keeping in mind the level structure of Fig. 5.1 (b), we locate the two-photon resonance (2PR) by a clear bunching peak of the Q-factor at $\omega_a \approx \omega_{\rm B}/2 = \omega_{\rm X} - \chi/2$ (at $-10g$ in the figures). This corresponds to the simultaneous emission of two cavity photons from $|{\rm B}\rangle$ as shown in Refs. [149, 150]. On the other hand, at the two possible one-photon resonances (1PR), namely at $\omega_a = \omega_1 \approx \omega_{\rm X} - \chi$ and $\omega_a = \omega_2 \approx \omega_{\rm X}$ (at $-20g$ and 0 in the figures), the Q-factor drops or even becomes negative. These features, accompanied by an enhancement in the cavity emission n_a, especially at the 2PR, are in agreement with the properties found for an ideal device that can be prepared in the biexciton state $|{\rm B0}\rangle$ [150]. There are, however, some differences between this ideal case and the two types of excitation. For instance, under coherent excitation, two new two-photon resonances appear at $\omega_{\rm X} - 3\chi/4$ and $\omega_{\rm X} - \chi/4$ (at $-15g$ and $-5g$ in the figure) that we call (i) and (ii). They arise when two photons match the transitions to Raman virtual states created by the laser, close to $|{\rm G}\rangle$ and $|{\rm B}\rangle$, respectively, as depicted on the right hand side of Fig. 5.5. These are excitation induced resonances. They show how the cavity emission can be strongly and qualitatively affected by the laser even though it has the orthogonal polarization.

In order to analyse other more subtle issues related to the excitation, regarding efficiency, degree of simultaneity or indistinguishability of the two-photon emission at the 2PR, we carry out some approximations on the master equation and obtain analytical expressions for the cavity/dot populations and Mandel parameter (Q) .

5.4.3 Analytical results

Let us tune the cavity to the two-photon resonance (2PR), $\omega_a \approx \omega_{\rm X} - \chi/2$, as in Fig. 5.1(b). Here, the effective one-photon and two-photon coupling strengths are much smaller than the cavity decay rate, $g_{\rm 1P} \approx g\kappa/\chi$ and $g_{\rm 2P} \approx 4g^2/(\sqrt{2}\chi) \ll \kappa$ [149]. Therefore, one can adiabatically eliminate the cavity and consider only the quantum dot effective dynamics in its reduced Hilbert space. The cavity simply provides three extra decay channels that are Purcell suppressed/enhanced, given by the rates [150]:

$$\kappa_{\rm 1P} = 4g_{\rm 1P}^2/\kappa \quad \text{and} \quad \kappa_{\rm 2P} = 4g_{\rm 2P}^2/(2\kappa)\,. \tag{5.17}$$

The first one provides a second de-excitation channel from $|{\rm B}\rangle$ to $|{\rm H}\rangle$ and from $|{\rm H}\rangle$ to $|{\rm G}\rangle$ via the emission of one cavity photon. The second rate provides a third de-excitation channel from $|{\rm B}\rangle$ to $|{\rm G}\rangle$ via the emission of two cavity photons.

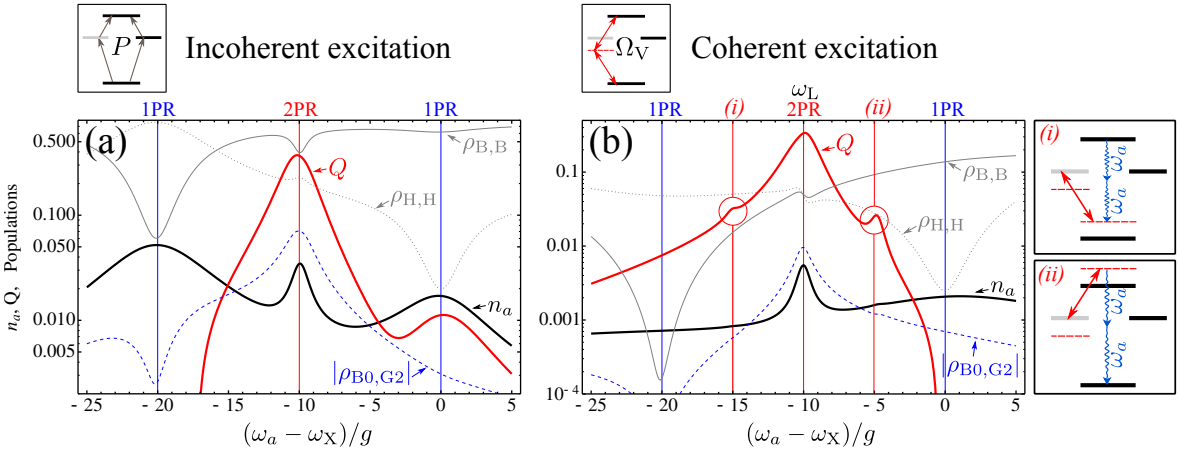

Figure 5.5: Steady state of the system under (a) incoherent and (b) coherent excitation when sweeping the cavity frequency through the different resonances. The results are exact, obtained by solving numerically the corresponding full master equation. I plot Q, n_a, $\rho_{B,B}$, $\rho_{H,H}$ and $|\rho_{B0,G2}|$. With vertical guide lines I have marked the two-photon and one-photon resonances. The laser frequency in (b) is set at the two-photon resonant excitation, $\omega_L = \omega_X - \chi/2$. In this case, I also find two additional bunching peaks in Q, (i) and (ii), due to the two-cavity-photon resonance with virtual (Raman) states driven by the laser. Parameters: $\chi = 20g$, $\kappa = g$, $\gamma = 0.01g$, $P = 0.06g$, $\Omega_V = 0.5g$.

5.4.3.1 Quantum dot properties

The master equation for the reduced dot density matrix ρ, where the cavity degree of freedom has been traced out, reads:

$$\begin{aligned}\partial_t\rho = i[\rho, H_{\rm dot} + H_{\rm las}] + \frac{\gamma+\kappa_{1P}}{2}\Big[\mathcal{L}_{|G\rangle\langle H|} + \mathcal{L}_{|H\rangle\langle B|}\Big](\rho) + \\ \frac{\kappa_{2P}}{2}\mathcal{L}_{|G\rangle\langle B|}(\rho) + \frac{\gamma}{2}\Big[\mathcal{L}_{|G\rangle\langle V|} + \mathcal{L}_{|V\rangle\langle B|}\Big](\rho) \\ + \frac{P}{2}\sum_{i=V,H}\Big[\mathcal{L}_{|i\rangle\langle G|} + \mathcal{L}_{|B\rangle\langle i|}\Big](\rho)\,. \end{aligned} \tag{5.18}$$

For simplicity, the small Stark shifts induced by the dispersive coupling on the exciton and cavity frequencies can be neglected as they are of the order of g_{1P}, g_{2P}. The equations under incoherent excitation involve only the populations:

$$\partial_t\rho_{G,G} = -2P\rho_{G,G} + \gamma\rho_{V,V} + (\gamma+\kappa_{1P})\rho_{H,H} + \kappa_{2P}\rho_{B,B}\,, \tag{5.19a}$$
$$\partial_t\rho_{V,V} = P\rho_{G,G} - (\gamma+P)\rho_{V,V} + \gamma\rho_{B,B}\,, \tag{5.19b}$$
$$\partial_t\rho_{H,H} = P\rho_{G,G} - (\gamma+P+\kappa_{1P})\rho_{H,H} + (\gamma+\kappa_{1P})\rho_{B,B}\,, \tag{5.19c}$$
$$\partial_t\rho_{B,B} = P\rho_{V,V} + P\rho_{H,H} - (2\gamma+\kappa_{1P}+\kappa_{2P})\rho_{B,B}\,. \tag{5.19d}$$

Together with the normalization $\mathrm{Tr}(\rho) = 1$, they provide analytical expressions, such as:

$$\rho_{H,H} \approx \frac{P\gamma\Gamma_B + P^2(\Gamma_B+\Gamma_H-\gamma)}{\gamma\Gamma_B\Gamma_H + 2P\big[\gamma(\Gamma_B-\Gamma_H)+\Gamma_B\Gamma_H\big] + 3P^2\Gamma_B + 2P^3} \xrightarrow{P\to 0} \frac{1}{\Gamma_H}P\,, \tag{5.20a}$$

$$\rho_{B,B} \approx \frac{P^2(\Gamma_H+\gamma) + 2P^3}{\gamma\Gamma_B\Gamma_H + 2P\big[\gamma(\Gamma_B-\Gamma_H)+\Gamma_B\Gamma_H\big] + 3P^2\Gamma_B + 2P^3} \xrightarrow{P\to 0} \frac{\Gamma_H+\gamma}{\gamma\Gamma_B\Gamma_H}P^2\,, \tag{5.20b}$$

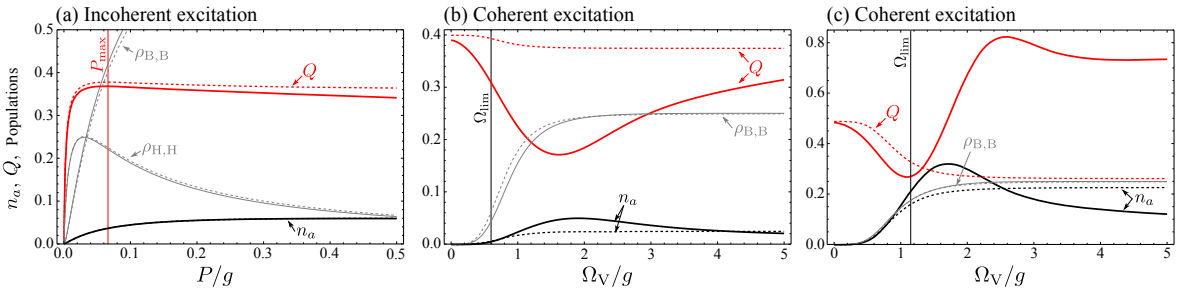

Figure 5.6: Steady state of the system at the 2PR under (a) incoherent and (b), (c) coherent excitation as a function of the corresponding excitation rates. The quantities Q, n_a, $\rho_{B,B}$ and $\rho_{H,H}$ are shown. The exact numerical results appear with solid lines and the analytical approximations discussed in the text in dashed lines. The formulas for n_a and Q are a good approximation for $P < P_{\rm lim}$ and $\Omega_V < \Omega_{\rm lim}$. The maximum Q under incoherent excitation is achieved at $P_{\max} = 0.066g$, which is the parameter used in Fig. 5.5(a). The optimum Q under coherent excitation is achieved at vanishing pumping. Parameters: $\chi = 20g$, $\omega_a = \omega_X - \chi/2$. In (a), (b) $\kappa = g$, giving $\kappa_{1P} = 0.01g$, $\kappa_{2P} = 0.04g$, $P_{\rm lim} = 0.5g$ and $\Omega_{\rm lim} = 0.63g$. In (c) $\kappa = 0.3g$ giving $\kappa_{1P} = 0.003g$, $\kappa_{2P} = 0.13g$ and $\Omega_{\rm lim} = 1.15g$. In (a), $\gamma = 0.01g$. In (b), (c), $\gamma = 0.1g$.

where $\Gamma_B = 2\gamma + \kappa_{1P} + \kappa_{2P}$ and $\Gamma_H = \gamma + \kappa_{1P}$ are the dissipation rates of levels the B and H. At vanishing pumping, we find the expected linear increase for single exciton populations and square increase for the biexciton population. In Fig. 5.6(a) we give an example of the quality of the approximation. Both the numerical exact solution of the full master equation (solid lines) and the approximated formulas (5.20) (dashed lines) are plotted for increasing excitation. They match almost perfectly for the whole pumping range. Eventually the system saturates on the biexciton state (not shown).

The equations under coherent excitation involve not only the populations but also some off-diagonal terms of the density matrix:

$$\partial_t \rho_{G,G} = \gamma\rho_{V,V} + \Gamma_H\rho_{H,H} + \kappa_{2P}\rho_{B,B} - i\Omega_V(\rho_{V,G} - \rho_{G,V})\,, \tag{5.21a}$$

$$\partial_t \rho_{G,V} = \big(i\frac{\chi}{2} - \frac{\gamma}{2}\big)\rho_{G,V} + i\Omega_V(\rho_{G,G} - \rho_{V,V} + \rho_{G,B})\,, \tag{5.21b}$$

$$\partial_t \rho_{G,B} = -\big(\frac{\gamma + \Gamma_H + \kappa_{2P}}{2}\big)\rho_{G,B} - i\Omega_V(\rho_{V,B} - \rho_{G,V})\,, \tag{5.21c}$$

$$\partial_t \rho_{V,V} = -\gamma\rho_{V,V} + \gamma\rho_{B,B} + i\Omega_V(\rho_{V,G} - \rho_{G,V} + \rho_{V,B} - \rho_{B,V})\,, \tag{5.21d}$$

$$\partial_t \rho_{V,B} = \big(-i\frac{\chi}{2} - \frac{2\gamma + \Gamma_H + \kappa_{2P}}{2}\big)\rho_{V,B} + i\Omega_V(\rho_{V,V} - \rho_{B,B} - \rho_{G,B})\,, \tag{5.21e}$$

$$\partial_t \rho_{H,H} = -\Gamma_H\rho_{H,H} + \Gamma_H\rho_{B,B}\,, \tag{5.21f}$$

$$\partial_t \rho_{B,B} = -\Gamma_B\rho_{B,B} + i\Omega_V(\rho_{B,V} - \rho_{V,B})\,. \tag{5.21g}$$

All off-diagonal terms involving the H-state vanish in the steady state. Including the nor-

malization $\mathrm{Tr}(\rho) = 1$, one obtains analytical expressions, such as:

$$\rho_{\mathrm{B,B}} = \rho_{\mathrm{H,H}} \approx \frac{4(2\Omega_{\mathrm{V}}^2)^2}{\Gamma_{\mathrm{B}}^2\chi^2 + \Gamma_{\mathrm{B}}(\gamma+\Gamma_{\mathrm{B}})\Omega_{\mathrm{V}}^2 + 64\Omega_{\mathrm{V}}^4} \xrightarrow{\Omega_{\mathrm{V}}\to 0} \frac{4(2\Omega_{\mathrm{V}}^2)^2}{\Gamma_{\mathrm{B}}^2\chi^2}\,, \tag{5.22a}$$

$$\rho_{\mathrm{V,V}} \approx \frac{4\Omega_{\mathrm{V}}^2(\Gamma_{\mathrm{B}}^2 + 4\Omega_{\mathrm{V}}^2)}{\Gamma_{\mathrm{B}}^2\chi^2 + \Gamma_{\mathrm{B}}(\gamma+\Gamma_{\mathrm{B}})\Omega_{\mathrm{V}}^2 + 64\Omega_{\mathrm{V}}^4} \xrightarrow{\Omega_{\mathrm{V}}\to 0} \frac{4\Omega_{\mathrm{V}}^2}{\chi^2}\,, \tag{5.22b}$$

$$\rho_{\mathrm{B,G}} \approx -i\frac{4\Omega_{\mathrm{V}}^2\Gamma_{\mathrm{B}}\chi}{\Gamma_{\mathrm{B}}^2\chi^2 + \Gamma_{\mathrm{B}}(\gamma+\Gamma_{\mathrm{B}})\Omega_{\mathrm{V}}^2 + 64\Omega_{\mathrm{V}}^4} \xrightarrow{\Omega_{\mathrm{V}}\to 0} -i\frac{4\Omega_{\mathrm{V}}^2}{\Gamma_{\mathrm{B}}\chi}\,. \tag{5.22c}$$

The behaviour at vanishing pumping is the expected one: the exciton populations increase as Ω_{V}^2 and the biexciton population as Ω_{V}^4. Consistently, the two-excitation off-diagonal term $|\rho_{\mathrm{B,G}}|^2$ increases as Ω_{V}^4. The population of the biexciton state is plotted in Fig. 5.5(b) and (c) for two different coupling strengths with the cavity, strong ($\kappa = g$) and very strong ($\kappa = 0.3g$). Again, a very good agreement between exact and approximated solutions us found. The agreement depends more critically on γ than under incoherent excitation, the larger γ the better the agreement. That is why it is increased from $\gamma = 0.01g$ to $\gamma = 0.1g$ in Figs. 5.5(b), (c). Of course, this means slightly decreasing the efficiency of the two cavity photon emission as compared to the total emission of the system [150]. However, in this Section we are more interested in identifying what plays a fundamental role in the dynamics under continuous excitation, in order to grasp the conditions for two-photon emission. Large pumping leads to saturation which in this case means equal population for all four dot levels, 1/4.

Then, we are going to derive analytical expressions for n_a and Q, in terms of the previous analytical matrix elements.

5.4.3.2 Cavity properties

In Eq. 5.8, the time-dependent cavity spectrum, $S(\omega, t)$, was split into its four main contributions. In this Section, due to the continuous source of pumping we are more interested in the steady state situation. Still in this case the separation into the main transitions of the spectra can be done:

$$S(\omega) = \frac{1}{\pi}\sum_{\alpha\in\{1,2,\mathrm{I},\mathrm{II}\}}\left(L_\alpha\frac{\frac{\gamma_\alpha}{2}}{(\frac{\gamma_\alpha}{2})^2 + (\omega-\omega_\alpha)^2} - K_\alpha\frac{\omega-\omega_\alpha}{(\frac{\gamma_\alpha}{2})^2 + (\omega-\omega_\alpha)^2}\right)\,, \tag{5.23}$$

with L_α quantifies the total intensity emitted through a given transition $\alpha = |\mathrm{i}\rangle \to |\mathrm{f}\rangle$, from a given initial state $|\mathrm{i}\rangle$ to a given final state $|\mathrm{f}\rangle$. The sum of all L_α is the total photon mean number in the steady state:

$$n_a = \mathrm{Tr}(\rho a^\dagger a) = \sum_{i,f}\rho_{i,i}|\,\langle f|\,a\,|i\rangle\,|^2 = L_1 + L_2 + L_{\mathrm{I}} + L_{\mathrm{II}}\,, \tag{5.24}$$

in the basis of states in which the density matrix is diagonal. Due to the dispersive (weak) coupling to the cavity, one can safely assume that the dynamics never involves more than two photons and truncate the dot-cavity Hilbert space as in Fig. 5.1(b-c). Moreover, only states with no photon are significantly populated. All other states remain virtual, in the sense that

they serve as intermediate states for perturbative second order processes but never achieve a sizable population. As a result, the initial states that we should consider are not exactly $|\mathrm{H},0\rangle$ and $|\mathrm{B},0\rangle$, with zero photon, because the dispersive interaction with the cavity couples each of them weakly to states with one or two photons. The photonic components can be obtained by diagonalising the Hamiltonian in each manifold of excitation. For instance, in the manifold of two excitations, states $|\mathrm{B},0\rangle$, $|\mathrm{H},1\rangle$ and $|\mathrm{G},2\rangle$ interact through the non-Hermitian Hamiltonian

$$H_{2\mathrm{P}} = \begin{pmatrix} -i\gamma & g & 0 \\ g & \chi/2 - i(\kappa+\gamma)/2 & \sqrt{2}g \\ 0 & \sqrt{2}g & -i\kappa \end{pmatrix}, \tag{5.25}$$

as shown in Fig. 5.1(b). we have added the corresponding dissipation of each level as an imaginary part to the frequency and considered the renormalization of the coupling by the number of photons involved (g or $\sqrt{2}g$ for one and two-photon states, respectively). One should be aware that the use of a non-hermitian hamiltonian to introduce losses has a certain range of applicability. However, in order to obtain mean values works well.

Diagonalising this Hamiltonian to second order at large χ and $\kappa \gg \gamma$, one obtains new eigenstates that differ from the bare ones in additional small components from all the other bare states. That is, state $|\mathrm{B}\rangle \approx |\mathrm{B},0\rangle$ becomes $|\mathrm{B}_2\rangle \approx C\,|\mathrm{B},0\rangle + C_{1\mathrm{P}}\,|\mathrm{H},1\rangle + C_{2\mathrm{P}}\,|\mathrm{G},2\rangle$ with $|C_{1\mathrm{P}}| = 2g/\chi$ and $|C_{2\mathrm{P}}| = 2\sqrt{2}g^2/(\chi\kappa)$. Similarly, in the manifold of one excitation, states $|\mathrm{H},0\rangle$ and $|\mathrm{G},1\rangle$ interact through the non-Hermitian Hamiltonian

$$H_{1\mathrm{P}} = \begin{pmatrix} \chi/2 - i\gamma/2 & g \\ g & -i\kappa/2 \end{pmatrix}, \tag{5.26}$$

as shown in Fig. 5.1(c). The state $|\mathrm{H}\rangle \approx |\mathrm{H},0\rangle$ becomes $|\mathrm{H}_1\rangle \approx C'\,|\mathrm{H},0\rangle + C_{1\mathrm{P}}\,|\mathrm{G},1\rangle$. In practical terms, one must consider as initial states in Eq. (5.24) the superpositions $|\mathrm{B}_2\rangle$ and $|\mathrm{H}_1\rangle$, with coefficient rewritten as $|C_{1\mathrm{P}}|^2 = \kappa_{1\mathrm{P}}/\kappa$ and $|C_{2\mathrm{P}}|^2 = \kappa_{2\mathrm{P}}/(2\kappa)$.[1] These results do not change within the same degree of approximation if one includes decoherence due to the incoherent pump (affecting all levels but $|\mathrm{B},0\rangle$) as long as $P \ll \chi$. Coherent excitation does not bring any additional decoherence.

From these perturbed initial states, there are four main possible transitions via the cavity mode (see Fig. 5.1(a)), at frequencies and with broadenings that we already described in the previous Section. The following analytical expressions for the intensities are obtained:

1) the decay from $|\mathrm{B}_2\rangle$ to $|\mathrm{H},0\rangle$, gives rise to the component $L_1 = \rho_{\mathrm{B,B}}|\,\langle \mathrm{H},0|\,a\,|\mathrm{B}_2\rangle\,|^2 = \rho_{\mathrm{B,B}}\kappa_{1\mathrm{P}}/\kappa$,

2) the decay from $|\mathrm{H}_1\rangle$ to $|\mathrm{G},0\rangle$, gives rise to the component $L_2 = \rho_{\mathrm{H,H}}|\,\langle \mathrm{G},0|\,a\,|\mathrm{H}_1\rangle\,|^2 = \rho_{\mathrm{H,H}}\kappa_{1\mathrm{P}}/\kappa$,

I) the decay from $|\mathrm{B}_2\rangle$ to $|\mathrm{G},1\rangle$, gives rise to the component $L_{\mathrm{I}} = \rho_{\mathrm{B,B}}|\,\langle \mathrm{G},1|\,a\,|\mathrm{B}_2\rangle\,|^2 = \rho_{\mathrm{B,B}}2\kappa_{2\mathrm{P}}/(2\kappa)$,

[1] In fact, this is an alternative way to estimate $\kappa_{1\mathrm{P}}$, $\kappa_{2\mathrm{P}}$, and then $g_{1\mathrm{P}}$, $g_{2\mathrm{P}}$ with Eq. (5.17). The effective photonic decay rate of $|\mathrm{H}_1\rangle$ is its photonic component $|C_{1\mathrm{P}}|^2$ times the associated decay rate κ, etc.

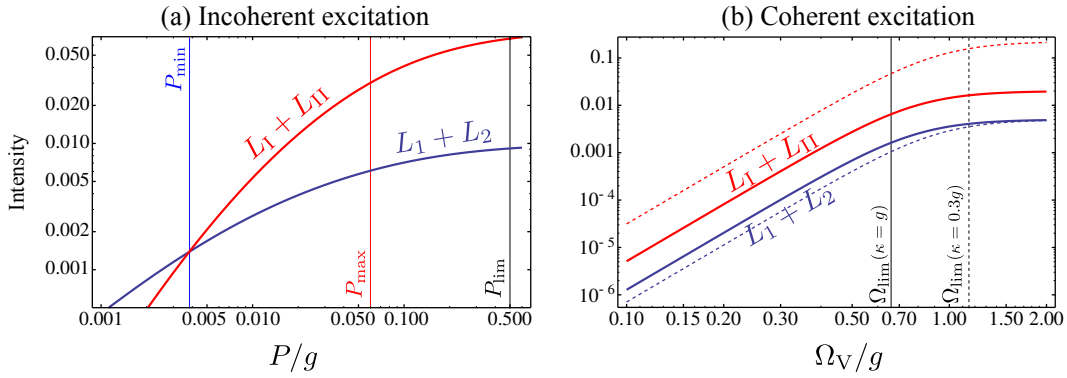

Figure 5.7: Analytical approximations for the two contributions to the cavity emission: from single photons, L_1+L_2, and from pairs of photons, $L_{\rm I}+L_{\rm II}$. Panel (a) corresponds to situation of Fig. 5.6(a) and panel (b) to situations of Fig. 5.6(b) and (c), plotted in solid and dashed lines, respectively.

II) the direct decay from $|{\rm G},1\rangle$ to $|{\rm G},0\rangle$, gives rise to the component $L_{\rm II} = \rho_{\rm G1,G1} |\langle {\rm G},0| a |{\rm G},1\rangle|^2 = \rho_{\rm G1,G1}$. This level has a very small population in the steady state. Its dynamics under incoherent excitation reads $\partial_t \rho_{\rm G1,G1} \approx \kappa_{\rm 2P}\rho_{\rm B0,B0} - \kappa\rho_{\rm G1,G1} - 2P\rho_{\rm G1,G1}$. Then,

$$\rho_{\rm G1,G1} \approx \kappa_{\rm 2P}/(\kappa + 2P)\rho_{\rm B,B}\,. \tag{5.27}$$

For the success of a simultaneous two-photon state emission from $|{\rm B},0\rangle$, the population of $|{\rm G},1\rangle$ should remain small, keeping its virtual nature. Moreover, the photon should also be quickly emitted before incoherent pumping drives the state upwards into $|{\rm H},1\rangle$. This means that one requires

$$P \ll P_{\rm lim} = \kappa/2 \quad \text{and} \quad \kappa \gg \kappa_{\rm 2P}\,. \tag{5.28}$$

in order not to break the indistinguishability and simultaneity of the two emission events.

In the case of coherent excitation we set $P \to 0$. We neglect the possible dynamics of state $\rho_{\rm G1,G1}$ due to the effective one- and two-photon effective driving to the off-resonant state $|{\rm V},1\rangle$ and the two-photon resonant state $|{\rm B},1\rangle$. They do not play a role as they are small in the regime of pumping where our approximations hold: $\Omega_{\rm 1P} \approx \Omega_{\rm V}\gamma/\chi$ and $\Omega_{\rm 2P} \approx 2\Omega_{\rm V}^2/\chi$.[1]

In total, the cavity intensity reads:

$$n_a \approx \rho_{\rm B,B}\Big[\frac{\kappa_{\rm 1P}+\kappa_{\rm 2P}}{\kappa} + \frac{\kappa_{\rm 2P}}{\kappa+2P}\Big] + \rho_{\rm H,H}\frac{\kappa_{\rm 1P}}{\kappa}\,. \tag{5.29}$$

Similarly, one can obtain the second order coherence function in two different ways,

$$G^{(2)} = {\rm Tr}(\rho a^\dagger a^\dagger a a) = \sum_{i,f} \rho_{i,i} |\langle f| a^2 |i\rangle|^2 \approx \rho_{\rm B,B}\kappa_{\rm 2P}/\kappa \tag{5.30a}$$

$$\approx (L_{\rm I}+L_{\rm II})/2 \approx \rho_{\rm B,B}\kappa_{\rm 2P}\Big[\frac{\frac{1}{\kappa}+\frac{1}{\kappa+2P}}{2}\Big]\,, \tag{5.30b}$$

[1] One can estimate them by comparing populations $\rho_{\rm V,V}$ and $\rho_{\rm B,B}$ in Eq. (5.22), to second order in $1/\chi$, with the occupation of a two-level system in the linear regime, given by $4\Omega^2/\Gamma$, with Γ its decay rate.

The two lines converge at low incoherent pumping.

5.4.3.3 Incoherent excitation

In the case of incoherent pumping, it is preferable to use the second line of Eq. (5.30) to compute $G^{(2)}$ because it incorporates the fact that the second photon in the two-photon de-excitation is less likely to be emitted due to the pumping induced transition $|\mathrm{G},1\rangle \rightarrow |\mathrm{H},1\rangle$ explained above. Fig. 5.6(a) shows that both n_a and Q calculated from Eq. (5.30b) are in good agreement with the exact solution. One may think that pumping strongly will be beneficial for our purposes as the biexciton level is more likely occupied and available for the two-photon de-excitation. However, when the pumping overcomes the cavity losses, $P_{\mathrm{lim}} \approx \kappa/2$, the Q-factor drops dramatically becoming very different from the analytical result (not shown). The states that we assumed virtual are no longer so, as the pumping forces them to participate in the dynamics. The cavity intensity increases and a truncation at two photons is not appropriate. Even though the coupling is not strong enough to achieve lasing [149], the system is not anymore in the spontaneous emission regime. Finally, the decoherence and disruptive effect of the pump dominates, quenching also the cavity emission. To sum up, the two-photon mechanism that we pursue and described analytically—that is, an efficient succession of fast two-photon emissions—is washed out when $P > P_{\mathrm{lim}}$. Remaining in the unsaturated regime of Fig. 5.6(a), the survival of the desired two-photon emission is ensured.

The Q-factor achieves a maximum at a pumping rate that we call P_{max}, marked with a vertical guideline in Fig. 5.7(a). At this point, the pumping is small enough to keep the virtual nature of $|\mathrm{G},1\rangle$ and, therefore, the simultaneity and indistinguishability of the emissions. At the same time, the population of the biexciton is already clearly larger than the other states, enough for the two-photon emission to dominate. This is shown in Fig. 5.7(a) where it is compared the intensity associated to the single photon emissions, $L_1 + L_2$, with that associated to the two-photon emission, $L_{\mathrm{I}} + L_{\mathrm{II}}$. Once the small pumping that we call P_{min} (where both contributions cross) is overcome, the two-photon emission dominates. Due to the fact that below P_{min} the one-photon emission dominates, the Q factor is zero for vanishing pumping. In the limiting case of $\gamma = 0$, the minimum pumping vanishes and the two-photon process dominates at all pumpings, depending on the system parameters only,

$$Q_0 = \lim_{P\to 0}\left(\lim_{\gamma\to 0} Q\right) = \frac{1}{3}\frac{4g^2}{4g^2+\kappa^2} \leq \frac{1}{3}\,. \tag{5.31}$$

Note that in this case, Q still increases from Q_0 and reaches its maximum value at a finite P_{max}, as when $\gamma \neq 0$.

5.4.3.4 Coherent excitation

In the case of coherent excitation, one also finds a maximum value of excitation intensity, Ω_{lim}, after which our analytical expressions do not hold, as shown in the two different examples of Fig. 5.6(b), (c). In principle, coherent excitation does not induce decoherence at high pumpings. However, passed the linear regime, it starts dressing the quantum dot four-level system, shifting the levels and changing its resonances. This becomes detrimental for our two-photon emission process. One would need to recalculate the conditions for a two-photon

resonance taking into account the dressing by the laser. A more careful analysis of the spectrum of emission (and the new peaks appearing) would then be required. Moreover, the two-photon absorption from the laser creates coherence between states $|\mathrm{G}\rangle$ and $|\mathrm{B}\rangle$ that may interfere with our mechanism. We already showed an example of such laser-cavity interaction in Fig. 5.5(i-ii). One can estimate Ω_{lim} as the point at which $\Omega_{2\mathrm{P}} = \kappa_{2\mathrm{P}}$, and get $\Omega_{\mathrm{lim}} \approx 2\sqrt{2}g^2/\sqrt{\chi\kappa}$. Similarly to the incoherent pumping case, $\Omega_{\mathrm{V}} > \Omega_{\mathrm{lim}}$ also leads to a growth in the cavity emission that we cannot reproduce analytically due to the truncation of the Hilbert space at two-photons.

In contrast with the incoherent excitation, the Q-factor starts from a local maximum at vanishing pumping. The reason is that the biexciton state has always the same population as the H-state so there can be a large ratio of two versus one-photon emission for arbitrarily small pumping, depending on $\kappa_{2\mathrm{P}}/\kappa_{1\mathrm{P}}$ only (always $\gg 1$ in our examples). This is shown in Fig. 5.6(b) where two-photon process always dominates, $L_{\mathrm{I}} + L_{\mathrm{II}} > L_1 + L_2$. The fraction $L_{\mathrm{I}} + L_{\mathrm{II}}/(L_1 + L_2) = 4g^2/\kappa^2$ is indeed constant over the whole region. Then, one can conclude that the maximum Q-factor achieved in the region of interest (before saturation) reads

$$Q_0 = Q_{\mathrm{max}} = \lim_{\Omega_{\mathrm{V}} \to 0} = \frac{1}{2}\frac{4g^2}{4g^2 + \kappa^2} \leq \frac{1}{2}\,. \tag{5.32}$$

This puts a upper limit to Q of $1/2$ in the present conditions. It also tells us that the better the system (deeper into the strong coupling regime), the higher the bunching in the linear regime, c. f. Fig. 5.6(b-c). However, one must bear in mind that the state $|\mathrm{G}, 1\rangle$ should remain virtual in order to have simultaneous and indistinguishable emissions, and this means keeping $\kappa_{2\mathrm{P}}/\kappa \ll 1$, that is, $\kappa \gg 4g^2/\chi$ (equal to $0.2g$ in our examples).

5.5 Conclusions

In conclusion, we have presented a scheme where the biexciton is in two-photon resonance with a microcavity mode, as an efficient two-photon source, both in terms of the purity of the two-photon state and of its emission efficiency. The timescale for two-photon emission, that limits the repetition rate, is of the order of $\kappa_{2\mathrm{P}}^{-1}$ and the linewidth of the 2P peak $\approx \kappa$ is determined by the cavity quality factor. The quantum character of the two-photon emission is demonstrated theoretically by a detailed analysis of all the processes involved in the biexciton de-excitation, which also allows us to find analytically the optimum conditions for its realization. We have shown that the two-photons are emitted simultaneously with no delay in the autocorrelation time. Experimentally, the ultimate proof of indistinguishability can be obtained by directing the central peak to a beam-splitter, which half of the time will separate the photon pair into two ports that can then be fed in an Hong-Ou-Mandel interferometer.

In the case of continuous excitation, we have studied the impact of both kind of excitations. Remarkably, we are able to characterize the regions for optimally generating the 2P states thanks to the analytical understanding of the problem. Further insight of them problem can be obtained by measuring time and frequency resolved correlations explained in detail in the Chapter 4 [152**?**].

Chapter 6

Strong-coupling between quantum emitters and surface plasmons.

6.1 Introduction

As already mentioned the introductory Chapter, surface plasmon polaritons (SPPs) have attracted a great interest very recently in the light-matter coupling community [58–60]. This interest has mainly emerged due to the enhancement of light-matter interaction (see Chapter 1 for more details). Many experiments have achieved the so-called reversible or strong-coupling (SC) regime between quantum emitters (QEs) and the SPP bath, where the EM modes and the QE are exchanging energy coherently. This foresees their application in quantum information technologies. From the the theoretical point of view, SPPs of a metal surface is a paradigmatic example of a structured reservoir: due to their characteristic dispersion relationship (see Fig. 1.4), almost flat for energies around the cut-off, it is induced a very high density of modes around it.

Within the experimental and theoretical literature, it has been considered two different regimes depending on the number of QEs interacting with the SPPs. Many of the experiments work in the limit where only one QE is in the presence of a metallic structure that supports the propagation of SPPs, such as metallic nanowires [56, 61] or two-dimensional surfaces [62]. In all these experiments, the system operates within the weak-coupling (WC) regime, as no signature of reversibility is observed. However, interesting applications have been still proposed within this regime. For example, when a few emitters are placed in front of these structures, it has been predicted that the SPP modes can mediate qubit entanglement [64–66], as we show in the next Chapter.

On the other hand, many experiments work in the situation where many QEs are placed in the surroundings of a metal-dielectric interface. In this case, the emergence of SC is due to the collective enhancement of the QE-SPP coupling contant with $\sqrt{N}$, being N the number of QEs. These experiments made use of different systems to play the role of QEs; ranging from organic molecules [67–70] to the excitons in quantum dots and quantum wells [71–73].

This Chapter focus on two-dimensional geometries, considering a two-dimensional metal layer of thickness h as depicted in Fig. 6.1 in both the single (in (a)) and many QE limit (in (b)). In both cases, our goal is to do a thorough analysis on determining the key experimental

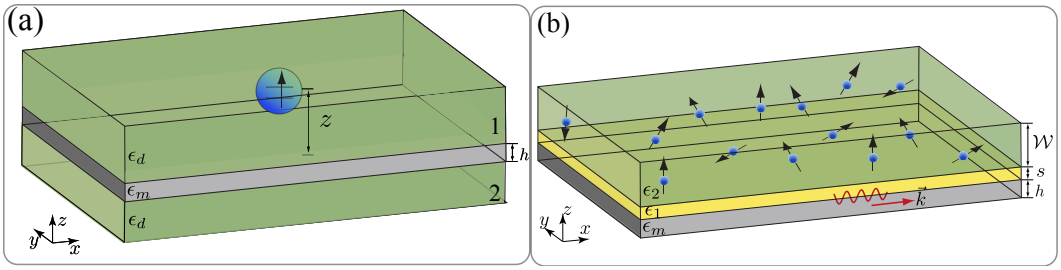

Figure 6.1: (a) Schematic picture of one QE placed at a distance z from the interface with a metal film of thickness h. (b) N QEs distributed in a dielectric host of width $\mathcal{W}$ that is separated by a distance s from a metal film of thickness h

parameters that play a role in the emergence or not the reversible dynamics. Despite both cases share the goal, the appearance of SC in each situation stems from different origins, so that we need to use different approaches for them. First in the case of many QEs, we consider them to be in a disordered homogeneous distribution, resembling the experimental conditions. This assumption implies translational invariance and conservation of parallel momentum. As a consequence, the SPP mode matching the energy of the QEs be the more relevant for the SC. On the contrary, in the single QE situation, the fixed position induced a coupling all the possible momenta and therefore the information from the whole range of SPPs energies is relevant. We study this limit with an analogue situation as the one considered in Chapter 2 for the Wigner-Weisskopf decay situation. In this approximation, the spectral density of the bath $J(\omega)$ in the *whole* range of frequencies was important for determining the full dynamics of the system.

Taking into account this last observation, Chapter 6 is divided as follows: in Section 6.2, we introduce the formalism needed to deal with the single QE limit and analyze what limits the observation of reversible dynamics in this regime. Then, in Section 6.3 we adopt an open quantum system approach for the many QE situation. Here, we separate the different contributions appearing in these systems and develop an self-consistent quantum formalism for treating coherent and incoherent mechanisms on the same footing. This framework not only allows us to characterize the regions of SC, which can be qualitatively obtained semiclassically, but also settles the theory for the prediction of new plasmonic quantum phenomena. Finally, Section 6.4 summarizes main points of the Chapter.

6.2 Analysis of the single emitter configuration.

This Section is devoted to the interaction of a single QE with the SPPs of a two-dimensional metal film such as the system depicted in Fig. 6.1(a). The QE is embedded into a dielectric host that is characterized by its dielectric constant, ϵ_d, and placed on top of a thin metal film (thickness h). The metal is characterized by means of a complex dielectric function given by the following Drude formula:

$$\epsilon_m(\omega) = \epsilon_{m,\infty} - \frac{\omega_p}{\omega(\omega + i\gamma_p)}\,, \tag{6.1}$$

where $\omega_p = 9$ eV and $\gamma_p = 0.03$ eV are the parameters for Silver [208]. In this Chapter

the acronym QE will refer to a quantum system with discrete electronic levels, like organic molecules or quantum dots. It will be represented within a two-level system (2LS) approximation, detailed in Chapter 2, characterized by its transition frequency (ω_0) and intrinsic decay rate (γ_0). The transition frequency we consider is $\omega_0 = 2eV$ so that we work in the optical regime. Unless stated otherwise, the dipole moment, $\vec{\mu}$, of the QE will be assumed to be oriented normal to the surface: $\vec{\mu} = \mu\hat{z}$, as this is the optimal configuration to couple to the SPP field [58].

After describing the main ingredients of the problem, we firstly make a brief review of the results that can be obtained within a semi-classical formalism where only classical Maxwell Equations are considered.

6.2.1 Green's function formalism: Classical description.

6.2.1.1 General framework.

When a dipole is placed in front of a metallic structure, its response can be characterized by means of the so-called Green's function formalism. The Green function defines the classical relationship between the electric field at given position $\vec{E}(\vec{r})$ and the dipole $\vec{\mu}$ placed at $\vec{r}_0$ that generates it[1]:

$$\vec{E}(\vec{r}) = \omega^2\mu_0\mu_1\hat{\mathbf{G}}(\vec{r},\vec{r}_0)\vec{\mu}(\vec{r}_0)\,. \tag{6.2}$$

In our problem, the dipole is placed at a distance z_0 above a metal surface. Thus, we just need the Green's function in the upper half-space ($z > 0$), that consists of a sum over the free-space and the reflected contributions [58]:

$$\hat{\mathbf{G}}(\vec{r},\vec{r}_0,\omega) = \hat{\mathbf{G}}_0(\vec{r},\vec{r}_0,\omega) + \hat{\mathbf{G}}_R(\vec{r},\vec{r}_0,\omega)\,. \tag{6.3}$$

From this tensor, the classical emission properties of the dipole can also be extracted, such as its modified decay rate [58], as follows:

$$\begin{aligned}\frac{\Gamma(\omega)}{\Gamma_0} = \frac{\mathrm{Im}\left\{\vec{\mu}\cdot\hat{\mathbf{G}}(\vec{r}_0,\vec{r}_0,\omega)\cdot\vec{\mu}\right\}}{\mathrm{Im}\left\{\vec{\mu}\cdot\hat{\mathbf{G}_0}(\vec{r}_0,\vec{r}_0,\omega_0)\cdot\vec{\mu}\right\}} = \\ 1 + \frac{6\pi}{\omega_0}\left[\vec{\mu}\cdot\mathrm{Im}\left\{\hat{\mathbf{G}}_R(\vec{r}_0,\vec{r}_0,\omega)\right\}\cdot\vec{\mu}\right]\,.\end{aligned} \tag{6.4}$$

As we have assumed a normal orientation of the dipole, we only need the zz component, which can be easily obtained from its normal mode expansion:

$$\mathbf{G}^{zz}(\vec{r}_0,\vec{r}_0,\omega) = \frac{i}{4\pi k_0^2}\int dk\frac{k^3}{k_z}\left[1 - r_p(k)e^{2ik_z z_0}\right]\,, \tag{6.5}$$

where k labels the in-plane momentum ($\vec{k} = (k\cos\theta, k\sin\theta, k_z)$). The first part of the sum corresponds to the direct emission into vacuum modes, whereas the second accounts for the reflected contribution. The latter is proportional to the reflection coefficient for p-polarization

[1]The dipole moment, $\vec{\mu}$, should not be confused with the magnetic permitivity of the medium, $\mu_0\mu_1$.

$r_p(k)$. For a layered structure as the one shown in Fig. 6.1, the reflection coefficients is the following:

$$r_p(k) = \frac{r_{1m} + r_{m2}e^{2ik_{m,z}h}}{1 + r_{1m}r_{m2}e^{2ik_{m,z}h}}\,, \tag{6.6}$$

with $r_{ij}(k)$:

$$r_{i,j}(k) = \frac{\epsilon_i(\omega)k_{z,j} - \epsilon_j(\omega)k_{i,z}}{\epsilon_i(\omega)k_{z,j} + \epsilon_j(\omega)k_{i,z}}\,, \tag{6.7}$$

where the indexes can label either one of the dielectrics $(1, 2)$ or the metal (m). We consider for simplicity a symmetric configuration where $\epsilon_1 = \epsilon_2 = \epsilon_d$. This implies that the SPP wavevectors perpendicular to the surface in the dielectric (metal) to be defined by: $k_{1,2,z} = k_z = \sqrt{\epsilon_d k_0^2 - k^2}$ ($k_{z,m} = \sqrt{\epsilon_m(\omega)k_0^2 - k^2}$) with $k_0 = \omega/c$. The cancelation of the denominator: $1 + r_{1m}r_{m2}e^{2ik_{m,z}h} = 0$, determines the resonances of the SPP field of the metal layer. In a symmetric configuration, this leads to the following two equations:

$$\epsilon_m(\omega)k_z + \epsilon_d k_{m,z}\tanh(-ik_{m,z}h/2) = 0\,, \tag{6.8}$$

$$\epsilon_m(\omega)k_z + \epsilon_d k_{m,z}\coth(-ik_{m,z}h/2) = 0\,, \tag{6.9}$$

which define the equations for the symmetric and antisymmetric SPP modes supported by the layered structure. Although, in general, these equations have to solved numerically, there are two limits in which they can be solved analytically, namely thin and thick film limit. In particular, these are going to be the two cases that are considered for the analysis of the dynamics.

6.2.1.2 Thick film limit.

Firstly, we consider the limit where $h \to \infty$. This implies that both hyperbolic functions in Eqs. 6.8-6.9 go to 1, $r_p(k) \approx r_{1,m}$ and the symmetric and antisymmetric SPP modes coincide. This regime will be named as the *thick film* limit. It is the most common experimental situation and consequently the main situation of interest for this Section[1]. In this case, both equations lead to the well known dispersion relationship for SPPs:

$$k_{spp}(\omega) = k_0\sqrt{\frac{\epsilon_d\epsilon_m(\omega)}{\epsilon_m(\omega) + \epsilon_d}}\,. \tag{6.10}$$

Fig. 6.2(a) shows the SPP dispersion relationship for a dielectric with $\epsilon_d = 1$. It can be easily observed that the momentum of the SPP field always lies always out of the light line, $k_{spp}(\omega) > \epsilon_d k_0$, leading to an evanescent behavior of the SPP field into the dielectric as $k_{1,z}$ is imaginary. Importantly, it also bends to an asymptotic value given by the condition $\epsilon_d + \epsilon_m(\omega) = 0$, which defines the so-called plasmon *cut-off* frequency. For $\omega > \omega_{cut}$, SPPs can

[1]From numerical calculations (not shown), we have checked that from $h \gtrsim 50\,nm$ the SPP resonances converge to the infinite case.

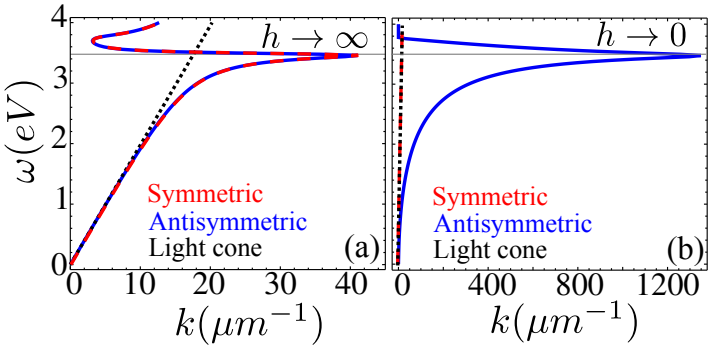

Figure 6.2: (a) SPP dispersion relationship for $\epsilon_d = 1$ for the limit $h \to \infty$ for the symmetric (dashed red) and antisymmetric (solid blue) mode .(b) SPP dispersion relationship for $\epsilon_d = 1$ for the limit $h \to 0$ for the symmetric (dashed red) and antisymmetric (solid blue) mode. In both panels the light line is plotted in dotted in black.

not be accurately defined. Its explicit expression depends of the different material parameters exposed in the previous Section and reads:

$$\omega_{cut} = \frac{\omega_p}{\sqrt{\epsilon_d + \epsilon_{m,\infty}}}. \tag{6.11}$$

Around this frequency there is a region of small group velocity $|\partial_q \omega| \approx 0$, which translates into a high density of modes. Therefore, this region plays a relevant role in the possible observation of reversible dynamics.

6.2.1.3 Thin film limit.

In the thin film limit, defined by $h \to 0$, the arguments of the hyperbolic functions in Eqs. 6.8-6.9 are very small and can be expanded by using $\tanh(x) = x = \coth^{-1}(x)$. Thus, the equation for the symmetric mode yields an energy dispersion that lies exactly in the light line $k^+_{spp}(\omega) = \sqrt{\epsilon_d} k_0$, as depicted in Fig. 6.2(b), whereas the equation for antisymmetric case mode reads:

$$k^-_{spp}(\omega) = k_0 \sqrt{1 + \left(\frac{2\epsilon_d}{\epsilon_m(\omega) h k_0}\right)^2}. \tag{6.12}$$

Both dispersion relationships are plotted in Fig. 6.2(b). It can be observed that the cut-off appears at the same frequency as for thick film limit, while, the in-plane momentum for the antisymmetric mode, k^-_{spp}, is much larger. As the SPP field in the dielectric decays proportional to $e^{-|k_z|z}$ and $|k_z| \propto k^-_{spp}$, this translates in a higher confinement of the field. Therefore, in the thin film limit the enhanced confinement favors larger interaction strengths. The reflection coefficient can be further simplified:

$$r_{p,h\to 0}(k) \approx \frac{-\epsilon_m(\omega) d}{\epsilon_m(\omega) k_z d + 2\epsilon_d i}, \tag{6.13}$$

which is formally the same expression that one obtains for a truly two dimensional systems as a graphene layer [209]. Once the SPP resonances of the problem for both the thick and

thin film limit have been identified, one can extract their contribution to the decay rate of a QE as we detail in the next subsection.

6.2.1.4 Contributions to the decay rate.

It was shown in Eq. 6.4 that the decay rate of a QE can be calculated semiclassically by using the Green Function of the system: $\Gamma(\omega) \propto \mathrm{Im}\{\hat{\mathbf{G}}(\vec{r},\vec{r}',\omega)\}$. In Eq. 6.5 this function was expressed as a sum over all k-modes of the system, containing then information about the different decay channels through which the energy can flow.

These channels can be classified depending on the radiative or non-radiative character. Radiative modes are characterized for showing an in-plane momentum which always inside the light line ($k < \epsilon_d k_0$). They are characterized for having a propagating behavior into the dielectric with $\mathrm{Im}\{k_z\} = 0$. Extracting their contribution from the total Green function can be done just by limiting the interval of integration to:

$$\mathbf{G}^{zz}_{\mathrm{rad}}(\vec{r},\vec{r},\omega) = \frac{i}{4\pi k_0^2}\int_0^{\epsilon_d k_0} dk \frac{k^3}{k_z}\left[1 - r_p(k)e^{2ik_z z}\right], \tag{6.14}$$

The other contribution comes strictly from the reflected part of the Green Function as it corresponds to non-radiative modes of the surface. They come from the modes with k's outside the light line ($k > \epsilon_d k_0$) thus having an evanescent character $\mathrm{Im}\{k_z\} \neq 0$. The SPP resonances of the metal film are part the non-radiative channel and if we were dealing with a lossless metal ($\mathrm{Im}\{\epsilon_m(\omega)\} \approx 0$) they will be the only contribution in the evanescent region. Under this assumption, it is possible to estimate the contribution of the resonances by using a extracting SPP pole from the integral of Eq. 6.5. It can be done by using:

$$\mathbf{G}^{zz}_{\mathrm{spp}}(\vec{r},\vec{r},\omega) = \int_{\epsilon_d k_0}^{\infty} \frac{f(k)}{k - k_{spp}} = i\pi f(k_{spp}) + \mathrm{P.V.}\int_{\epsilon_d k_0}^{\infty} dk \frac{f(k)}{k - k_{spp}}, \tag{6.15}$$

where $f(q)$ is different for the thick and thin film limit, though in both cases can be calculated analytically. When considering small but non-negligible losses, the plasmon pole approximation can still be made but a new channel of decoherence appears. This accounts for direct excitation of electron-hole pairs in the metal which correspond to high k modes mostly relevant when the QE is placed very close to the interface.

In Fig. 6.3, the total decay rate together with its different contributions is plotted for a QE with energy $\omega_0 = 2\ eV$ and for the two limits of interest. As expected, for very small distances, $k_0 z \ll 1$, the ohmic losses contribution dominates (green region). This contribution scales as z^{-3} [58] and increases the Purcell factor, defined by ratio Γ/γ_0, of the QE. In this region the QE is said to be *quenched* and no interesting effects are expected [18]. However, in the next Sections it is shown that this is not strictly true from an integration of the dynamics beyond the Fermi golden rule [36]. As the distance from the surface increases, this contribution becomes less relevant and the SPP channel (red region) starts to dominate. At distances around 180 nm (25 nm) for the thick (thin) metal film, the emission into the SPP channel compared with the rest –characterized by the so-called β-factor ($\beta = \Gamma_{spp}/\Gamma$)– is almost perfect. By further separating the QE, the effect of the metal surface is negligible and most energy is going into vacuum radiative modes (blue region).

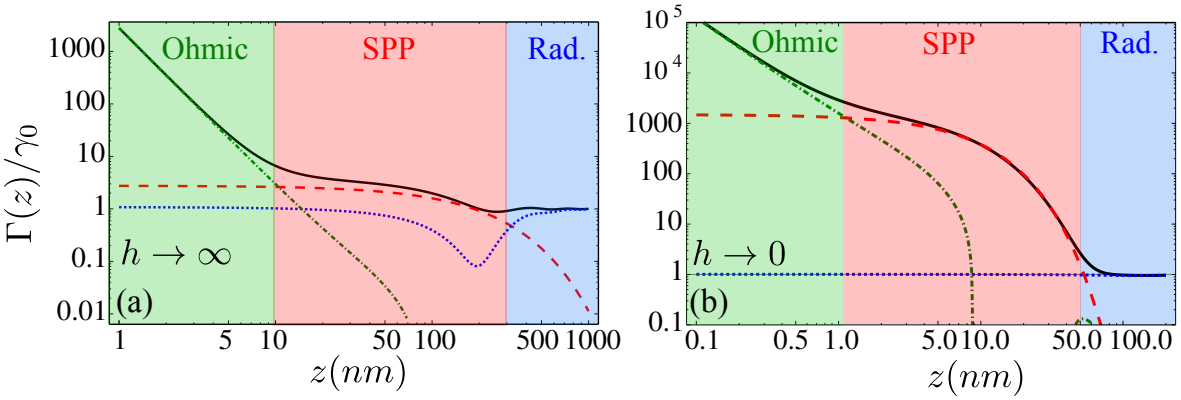

Figure 6.3: (a) Total decay rate Γ/γ_0 (solid black) for a QE with frequency $\omega_0 = 2eV$ as a function of its distance z to a thick metal film ($h \to \infty$) , together with the contribution of the three different channels: radiative (dotted blue), SPP (dashed red) and ohmic losses (dashed-dotted green). (b) Same as in panel (b) for a thin metal film ($h \to 0$).

Regarding the comparison between the thick and thin film limits, two main features can be observed due to the aforementioned higher confinement of the field as h decreases. First, the Purcell ratios available are two orders of magnitude higher in the limit of $h \to 0$. Moreover, the distances to observe surface-related effects are less than 50 nm in the thin film limit due shorter penetration length of the electric field in the dielectric.

Some initial works in the field identified the regions where the SPP contribution dominates (in red) with the regions of SC [63, 210]. However there are reasons that prevent this identification. Firstly, it should be emphasized that all these semi-classical calculations have been made by using the Fermi golden rule [36, 58]. This approach is based on a second order perturbation theory, neglecting any back-action of the bath into the QE system, implying then unambiguously an irreversible decay dynamic of the QE population. Thus, this formalism is not suitable to set the conditions where SC or reversible dynamics between QE and the SPP bath occurs.

The second bottleneck appears in the separation of the contributions of the non-radiative modes. As it was pointed out, this separation is only valid if $\mathrm{Im}\{\epsilon_m(\omega)\} \approx 0$, which is not satisfied in the frequency region close to the cut-off frequency ω_{cut}. The SPP losses are so big that plasmons are overdamped –propagating less than its wavelength– and the SPP resonance is not well-defined. Consequently, at these frequency region, which can be important in the study of reversibility, all the evanescent part of the fields should be taken into account as a whole. In the next Section, we will show how to do the proper treatment of these surface lossy modes in a self-consistent formalism that is able to deal with all frequency ranges.

6.2.2 Theoretical quantum framework.

In the previous Section, some difficulties due the complex dielectric function $\epsilon_m(\omega)$ in metallic systems have been highlighted. Its imaginary part takes into account the dissipation in metals and is responsible for the finite propagation length of the SPP field in the surface. In the regions where the losses are not so big, the SPP contribution can be separated from pure losses and even a canonical quantization of the SPP field can be performed [211, 212]. The

inclusion, a posteriori, of the the losses can then be done within a master equation theory [213] (more details in this Chapter).

However, a proper quantization with a complex permitivity is not a trivial issue as Maxwell equations cannot be obtained from a Lagrangian in this case. Thus a straightforward canonical quantization is not possible. The alternative is to assume that dissipation is linear and that it can be modeled by coupling the EM field of the SPPs to an additional bath of harmonic oscillators, which represents the ohmic losses. Importantly, the system and bath can be cast to a *total* Lagrangian and consequently this allows the quantization of the EM field in dispersive media [214].

To apply this quantization to complex geometries, the theory can be conveniently reformulated in terms of the Green's tensor of the classical problem [215–217]. The usefulness of this approach can be appreciated by looking at a key result, the quantum expansion of the electric field:

$$\vec{E}(\vec{r},\omega) = i\sqrt{\frac{\hbar}{\pi\epsilon_0}}\frac{\omega^2}{c^2}\int d^3\vec{r}_1\sqrt{\mathrm{Im}[\epsilon_m(\omega)]}\hat{\mathbf{G}}(\vec{r},\vec{r}_1,\omega)\vec{f}(\vec{r}_1,\omega)\,. \tag{6.16}$$

Here, the electric field can be expanded in normal modes where the coefficients are given by the Green's function of the classical field. These normal modes of the combined EM field *and* the dispersive media are represented by the bosonic creation (annihilation) operators $\vec{f}^{\dagger}(\vec{r},\omega)$ $(\vec{f}(\vec{r},\omega))$. Due to the dispersive character of the media, the resulting combined SPP+losses operators have to be space and frequency dependent $\vec{f}(\vec{r'},\omega)$. They obey the commutation relation $\left[\vec{f}(\vec{r},\omega),\, \vec{f}^{\dagger}(\vec{r}_1,\omega_1)\right] = \delta(\omega-\omega_1)\,\delta(\vec{r}-\vec{r}_1)$. We use ϵ_0 to denote the vacuum permittivity and c the speed of light. Finally, $\hat{\mathbf{G}}(\vec{r},\vec{r}_1,\omega)$ is the dyadic Green's function of the classical field defined as [58]

$$\left[\nabla\times\nabla\times-\frac{\omega^2}{c^2}\epsilon_m(\omega)\right]\hat{\mathbf{G}}(\vec{r},\vec{r}_1,\omega) = \mathbf{I}\,\delta(\vec{r}-\vec{r}_1)\,. \tag{6.17}$$

Therefore, within this formalism the quantum fields Eq. (6.16) are determined by the classical Green's function, Eq. (6.17). The Green's tensor also has the following interesting property:

$$\int d^3\vec{x}\mathrm{Im}[\epsilon_m(\omega)]\hat{\mathbf{G}}(\vec{r},\vec{x},\omega)\hat{\mathbf{G}}^*(\vec{x},\vec{r}_1,\omega) = \mathrm{Im}[\hat{\mathbf{G}}(\vec{r},\vec{r}_1,\omega)] \tag{6.18}$$

that is useful for calculations. The dispersive field hamiltonian is then given by :

$$H_f = \int d^3\vec{r}\int_0^{\infty} d\omega\,\omega\,\vec{\hat{f}}^{\dagger}(\vec{r},\omega)\cdot\vec{f}(\vec{r},\omega)\,. \tag{6.19}$$

In order to define the interacting hamiltonian between a quantum emitter and the dispersive electromagnetic field, it is useful to divide the electric field in the real space: $\vec{E}(\vec{r}) = \vec{E}^{-}(r) + \vec{E}^{+}(\vec{r})$. Here, $\vec{E}^{\pm}(\vec{r})$ represents the annihilation/creation operator that is defined by;

$$\vec{E}(\vec{r}) = \int_0^{\infty} d\omega\vec{E}(\vec{r},\omega)\,, \tag{6.20}$$

where $\vec{E}(\vec{r},\omega)$ has been already defined in Eq. 6.16. With this definition, the interaction Hamiltonian between the quantum emitter and the electromagnetic field in the dielectric-absorbing medium interface becomes:

$$H_{\text{int}} = -\vec{\mu}\cdot\vec{E}(\vec{r}_0,\omega)\sigma^\dagger + \text{h.c.}\,, \tag{6.21}$$

where $\vec{r}_0 = (\vec{R}_0, z_0)$ is the position of the QE. With this hamiltonian, the dynamic of the problem is fully determined. However, the complicated functional form of the $\vec{f}(\vec{r},\omega)$ makes them operationally difficult to deal with, limiting its applicability to simple problems.

6.2.3 Characterization of Strong-Coupling.

6.2.3.1 Wigner-Weisskopff approach: spectral densities.

Once we have introduced the theoretical quantum framework to deal with absorbing media, the goal of this Section is to study the possibility of finding reversible dynamics between the QE and the SPP modes. A standard approach to define the regions of reversibility is to study the so-called *Wigner-Weisskopf* problem, already sketched in Chapter 2. First, the QE is assumed to be initially in its excited state, $|e,0_\omega\rangle$, and only subject to the interaction with the bath. Then, if the emitter decays irreversibly, the system is said to be in weak-coupling (WC). In the case some reversibility appears (manifested in oscillations in the excited state population), the system is said to be strong-coupling (SC) or subject to a non-markovian decay [1].

Let us consider the Wigner-Weisskopf problem for the complete Hamiltonian given by: $H = H_0 + H_f + H_{\text{int}}$. As a result of the rotating-wave approximation, it conserves the number of excitations, the overall-system state ansatz:

$$|\Psi(t)\rangle = C_e(t)\,|e,0_\omega\rangle + \int d^3\vec{r}\int d\omega C_1(\vec{r},\omega,t)\,\left|g,1_{\vec{r},\omega}\right\rangle\,, \tag{6.22}$$

where $\vec{f}^{(\dagger)}(\vec{r},\omega)\,|g,0_\omega\rangle = \left|g,1_{\vec{r},\omega}\right\rangle$. Using the non-local operators $\vec{f}^{(\dagger)}(\vec{r},\omega)$ of Section 6.2.2 and the expression 6.18 it is straightforward to arrive to the following integro-differential equation for $C_e(t)$:

$$\dot{C}_e(t) = -\int_0^t K(t-t_1)C_e(t_1)dt_1\,, \tag{6.23}$$

with the initial condition $C_e(0) = 1$ and being the excited state population $n_\sigma(t) = |C_e(t)|^2$. The so-called kernel of this integro-differential equation is given by:

$$K(\tau;z_0) = \int_0^\infty d\omega J(\omega;z_0)e^{i(\omega_0-\omega)\tau}\,, \tag{6.24}$$

[1] The naming of these oscillations appearing due to the interaction with structured reservoirs is not unified within the literature. In this Chapter, we use the terms reversible dynamics, strong-coupling or non-markovian decay interchangeably.

where $J(\omega; z_0)$ is the so-called *spectral density* of the metal-dielectric system, which is obtained from the *total* Green function of the system:

$$J(\omega; z_0) = \frac{\omega^2}{\pi\epsilon_0 c^2}\vec{\mu}\cdot \mathrm{Im}[\hat{\mathbf{G}}^*(\vec{r}_0, \vec{r}_0, \omega)]\cdot\vec{\mu}\,. \tag{6.25}$$

The spectral density contains information of both the coupling, $g(\omega)$, and the density of modes of the bath, $\rho(\omega)$, which determines the whole dynamics of the system. When it is *smooth* enough around ω_0, one can approximate in Eq. 6.24 $J(\omega; z_0) \approx J(\omega_0; z_0)$ and then:

$$K(\tau; z_0) \approx \frac{\Gamma(\omega_0)}{2}\delta(\tau) + i\mathrm{P.V.}\int_0^\infty d\omega J(\omega; z_0)e^{i(\omega_0-\omega)\tau}\,, \tag{6.26}$$

with $\Gamma(\omega_0) = 2\pi J(\omega_0)$. Then, it is straightforward to integrate the integro-differential equation arriving to an irreversible exponential decay of the excited state population of the QE $n_\sigma(t) = e^{-\Gamma(\omega_0)t}$. The principal value part gives the well-known *Lamb-shift* of the QE energy and it is irrelevant for the discussion of this Chapter, we embed it in the definition of ω_0. Assumming the $J(\omega)$ to be smooth is related to the so-called *Born-Markov* approximation [25], which consists of neglecting any memory effect from the bath. This approximation is also implicit in the use of the Fermi Golden rule, so that all the approaches give formally the same results in this limit. However, in order to be fully sure that this condition is satisfied, one should integrate exactly the integro-differential equation. Before going into the complete problem metal-dielectic problem, let us review a particularly relevant example that helps to understand subsequent results.

- **A case of common interest: pseudo-mode spectral density.**

  In this Section we study a simplified problem but insightful problem. Let us assume that the QE interacts with a bath with the same coupling constant at all frequencies, namely g, and whose density of modes is peaked at frequency ω_a with a Lorentzian profile of width γ_a. The spectral density,$J(\omega) = g^2(\omega)\rho(\omega)$, of the bath reads:

$$J_{pm}(\omega) = \frac{g^2}{\pi}\frac{\gamma_a/2}{(\gamma_a/2)^2 + (\omega-\omega_a)^2}\,. \tag{6.27}$$

  This equation describes the spectral density of the so-called pseudo-mode, that describes e.g. the physics of the coupling to a cavity mode. The spectral density energy dispersion is given by γ_a and represents the loss rate of the pseudo-mode. The spectral density's height is directly proportional to g^2, that measures the efficiency of the coupling with the QE. The kernel in this case admits an analytical solution:

$$K_{pm}(\tau) = g^2 e^{-\gamma_a\tau/2}e^{i\Delta\tau}\,, \tag{6.28}$$

  where $\Delta = \omega_a - \omega_0$ is the detuning between the pseudo-mode and the QE energy. In this case the problem admits an analytical solution by going to the Laplace space, where the integro-differential equation can be easily integrated:

$$sC_e(s) = -K_{pm}(s)C_e(s) + 1 \rightarrow C_e(s) = \frac{1}{s + K_{pm}(s)}\,. \tag{6.29}$$

Then, it is possible to go back to the real space and find a lengthy but analytical solution for $C_e(t)$. Importantly, the behavior of the dynamics is determined by some exponentials of the form e^{iRt}, where R is the so-called Rabi frequency, which can be written as follows $R = \sqrt{g^2 - (\gamma_a + i2\Delta)^2/16}$. It can happen that the QE has some intrinsic losses which are not decaying through the pseudo-mode. Still, they can be described within this framework as follows:

$$\dot{C}_e(t) = -\int_0^t K(t - t_1)C_e(t_1)dt_1 - \frac{\gamma_\sigma}{2}C_e(t)\,, \tag{6.30}$$

then, they also appear within the Rabi frequency, which is written in its definite form:

$$R = \sqrt{g^2 - \left(\frac{\gamma_a - \gamma_\sigma + 2i\Delta}{4}\right)^2}\,. \tag{6.31}$$

Within this model, SC is usually defined at resonance [109]: when the coupling (g) is bigger than the intrinsic losses of the system (γ_a, γ_σ), $R_{\Delta=0} \in \Re$ and the system is said to be in SC. In the opposite situation, when $R_{\Delta=0}$ is purely imaginary, the system shows an irreversible decay with a modified lifetime given by:

$$\Gamma_{\mathrm{WC}}(\Delta = 0) = \gamma_\sigma + \frac{4g^2}{\gamma_a}\,. \tag{6.32}$$

When the two modes are out of resonance, i.e., $\Delta \neq 0$, SC is not well defined. In this case, there is always be some $\mathrm{Re}R \neq 0$, which yields some oscillatory behavior in the population. The visibility of the oscillations depends of both the losses and the detuning. The intrinsic losses of the modes, which damp the oscillations, set the time scale ($\gamma_a^{-1}, \gamma_\sigma^{-1}$) at which these oscillations are visible. Nevertheless, even in the absence of losses the visibility of the oscillations is attenuated by the detuning. In fact, an analytical expression for the visibility can also be obtained:

$$\mathrm{V} = \frac{1}{1 + \left(\frac{\Delta}{\sqrt{2}g}\right)^2}\,, \tag{6.33}$$

which can be controlled through the ratio $\Delta/\sqrt{2}g$. The meaning of this visibility parameter is very intuitive as it basically corresponds to the amplitude of the oscillations of the populations, i.e., when $\mathrm{V} = 1$ the system exhibits complete oscillations from 0 to 1.

As a last remark, we would like to emphasize that there is an implicit assumption in the starting interaction hamiltonian that sets a limit to the validity of these results. In the interaction hamiltonian from Eq. 6.21, the counter-rotating terms appearing in the

dipolar coupling have been neglected. This can be done as long as the coupling constant satisfies: $g \ll \omega_0 + \omega_a$, usually named as *Rotating Wave Approximation* [25]. When g is comparable to these magnitudes, new effects appear due to the counter-rotating terms [218], which start to be noticeable approximately when $g \gtrsim 0.1\omega_0$.

- **Spectral densities for the thick and thin metal film.**

  Let us now focus on the system of interest: a QE interacting with the mode(s) appearing at the metal-dielectric interface. From the general expression of the spectral density of Eq. 6.25 and Green's functions obtained in Section 6.2.2 for the thick and thin metal film limits, it is straightforward to get the spectral density of the *complete* bath. In Fig. 6.4, the spectral densities of the two limits are plotted for different QE separations to the interface, z. Some useful information can be extracted for this plot:

  - In both cases the spectral density is peaked around ω_{cut} (around 3.55 eV for the $\epsilon_d = 1$ chosen). At these frequencies, the energy dispersion relationship is almost flat which leads to a high-density of modes at the surface. This high-density of modes makes that in spite of being extremely lossy modes, they still play a relevant role for the possible observation of reversible dynamics. The intuitive picture is that their slow group velocity allows them to interact with the QE before propagating far from it.
  - For both limits (thin and thick metal films), there are three effects that appear when the separation of the QE to the surface increases: firstly, the maximum of the peak moves to lower frequencies, which is favorable for the observation of SC as QEs energies usually lie in the optical regime (around 2 eV). However, two harnessing effects appear at the same time: the bigger spreading of energies increases and the height of the peak decreases.
  - Finally, by comparing the thick and thin films one can see that the spectral density is one order of magnitude higher in the film limit than for the thick film. However, thin films also result in a bigger spectral width, yielding a higher loss rate. The smallest dispersions in energies appear at small separations from the surface, and are of the order of approximately 0.1 eV and $0.5eV$ for the thick and thin film limit respectively.

The next step is to separate the different contributions to the spectral density as we did in Section 6.2.1.4. It is possible to isolate the radiative contribution by taking only the contribution of the traveling modes in the k-integral contributing to the complete spectral density. By doing so, it is obtained a background to the total spectral density, $J_{rad}(\omega) \propto \omega^3$. Thus, the peak structure stems solely from the surface evanescent modes, that we denote as $J_{nr}(\omega)$. Unfortunately, the SPP contribution can not be extracted from the plasmon pole approximation, as it fails for the relevant frequencies close to the cut-off, ω_{cut}. Therefore, in order to be consistent one should not divide the contribution from the evanescent mode, but just consider them as a whole[1].

[1] Only, when the frequency region close to the cut-off is not important, which happens for big enough separations z, the separation of the SPP contribution from $J_{nr}(\omega)$ can be made.

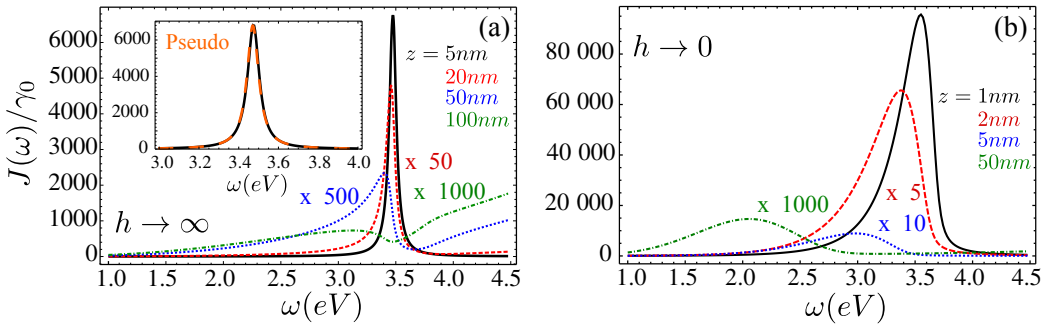

Figure 6.4: (a) Total spectral density for a thick metal film a dielectric $\epsilon_d = 1$ and dipole frequency ω_0 for four different separations z to the metal surface. Inset: Fitting to a pseudo-mode spectral density for the $z = 5nm$. (b) Same as in (a) for the thin film limit.

As a last remark, let us highlight that the thick film limit and small distances, $k_0 z << 1$, the non-radiative spectral density can be accurately approximated by the one of a pseudo-mode: $J_{nr}(\omega) \approx J_{pm}(\omega)$, as shown in the inset of Fig. 6.4(a). From this fitting, one can extract the parameters (g, γ_a) to study the conditions of reversibility as explained in the last subsection. The background of radiative modes is responsible of a finite modified lifetime, γ_σ, for the QE. For the thin-film limit there is an asymmetry at the cut-off frequency that makes the fitting not very accurate. However, the kernel is very similar to the one of a pseudo-mode of Eq. 6.28 and an approximate extraction of the parameters can be made.

6.2.3.2 Analysis of the dynamics.

As mentioned in the introduction of this Chapter, the have been several approaches to study reversibility in single QE-SPP system that always relied in important approximations. In a first approach, the SC conditions for the one-dimensional SPP modes of cylindrical waveguides [63, 210] were defined based on a separation of the different contributions as we showed in Section 6.2.2. According to their criterion, the system operates in SC as long as $\Gamma_{\rm spp} > \Gamma_{\rm rad} + \Gamma_{\rm rad}$. However, from a straightforward analysis of the Wigner-Weisskopff theory, it is easy to prove that this criterion flaws: the dynamics is fully determined by the Γ's only if the dynamics is irreversible. More accurate approaches, taking into account the whole frequency range appeared [219]. They assume $\mathrm{Im}[\epsilon_m(\omega)] = 0$, and do the full integration of the dynamics. However, this assumption is quite relevant as they are taking out one of the fundamental ingredients in metallic systems. In a first attempt, we used the the full spectral density[220], but using an approximated method, (Time-Convolutionless approach), for the numerical integration of the master-equation. The time-convolutionless method [25] consists of transforming the integro-differential equation into a set of linear differential equations that are straightforwardly solved.

In this Section, we perform a more complete approach for these kind of systems. The analysis relies only in one reasonable assumption, that is to separate the radiative background from the contribution of the evanescent modes. The radiative modes give a certain modified lifetime to the emitter, $\gamma_\sigma = 2\pi J_{rad}(\omega_0)$. The peak structure from the surface modes is the only possible source of reversibility of the system and can not be treated perturbatively

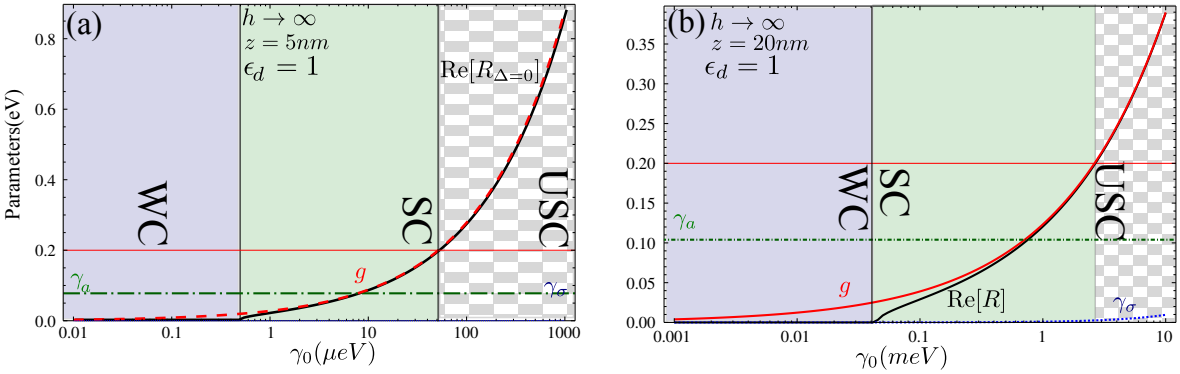

Figure 6.5: (a) & (b) Coupling and losses parameters extracted from a pseudo-mode approximation for a dipole with $\omega_0 = 2\,eV$, embedded in a dielectric with $\epsilon_d = 1$ and with separations $z = 5\,nm$ and $20\,nm$ respectively. The real part of the Rabi frequency is also plotted in solid black to identify the regions of WC, SC and USC.

if the emergence of SC is to be studied. The integro-differential equation obtained from Eq. 6.23 obtained and this assumptions is:

$$\dot{C}_e(t) = -\int_0^t K_{nr}(t-t_1)C_e(t_1)dt_1 - \frac{\gamma_\sigma}{2}C_e(t)\,. \tag{6.34}$$

The solution of this Equation and the observation or not of oscillations is the only way of determining the emergence of reversibility. However, in order to give a more visual estimate of the regions of SC, in terms of the parameters of the system (e.g., γ_0 or z), we make use of the fact that in most of the regions of interest, the non-radiative spectral density, $J_{nr}(\omega)$, or its kernel, can be very well fitted to the one of a pseudo-mode. From this fitting, we are able to extract g, γ_a, which together with γ_σ, allowing us to define a SC criterion in terms of the Rabi frequency defined in Eq. 6.32.

Thick film limit. In Fig. 6.5, the situation for a dielectric with $\epsilon_d = 1$ and a QE with two different separations ($z = 5\,nm$, $20\,nm$) from the metal surface is analyzed. In panels (a)-(b), the evolution of the relevant parameters for SC: g, γ_a, γ_σ, extracted from the pseudo-mode approximation is plotted. Also the real part of the Rabi frequency (in resonance) is shown in solid black line, as it is good criterion for determining the onset of SC. Notice that a third region has also been included characterized by the values of $g \gtrsim 0.1\omega_0$. This region corresponds to a set of parameters in which the rotating wave approximation implicit in the starting Hamiltonian is not valid. In order to describe properly this region, usually named as ultra SC (USC), one should include the counter-rotating terms before obtaining the integro-differential equation. Even though this limit is a noteworthy limit that should be explored, it is beyond the scope of this Thesis. Thus, for the numerical integration of Eq. 6.34 we restrict ourselves only to regions where our formalism is still adequate.

Panel 6.5(a) corresponds to a situation where $z = 5\,nm$. Due to the high enhancement of the field at this distance, the γ_0's where SC emerges are of the order of μeV, which is within the state-of-art of current QE parameters. In fact, it quickly reaches the USC region where our description is not valid. For $z = 20\,nm$, we already showed in Fig. 6.4(a), that the

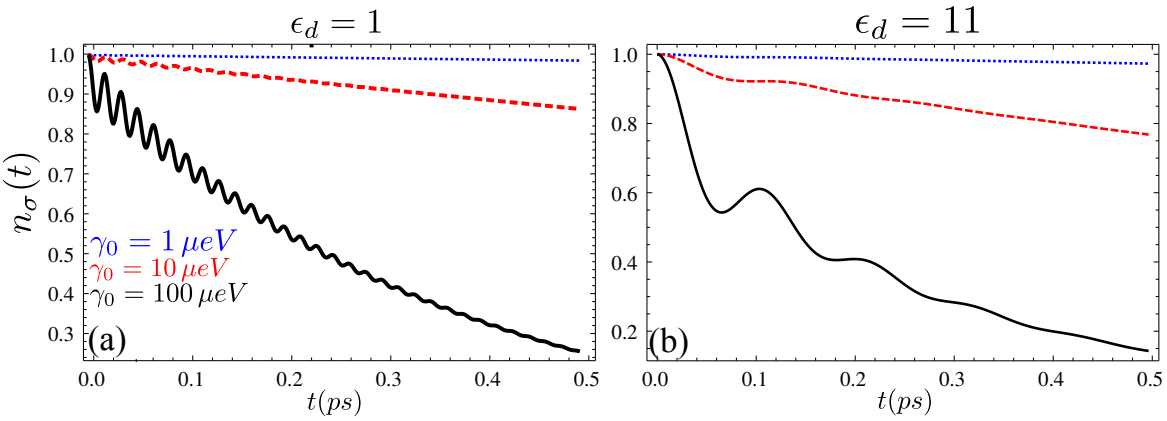

Figure 6.6: Panel (a): Dynamics of the excited state QE population, with $z = 5\,nm$, embedded in a dielectric with $\epsilon_d = 1$ in front of a thick metal film for different γ_0's as specified in the legend. Panel (b): Same as in panel (a), but for a dielectric with $\epsilon_d = 11$.

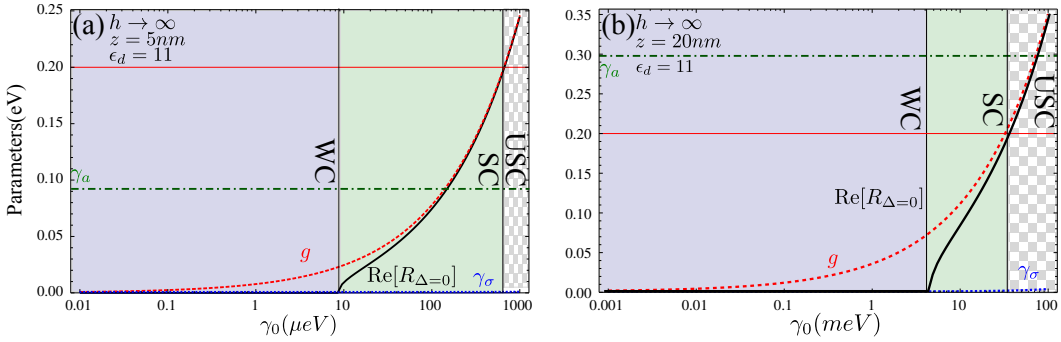

Figure 6.7: (a) & (b) Coupling, losses parameters extracted from a pseudo-mode approximation for a dipole with $\omega_0 = 2\,eV$, with separation $z = 5\,nm$ and a dielectric $\epsilon_d = 11$. The real part of the Rabi frequency is also plotted in solid black to identify the regions of WC, SC and USC.

spectral density is around two order of magnitude smaller. Thus, the SC emerges for higher values of γ_0 ($> 0.1\,meV$) that start to be beyond the currently available QE parameters. In Fig. 6.6(a), we show the results of the numerical integration of Eq. 6.34 for $z = 5\,nm$ and increasing values of $\gamma_0's$. It can be observed how the visibility of the oscillations increases with γ_0, due to the increase of g. As the QE energy and the peak of the spectral density are highly detuned, the onset of the oscillations is not abrupt. The oscillations increase their visibility as g increases its value, as shown in Eq. 6.33. Due to the high detuning even in the regions of SC, the visibility of the oscillations is small.

Once we have identified the detuning as such a determinant factor to observe a reversible decay in the QE population, let us look for alternative ways to decrease it. A straightforward way of decreasing Δ, and consequently favor the observation of oscillations, is to use different QEs with higher energy. However, we can also keep fixed the QE energy and lower the cut-off energy. As we showed in Eq. 6.11 that $\omega_{cut} \propto 1/\sqrt{\epsilon_d}$, then by embedding the QE into a dielectric with higher ϵ_1, the cut-off frequency decreases and so does the energy where the plasmon peak appears in the spectral density.

As an example in Fig. 6.7 we consider the case of a dielectric with $\epsilon_d = 11$, similar to the one of Si, which yields $\omega_{cut} \approx 2.2\ eV$. Then we study the same cases ($z = 5, 20\,nm$) as in Fig. 6.5. In panels (a) and (b), we show the results from extracting the parameters from a pseudo-mode approximation. As the higher dielectric constant has the effect of damping more the electric field, the onset of SC emerges at higher γ_0's. For $z = 5nm$, they still lie into the available state of art parameter, whereas for $z = 20\,nm$ again are a bit beyond. As a consequence, the window where SC appears is even smaller than for the $\epsilon_d = 1$ case. In order to illustrate the consequences of using a higher dielectric in the visibility of the oscillations, in Fig. 6.6(b), the QE excited state population is plotted for QE-metal distance of $z = 5\,nm$. By using the same γ_0's than for the $\epsilon_d = 1$ case, we can see how the oscillations are more clearly resolved in high refractive dielectric. The main drawback is the that higher losses damp the oscillations faster than in the $\epsilon_d = 1$ situation.

Thin film limit. As explained in Section 6.2.1, decreasing the lateral size of the film induced a larger confinement of the antisymmetric mode. This can already be seen when the spectral density plotted in Fig. 6.4(b), through the observation of a higher peak than for the thick film limit case. In principle, this behavior is favorable for SC observation. The enhancement of the antisymmetric moed is done at expense of increasing its losses. This is also reflected in the larger spread of energies of the SPP peak which results in stronger dissipation in the metal.

In order to study the effect of this competition in the observation of reversible dynamics, in Fig. 6.8 we consider the case of a very thin metal layer ($h = 2\,nm$) for a fixed separation ($z = 2\,nm$) with two different dielectric surroundings: $\epsilon_d = 1$ in (a) and $\epsilon_d = 11$ in (b). For both of cases, the higher interaction strength makes the γ_0's required for SC to be lower. On the other hand, the higher losses diminish the window of γ_0's to observe SC under the rotating wave approximation . In the case of $\epsilon_d = 11$, the window is so small that it completely quenches the possibility of observing any complete oscillation (dynamics not shown) within our rotating wave approximation, only observing the deviation from the exponential decay at very small times.

From this study, one can conclude that the beneficial effect of increasing interaction achieved by decreasing the size of the film is not enough to compensate for the higher losses associated to it.

6.3 Analysis of the many emitters configuration.

In the previous Section we concluded that the observation of reversible dynamics between a single single QE and the SPPs of a two-dimensional metal-dielectric interface is very challenging. The main reason for this was that the complete evolution is governed by the coupling to all the possible k's. Morover, the one with a higher density of modes correspond the most lossy ones. Very attractive proposals are based on decreasing the size of the metallic surface by using metallic nano particles [59], combine metal structures with layered dielectrics to form the so called Tamm Plasmon [221, 222] or the use of plasmonic resonators [223].

Apart from these alternatives, which are technologically demanding, the experimental efforts have been mainly devoted to two-dimensional systems like the one treated in the previous Section, but where many QEs interact with the SPP field [67–73, 224]. The typical

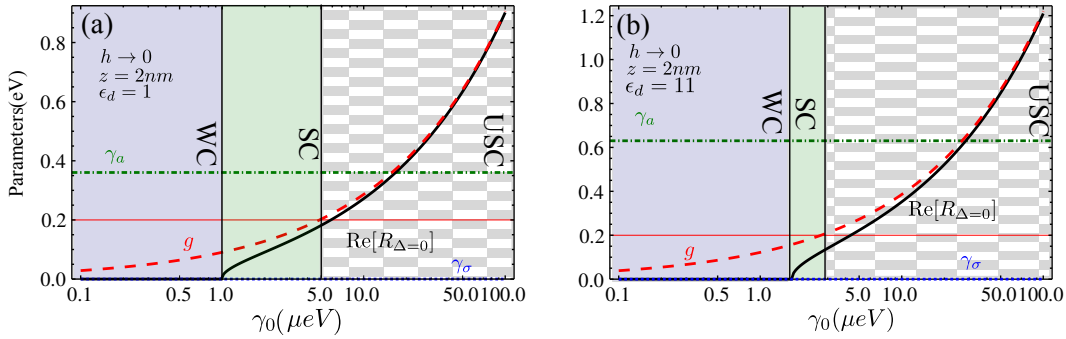

Figure 6.8: (a) & (b) Coupling, losses parameters extracted from a pseudo-mode approximation for a dipole with $\omega_0 = 2\,eV$ for a thin metal film, with separation $z = 2\,nm$ and a dielectrics $\epsilon_d = 1$ and $\epsilon_d = 11$ respectively. The real part of the Rabi frequency is also plotted in solid black to identify the regions of WC, SC and USC.

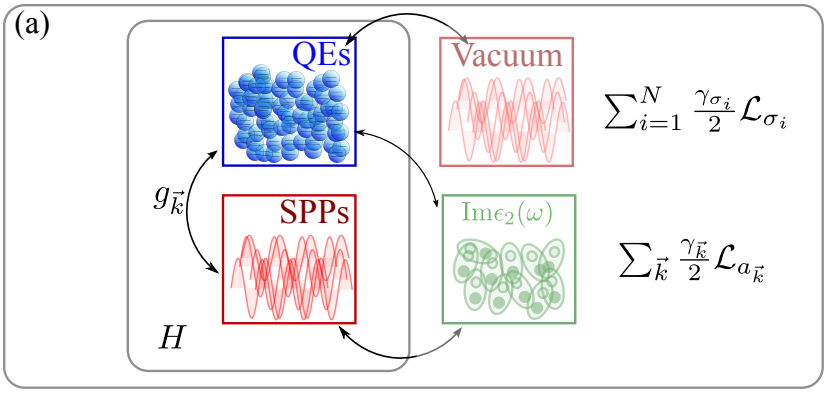

Figure 6.9: Open Quantum system perspective of the system of N emitters interacting with the SPP field of a two-dimensional metal-dielectric interface. The rest of the elements, namely the vacuum radiative modes and the ohmic modes will be treated perturbatively within a master equation descriptions.

experimental scheme is depicted in Fig. 6.1(b): a layer of thickness $\mathcal{W}$ with N QEs embedded in a given dielectric (with ϵ_2) is placed in front of a metal surface, separated by another empty layer (which can have another dielectric constant ϵ_2) to avoid quenching. For simplicity, we use a symmetric situation with $\epsilon_1 = \epsilon_2 = 1$ and, in order to reproduce the common experimental condition, a thick metal film ($h \gtrsim 40\,nm$).

The advantages of this configuration are two-fold: first, the collective coupling stems from a momentum-conservation in the QE-SPP interaction. This selection rule imposes a one-to-one coupling between the QE and the SPP having the same momentum. Secondly, the collective coupling benefits from the well-known $\sqrt{N}$ factor appearing when N 2LS are interacting with a common mode. During this Chapter, we are mainly interested in the optical regime, where the energy of the QEs is around 2 eV. This corresponds to a region where $\mathrm{Im}\{\epsilon_m(\omega)\} \approx 0$. This allows us to separate the contributions to $J(\omega)$ that we were not able to do in the previous Section. This separation allows us to adopt a open quantum system perspective, like the one sketched in Fig. 6.9, to deal with this problem.

We presented in Section 6.2.1 that when a QE is placed in the vicinity of a metal surface, it can decay into three different channels [225]: excitation of SPPs that propagate along the metal surface, radiation of photons into the far field and dissipation through ohmic losses in the metal. In the optical regime, the ohmic dissipative bath and vacuum radiative modes can be considered as a perturbation to the QE-SPP dynamics. Their effect is basically to induce a modified lifetime for the QE and SPP. Therefore, it is useful to adopt an open quantum system perspective which consists of treating these two elements perturbatively as dissipation mechanisms. The QE-SPP interaction, however, is treated within a hamiltonian description. During this Section, we explain how to describe properly metallic systems within this approach and detail the results that can be obtained from it.

6.3.1 Theoretical framework: the open quantum system approach.

Following the ideas sketched before, we detail how to adopt an open quantum system perspective for metallic system. This approach separates the complete systems into several subsystems, which in this case are: the ensemble of QEs, the ubiquitous vacuum radiative modes, the SPP bath and the ohmic losses in the metal [1].

In principle, the different baths are connected to each other as shown in Fig. 6.9 and their description can be done within a Hamiltonian description by considering the full hamiltonian of the system. However, the large number of degrees of freedom that one needs to take into account makes this approach intractable. Moreover, our main interest is the possibility of observing reversible evolution between the QE ensemble and the SPP. Thus, this is the kind of situations is where the open quantum system formalism appears to be very useful. Following the steps of Chapter 2: we consider the combined QEs and SPPs subsystems as the system of interest, and the rest of the baths ware treated perturbatively. The former will be described within a hamiltonian description, whereas the latter will be traced out and its information will be included in the formalism through the appropriate Lindblad terms.

6.3.1.1 Hamiltonian description.

This Section is devoted to establishing the hamiltonian description of the system of interest: QEs+SPPs. The ensemble of QEs will be modeled as a a collection of N 2LS embedded in a dielectric host of thickness $\mathcal{W}$ that is placed on top of the metal surface. A spacer layer (thickness s) is placed between the dielectric host and the metal surface. To resemble the typical experimental configuration, the volume distribution of QEs is assumed to be distributed in N_L layers with N_s QEs each ($N = N_L \times N_s$), such that their positions are defined by $\vec{r}_i = (\vec{R}_i, z_i)$, with $i = 1, ..., N$. Assuming the same transition frequency for all the emitters, $\omega_i = \omega_0$, the Hamiltonian for the N QEs reads:

$$H_0^N = \sum_{j=1}^{N_L} \sum_{i=1}^{N_s} \omega_0 \sigma_{i,j}^\dagger \sigma_{i,j} \,. \tag{6.35}$$

Assuming that $\mathrm{Im}\{\epsilon_m(\omega)\} \approx 0$, the two-dimensional SPP field can be quantized by using the standard procedure of canonical quantization reviewed in Chapter 2, now applied for 2D

[1] This separation into different subsystems can be done here because in the optical regime $\mathrm{Im}\{\epsilon_m(\omega_0)\} \approx 0$. This is sufficient condition which justifies the separation of the ohmic losses and the SPPs.

fields. The normal modes of Maxwell equations are found for a quantization area A and then replaced by the creation and destruction operators of the 2D EM field, $a_{\vec{k}}$ and $a^{\dagger}_{\vec{k}}$, where $\vec{k}$ indicates the in-plane momentum of the EM field. This procedure leads to the following expression for the quantized EM field [211, 212, 226]:

$$\vec{E}(\vec{R}) = \sum_{\vec{k}} \sqrt{\frac{\omega(\vec{k})}{2\epsilon_0 A}} \vec{u}_{\vec{k}}(z) a_{\vec{k}} e^{i\vec{k}\cdot\vec{R}}\,, \tag{6.36}$$

where the vector $\vec{u}_{\vec{k}}(z)$ is given by:

$$\vec{u}_{\vec{k}}(z) = \frac{1}{\sqrt{L(\vec{k})}} e^{-k_z z}\big(\hat{u}_{\vec{k}} + i\frac{|\vec{k}|}{k_z}\hat{u}_z\big)\,. \tag{6.37}$$

Here, $\hat{u}_z$ ($\hat{u}_{\vec{k}}$) is the unit vector in the z (in-plane) direction and k_z is the vertical component of the momentum in the dielectric medium, $k_z = \sqrt{k^2 - \epsilon_d k_0^2}$, with $k_0 = \omega/c$. $L[\vec{k}(\omega)]$ is the "effective length" of the mode, that is chosen so that the EM energy of the mode is normalized [211, 212]:

$$L[\vec{k}(\omega)] = \frac{\pi}{2}\frac{\epsilon_m(\omega) - \epsilon_d}{\sqrt{\epsilon_d \epsilon_m(\omega)}|\vec{k}(\omega)|}\left[\epsilon_m(\omega) + \epsilon_d\big(1 + \omega\frac{d\epsilon_m(\omega)}{d\omega}\big)\right]\,. \tag{6.38}$$

The Hamiltonian of the quantized SPP field is then given:

$$H_{EM} = \sum_{\vec{k}} \omega(\vec{k}) a^{\dagger}_{\vec{k}} a_{\vec{k}}\,, \tag{6.39}$$

where $\omega(\vec{k}) = \omega(k)$ represents the dispersion relationship of the SPP field.

The interaction Hamiltonian is obtained from the classical EM interaction energy between the dipole moment of the ensemble of QEs, $\vec{\mu}(\vec{r}) = \sum_{j=1}^{N_L}\sum_{i=1}^{N_s} \vec{\mu}_i \delta(\vec{R} - \vec{R}_i)\delta(z - z_j)(\sigma_{i,j} + \sigma^{\dagger}_{i,j})$, and the 2D EM field:

$$H_{int} = \int d\vec{r}\vec{\mu}(\vec{r}) \cdot \vec{E}(\vec{r})\,. \tag{6.40}$$

Making use of the expression of the quantized SPP field (Eq. 6.36), the following Hamiltonian for the dipolar interaction is obtained within the rotating wave approximation ($g_{\vec{\mu}}(\vec{k}) \ll \omega_0, \omega(\vec{k})$):

$$H^N_{int} = \sum_{\vec{k}}\sum_{j=1}^{N_L}\sum_{i=1}^{N_s} \frac{g_{\vec{\mu}}(\vec{k}; z_j)}{\sqrt{A}}\big(a_{\vec{k}}\sigma^{\dagger}_{i,j} e^{i\vec{k}\cdot\vec{R}_i} + a^{\dagger}_{\vec{k}}\sigma_{i,j} e^{-i\vec{k}\cdot\vec{R}_i}\big)\,, \tag{6.41}$$

where the coupling constant is now given by:

$$g_{\vec{\mu}}(\vec{k}; z_j) = \sqrt{\frac{\omega(\vec{k})}{2\epsilon_0 L(\vec{k})}} e^{-k_z z_j}\,\vec{\mu}\cdot\big(\hat{u}_{\vec{k}} + i\frac{|\vec{k}|}{k_z}\hat{u_z}\big)\,. \tag{6.42}$$

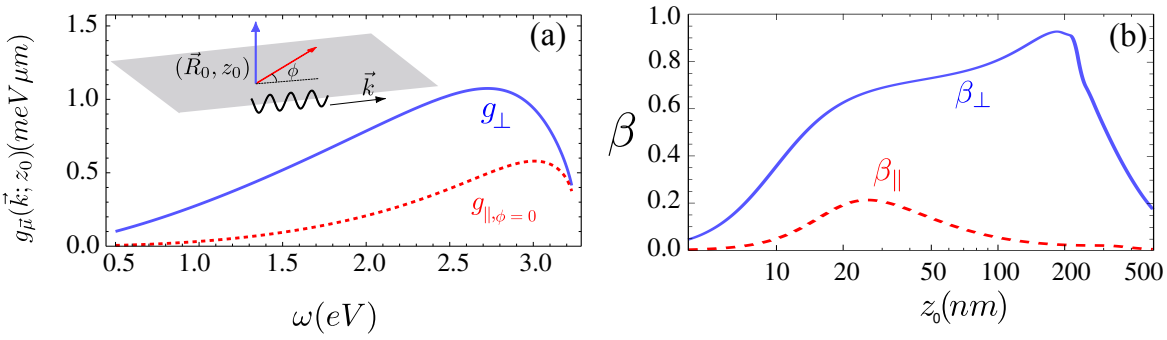

Figure 6.10: Panel (a): Coupling constant, $g_{\vec{\mu}}(\vec{k}; z_0)$, for a single QE with perpendicular (solid blue) and parallel (red dashed) orientations (see upper left inset), placed at $z_0 = 20$nm and interacting with a SPP of momentum $\vec{k}(\omega)$. Panel (b): β-factor as a function of z_0 for perpendicular (solid blue) and parallel (red dashed) orientations of the QE-dipole.

The dependence of $g_{\vec{\mu};z_j}$ with z_j is dictated by the decay length of the SPP in the z-direction via k_z. In Fig. 6.10, we plot the evolution of $g_{\vec{\mu}}(\vec{k}; z_0)$ with frequency for two possible orientations of the dipole: parallel to the momentum $\vec{k}$ and perpendicular to the metal surface. In both cases, these couplings are evaluated for QEs characterized by $\gamma_0 = 0.1$meV, which is a typical value for the QEs used in the experiments [67–73, 224]. As shown in Fig. 6.10, the coupling constant between the QE and the SPP mode is larger for the perpendicular orientation, as k_z is always smaller than $|\vec{k}|$. The so-called β-factor (the fraction of the radiation emitted by the QE that goes to the SPP modes) is also larger for the perpendicular orientation [see panel (b) of Fig. 6.10]. However, it is important to note that $g_{\vec{\mu};z_j}$ is maximum at $z_j = 0$ [see Eq. 6.42] instead of being where β is maximum.

The complete hamiltonian for the system can then be written as:

$$H^N = \sum_{j=1}^{N_L}\sum_{i=1}^{N_s} \omega_0 \sigma_{i,j}^\dagger \sigma_{i,j} + \sum_{\vec{k}} \omega(\vec{k}) a_{\vec{k}}^\dagger a_{\vec{k}} + \sum_{\vec{k}}\sum_{j=1}^{N_L}\sum_{i=1}^{N_s} \frac{g_{\vec{\mu}}(\vec{k}; z_j)}{\sqrt{A}} \left(a_{\vec{k}} \sigma_{i,j}^\dagger e^{i\vec{k}\cdot\vec{R}_i} + a_{\vec{k}}^\dagger \sigma_{i,j} e^{-i\vec{k}\cdot\vec{R}_i} \right). \tag{6.43}$$

From the structure of the interaction part of this hamiltonian, a collective mode of the N_s emitters in each j-layer can be written:

$$D_{j,\vec{q}}^\dagger = \frac{1}{\sqrt{N_s}} \sum_{i=1}^{N_s} \sigma_{i,j}^\dagger e^{i\vec{q}\cdot\vec{R}_i}. \tag{6.44}$$

The inverse transformation can be obtained by making use of the relation: $\sum_{\vec{q}} e^{i\vec{q}\cdot(\vec{R}_i - \vec{R}_j)} = N_s \delta_{ij}$, yielding the following expression for the $\sigma_{i,j}$ operators:

$$\sigma_{i,j}^\dagger = \frac{1}{\sqrt{N_s}} \sum_{\vec{q}} D_{j,\vec{q}}^\dagger e^{-i\vec{q}\cdot\vec{R}_i}. \tag{6.45}$$

In terms of these new collective mode operators $D_{j,\vec{q}}$, the interaction Hamiltonian can be

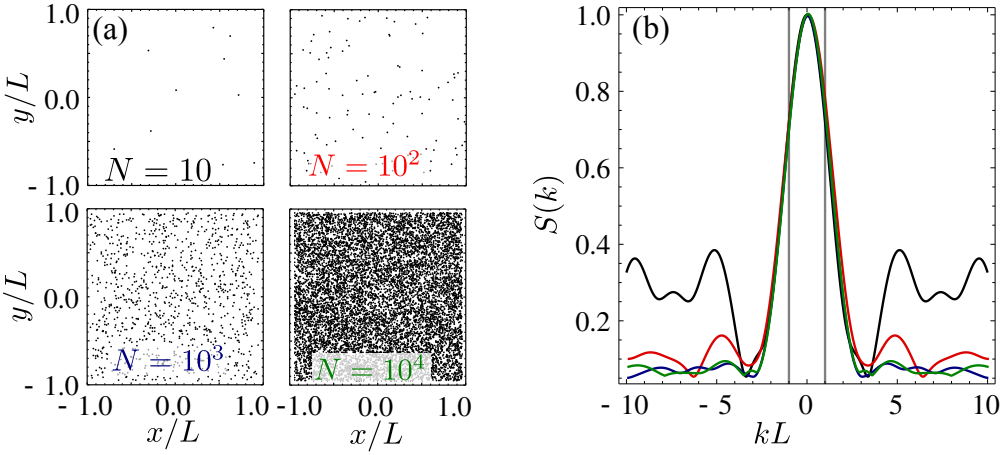

Figure 6.11: Panel (a): Randomly distributed ensembles of QEs in a two-dimensional areas $A = L^2$ with different number of QE: $N = 10, 10^2, 10^3$ and 10^4. Panel (b): Two-dimensional structure factor, $S(\vec{k} = (k,k)) = S(k)$, for the disordered distributions of QE of Panel (a). The different colors correspond to the different number of QE: $N = 10$ (black), 10^2 (red), 10^3 (blue) and 10^4 (green).

written as:

$$H_{int}^{N} = \sum_{\vec{k},\vec{q}} \sum_{j=1}^{N_L} \sum_{i=1}^{N_s} \frac{g_{\vec{\mu}}(\vec{k}; z_j)\sqrt{n_s}}{N_s} \left(S(\vec{k} - \vec{q}) a_{\vec{k}} D_{j,\vec{q}}^{\dagger} + \text{H.c} \right), \tag{6.46}$$

where $n_s = \frac{N_s}{A}$ is the surface density of emitters and $S(\vec{k})$ the structure factor of the distribution of QEs in each layer defined as follows: $S(\vec{k}) = \frac{1}{N_s} \sum_{i=1}^{N_s} e^{i\vec{k}\cdot\vec{R}_i}$. For the case of a completely homogeneous distributions this can be rewrite it as:

$$S(\vec{k}) = \int d\vec{r} \rho(\vec{r}) e^{i\vec{k}\cdot\vec{r}}, \tag{6.47}$$

where $\rho(\vec{r})$ represents the density of emitters. The discrete definition is recovered with $\rho(\vec{r}) = \frac{1}{N_s} \sum_i \delta(\vec{r} - \vec{R}_i)$. In the case $N \gg 1$, where the distribution of emitters can be considered homogeneous $\rho(\vec{r}) = \rho_0$, then one can obtain analytical solutions for the structure factor in terms of the Bessel function,

$$S(k) = \rho_0 \int_0^L dr J_0(kr), \tag{6.48}$$

that has an dispersion in k's: $\Delta k \propto 1/L$, with $L^2 = A$. Thus, the quantization needs to be large enough in order to ensure the k-conservation[1]. The dependence of $S(\vec{k})$, for a fixed direction $\vec{k} = (k,k)$, on the number of QEs is shown in Fig. 6.11. The numerically computed structure factor has been plotted for a random distribution of different number of QEs. For $N \gtrsim 100$ disordered QEs, the structure factor is well approximated by its homogeneous shape. The experimental conditions reported so far allow us to consider $S(\vec{k})$ to be peaked at $\vec{k} = 0$,

[1]The quantization area will be determined either by the total area of the sample, or by the laser spot area that excites the system.

i.e. $S(\vec{k}-\vec{q}) \approx \delta_{\vec{k},0}$. Within this approximation, the interaction Hamiltonian simplifies to:

$$H_{int}^{N} = \sum_{\vec{k}} \sum_{j=1}^{N_L} g_{\vec{\mu}}(\vec{k}; z_j)\sqrt{n_s}\left(a_{\vec{k}} D_{j,\vec{k}}^{\dagger} + a_{\vec{k}}^{\dagger} D_{j,\vec{k}}\right). \tag{6.49}$$

One can now define a collective mode of the whole ensemble of QEs by summing over layers:

$$D_{\vec{k}}^{\dagger} = \frac{1}{g_{\vec{\mu}}^{N}(\vec{k})} \sum_{j=1}^{N_L} g_{\vec{\mu}}(\vec{k}; z_j) D_{j,\vec{k}}^{\dagger}. \tag{6.50}$$

In order to make this transformation unitary, $g_{\vec{\mu}}^{N}(\vec{k})$ should be defined as:

$$g_{\vec{\mu}}^{N}(\vec{k}) = \sqrt{\sum_{j=1}^{N_L} |g_{\vec{\mu}}(\vec{k}, z_j)|^2}. \tag{6.51}$$

Assuming a continuum of layers in the z-direction with total thickness $\mathcal{W}$, becomes:

$$g_{\vec{\mu}}^{N}(\vec{k}) = \sqrt{n \int_{s}^{s+\mathcal{W}} \mathrm{d}z\, |g_{\vec{\mu}}(\vec{k}, z)|^2}, \tag{6.52}$$

where $n = N_s N_L/(A\mathcal{W})$ is the volume density of emitters. Finally, the total Hamiltonian for the collective mode $D^{\dagger}(\vec{k})$ can be written as $H^N = \sum_{\vec{k}} H_{\vec{k}}^{N}$, with:

$$H_{\vec{k}}^{N} = \omega_0 D_{\vec{k}}^{\dagger} D_{\vec{k}} + \omega_{\vec{k}} a_{\vec{k}}^{\dagger} a_{\vec{k}} + g_{\vec{\mu}}^{N}(\vec{k})(a_{\vec{k}} D_{\vec{k}}^{\dagger} + a_{\vec{k}}^{\dagger} D_{\vec{k}}). \tag{6.53}$$

This hamiltonian can be easily diagonalized through the following unitary transformation :

$$L_{\vec{k}} = x_{\vec{k}} D_{\vec{k}} + c_{\vec{k}} a_{\vec{k}}, \tag{6.54}$$

$$U_{\vec{k}} = -c_{\vec{k}} D_{\vec{k}} + x_{\vec{k}} a_{\vec{k}} \tag{6.55}$$

which energies will determine the energy dispersion of the dressed states of the systems, namely the QE-SPP polaritons. The amplitudes of the so-called Hopfield coefficients $|x_{\vec{k}}|^2, |c_{\vec{k}}|^2$ determine the ratio that each polariton contains of each mode. With this the hamiltonian can be rewritten:

$$H_{\vec{k}}^{N} = \sum_{\vec{k}} \omega_{LP}(\vec{k}) L_{\vec{k}}^{\dagger} L_{\vec{k}} + \omega_{UP}(\vec{k}) U_{\vec{k}}^{\dagger} U_{\vec{k}} \omega(\vec{k}). \tag{6.56}$$

The hamiltonian as written in Eq. 6.53 is one of the main results of this Section, as it allows an quantum treatment of the coherent coupling between an ensemble of N QEs and SPPs. When evaluating the coupling constant for a momentum $\vec{k}$, $g_{\vec{\mu}}^{N}(\vec{k})$, there is no need to rely on fitting parameters and it can be calculated from first principles, as shown below. Notice that this interaction conserves the total momentum of the system composed of the supermode of QEs and the SPP.

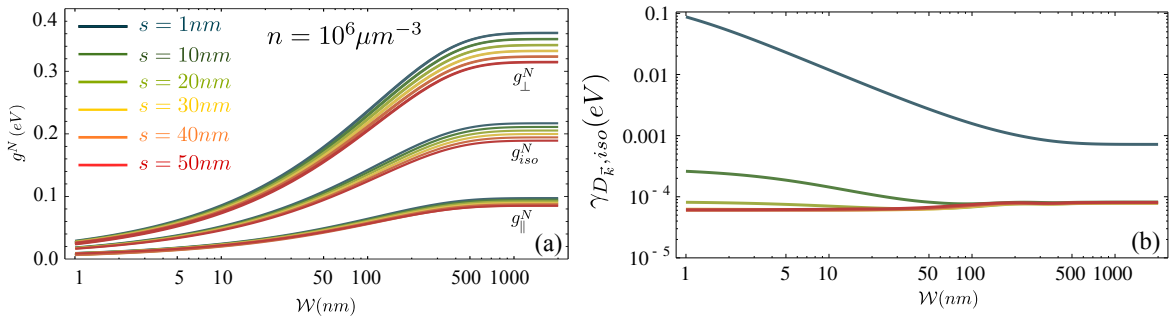

Figure 6.12: Panel (a): Coupling constant, $g^N(\mathcal{W})$, for separations s ranging from 1 to 50nm and for parallel, perpendicular and isotropic orientations of the QEs with $\gamma_0 = 0.1\ meV$. Panel (b): Collective mode losses, $\gamma_{D_{\vec{k}}}(\mathcal{W})$, for isotropic orientation of the QEs and the same parameters as Panel (a).

In order to do a quantitative analysis of the possibilities of SC in these systems, Fig. 6.12(a) shows the effective coupling constant g^N evaluated at $\vec{k}(\omega_0)$ for a density of emitters $n = 10^6 \mu\text{m}^{-3}$ (of the order of the volume densities used in the experiments) as a function of $\mathcal{W}$ and for different values of the spacer width. The coupling constant depends on the orientation of the QE dipoles. Here we render the two limiting cases (all dipoles oriented perpendicularly or parallel to the metal surface) as well as an isotropic average over these two orientations. Two main conclusions can be extracted from this figure. First, g^N depends strongly on $\mathcal{W}$ but saturates for thick enough films. This saturation is due to the exponential dependence of $g_{\vec{\mu}}$ on z, related to the spatial decay of the SPP mode, and, therefore, is determined by the dielectric environment of the metal film (ϵ_1 and ϵ_2). Second, the dependence on the widths of the spacer layer is not very strong.

Another term appearing in the experiments that should be included within the Hamiltonian description is a possible source coherent excitation. The most common experimental configurations is a coherent excitation with a laser field acting on the SPPs. The SPP in-plane momentum lies out of the light line, so it can not couple directly to the laser. Then, in order to excite them with a laser, some element should be added to take the extra momentum, e.g. a prism or some other periodical structure. It can be proven [226] that this process preserves the coherence of the laser, so that it can then be described by:

$$H^L_{\vec{k}}(t) = \Omega_{\vec{k}}(a_{\vec{k}} e^{i\omega_L t} + a^\dagger_{\vec{k}} e^{-i\omega_L t})\,, \tag{6.57}$$

in which $\Omega_{\vec{k}}$ measures the intensity of the laser field and ω_L is the operating frequency of the laser.

6.3.1.2 Reservoir description.

So far, we have focused on the Hamiltonian part of the system. In order to complete the description, the effect of the reservoirs, i.e., the vacuum radiative modes and ohmic losses of the metal, should be included within a perturbative approach. The standard approach consists of tracing out the degrees of freedom of these baths to obtain a Markovian master equation for a density matrix, $\rho(t)$, that describes the evolution of our system (QE-SPP). Following the steps described in Chapter 2, one can obtain the corresponding Lindblad operators for

each degree of freedom as depicted in Fig. 6.9. Recalling the general expression of a Lindblad term associated with operator c is $\mathcal{L}_c[\rho] = (2c\rho c^\dagger - c^\dagger c\rho - \rho c^\dagger c)$, the density matrix satisfies:

$$\dot{\rho} = i[\rho, H] + \sum_{j=1}^{N_c}\sum_{i=1}^{N_s} \frac{\gamma_\sigma(z_j)}{2}\mathcal{L}_{\sigma_{i,j}}[\rho] + \sum_{\vec{k}} \gamma_{a_k}/2\mathcal{L}_{a_{\vec{k}}}[\rho]\,. \tag{6.58}$$

Here $\mathcal{L}_\sigma[\rho]$ takes into account the QE's losses, i.e., the coupling of the QE to all EM modes other than SPPs. Thus $\gamma_\sigma(z_j) = (1-\beta(z_j))\Gamma(\omega_0)$, with $\Gamma(\omega_0)$ is the total decay rate of the system as obtained in the previous Section. In the master equation, $\mathcal{L}_{a_{\vec{k}}}[\rho]$ accounts for SPP losses and the SPP decay rate (γ_a) can be calculated from the SPP propagation length, L_{SPP}, and group velocity, v_{g} as $\gamma_{a_k} = L_{\mathrm{SPP}}/v_{\mathrm{g}}$. This SPP lifetime increases as the frequency approaches the SPP cut-off frequency, being around 30 meV for $\omega = \omega_0 = 2\ eV$.

By using the collective mode description we obtain the decay rate of the $D_{\vec{k}}$:

$$\sum_{j=1}^{N_c}\sum_{i=1}^{N_s} \frac{\gamma_\sigma(z_j)}{2}\mathcal{L}_{\sigma_{i,j}}[\rho] \to \sum_{\vec{k}} \frac{\gamma_{D_{\vec{k}}}}{2}\mathcal{L}_{D_{\vec{k}}}[\rho] + [\dots]\,, \tag{6.59}$$

where each layer contributes according to $g^N_{\vec{\mu}}(\vec{k}, z)$:

$$\gamma_{D_{\vec{k}}} = \frac{n}{|g^N_{\vec{\mu}}(\vec{k})|^2}\int_s^{s+\mathcal{W}} \mathrm{d}z\, \gamma_\sigma(z)|g^N_{\vec{\mu}}(\vec{k}, z)|^2\,. \tag{6.60}$$

6.12(b) shows this value for the case of an isotropic distribution of QEs as a function of $\mathcal{W}$ and for different spacer thickness. As a general rule, one can see that, excepting the case with $s = 1\,nm$, the value of $\gamma_{D_{\vec{k}}}$ is generally in order of γ_0, with a very small dependence on $\mathcal{W}$. This proves that this dissipative mechanism does not play a significant role as it is negligible compared with other decoherence process, e.g., SPP losses. Only in the case of a very thin spacer ($s = 1\,nm$), the $\gamma_{D_{\vec{k}}}$ acquires a considerable value due to the high decay rate into the ohmic losses. Fortunately, for thick enough layers, the average makes that this value decreases again to values below the SPP losses.

For completeness, one should be aware that due to the inhomogeneity in the coupling and $\gamma_\sigma(z_j)$ in the different layers, on top of the k-diagonal Lindblad term a new term appears in the transformation of Eq. 6.59:

$$[\dots] = \sum_{\vec{k},\vec{k}'} \frac{\gamma_{\vec{k},\vec{k}'}}{2}(2D_{\vec{k}'}\rho D^\dagger_{\vec{k}} - D^\dagger_{\vec{k}}D_{\vec{k}'}\rho - \rho D^\dagger_{\vec{k}}D_{\vec{k}'})\,. \tag{6.61}$$

This Lindblad term incoherently connects our bright state at $\vec{k}$, with the reservoir of dark states of different $\vec{k}$'s. The contribution of these dark states leads to an inhomogeneous broadening [227], that will be more important the more inhomogeneous the couplings and $\gamma_\sigma(z_j)$ are. As $|\gamma_{\vec{k},\vec{k}'}| \lesssim \gamma_{D_{\vec{k}}}$, and we have shown that this value is small compared to other energy scales in the problem, we are going to neglect this contribution of Eq. 6.61 as a first approximation to the problem. To minimize this effect, one should work with thinner QE layers, so that the couplings and decay rates are similar in all the QEs.

Finally, as most of the experiments has been done with organic molecules at room temperature, to be as close to the experimental situation, we also include in the description the

existence of vibro-rotational molecular states. These additional degrees of freedom within the QE can be incorporated into the 2LS model by means of pure dephasing mechanisms, characterized by a dephasing rate, γ_ϕ, and introduced into the master equation via also a Lindblad term, $\gamma_\phi/2\mathcal{L}_{D^\dagger_{\vec{k}}D_{\vec{k}}}[\rho]$ as shown in previous Chapters of this Thesis. For this Chapter, we take a $\gamma_\phi = 40\ meV$ [228], which is a typical value at room temperature for the organic molecules used to observe SC between N QEs and SPPs.

Finally, we introduce the incoherent counterpart of the excitation with a laser field. In some situations, the excitation is not done resonantly with a laser. Sometimes it is convenient to use an off-resonant excitation at a different $\vec{k}'$. From there, the system incoherently relaxes to the $\vec{k}$ of interest, e.g. through the $\gamma_{\vec{k},\vec{k}'}$ mechanisms. As a first approximation to the problem, let us not consider about the microscopic description of this source of excitation, but just introduce it through a phenomenological pumping rate $P_{\vec{k}}$ via an incoherent Lindblad term $\sum_{\vec{k}} P_{D_{\vec{k}}}\mathcal{L}_{D^\dagger_{\vec{k}}}[\rho]/2$.

6.3.2 Characterization of the Strong-Coupling regime.

Once we have described all the ingredients of the experiment and we have a suitable formalism that self-consistently takes into account all of them, let us identify the key elements determining the emergence of SC in QE-SPP systems.

6.3.2.1 Bosonization of the collective modes operator.

So far, we have not made any assumptions on the collective modes $D^\dagger_{\vec{k}}$ or $D^\dagger_{j,\vec{k}}$, just imposed that the different transformations should be unitary. At this point, it is useful to recourse to the Holstein-Primakoff approximation already detailed in Chapter 3. In the low-excitation regime, the ensemble of QEs behaves collectively as an harmonic oscillator without saturation because there are many QEs to fill in with excitations. Mathematically, the Holstein-Primakoff approximation is usually defined by the following transformation [108]:

$$D^\dagger_{\vec{k}} = X^\dagger_{\vec{k}}\sqrt{1 - \frac{X^\dagger_{\vec{k}}X_{\vec{k}}}{N}}\,, \tag{6.62}$$

where $X_{\vec{k}}$ is an operator that satisfies the bosonic commutation relationships: $[X_{\vec{k}}, X^\dagger_{\vec{q}}] = \delta_{\vec{k},\vec{q}}$. The term of the square root takes into account the saturation effects due to the fermionic behaviour of the constituents of $D_{\vec{k}}$. In the linear regime, when the excitation is very low ($\langle X^\dagger_{\vec{k}}X_{\vec{k}}\rangle \ll N$), then $X_{\vec{k}} \approx D_{\vec{k}}$ and therefore the Hamiltonian to lowest order is given by:

$$H^N_{(0),\vec{k}} = \omega_0 X^\dagger_{\vec{k}}X_{\vec{k}} + \omega_{\vec{k}}a^\dagger_{\vec{k}}a_{\vec{k}} + g^N_{\vec{\mu}}(\vec{k})(a_{\vec{k}}X^\dagger_{\vec{k}} + a^\dagger_{\vec{k}}X_{\vec{k}})\,, \tag{6.63}$$

This is the regime where the experiments usually operates. Thus, the lowest order hamiltonian succeed to reproduces most of the experimental signatures observed in experiments which are related to "one-excitation" properties: spectra, intensities,... as we will detail in the next subsection. However, the effect of neglecting the saturation, which is implicit in this semi-classical approximation, has strong consequences in other properties that characterize the statistic of the system, i.e. $g^{(2)}(\tau)$.

In order to include saturation effects to first order, one can go to the next order by expanding the square root, obtaining two extra terms in the Hamiltonian:

$$H^N_{(1),\vec{k}} = H^N_{(0),\vec{k}} - \frac{\omega_0}{N} X^\dagger_{\vec{k}} X^\dagger_{\vec{k}} X_{\vec{k}} X_{\vec{k}} - \frac{g^N_{\vec{\mu}}(\vec{k})}{2N} (a_{\vec{k}} X^\dagger_{\vec{k}} X^\dagger_{\vec{k}} X_{\vec{k}} + a^\dagger_{\vec{k}} X_{\vec{k}} X^\dagger_{\vec{k}} X_{\vec{k}}) \,. \tag{6.64}$$

Both terms in the sum induce a non-linear behavior. Their main effects are:

- The first term moves the energy of the exciton mode. When the system is in SC its effect is to shift the energy of both polariton branches. A similar non-linear term can arise also from other mechanisms such as exciton Coulomb interaction [229]. So as to be as general as possible, we use the notation U_X, and consider that it can stem from different origins.
- The second term effectively decreases the splitting between the polariton modes. It defines a critical number of excitations where the splitting is completely destroyed. By doing the factorization: $a_{\vec{k}} X^\dagger_{\vec{k}} X^\dagger_{\vec{k}} X_{\vec{k}} \approx a_{\vec{k}} X^\dagger_{\vec{k}} \langle X^\dagger_{\vec{k}} X_{\vec{k}} \rangle$, one can easily find that: $\langle X^\dagger_{\vec{k}} X_{\vec{k}} \rangle_{sat} = 2N$.

As $g^N_{\vec{\mu}}(\vec{k}) \lesssim 0.1\omega_0$, as a first approximation we focus on the effect of the first term and neglect the second one, being aware of the upper bound introduced by $\langle X^\dagger_{\vec{k}} X_{\vec{k}} \rangle_{sat}$.

6.3.3 Identifying SC through one-excitation properties.

In most situations, the number of active QEs, N, is large so that the non-linear term, U_X, can be neglected. Thus, in this Section, we consider results to first order in the Holstein-Primakoff approximation, $H^N_{(0),\vec{k}}$. In order to do a quantitative analysis of the SC in these systems, we consider a typical experimental situation where the SPP are excited through a laser field that fixes the $\vec{k}$ and then study the absorption/reflectivity spectrum by moving $\omega_{\rm L}$. We self-consistently compute the dynamics of the system by means of the following master equation:

$$\dot{\rho}_{\vec{k}} = i[\rho_{\vec{k}}, H^N_{(0),\vec{k}} + H^L_{\vec{k}}] + \frac{\gamma_{X_{\vec{k}}}}{2} \mathcal{L}_{X_{\vec{k}}} + \frac{\gamma_{a_{\vec{k}}}}{2} \mathcal{L}_{a_{\vec{k}}} + \frac{\gamma_\phi}{2} \mathcal{L}_{X^\dagger_{\vec{k}} X_{\vec{k}}} \,. \tag{6.65}$$

By solving the master equation for $\vec{k}_0 = \vec{k}(\omega_0)$, $\rho_{\vec{k}_0}$ can be found to be proportional to $\exp(iRt)$ where R is the so-called Rabi splitting at resonance:

$$R = \sqrt{[g^N_{\vec{\mu}}(\vec{k}_0)]^2 - (\gamma_{X_{\vec{k}_0}} + \gamma_\phi - \gamma_{a_{\vec{k}_0}})^2/16} \tag{6.66}$$

Then, following the standard notation, we will say that our hybrid system is within the SC regime when the imaginary part of the Rabi splitting is zero. In Fig. 6.13(a), it is plotted the evolution of $R \equiv R_r + iR_i$ with volume density n for an ensemble of N QEs whose dipoles are oriented isotropically. For very low densities (for this set of parameters, $n < 2 \times 10^3 \mu m^{-3}$), R is a purely imaginary number and, therefore, the system operates in the WC regime. This density threshold, n_t, is mainly controlled by γ_ϕ and γ_a as $\gamma_\phi, \gamma_a \gg \gamma_D$ for this set of decay rates. Notice that as γ_ϕ decreases exponentially when lowering the temperature [228], so that

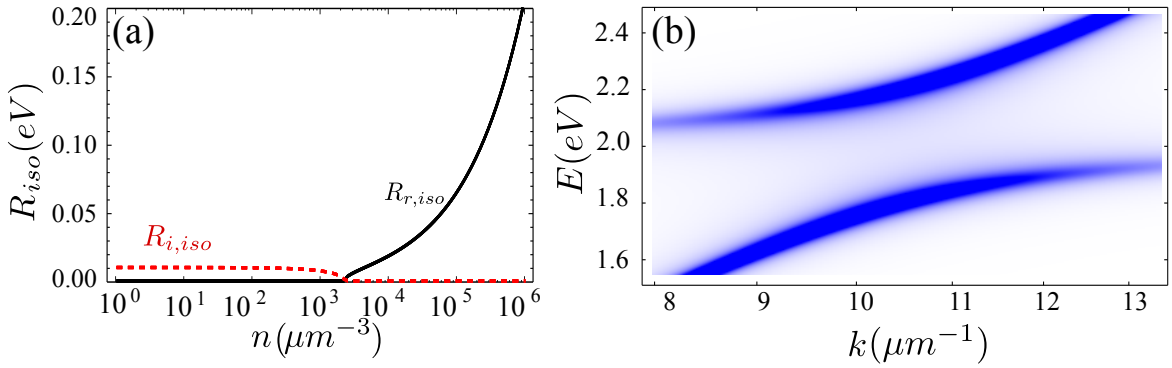

Figure 6.13: (a) Real (solid black) and imaginary (red dashed) parts of the Rabi splitting at resonance for dipoles oriented isotropically, R_{iso}, as a function of n for the geometrical parameters: $s = 1$ nm and $\mathcal{W} = 500$ nm and $\gamma_\phi = 40$ meV. (b) Polariton population (see main text) of a distribution of QEs as a function of $\vec{k}$, with the same geometrical parameters as in panel (a) and with $\Omega_{\vec{k}} = 0.1g^N$. The volume density in this case is $n = 10^6 \mu m^{-3}$.

n_t is expected to be limited only by γ_a. For high enough densities ($n \approx 10^5 - 10^8 \mu m^{-3}$, typical densities in the experiments [69]), R_r (the so-called vacuum Rabi splitting) is dominated by the coupling constant g^N as $g^N \gg \{\gamma_D, \gamma_a, \gamma_\phi\}$ and $R_r \approx g^N$. As this coupling constant scales as $\sqrt{n}$, so does R_r, as observed in the experiments.

The decoherence mechanisms are responsible for the threshold density that determines the onset of SC. From the analysis of the decoherence mechanisms, we can give a few hints about what are the optimal conditions to observe SC:

- From all the decoherence mechanisms analyzed, the most important one appears to be the pure dephasing induced by vibro-rotational states of the molecules. The only way to reduce its importance is to lower the temperature of the experiments which has been shown to reduce the dephasing of the molecules in orders of magnitude [228].

- The second most important ingredient are the SPP losses. They depend both on the material properties and the operating frequency of the QEs. The former is difficult to optimize as silver is already of less lossy metallic systems available. The only alternative is to look for QEs with smaller energies or use low temperatures where they are also expected to decrease considerably [223].

- Regarding the QEs losses, we have shown that these can be optimized very easily. A spacer of around 10 nm is enough to lower them to almost its intrinsic value (γ_0). The only important issue is to use thin QE layers so that the QE losses are homogeneous to avoid the incoherent coupling of the bright state with the reservoir of the dark states. The latter should compete with the fact that the thicker the layer, the bigger the coupling constant is.

Finally, within this formalism, it is also possible to evaluate the absorption spectra. This is the magnitude usually measured in experiments. It is proportional to the polariton populations, $\langle L^\dagger_{\vec{k}} L_{\vec{k}} \rangle + \langle U^\dagger_{\vec{k}} U_{\vec{k}} \rangle$, which is what we show in Fig. 6.13(b). There, we can observe the anti-crossing between the flat band at ω_0 associated with the collective mode of the N QEs and the dispersive band of the SPPs.

6.3.4 Outlook: predicting quantum phenomena beyond the semi-classical description.

Even though the results of the previous Section are obtained from a microscopic description of the interaction hamiltonian, a semi-classical description of the problem would give qualitatively similar results. However, more interesting properties related to the statistics of the system, such as the second order correlation function [230], are not well described by a classical approach.

The most common experimental experimental situation is to excite resonantly the SPPs and then either study the reflected light coming from them or to collect the light from the QEs. In this Section, we consider the latter situation in which the dynamics of the system is studied through the statistics of the light emitted from the QEs collective mode. The second-order coherence function of this mode is defined as:

$$g^{(2)}(\tau) = \lim_{t\to\infty} \frac{\langle X^\dagger_{\vec{k}}(t)(X^\dagger_{\vec{k}}X_{\vec{k}})(t+\tau)X_{\vec{k}}(t)\rangle}{\langle X^\dagger_{\vec{k}}X_{\vec{k}}(t)\rangle^2} \tag{6.67}$$

As we have extensively seen during this Thesis. this magnitude is of paramount importance in quantum optics as it distinguishes between classical/quantum systems. In particular, the fact that the light emitted from a system exhibits antibunching, defined by $g^{(2)}(0) < 1$, proves that the system is quantum as antibunching can never appear within a semi-classical description.

In Fig. 6.14(a), this magnitude is studied for different pumping configurations in a situation where dephasing is negligible (low temperature experiments). For incoherent pumping (in dashed green), the magnitude starts always in $g^{(2)}(0) = 2$ and displays some oscillations due to SC dynamics, but one can not infer whether the nature is quantum. For the case of a coherent pumping on the SPP field (dashed blue line), the system acquires the same statistics as the laser, $g^{(2)}(\tau) = 1$, which is still of classical nature.

The quantum nature of the problem appears when one includes an element which so far we have been neglecting: the QE-QE interaction discussed when we did the bosonization of the collective mode. Without focusing on its origin, which can be due either to saturation or Coulomb interaction [231], it can be described as a first approximation through an effective non-linear hamiltonian: $H_{nl} = \sum_{\vec{k}} U_X (X^\dagger_{\vec{k}}X_{\vec{k}})^2$, where U_X describes the strength of the non-linearity. Interestingly, the combination of this non-linear term and coherent pumping can lead to antibunching conditions $g^{(2)}(0) < 1$ (see Fig. 6.14(b)), that is the smoking gun of quantum phenomena. We finally note that pure dephasing hinders the observation of antibunching (calculations not shown), so the optimal configuration to observe quantum effects in this systems will be at low temperatures.

In the contour plot of Fig. 6.14(b), we have also included the dependence of $g^{(2)}(0)$ with the laser frequency ω_{L}. Remarkably, a slight detuning of the laser can help to increase the antibunching effect. For example, for $U_X = 5\,meV$ when a value $g^{(2)}(0) \approx 0.9$ is obtained for $\omega_{\mathrm{L}} = \omega_0$, a slight detuning decreases the value below to 0.8. Although the values of the non-linearities are not usually very high, this might be a useful hint for the experimentalist in order to look for antibunching in these systems. Another interesting property is the appearance of three different minima for antibunching. The ones appearing at the polariton energies $|\omega_0 - \omega_{\mathrm{L}}| \approx g^N$ are due to the fact that both polariton modes are affected by the

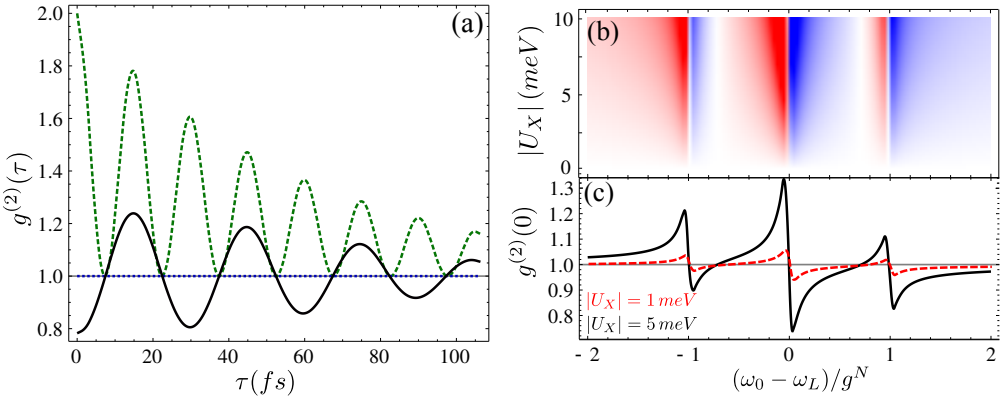

Figure 6.14: (a) Second order coherence dynamics $g^{(2)}(\tau)$ for different experimental configurations configurations: incoherent pumping with $U_X = 0$ (dashed green), coherent pumping with (dotted blue) and coherent pumping with $U_X = 5\,meV$ and $\omega_L \approx \omega_0$ (solid black). The geometrical parameters are the ones of Fig. 6.13. Panel (b): Contour plot of $g^{(2)}(0)$, for the coherently pumped situation as a function of detuning $(\omega_0 - \omega_L)$ and non-linearity U_X. The color code is blue for $g^{(2)}(0) < 1$, white for $g^{(2)}(0) = 1$ and red for $g^{(2)}(0) > 1$. Panel (c) corresponds to two cuts of the contour plot with $U_X = 1\,meV$ (dashed red) and $U_X = 5\,meV$ (solid black)

non-linearity and thus are effectively anharmonic oscillators, whereas the one in the center which appears at the energy of the bare modes ($\omega_L \approx \omega_0$) is due to the intrinsic non-linear behaviour of the bare mode $X_{\vec{k}}$ at this frequency.

6.4 Conclusions.

To summarize, in the first part of the Chapter, we use a suitable formalism to deal with absorbing media. We have studied the conditions under which reversible dynamics between a single QE and SPPs at metal-dielectric interfaces can be observed. We have identified the key parameters which determine both the emergence and the visibility of the oscillations in the excited-state QE population. Both the thick and thin metal film limits have been presented. The use of high refractive index dielectric is favorable to resolve oscillations with an optical QE as it moves the cut-off frequency to the optical regime. The larger confinement achieved in the thin film limit does not help due to the unavoidable increase of losses in this regime.

Then, in the second part, we have presented a self-consistent quantum formalism to study the phenomenon of SC between QEs and propagating SPPs in two-dimensional metal surfaces. Based on this formalism, we are able to:

- Obtain the critical density where SC emerges for a given geometry and distribution of QEs.
- Determine the optimal geometrical parameters that maximize SC.
- Predict experimental configuration where purely quantum phenomena can be observed.

The results show that, for experiments carried out at room temperature, QE and SPP losses play a minor role in the emergence of SC. The competition between QE-SPP coherent

coupling and pure dephasing mechanisms determines the strength of the phenomenon in this case. Additionally, the development of this general quantum framework paves the way for studying and predicting new interesting quantum applications for this type of hybrid plasmonic systems as, for example, the preparation of squeezed and entangled states of polaritons or the design of quantum memories of light [232].

Chapter 7

Two-qubit entanglement mediated by plasmons.

7.1 Introduction

In the previous Chapter, we studied in detail the limitations of surface plasmon polariton (SPP) to achieve strong-coupling regime in the single quantum emitter (QE) limit, observing that in most of the situations the QE in the presence of SPPs will be operating in the weak-coupling or *Purcell* regime. In principle, this seems a huge limitation for developing quantum computation and information applications with SPP's as most of their protocols are based in unitary dynamics [7] where decoherence only plays a negative role.

One requirement of quantum computation is the possibility of building two-qubit gate which needs some interaction between the qubits. The current proposals rely either on generating coherent unitary evolution by the coupling of the two QEs to a common cavity mode [15, 144, 233] or to a guided mode [234, 235] to generate the coherent unitary evolution.

However, it has recently been proposed a new paradigm of quantum computation which uses decoherence as a useful resource [20, 236]. The idea consists of engineering the coupling of the systems playing the role of qubits and their baths, so that the dissipative dynamics drives the system into the one needed for the quantum computation. It has been inspired in the concept of *Decoherence-free subspaces* [237–244] which are set of states disconnected from the bath dynamics, which therefore does not suffer from decoherence. Implementation of such ideas has shown their tremendous potential demonstrating entanglement generation between atomic ensembles [23, 245].

There are several ways of building such decoherence free subspaces, namely through the common interaction with a EM field. Many structures have been proposed to do it, ranging from photonic crystal cavities [143, 246] and waveguides [247, 248], photonic nanowires [249], and dielectric slot waveguides [250]. A crucial requirement for such devices is the enhancement of the EM field, leading to a large Purcell factor, defined as the decay rate of the emitter in the presence of the structure normalized to the decay rate in vacuum. Electric field intensification is favored by a tighter confinement of the EM modes.

Here it is where metallic waveguides, supporting SPP modes, appear as ideal candidates to outperform the aforementioned systems. The interaction between QEs and SPP, has

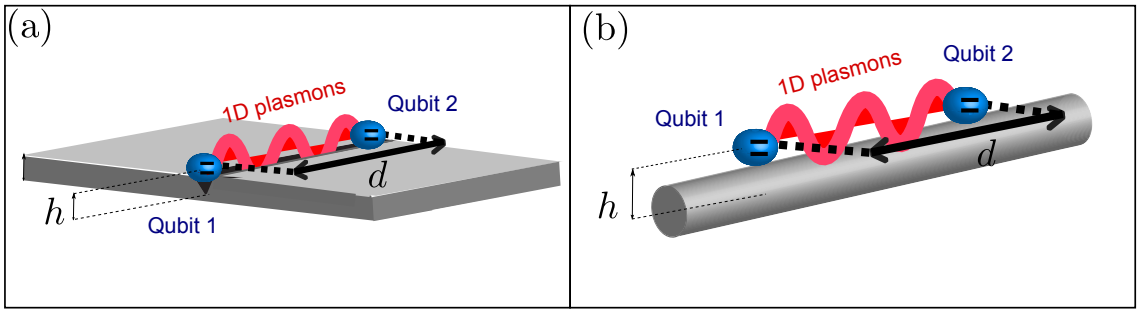

Figure 7.1: Two qubits separated a horizontal distance d are positioned at a vertical distance h from the bottom of a channel/ cylindrical waveguide in panels (a) & (b) respectively. The plasmon modes supported by the structure mediate the electromagnetic interaction between the qubits.

already been used to control decay rate [251], angular directionality [252], and energy transfer [253, 254]. In Chapter 1, it was shown that since the seminal experiments proving single plasmon emission from a plasmonic nanowaveguide [56] coupled to a single QE, there has been a lot of theoretical [63, 210] and experimental efforts in this direction proving a finer control of the coupling [61], detection at the single quanta of excitation limit [255, 256].

In this Chapter, the possibilities of generating entanglement between two QEs linked by a one-dimensional plasmonic waveguide (PW) in the optical regime will be explored [64, 66, 257]. It is done in both a spontaneous emission configuration and for stationary situation where an steady-state is reached with the help of one or two additional lasers.

The Chapter is divided as follows: first, in Section 7.2 we introduce the system of study which consists of a V-shaped channel milled in a flat metallic surface and operating in the optical regime [64, 257] (see panel (a) Fig. 7.1). During the rest of the chapter, it will be compared its efficiency with a traditional cylindrical PW (see panel (b) of Fig. 7.1), which are the ones usually considered in the experiments [56, 61]. Then, in Section 7.3, we give a brief overview of the master equation obtained after tracing out the degrees of freedom of the SPP bath, detailing the main ingredients of the process. The starting point is the formalism already introduced in the previous Chapter to deal with metallic systems [216, 217], using the information of the classical Green Function of the system that appears when quantizing the field in the presence of absorbing media. In Section 7.4, we make a summary of the results of the EM calculations for both geometries such as Purcell factor, collective decay, ... paying special attention to the role of dipole moment misalignments as it is one of the experimental ingredients most difficult to control. Next, in Section 7.5 the possibilities of obtaining entanglement are analyzed under two different configurations, namely spontaneous emission and under continuous coherent excitation. A overview of possible experimental characterizations is also presented together with the analysis of the degradation of entanglement in the presence of other non-radiative mechanisms such as pure dephasing. Finally, in Section 7.6, we make a summary of the main points of the Chapter. The work in this Chapter has resulted from a strong collaboration with the Nanophotonics group leaded by García-Vidal. This group has brought the expertise in the classical calculation of the EM field in the PW structures. Here, I just briefly summarize the results which are important for understanding our scheme, but more details can be found in Diego Martin-Cano's Thesis which accounts extensively for this

type of classical calculations.

7.2 System description: plasmonic waveguides.

The system of study in this Chapter consists of two identical QEs positioned in closed proximity to a metallic plasmonic waveguide (PW) (Fig. 7.1), in such a way that their EM interaction is dominated by the plasmonic modes supported by the quasi one-dimensional structure. The QEs, could be atoms, molecules, QDs, or nitrogen-vacancy centers in diamond. However, as they are required to be at fixed positions of space, solid state QEs are the most promising candidates. As in the rest of Chapters, excepting Chapter 4, we model the QE by a two-level system (2LS), with transition frequency ω_0, described within a point dipole approximation [1]. The solid-state QEs usually have energies around the optical regime, so for the rest of the Chapter it is considered a QE with an emission wavelength of $\lambda = 600\,\mathrm{nm} (\approx 2\,eV)$.

In order to determine the influence of the PW geometry, it will be considered two different metallic structures: the first is a cylindrical nanowire, which is the one that is mainly used of quantum plasmonics experiments so far [56, 61] and the second a channel waveguide, both depicted in panels (a) & (b) respectively of Fig. 7.1. The exact geometry of both structures is detailed in panels (a) and (b) of Fig. 7.2. The radius of the cylindrical nanowire is $R = 35\,\mathrm{nm}$, the depth of the V-shaped groove is $L = 138\,\mathrm{nm}$, and its angle is $\theta = 20^\circ$ are chosen so that at the operating wavelength, only one mode is relevant. Importantly, with this choice of parameters the propagation length for cylinders and channels are the same, so that a meaningful comparison of the results can be assured. The considered metal is silver, as in Chapter 6, whose electric permittivity at the mentioned wavelength is [259] $\epsilon = \ epsilon_{\mathrm{r}} + i\epsilon_{\mathrm{i}} = -13 + i0.8$.

As shown in panel (c) of Fig. 7.2 the channel waveguide is single-moded and the cylinder supports two modes but the second one (black dashed line), being extremely close to the light line, is very much extended in the transverse cross plane and will not play a relevant role in what follows. Since the QE-QE interaction will be mediated by the plasmonic modes, having identical propagation length ensures a meaningful comparison of the results obtained with both PWs. The propagation length is $L_{\mathrm{prop}} = [2k_{\mathrm{i}}]^{-1} = 1.7\,\mu\mathrm{m}$, k_{i} being the imaginary part of the (complex) modal wave vector, $k = k_{\mathrm{r}} + ik_{\mathrm{i}}$. The dispersion relation for both PWs is rendered in Fig. 7.2 (c) and it is observed that the curve corresponding to the cylinder (black circles) lies to the right of that corresponding to the channel (red triangles), implying that the EM field of the former is more tightly confined. This is confirmed by a comparison of panels (a) and (b), where the transverse electric field modal profiles and polarizations are plotted. For both waveguides the modal size is deep-subwavelength. In spite of the fact that the electric field of both structures includes transverse and longitudinal components, the former dominate by a factor of about 10, making that parallel placing of the emitters to the transverse plane the optimal direction to couple the SPP modes of the PW.

[1] One should be aware that if solid-state emitters are large, as it can occur with QDs, the point dipole approximation may not be enough of the problem and a more detailed description is needed, i.e. quadrupolar calculation [258], to get more accurate results.

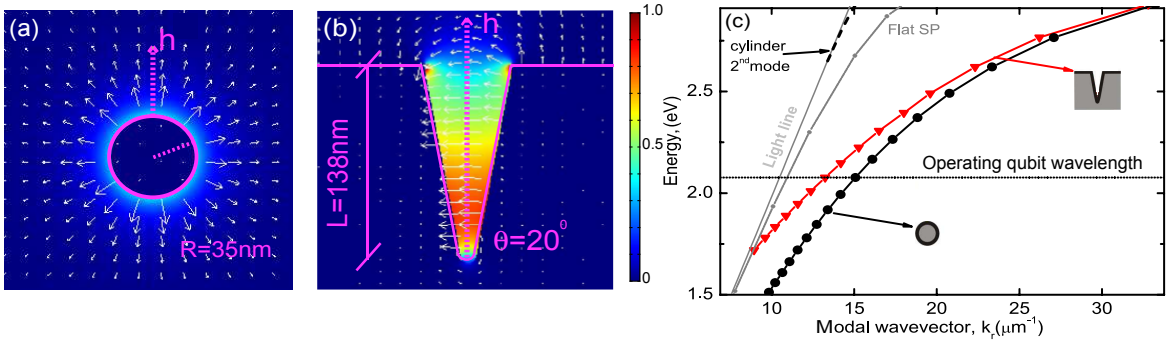

Figure 7.2: Transverse cross section of a cylindrical nanowire (a) and a channel waveguide (b). The color scale in (a) and (b) renders the transverse electric field amplitude of the supported plasmonic modes, and the arrows show the electric field polarization. (c) Dispersion relation for the fundamental mode of the cylindrical nanowire (black circles) and channel waveguide (red triangles). The vacuum light line, the dispersion relation of a plasmon on a flat silver surface, and that of the second mode supported by the cylinder are also plotted.

7.3 Two-qubit dynamics and entanglement.

In this Section, the tools required to determine the quantum state of two qubits and their entanglement degree will be introduced. The evolution of the two qubits in interaction with a common EM field supported by a PW can be approached in two ways: one can either use a microscopic derivation similar to the one derived in Chapter 6, or rely in a macroscopic quantum electrodynamics (QED) description where the modes supported by the PW are represented using a the classical Green's tensor [216, 260, 261]. In both methods, as the SPP bath is weakly coupled to the qubits system, one obtain a markovian master equation for the reduced density matrix for the two qubits by tracing out the degrees of freedom of the SPP, similarly to what was done in Chapter 6 with the ohmic and radiative modes. It has been checked that both methods converge to the same two-qubit master equation [217, 237], but one important advantage of the macroscopic QED method is that all magnitudes describing the coupling between the qubits and the EM field can be obtained from the classical Green's tensor appropriate for the corresponding structure.

Now, we will generalize in a few lines for the case of two QEs the formalism developed in Chapter 6 for a single QE. The Hamiltonian for two QE's system in the presence of a dispersive and absorbing material is written in the electric dipole approximation as:

$$\hat{H} = \int d^3\vec{r} \int_0^\infty d\omega\, \omega\, \vec{f}^\dagger(\vec{r},\omega)\cdot\vec{f}(\vec{r},\omega) + \sum_{i=1,2} \omega_0\, \sigma_i^\dagger \sigma_i - \sum_{i=1,2} \int_0^\infty d\omega [\hat{\vec{\mu}}_i \vec{E}(\vec{r}_i,\omega) + \text{h.c.}]\,. \quad (7.1)$$

Here $\vec{f}^\dagger$ and $\vec{f}$ represent the bosonic fields in the medium with absorption, which play the role of the fundamental variables of the electromagnetic field. The $\sigma_i^\dagger$ is the i-qubit rising operator, $\vec{r}_i$ its spatial position, ω_0 is the transition frequency. The interaction term includes the dipole moment operator $\hat{\vec{\mu}}_i = \vec{\mu}_i(\sigma_i + \sigma_i^\dagger)$, where $\vec{\mu}_i$ is the dipolar transition

matrix element. In addition,

$$\vec{E}(\vec{r},\omega) = i\sqrt{\frac{1}{\pi\epsilon_0}}\frac{\omega^2}{c^2}\int d^3\vec{r'}\sqrt{\mathrm{Im}[\epsilon_m(\omega)]}\hat{\mathbf{G}}(\vec{r},\vec{r'},\omega)\vec{f}(\vec{r'},\omega)\,, \tag{7.2}$$

is the electric field operator, which was already defined in Eq. 6.16. Notice the explicit appearance of the Green's tensor $\hat{\mathbf{G}}(\vec{r},\vec{r'},\omega)$, which satisfies the classical Maxwell equations for an infinitesimal dipole source located at the spatial position $\vec{r'}$. Physically, the Green's tensor carries the electromagnetic interaction from the spatial point $\vec{r'}$ to $\vec{r}$.

This Hamiltonian description contains all the information of the SPP of the PW and the qubits, however, as we already showed in Chapter 6, due to the high losses of the SPPs the QEs are in most of the situations weakly coupled to the SPP bath. This justifies treating the SPP as a *reservoir* and use a Markovian approximation to adiabatically eliminate the degrees of freedom of SPP. The details of the derivation has been sketched in Chapter 2 for a similar system, but it can also be found explicitly in references [216, 237].

The result is a master equation which governs the dynamics of the reduced density matrix ρ corresponding to the two-qubit system which reads as follows:

$$\frac{\partial\rho}{\partial t} = -i[H_\mathrm{s},\rho] - \frac{1}{2}\sum_{i,j}\Gamma_{ij}(\rho\sigma_i^\dagger\sigma_j + \sigma_i^\dagger\sigma_j\rho - 2\sigma_j\rho\sigma_i^\dagger)\,. \tag{7.3}$$

where the hamiltonian included in the coherent part of the dynamics is

$$H_\mathrm{s} = \sum_i(\omega_0+\delta_i)\,\sigma_i^\dagger\sigma_i + \sum_{i\neq j} g_{ij}\,\sigma_i^\dagger\sigma_j. \tag{7.4}$$

The interpretation of the various constants appearing in Eqs. (7.3) and (7.4) is the following. The Lamb shift, δ_i, is due to the qubit EM self-interaction in the presence of the PW. At optical frequencies, for qubit-metal distances larger than about 10 nm, δ_i is very small [58] and as usually done it is included in a renormalized energy of the qubit $\omega_0+\delta_i \equiv \omega_0$. The level shift induced by the dipole-dipole coupling is given by g_{ij}, and can be calculated from the classical Green's tensor and the dipole moment $\vec{\mu}_i$ of the qubits involved:

$$g_{ij} = \frac{\omega_0^2}{\varepsilon_0 c^2}\vec{\mu}_i\cdot\mathrm{Re}\hat{\mathbf{G}}(\vec{r}_i,\vec{r}_j,\omega_0)\cdot\vec{\mu}_j. \tag{7.5}$$

Finally, the parameters in the dissipative (noncoherent) term of Eq. (7.3) are given by:

$$\Gamma_{ij} = \frac{2\omega_0^2}{\hbar\varepsilon_0 c^2}\vec{\mu}_i\cdot\mathrm{Im}\hat{\mathbf{G}}(\vec{r}_i,\vec{r}_j,\omega_0)\cdot\vec{\mu}_j, \tag{7.6}$$

The Γ_{ii} represents the decay rate of the i-th qubit whereas Γ_{ij} accounts for the collective decay rate. Expressions (7.5) and (7.6) are obtained by integration of the EM field Green's function in the frequency domain [216]. To reach the result that the coherent and incoherent contributions to the coupling are proportional to the real and imaginary parts of the Green's function, respectively, the Kramers-Kronig relation between the real and imaginary parts of the Green's function has to be applied [65, 216, 261].

To solve Eq. (7.3) a basis for the vector space corresponding to the two-qubit system has to be chosen. A convenient basis to study entanglement in two-qubits system is the one usually

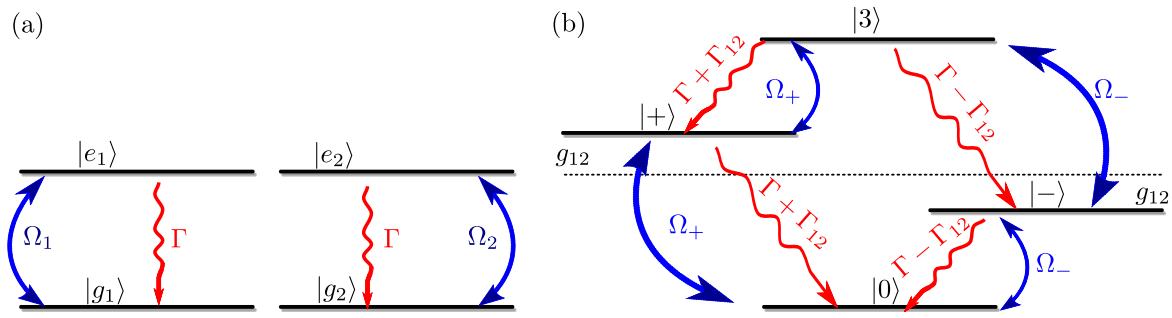

Figure 7.3: Scheme of levels for two identical qubits located at equivalent positions with respect to the PW and with identical orientations ($\Gamma_{11}=\Gamma_{22}=\Gamma$ and $\Gamma_{12}=\Gamma_{21}$) and coherently pumped with two lasers in the two-qubit single basis (Panel (a)) and in the Dicke basis (Panel (b)).

known as the Dicke basis, which is given by the following states: $\mathcal{B}=\{|0\rangle,|-\rangle,|+\rangle,|3\rangle\}$, where $|3\rangle=|e_1e_2\rangle$, $|0\rangle=|g_1g_2\rangle$, $|\pm\rangle=\frac{1}{\sqrt{2}}(|g_1e_2\rangle\pm|e_1g_2\rangle)$, and $|g_i\rangle$ ($|e_i\rangle$) labels the ground (excited) state of the i-qubit. The advantage of this basis is that already contains two states $|\pm\rangle$, namely the symmetric/antisymmetric states which are entangled. It is straightforward to get from Eq. 7.3 that the diagonal elements (populations) using this basis evolve with the following set of equations:

$$\begin{aligned}
\dot{\rho}_{33}(t) &= -2\Gamma\rho_{33}(t)\\
\dot{\rho}_{++}(t) &= (\Gamma+\Gamma_{12})\rho_{33}(t)-(\Gamma+\Gamma_{12})\rho_{++}(t)\\
\dot{\rho}_{--}(t) &= (\Gamma-\Gamma_{12})\rho_{33}(t)-(\Gamma-\Gamma_{12})\rho_{--}(t)\\
\dot{\rho}_{00}(t) &= (\Gamma+\Gamma_{12})\rho_{++}(t)+(\Gamma-\Gamma_{12})\rho_{--}(t),
\end{aligned} \tag{7.7}$$

Here it has been assumed that the positions and orientations of the two qubits in their respective planes transverse to the PW are identical, so that $\Gamma_{11}=\Gamma_{22}=\Gamma$ and $\Gamma_{12}=\Gamma_{21}$. The diagonal character of $\hat{H}_{\rm s}$ in the above mentioned basis and the interpretation of Eqs. (7.7) is depicted in Fig. 7.3, including the level scheme and the collective decay rates induced by the coupling to the EM field. Once these decay rates are evaluated in Sec. 7.4, the generation of entanglement will be studied with the help of this diagram. Notice that the qubit-qubit dissipative coupling induces modified decay rates $(\Gamma+\Gamma_{12})$ and $(\Gamma-\Gamma_{12})$ for the symmetric, $|+\rangle$, and antisymmetric, $|-\rangle$, state of the basis.

So far we have assumed that the system evolves without the influence of any source of pumping. In this configuration, one can initialize the system in some initial state with a given population and leave the system freely evolve into the ground state $|0\rangle$. This will be named as *spontaneous emission* configuration, and under certain conditions it will lead to a transitory creation of entanglement as we will review in Sec. 7.5.1. However, for applications it is more interesting to study the possibility of achieving some steady-state entangled configuration. As dissipation always drives the system into the ground state $|0\rangle$, one needs to include a external source of pumping to get a stationary situation. In semiconductor cQED, the usual situation is that of incoherent pumping [242, 244] due to the practical difficulties of coherently exciting qubits which are embedded in a cavity. As the generation of entanglement relies on

dissipation and incoherent pumping is known to decohere the system as well, its application will prevent the formation of higher degrees of entanglement. Thus, one can take advantage that our system is geometrically simpler as the QEs are not embedded inside a photonic band-gap structure and one can excite them coherently by means of a laser whose frequency, $\omega_{\rm L}$, is close to resonance with the frequency of the qubits [64, 257]. The description of this new element requires the inclusion of an additional term in the Hamiltonian, as described in other Chapters of this Thesis [77, 262], of Eq. (7.4):

$$H_{\rm L}(t) = \sum_i [\Omega_i \, \hat{\sigma}_i^\dagger e^{i\omega_{\rm L} t} + \text{h.c.}]. \tag{7.8}$$

Here the strength and phase of the laser are characterized by the Rabi frequencies $\Omega_i = \vec{\mu}_i \cdot \vec{E}_{\rm L} \, e^{i\vec{k}_{\rm L}\vec{r}_i}/\hbar$, where $\vec{E}_{\rm L}$ and $\vec{k}_{\rm L}$ are the amplitude and wave vector of the driving laser field, respectively. The effect of the laser in the states of the Dicke basis $\mathcal{B}$ is sketched in panel (b) of Fig. 7.3, where one can see how it populates states $|\pm\rangle, |3\rangle$ with different intensities depending on the side of the ladder. The intensities $\Omega_\pm$ are combinations of the single qubit intensities $\Omega_{1,2}$ given by the following relationship: $\Omega_\pm = (\Omega_1 \pm \Omega_2)/\sqrt{2}$.

In the most general case, the determination of the density matrix $\rho(t)$ requires the numerical integration of Eq. (7.3) with appropriate initial conditions. When the system is pumped, the steady state solution can be obtained by setting $\dot{\rho} = 0$ and solving the corresponding set of linear equations. In both scenarios (pumped and non-pumped), once the density matrix $\rho(t)$ is known it is possible to compute various magnitudes of interest, such as those quantifying the two-qubit entanglement, or first and second order coherence functions, which are directly related with measurable properties. Regarding the quantification of entanglement, there are several alternatives but all of them are related to each other for a bipartite system [263]. In this Chapter, we use of the *Wooters* Concurrence [264], which ranges from 0 for unentangled states to 1 for maximally entangled states. Its definition is the following: $C \equiv [\max\{0, \sqrt{\lambda_1} - \ sqrt\lambda_2 - \sqrt{\lambda_3} - \sqrt{\lambda_4}\}]$, where $\{\lambda_1, \lambda_2, \lambda_3, \lambda_4\}$ are the eigenvalues of the matrix $\rho T \rho^* T$ in decreasing order (the operator T is $\sigma_y \otimes \sigma_y$, σ_y being the Pauli matrix), and spite of not being very transparent, it is easily calculated from the density matrix $\rho(t)$. The concurrence ranges from 0 in separable states to 1 in maximally entangled states. Typical measurable magnitudes in experiments to characterize systems include one-photon spectra and two-times coherence functions as explained in detail in Chapter 2. As reviewed there, once the density matrix of the system is found, the quantum regression theorem [77, 262] establishes that any two-times coherence function obeys the same dynamics as $\rho(t)$, i.e., Eq. (7.3).

After having reviewed the basic theory needed in order to characterize the dynamics and experimental features of our particular two-qubit system, we explore first the EM properties of the qubits when they are placed in the vicinity of PW.

7.4 Computation of the Green's tensor, decay rates, and dipole-dipole coupling

In this Section, the Green's tensor corresponding to the PWs described in the previous Section will be calculated. After tracing out the degrees of freedom of the SPP bath of the PWs, this

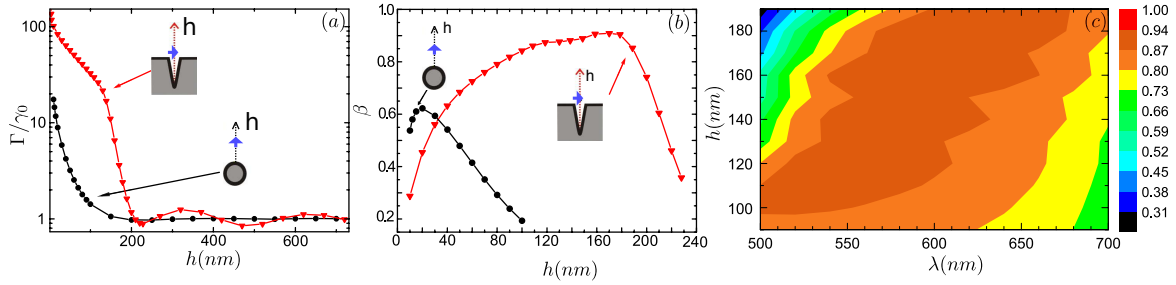

Figure 7.4: Panel (a) Purcell factor (Γ/γ_0) versus vertical height h of the emitter along the lines displayed in the insets. Panel (b) (& (c)) Beta factor ($\Gamma_{\rm pl}/\Gamma$) versus vertical height h (and versus Λ) of the emitter along the lines displayed in the insets. Cylinder (black circles) and channel (red triangles).

tensor contains all the information from environment and is required for the determination of the decay rates, Γ_{ij}, and dipole-dipole shifts, g_{ij}, appearing in the master equation 7.3. This Section will be divided as follows: firstly, we characterize the efficiency of the coupling of a single qubit to the SPP in the two different geometries in Sec. 7.4.1. Then, we explore the two-qubit properties, i.e., γ_{ij} and g_{ij} in Sec. 7.4.2 and finally, we put special emphasis on the effect of fabrication defects, such as dipole misalignments, in the aforementioned properties.

7.4.1 Purcell and β factor

In Chapter 5, we studied the case of the SPP supported by a semi-infinite dielectric-metal interface. Due to the high symmetry of the problem, an analytical formula for the Green's tensor can be found [265]. In other not so simple geometries, but with a high degree of symmetry, such as cylinders [266], still analytical expressions for the Green's tensor are available. However, in most complicated cases, as it is the case of the channel PW that we described in Sec. 7.2 numerical simulations are necessary. Using the relationship [58]

$$\vec{E}(\vec{r}) = \omega^2 \mu_0 \hat{\mathbf{G}}(\vec{r}, \vec{r'}, \omega_0)\vec{\mu}\,, \tag{7.9}$$

the Green's tensor can be inferred if the electric field $\vec{E}(\vec{r})$ in position $\vec{r}$ radiated by a classical oscillating electric dipole $\vec{\mu}$ at the source position $\vec{r'}$ is known. The numerical simulations has been done with a commercial software (COMSOL). This part of the work, simulating the EM field of the PW, has been done by our collaborators and for more extensive review of the details calculations, one should look in their papers [66, 254]. In this Chapter I will limit to basically summarize the results obtained within the collaboration.

Following the explained procedure one evaluates Eq. (7.6) to compute the total decay rate, $\Gamma = \Gamma_{11}$, of one qubit in the presence of a PW. This magnitude appears in Eq. (7.7) setting the time scale of the dynamics. The Purcell factor, Γ/γ_0, which measures the enhancement of the decay rate due to the presence of the PW is plotted in Fig. 7.4 as a function of the vertical distance h between the PW and the qubit along the vertical lines displayed in the insets (γ_0 denotes the intrinsic decay rate in vacuum of the QE). To achieve optimal coupling the dipole is aligned parallel to the field polarization, *i.e.*, vertically for the cylindrical waveguide and horizontally for the channel. The Purcell factor is strongly enhanced when the emitter is

very close to the metal surface ($h \to 0$), as it occurred for the metallic surface case studied in Chapter 5. This is a well-known phenomenon that we extensively addressed in the previous Chapter stemming from the decay into the lossy non-radiative (i.e. ohmic losses) modes in the metal. This effect is more pronounced for the channel, due to a higher electric field when the emitter lies at the bottom of the groove. The curve corresponding to the channel waveguide displays distinct oscillations for large h. These are the result of constructive and destructive interference of the direct field and the field reflected mainly at the flat metallic interface surrounding the channel.

However, not all the energy is flowing into guided modes. As already shown in the previous chapter, when an emitter is placed close to a metallic surface it can decay into three different decay channels: the energy can be either radiated to vacuum, non-radiatively absorbed in the metal, or coupled to guided SPP modes. It is thus customary to express the total decay rate as the sum of those three contributions, $\Gamma = \Gamma_{\rm rad} + \Gamma_{\rm dis} + \Gamma_{\rm pl}$. As the energy absorbed in the metal and most photons radiated to vacuum do not contribute to the qubit-qubit coupling, a new figure of merit is usually defined: the so-called β-factor, which accounts for the fraction of all the emission flowing into plasmons compared to the total decay rate $\beta = \Gamma_{\rm pl}/\Gamma$. In order to calculate β, one needs to be able to obtain Γ and the fraction of all emission that is coupled to plasmons, $\Gamma_{\rm pl}$. As it will be shown later, this magnitude plays a dominant role in the qubit-qubit interaction for appropriate qubit-PW vertical distance. In a similar way to the above mentioned total decay rate decomposition, the total Green's tensor can be separated as the sum of several terms corresponding to the three emission channels. Sometimes this decomposition can be done analytically, as it was the case of the metallic surface in Chapter 5, whereas in most of the cases the calculation of $\Gamma_{\rm pl}$ has to be done numerically using the following expression [267, 268]:

$$\mathbf{G}_{\rm pl}(\vec{r},\vec{r}') = \frac{i\ \vec{E}^{\rm t}(\vec{r}^{\rm t}) \otimes \vec{E}^{\rm t}(\vec{r}'^{\rm t})}{2\omega\mu_0 \int_{S_\infty} dS\, \mathbf{u}_z (\vec{E}^{\rm t} \times \vec{H}^{*\rm t})}\ e^{ik(z-z')}. \tag{7.10}$$

The occurrence of the exponential factor $e^{ik(z-z')}$ mirrors the quasi one-dimensional character of the PW-mediated interaction. The lateral extension of the plasmon is taken into account by $\vec{E}^{\vec{t}}(\vec{r}^{\rm t})$ and $\vec{H}^{\rm t}(\vec{r}^{\rm t})$, which are the transverse EM fields corresponding to the mode supported by the PW [Figs. 7.2(a) and (b) display the transverse electric field] and are evaluated at the transverse position $\vec{r}^{\rm t} = (x, y)$. S_∞ is the (infinite) transverse area, $\hat{u}_z$ is a longitudinal unit vector, and $\otimes$ denotes the tensor product. The derivation of Eq. (7.10) assumes that the mode propagates towards the right ($z > z'$) and its absorption is not too high. To be more precise, Eq. (7.10) is the transverse part of the Green's tensor, which is the relevant part since only the transversely oriented dipole moments will be considered. The modal fields entering Eq. (7.10) can be obtained by Finite Element Method numerical simulation of the corresponding eigenvalue problem [254, 269, 270]. Inserting Eq. (7.10) in the expression for the decay rate (Eq. 7.6) one obtain

$$\Gamma_{ij,\,\rm pl} = \frac{\omega\ [\vec{\mu}_i \vec{E}^{\rm t}(\vec{r}_i^{\rm t})]\,[\vec{d}_j \vec{E}^{\rm t}(\mathbf{r}_j^{\rm t})]}{\hbar \int_{S_\infty} dS\, \hat{u}_z (\hat{E}^{\rm t} \times \vec{H}^{*\rm t})} e^{-k_{\rm i}(z-z')} \cos[k_{\rm r}(z-z')], \tag{7.11}$$

which, for $\vec{r}_i = \vec{r}_j$ and $\vec{\mu}_i = \vec{\mu}_j$, becomes the plasmonic decay rate, $\Gamma_{\rm pl}$. This expression clarifies that $\Gamma_{\rm pl}$ is largest when the emitter is positioned at the field maximum and aligned

with the field polarization. Again for the curious reader of the details of this calculation, one should look into Diego Martin-Cano's Thesis where extensive details on the method are reviewed.

Once Γ and $\Gamma_{\rm pl}$ have been determined, one can plot the β factor as a function of the vertical distance h between the PW and the qubit (Fig. 7.4(b)). The general behavior is similar for both the cylindrical and channel PWs. First, the β factor is very low for small emitter-PW distance, in sharp contrast to what is observed for the Purcell factor in Fig. 7.4(a). The explanation is that $\Gamma_{\rm dis}$ behaves as h^{-3}, where h is the qubit-metal distance, being the dominant contribution to Γ for $h \to 0$ and effectively quenching the plasmon emission. For intermediate h the plasmonic decay dominates and β attains a maximum as it occurred for the metal . Finally, for large h the emitter is outside the reach of the plasmon mode and the unbounded radiative modes have a larger weight leading to a decrease in β. Nevertheless, the precise behavior of β is not identical for both PWs. Channels display a higher maximum value than cylinders (0.91 at $h = 160\,\text{nm}$ versus 0.62 at $h = 20\,\text{nm}$, respectively) and, in addition, the maximum is broader for channels than for cylinders (β deviates less than a 10% of the maximum value within a h-range of $\Delta h = 100\,\text{nm}$ for channels and of only $\Delta h = 30\,\text{nm}$ for cylinders). In panel (c) of Fig. 7.4, a contour plot of the β-factor is shown as a function of both vertical distance h and also the wavelength of excitation λ, proving that the high efficiency is also preserved a broadband of wavelengths ($\Delta\lambda \approx 100nm \approx 0.3eV$). All these features make channels a more attractive structure to enhance the interaction mediated by plasmons and therefore more suitable to mediate entanglement between them.

7.4.2 Dipole-dipole shift and decay rates

For high β factor, a dipole couples mainly to plasmon modes and this, in turn, warrants that the qubit-qubit interaction is predominantly plasmon-assisted. Under this condition, Eqs. (7.5) and (7.6) for g_{ij} and Γ_{ij} can be evaluated using the plasmonic contribution of the Green's tensor, $\hat{\mathbf{G}}_{\rm pl}(\vec{r},\vec{r}')$, of Eq. (7.10) instead of the total one, $\hat{\mathbf{G}}(\vec{r},\vec{r}')$. The resulting approximations for the dipole-dipole shift and collective decay rates are as follows [64, 254]:

$$g_{ij} \simeq g_{ij,\,\rm pl} = \frac{\Gamma}{2}\beta e^{-d/(2L_{\rm prop})}\sin(k_{\rm r}d) \tag{7.12}$$

$$\Gamma_{ij} \simeq \Gamma_{ij,\,\rm pl} = \Gamma\beta e^{-d/(2L_{\rm prop})}\cos(k_{\rm r}d), \tag{7.13}$$

where it has been assumed that the transverse position of both qubits and their orientations are identical. In order to check the validity of this approximation a comparison of the exact parameters (g_{ij}, Γ_{ij}) and the approximate ones ($g_{ij,\,\rm pl}$, $\Gamma_{ij,\,\rm pl}$) is presented in Fig. 7.5 for the cylinder [panel (a)] and the channel [panel (b)]. All parameters are normalized to the vacuum decay rate γ_0. In both cases, the position and orientation of the qubits are chosen to maximize β, *i.e.*, $h = 20\,\text{nm}$ and vertical orientation for the cylinder, and $h = 150\,\text{nm}$ and horizontal orientation for the channel. The parameters are represented as a function of the qubit-qubit separation, d, normalized to the modal wavelength, $\lambda_{\rm pl} = 2\pi/k_{\rm r}$ (at the operating wavelength $\lambda_{\rm pl}$ is 417 nm for the cylinder and 474 nm for the channel). As expected, the approximation is good for the cylinder and excellent for the channel, in consonance with the corresponding β factors (0.6 and 0.9, respectively). For the cylinder, at the chosen h, the radiative modes play

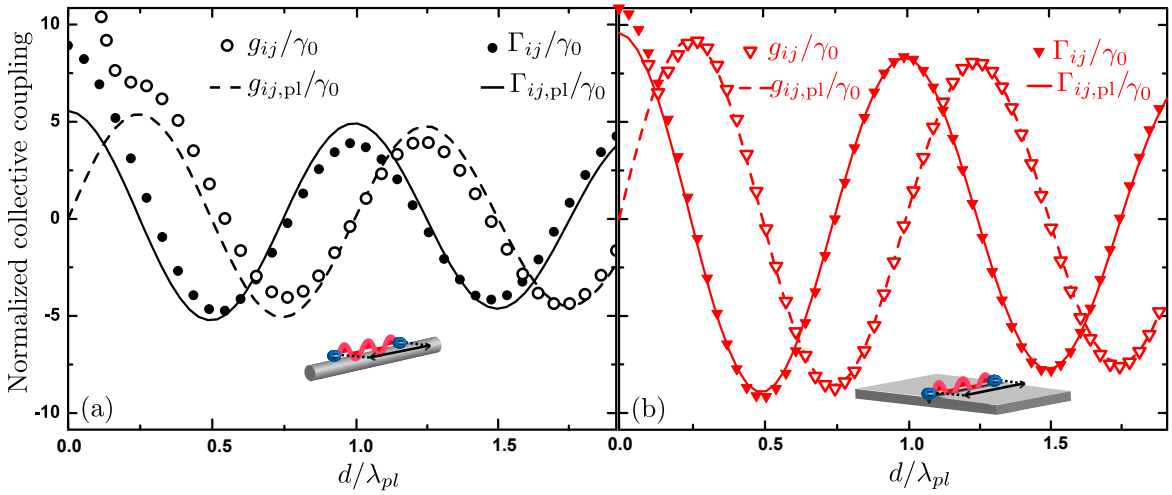

Figure 7.5: Comparison of the exact coupling parameters (Γ_{ij}, g_{ij}) with their plasmonic contributions ($\Gamma_{ij,\,\mathrm{pl}}$, $g_{ij,\,\mathrm{pl}}$), as a function of the qubit-qubit horizontal separation normalized to the plasmon modal wavelength, d/λ_{pl}. All parameters are normalized to the vacuum decay rate γ_0. (a) Cylindrical and (b) channel waveguide. The position and orientations of the dipoles are detailed in the main text.

a small but non-negligible role which shows up as a small disagreement between the exact and approximate results. For both PWs and very small d, many radiative and guided modes contribute to the interaction and the approximation breaks down. A different approach to this issue leading to the same result can be found in Ref. [65]. The coupling parameters g_{ij} and Γ_{ij} are functions of the separation d which oscillate with a periodicity given by the plasmonic wavelength, λ_{pl}, and decay exponentially due to the ohmic absorption of the plasmonic mode. Notice that the maxima of Γ_{ij} and those of g_{ij} are shifted a distance $\lambda_{\mathrm{pl}}/4$. In fact, in the next Chapter we will show that this is a general property of one-dimensional EM fields that can be exploited for further applications in many qubit systems. A general derivation for one-dimensional optical reservoirs is done in the Appendix II of this Thesis. The interest of this property is that this shift between the dissipative and coherent terms of the master equation allows to switch the dynamics between purely dissipative or Hamiltonian which leads to very interesting application such as the entanglement generation that we will review in Sections 7.5 and in the next Chapter.

7.4.3 Influence of the dipole orientation

Before going into details of entanglement generation, the analysis of the coupling parameters will be closed by considering the influence of the dipole moment orientation. This is very important from the experimental point of view since a controlled positioning of the emitters is technically challenging [271], even though significant advances in this direction has been recently made [61]. When the orientations of the two dipoles are different, the mutual decay rates are obtained in a similar way than Eq. (7.13) and can be expressed as

$$\Gamma_{ij,\,\mathrm{pl}} = \sqrt{\Gamma_{ii}\Gamma_{jj}}\sqrt{\beta_i\beta_j}e^{-d/(2L_{\mathrm{prop}})}\cos(k_{\mathrm{r}}d), \tag{7.14}$$

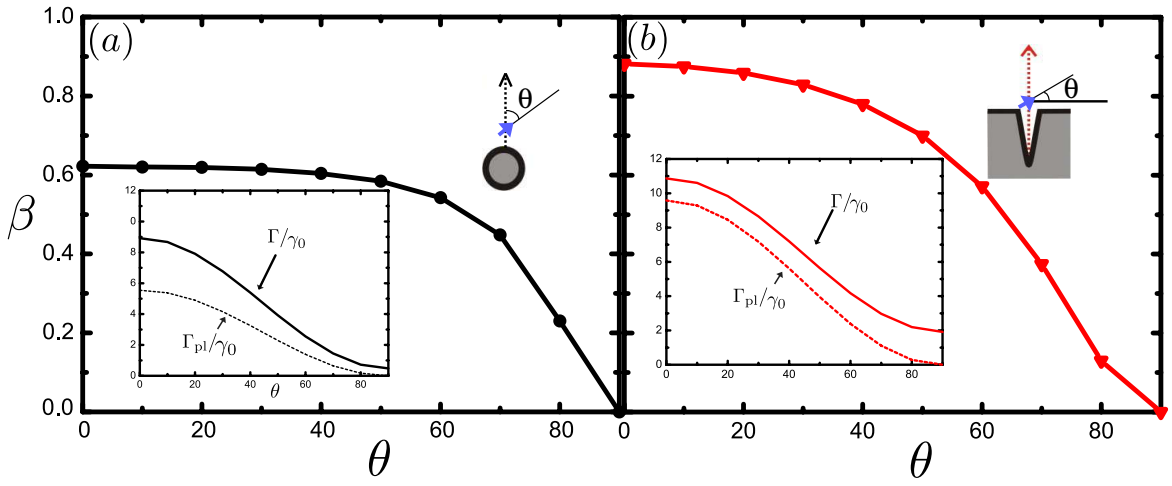

Figure 7.6: β-factor of one emitter as a function of the angle, θ, formed by the electric field and the dipole moment. (a) Cylinder, and (b) channel. The insets show the total (continuous line) and plasmon (dashed line) decay rates normalized to the vacuum decay rate, (Γ/γ_0, $\Gamma_{\rm pl}/\gamma_0$), as a function of θ. The positions of the dipoles are detailed in the main text.

which indicates that β and Γ of both dipoles should be as high as possible. The dependence of β with the angular deviation of the dipole with respect to the electric field polarization is illustrated in Fig. 7.6. Panels (a) and (b) correspond to the cylinder and the channel, respectively. In both cases the emitter position is chosen to maximize β ($h = 20\,$nm for the cylinder, and $h = 150\,$nm for the channel). The dipole moment is parallel to the transverse plane, and the definitions of the angular deviation, θ, are sketched in the diagrams of the corresponding panels. As a general rule, the deviation of the dipole from the electric field direction has a detrimental effect, and β becomes null for $\theta = 90°$. Nevertheless, there is a broad angular range where β remains relatively stable so that it is not critically affected by relatively large misalignements. Figure 7.6 shows that *beta* deviates less than a 10% of the maximum value within a θ-range of $\Delta\theta = 60°$ for cylinders and of $\Delta\theta = 40°$ for channels, proving again the robustness of channel PWs compared to the cylindrical geometry. The functional dependence of β with θ is not simple because although $\Gamma_{\rm pl} \propto \cos\theta$ [see Eq. (7.11)], Γ has a more complex dependence. This can be observed by comparison of the curves in the insets of Fig. 7.6.

After all this numerical evidence, it can be concluded that channel PWs are more suitable to mediate QE interaction than standard cylindrical ones. Thus, from now on the results will be devoted to this type of waveguides unless stated otherwise.

7.5 Entanglement generation

In this Section, we will study in detail the possibility of generating entanglement between two-qubits exploiting all the interesting properties shown for channel PWs. we will explore two different situations: in Sec. 7.5.1 a situation where the two-qubit system is initialized in a given state and then the system is left free to evolve. Then in Sec. 7.5.2, two additional

lasers will be introduced in the scheme that will coherently excite each inducing a stationary situation that depending on the geometry can create entanglement or not.

7.5.1 Spontaneous formation of entanglement

Assuming one puts two identical qubits in front of a channel PW without external pumping, with separation set to $d = \lambda_{\rm pl}$ and their transverse positions and orientations are identical and chosen to maximize the β factor. In this simple but insightful configuration, g_{ij} vanishes and Γ_{ij} attains its maximum value [Fig. 7.5], which means that the two-qubit dynamics is purely dissipative.

As a starting example one can initialize the system in the (unentangled) state $|1\rangle = |e_1 g_2\rangle = \frac{1}{\sqrt{2}}(|+\rangle + |-\rangle)$. In this case the only non-zero elements of the initial density matrix are: $\rho_{++}(0) = \rho_{--}(0) = \rho_{+-}(0) = \rho_{-+}(0) = 1/2$, so the dynamics is confined to the subspace spanned by these three vectors: $\{|0\rangle, |\pm\rangle\}$ where the dynamics is governed by the following set of equations:

$$\begin{aligned}
\dot{\rho}_{++}(t) &= -(\Gamma + \Gamma_{12})\rho_{++}(t) \\
\dot{\rho}_{--}(t) &= -(\Gamma - \Gamma_{12})\rho_{--}(t) \\
\dot{\rho}_{00}(t) &= (\Gamma + \Gamma_{12})\rho_{++}(t) + (\Gamma - \Gamma_{12})\rho_{--}(t), \\
\dot{\rho}_{+-}(t) &= -\Gamma\rho_{+-}(t).
\end{aligned} \tag{7.15}$$

There are only a few non-zero entries in $\rho(t)$ and the resulting expression for the concurrence is very simple:

$$C(t) = \sqrt{[\rho_{++}(t) - \rho_{--}(t)]^2 + 4\mathrm{Im}[\rho_{+-}(t)]^2}, \tag{7.16}$$

where we see that an imbalance of the populations ρ_{++} and ρ_{--} results in a non-zero concurrence ($\rho_{+-}(t)$ is real for the chosen conditions). Solving Eq. (7.15), the concurrence can be obtained analyticaly:

$$C(t) = e^{-\Gamma t} \sinh\left[\Gamma\beta e^{-\lambda_{\rm pl}/(2L_{\rm prop})}t\right]. \tag{7.17}$$

This concurrence and the relevant populations are plotted in Fig. 7.7 as a function of time (C is the black thick line, and ρ_{++}, ρ_{--}, ρ_{33} are the red dashed, blue dotted lines and green lines respectively) and in contour plots as a function of the inter-qubit distance as well. Panel (a) shows the dynamics corresponding an idealized case where $\beta = 1$ and the plasmon propagation length is $L_{\rm prop} = \infty$. The entanglement grows with time monotonically up to a value of $C = 0.5$. This process can be easily understood using Eq. (7.16) and observing the mentioned population imbalance. Since $\Gamma_{12} = \Gamma$, the population ρ_{++} decays at an enhanced rate 2Γ, whereas ρ_{--} stays constant due to its zero decay rate. In the contour plot associated to this panel one observes that this monotonic behavior only occurs at distances $d = n\lambda_p/2$ where $\Gamma = \Gamma_{12}$ for this case, whereas for the rest of the regions the entanglement is lost with time. Panel (b) corresponds to a realistic channel PW with $\beta = 0.9$ and $L_{\rm prop} = 1.7\,\mu$m. In this case the concurrence reaches a maximum value of

$C = 0.33$ for $t \simeq 1/\Gamma$ and then decays exponentially to zero. Again, the entanglement generation is a consequence of the populations imbalance. For this realistic structure both populations have finite decay rates and the concurrence eventually vanishes. The same setup with a cylindrical waveguide produces qualitatively similar results as in Fig. 7.7 (b) but, since $\beta = 0.6$ in this case, the maximum of the concurrence is lower, $C = 0.21$. In all three cases, $|+\rangle$ and $|-\rangle$ are examples of superradiant and subradiant states, respectively. In this configuration, a transitory entanglement builds up spontaneously from an unentangled configuration and this is why it is usually referred as *spontaneous formation of entanglement*. The qualitative picture can be understood very easily from Fig. 7.3: the collective decay rate Γ_{12} creates an asymmetry in the timescale of both sides of the cascades depending on both its sign and absolute value. This asymmetry creates a transitory imbalance of population of both intermediate states $|\pm\rangle$ which is one the contributions creating entanglement in this configuration as can be induced from Eq. (7.16).

For the sake of completeness, we explore other phenomenology related with entanglement in this system. Let us consider a situation where the two-qubit system is initially prepared in a non-maximally entangled state: $|\Phi_0\rangle = \sqrt{q}\,|0\rangle + \sqrt{1-q}\,|3\rangle$, where $0 \leq q \leq 1$. Consequently the initial non-zero elements of the density matrix are: $\rho_{00}(0) = q, \rho_{33}(0) = 1-q, \rho_{03} = \sqrt{q(1-q)}$. So, as in the previous case, the rest of the density matrix remains zero except for the symmetric and antisymmetric populations that build up during the evolution. The expressions for the non-zero elements are given by:

$$\begin{aligned}
\rho_{33}(t) &= qe^{-2\Gamma t} \\
\rho_{++}(t) &= q\frac{\Gamma_+}{\Gamma_-}e^{-2\Gamma t}\left[e^{\Gamma_- t} - 1\right] \\
\rho_{--}(t) &= q\frac{\Gamma_-}{\Gamma_+}e^{-2\Gamma t}\left[e^{\Gamma_+ t} - 1\right] \\
\rho_{03}(t) &= \sqrt{q(1-q)}e^{-(\Gamma - 2i\omega_0)t}\,,
\end{aligned} \tag{7.18}$$

where $\Gamma_\pm = \Gamma \pm \Gamma_{12}$. After a tedious but simple algebra, the following expression for the concurrence $C(t) = \max\{0, C_1(t), C_2(t)\}$ is obtained, where:

$$\begin{aligned}
C_1(t) &= 2|\rho_{03}(t)| - |\rho_{++}(t) + \rho_{--}(t)| \\
C_2(t) &= -2\sqrt{\rho_{00}(t)\rho_{33}(t)} + |\rho_{++}(t) - \rho_{--}(t)|\,.
\end{aligned} \tag{7.19}$$

Considering the limiting case where $q = 1$, so that our initial state is given by $|\Phi_0\rangle = |3\rangle$ (which is unentangled) then the only non-zero element of the initial density matrix is given by $\rho_{33} = 1$. Therefore the $\rho(t)$ remains diagonal during its evolution, being the populations the only non-zero elements:

$$\begin{aligned}
\rho_{33}(t) &= e^{-2\Gamma t}\,, \\
\rho_{++}(t) &= \frac{\Gamma_+}{\Gamma_-}e^{-2\Gamma t}\left[e^{\Gamma_- t} - 1\right], \\
\rho_{--}(t) &= \frac{\Gamma_-}{\Gamma_+}e^{-2\Gamma t}\left[e^{\Gamma_+ t} - 1\right],
\end{aligned} \tag{7.20}$$

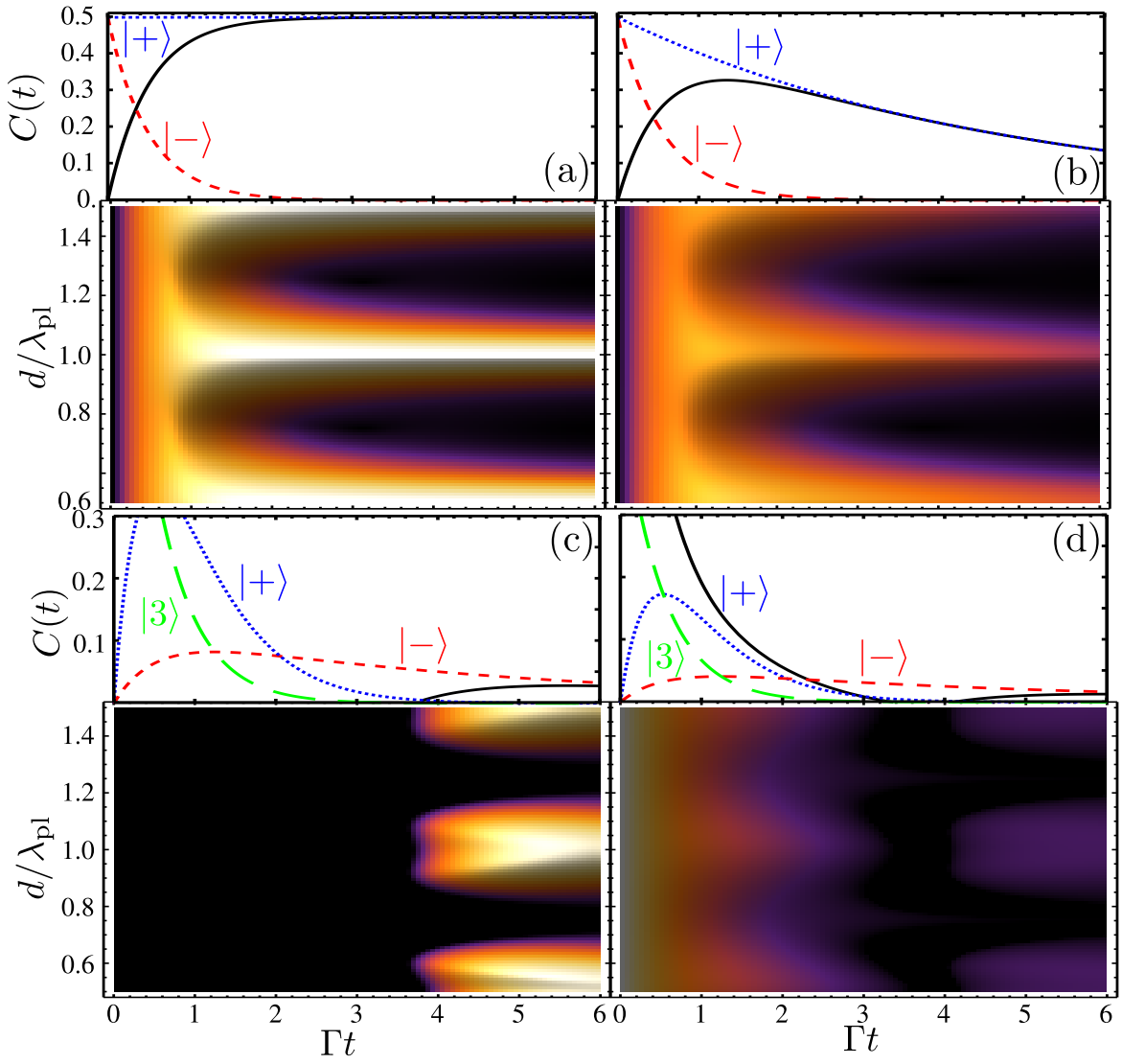

Figure 7.7: Concurrence (black thick line) and populations ρ_{++} (red dashed line), ρ_{--} (blue dotted line) and ρ_{33} (green dashed line) versus time. (a) Ideal PW satisfying $\beta = 1$ and $L_{\text{prop}} = \infty$. (b), (c) and (d) Realistic channel PW. The time is scaled with the emitter lifetime ($1/\Gamma$) for different initial conditions.

After some simple algebra one arrives to the following expression for the concurrence:

$$C(t) = \max\{0, |\rho_{++}(t) - \rho_{--}(t)| - 2\sqrt{\rho_{00}(t)\rho_{33}(t)}\} \tag{7.21}$$

Again, if the difference of population between the symmetric and antisymmetric states overcomes the second term $\rho_{00}\rho_{33}$ in Eq. 7.21, some concurrence can build up. Again, the crucial element is the collective decay rate Γ_{12} and not the coherent coupling g_{12}. In panel (c) of Fig. 7.7 for the parameters of the channel PW a new phenomenon, known as *sudden birth* of entanglement [272, 273] can be found: no concurrence is found for the initial times and suddenly a 2% degree of entanglement is created, with a very slow decay rate.

The double criterion for entanglement in Eq. 7.19 leads also to a very interesting phenomenon, well-known in other systems, which has been called as *revival* of entanglement [274]. In panel (d) of Fig. 7.7, We have plotted the concurrence for a system with $q = 0.5$, which is initially entangled. After a short time, of the order $t/\gamma = 4$ entanglement disappears for a time, but latter it, counterintuitively, revives. The entanglement revival is clearly related with Γ_{12} as one can see in the corresponding contour plot that for distances where it is small, the revival does not take place. Counterintuitively, as the $\{|1\rangle, |2\rangle\}$ (or $|\pm\rangle$) are initially uncoupled, and remain uncoupled forever, the coherent coupling g_{12} of the dipole does not play a significant role in the dynamics of the system, as it can only change one excitation, but not two. The first region of entanglement it is related with $|\rho_{03}|$ which dies after sometime, whereas the revival comes again from the population imbalance between $|\pm\rangle$. Quantitatively, however, the phenomenon is weak and after the revival the maximum entanglement achieved is around 3 %.

7.5.2 Formation of stationary entanglement under external continuous pumping

In the previous Section, it was shown the spontaneous generation of entanglement which is a transient phenomenon. To compensate the depopulation of the upper levels, the system can be externally pumped by means of a laser in resonance with the frequency of the qubits [64, 66, 257] and with intensities $\Omega_{1,2}$. In Fig. 7.3 it was sketched the way the combination of pumping intensities entered in the level scheme of the problem, showing that the population of the symmetric/antisymmetric states $|\pm\rangle$ is proportional to the following combination of intensities: $\Omega_{\pm} = (\Omega_1 \pm \Omega_2)/\sqrt{2}$. The introduction of this pumping term is done through the already introduced Hamiltonian, H_L, which enters in the coherent part of the master equation and driving our system into a steady-state situation calculated by solving the equation $\dot{\rho} = 0$.

The concurrence reached in the corresponding steady state, C_∞, is plotted in panel (a) Fig. 7.8 as a function of both the inter-qubit distance normalized to the modal wavelength, $d/\lambda_{\rm pl}$ and different pumping configurations by fixing Ω_1 and moving Ω_2 in the range $(-\Omega_1, \Omega_1)$. It is very important to realize that we consider now arbitrary separations between the qubits and this implies that both coherent and dissipative dynamics are active, its relative weight depending on d (Fig. 7.5). In this plot darker areas correspond to regions with a high degree of entanglement, whereas white means no entanglement. One can see, as it happened for the transient entanglement that the regions with higher concurrence are found at inter-qubit distances $d = \frac{1}{2}\lambda_{\rm pl}, \lambda_{\rm pl}, \frac{3}{2}\lambda_{\rm pl}, \ldots$, corresponding to distances where $|\Gamma_{12}|$

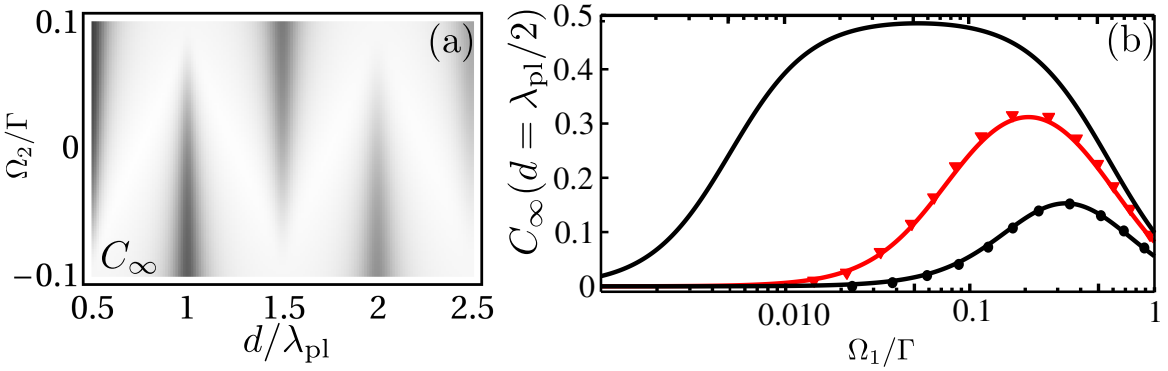

Figure 7.8: Panel (a): Steady state concurrence as a function of the separation between two equal qubits for the parameters of the channel PW and for a pumping configuration with $\Omega_1 = 0.1\gamma$ and Ω_2 ranging from $-\Omega_1$ to Ω_1. Black regions correspond to higher values of concurrence while the white regions correspond to zero concurrence. Panel (b): Steady state concurrence as a function of the driving laser power for asymmetric pumping ($\Omega_1 \neq 0$, $\Omega_2 = 0$) and qubits separation $d = \lambda_{\rm pl}/2$. Ideal case $\beta = 1$ (but finite propagation length) (black line), cylinder $\beta = 0.6$ (black circles), and channel $\beta = 0.9$ (red triangles).

is maximum whereas the region with maximum g_{12} no steady-state entanglement can be found. However, there is also an strong-dependence on the pumping configuration: when $\Omega_2 = 0$, all the maxima of $|\Gamma_{12}|$ are transfered into maxima of entanglement, which is not the case when $\Omega_2 \neq 0$ where also the the sign of Γ_{12} appears to be relevant.

In order to make this behavior more explicit, three cuts on this graphic have been plotted separately in Fig. 7.9 to consider three kinds of coherent driving, differing in the relative phase of the laser fields acting on qubit 1 and 2: symmetric pumping means identical Rabi frequencies, $\Omega_1 = \Omega_2$ [panel (a)], antisymmetric pumping means $\Omega_1 = -\Omega_2$ [panel (b)], and asymmetric pumping corresponds to $\Omega_1 \neq 0$, $\Omega_2 = 0$ [panel (c)]. The absolute value of the non-zero Rabi frequencies is 0.15Γ for the asymmetric pumping and 0.1Γ for the other two situations, *i.e.*, relatively weak. As it was shown in the contour plot, with independence of the pumping scheme the concurrences C_∞ in Fig. 7.8 present an oscillating behavior with the qubits separation, and now it is better resolved that is also damped due to the plasmon absorption. Importantly, the concurrence maxima occur for those $d/\lambda_{\rm pl}$ where the absolute value of Γ_{12} is maximum (Fig. 7.5). When the pumping is symmetric [panel (a)], the laser populates the symmetric state $|+\rangle$. This state is subradiant for $d = \frac{1}{2}\lambda_{\rm pl}, \frac{3}{2}\lambda_{\rm pl}, \ldots$ leading to a population imbalance and the corresponding concurrence. For $d = \lambda_{\rm pl}, 2\lambda_{\rm pl}, \ldots$, $|+\rangle$ is superradiant and the pumping is not able to induce a significant ρ_{++} population. For antisymmetric pumping [panel (b)] it is the state $|-\rangle$ which is populated. This state is subradiant for $d = \lambda_{\rm pl}, 2\lambda_{\rm pl}, \ldots$ again leading to a population imbalance and entanglement. For $d = \frac{1}{2}\lambda_{\rm pl}, \frac{3}{2}\lambda_{\rm pl}, \ldots$, the situation is reversed. Finally, for asymmetric pumping [panel (c)] both $|+\rangle$ and $|-\rangle$ are populated and the situation is a mixture of the previous two. In this case, maxima are found for $d = \frac{1}{2}\lambda_{\rm pl}, \lambda_{\rm pl}, \frac{3}{2}\lambda_{\rm pl}, \ldots$, their concurrence being slightly smaller than that found for the symmetric or antisymmetric pumping.

At this point we have only studied the dependence of entanglement on the relative phase-shifts on the laser, however for an experimental implementation of our proposal, it is impor-

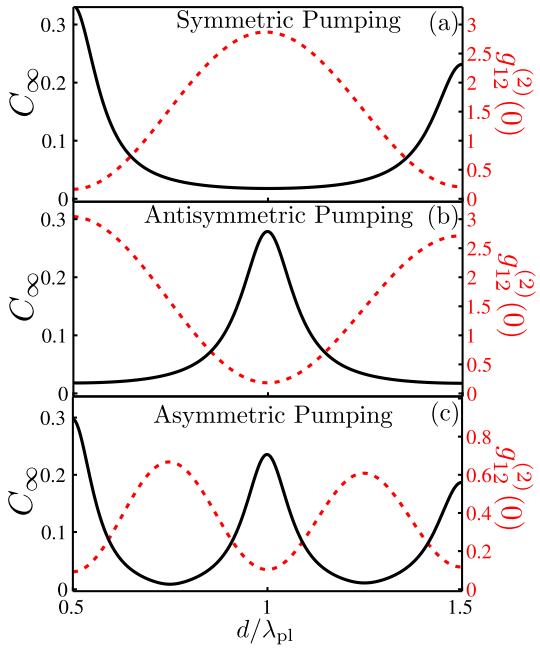

Figure 7.9: Steady state concurrence (black line) and qubit-qubit correlation (red dashed line) as a function of the normalized separation $d/\lambda_{\rm pl}$. (a) Symmetric pumping ($\Omega_1 = \Omega_2 = 0.1\gamma$), (b) antisymmetric pumping ($\Omega_1 = -\Omega_2 = 0.1\gamma$), and (c) asymmetric pumping ($\Omega_1 = 0.15\gamma$, $\Omega_2 = 0$).

tant to determine the pumping rate range for which the described phenomena can happen and is optimized. The influence of the pumping intensity is analyzed in panel (b) of Fig. 7.8, which renders C_∞ versus Ω_1/Γ. Here asymmetric pumping is considered and a qubit separation $d = \lambda_{\rm pl}/2$. The results are computed for three waveguides: a cylinder ($\beta = 0.6$, black circles), a channel ($\beta = 0.9$, red triangles), and a waveguide with perfect coupling ($\beta = 1$) but with some absorption (finite $L_{\rm prop}$). Each structure presents an optimum pumping power to achieve maximum concurrence. In order to obtain a non-negligible concurrence, the sub-radiant state has to be populated at a rate faster than its lifetime, which explains both why concurrence is small at low pumping rates and why the structures with lower β require a higher pumping to reach their optimum entanglement. In an ideal case with perfect coupling and no absorption ($L_{\rm prop} \to \infty$) the sub-radiant states are completely uncoupled from the dynamics and the optimal entanglement is achieved at $\Omega \to 0$. In fact, defining $\bar{\beta} = \beta e^{-\lambda_{\rm pl}/(2L_{\rm prop})}$, the optimal pumping can be approximated in this asymmetric configuration to:

$$\Omega_{\rm opt}/\Gamma \approx \frac{\sqrt{1-\bar{\beta}}}{2}\,. \tag{7.22}$$

In addition, one observes that the maximum attainable concurrence improves for higher β factor, which again justifies the use of channel instead of cylindrical PWs. At very high pumping rates, the laser manages to populate all the states equally, killing the population imbalance between $|\pm\rangle$ and quenching the entanglement is all kind of PWs.

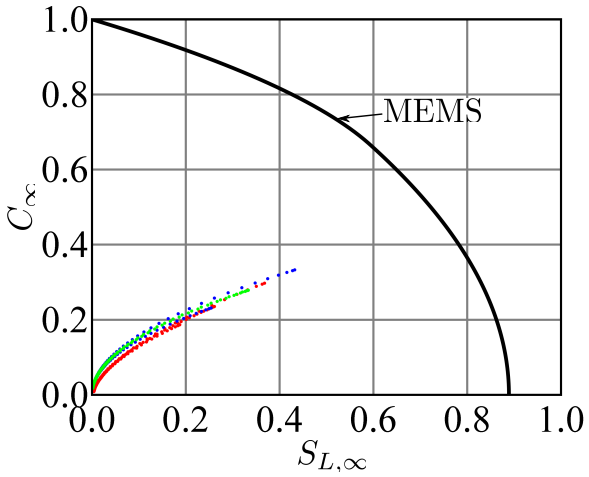

Figure 7.10: Concurrence-Linear entropy diagram for channel PW system parameters with each point corresponding to different inter-qubit distance ranging from $d/\lambda_{\rm pl} = 0.5 - 1.5$, whereas the three different color correspond to three different pumping configurations considered before: asymmetric (red), symmetric (blue), and anti (green)

7.5.2.1 Concurrence-Purity diagram.

The dissipative environment has as a consequence that the quantum state of the system is never pure. Its degree of purity, together with concurrence, is very relevant for its possible application in quantum information protocols [275]. One standard measurement for characterizing the degree of mixture of a system with a given ρ density matrix is the *linear entropy* [276] defined as:

$$S_L = \frac{4}{3}\big(1 - \mathrm{Tr}(\rho^2)\big) \tag{7.23}$$

When one has a pure state then $\mathrm{Tr}(\rho^2) = 1$ so the linear entropy becomes $S_L = 0$, whereas for a maximally mixed state $\mathrm{Tr}(\rho^2) = 1/4$ so that $S_L = 1$. However, the most interesting regime for us is what happens in between when some entanglement is present but the purity of your system is not perfect. It is well-known that if a density matrix is describing a two-qubit system with a certain degree of mixture, then there is a maximum degree of entanglement this system may achieve by means of unitary transformations. These states are usually called *Maximally Entangled Mixed States* and were first proposed by Ishizaka and Hiroshima [277] and they occupy a region the concurrence-linear entropy diagram [278] below the black line in Fig. 7.10. We have included the points resulting from the calculations in our channel PW system for the three different pumping configuration that we used for Fig. 7.9 where one can check how the distance from the *Maximally Entangled Mixed States*, which could be reduced with higher values of β's.

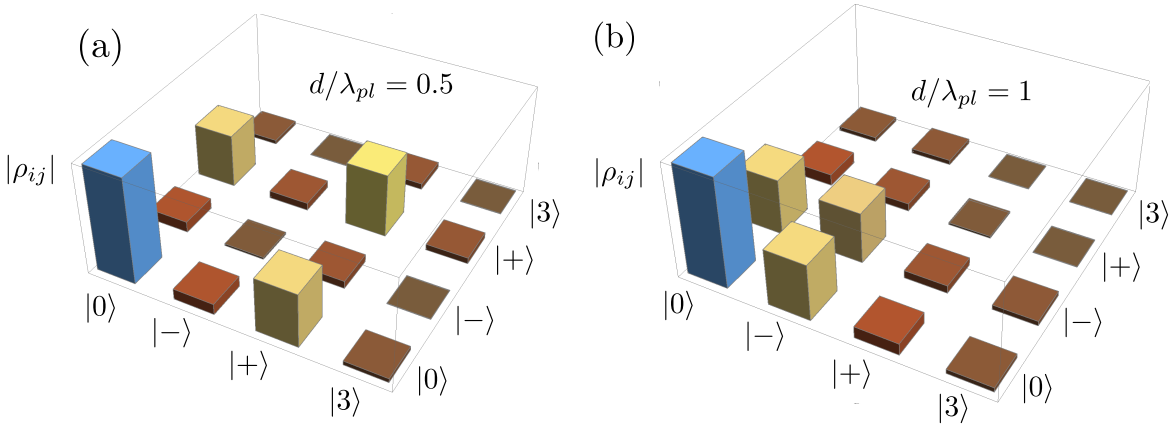

Figure 7.11: Tomography of the absolute value of the elements of the steady state density matrix for asymmetric pumping ($\Omega_1 = 0.15\gamma$, $\Omega_2 = 0$). (a) $d = \lambda_{\rm pl}/2$, and (b) $d = \lambda_{\rm pl}$.

7.5.2.2 Experimental characterization.

Hitherto, it has only been considered the theoretical optimization of the generation of entanglement but from a practical perspective it is also interesting to consider how the experimental characterization of this system can be done. It has been shown before that in order to theoretically calculate concurrence one needs the information of the whole density matrix. This information can also be obtained through quantum tomography experiments, which are routinely done in other systems and have started to be successfully applied as well in plasmonic systems [61]. In Fig. 7.11 is plotted the output of quantum tomography of the steady state of our system. It has been chosen the case of asymmetric pumping and two different qubit separations. In panel (a) $d = \lambda_{\rm pl}/2$ and, besides the population of the ground state, one recognizes the large ρ_{++} population of the subradiant state $|+\rangle$ driven by the pumping, and the negligible ρ_{--} population of the superradiant state $|-\rangle$. For $d = \lambda_{\rm pl}$ [panel (b)], one can observe a large ρ_{--} population of the subradiant state $|-\rangle$ driven by the pumping, and a negligible ρ_{++} population of the superradiant state $|+\rangle$. Let us remark that, strictly speaking, Eq. (7.16) is not correct when pumping is included, because now further elements of ρ are non zero. However, the tomography shows that these additional elements are very small and Eq. (7.16) should be approximately valid, reinforcing the argument that population imbalance leads to concurrence.

Once the tomography of the density matrix is known, the calculation of concurrence (or any other equivalent entanglement quantifier) is straightforward. However, tomographic procedures are experimentally cumbersome and, for this reason, it is of interest to establish connections between entanglement and other more easily measurable magnitudes. Among these magnitudes one counts with the correlations between the emitted photons as already introduced in detail in Chapter 2. In our two-qubit system, entanglement is associated to the probabilities that each state is given by $|+\rangle$ or $|-\rangle$. Restated in other words, entanglement requires having strong correlation between the states $|1\rangle = |e_1 g_2\rangle$ and $|2\rangle = |g_1 e_2\rangle$. As a consequence, the correlation of the photons emitted in the decay of the qubits, which is related to the correlation of the qubits themselves, should contain information about the

two-qubit entanglement degree. Photon-photon correlations can be detected in a Hanbury Brown- Twiss- like experiment (detailed in Chapter 2) measuring the cross-term second order coherence function which, for zero delay, takes the form [77, 262]

$$g_{12}^{(2)} = \frac{\langle \hat{\sigma}_1^\dagger \hat{\sigma}_2^\dagger \hat{\sigma}_2 \hat{\sigma}_1 \rangle}{\langle \hat{\sigma}_1^\dagger \hat{\sigma}_1 \rangle \langle \hat{\sigma}_2^\dagger \hat{\sigma}_2 \rangle} \,. \tag{7.24}$$

Figure 7.9 displays together the concurrence C_∞ (black continuous lines) and the second order correlation function at zero delay $g_{12}^{(2)}$ (red dashed lines). In all three panels it is observed that when C_∞ is large, a clear antibunching ($g_{12}^{(2)} \to 0$) takes place, which is consistent with the system predominantly being in a state $|+\rangle$ or $|-\rangle$. On the other hand, when $C_\infty \to 0$, $g_{12}^{(2)}$ grows and the antibunching is reduced, which is now consistent with a decreased correlation between $|1\rangle$ and $|2\rangle$. The main result to be drawn is the distinct relationship between C_∞ and $g_{12}^{(2)}$. Lacking an analytical expression relating C_∞ and $g_{12}^{(2)}$, our results clearly support the idea of measuring cross-terms of the second order coherence, at zero delay, as a manifestation of entanglement [115]. Experimentally, this two-photon cross correlation can be done in two-different ways: firstly, by detecting the photons emitted to vacuum from each qubit, as β-factor is never 1, or basically detecting the plasmon emitted by each of the emitters. Both approaches have it pros and cons: while photon-correlations are a straightforward measure, the light emitted from the qubit will be presumably small as β-factor is close to 1 and this increases the noise ratio in the measurement. On the other hand, plasmon are the main decay channel but single-plasmon detection technology has just been recently developed [255, 256] and some time is needed until two-plasmon correlations are controlled experimentally.

7.5.2.3 Degradation due to pure dephasing.

Finally, the focus is set on the degradation of entanglement with an ubiquitous element present in solid-state emitters: *pure dephasing*. In Chapters 3 and 5, we have already pointed that it is a very important ingredient in semiconductor QED and molecular systems, where the fluctuating environment in the former and the coupling to vibro-rotational degrees of freedom in the latter may induce this kind of dephasing affecting the coherence of the system without having a direct effect on population. In order to study the robustness of our proposal against this unavoidable element, one needs to compute again the dynamics of the system including now in the master equation (7.3) an additional term representing pure dephasing. Even though, it has already been introduced before, we rewrite the formula of this new Lindblad term in the master equation [115, 139]:

$$\mathcal{L}_{\rm deph}[\hat{\rho}] = \frac{\Gamma^\phi}{2} \sum_i \Big[[\hat{\sigma}_i^\dagger \hat{\sigma}_i, \hat{\rho}], \hat{\sigma}_i^\dagger \hat{\sigma}_i \Big]. \tag{7.25}$$

The value of the dephasing rate Γ^ϕ is very dependent on the particular realization of the qubit. In our calculations we use values that can be achieved for nitrogen-vacancy centers in diamond, where dephasing times as large as milliseconds have been reported [279, 280]. This corresponds to Γ^ϕ in the range of a few tenths of the emission rate Γ. Figure 7.12 shows the steady state concurrence as a function of the qubit-qubit separation d for different

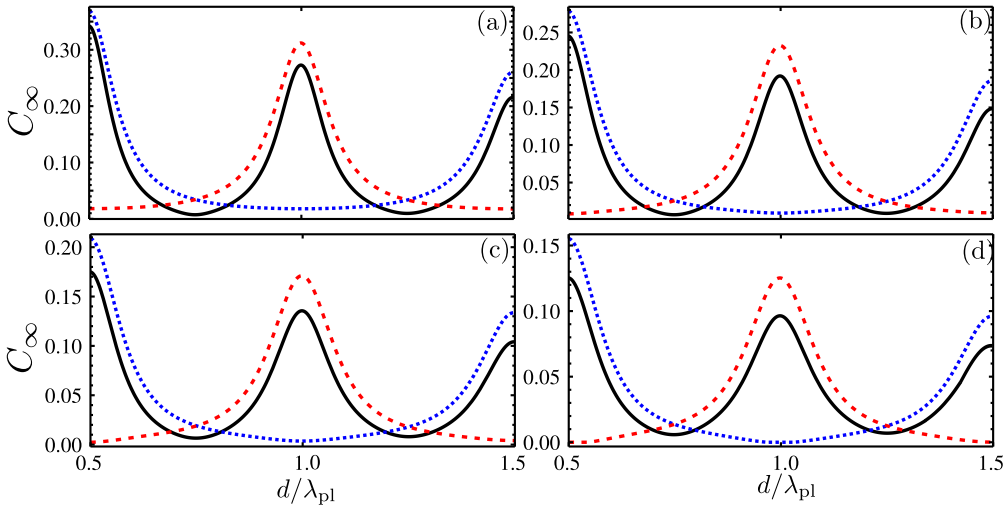

Figure 7.12: Steady state concurrence as a function of the normalized separation $d/\lambda_{\rm pl}$ for different pumping conditions and dephasing rates. (a) $\Gamma^\phi/\Gamma = 0.0$, (b) $\Gamma^\phi/\Gamma = 0.1$, (c) $\Gamma^\phi/\Gamma = 0.2$ and (d) $\Gamma^\phi/\Gamma = 0.3$. In all panels the blue dotted (symmetric pumping) ($\Omega_1 = \Omega_2 = 0.1\Gamma$), the red dashed lines (antisymmetric pumping) ($\Omega_1 = -\Omega_2 = 0.1\Gamma$), and the black solid lines (asymmetric pumping) ($\Omega_1 = 0.15\Gamma$, $\Omega_2 = 0$).

values of the pure dephasing rate and various pumping conditions. Dephasing grows from zero in panel (a) to $\Gamma^\phi/\Gamma = 0.3$ in panel (d). The qualitative behavior is the same in all panels but the value of C_∞ decreases as the dephasing rate grows (notice that the vertical scale is not the same in all panels). Nevertheless, the value of the concurrence maxima are non-negligible even in the worst case of panel (c). Moreover, this decrease can be partially compensated by increasing the intensity of the pumping laser. Therefore, our results show that pure dephasing reduces qubit-qubit entanglement but not as much as to preclude its formation by the mediation of the surface modes supported by 1D plasmonic waveguides.

7.6 Conclusions

In this Chapter, it has been presented a detailed analysis of how plasmonic waveguides can be used to achieve a high degree of entanglement between two distant qubits. A full account of the theoretical framework has been also described. Importantly, the degrees of freedom associated with the surface plasmons can be traced out, leading to a master equation formalism for the two qubits in which the two contributions to the effective interaction between them (coherent and dissipative terms) are then obtained by means of the *classical* electromagnetic Green's function.

It has also been shown that the main ingredients to obtain a high value for the concurrence are a large β-factor and the one-dimensional character of the surface modes supported by the plasmonic waveguide. By studying how steady-state entanglement can be generated, it has been demonstrated that the dissipative part of the qubit-qubit interaction mediated by plasmons is the main driving force in order to achieve entanglement. It has also been

analyzed the sensitivity of this plasmon-mediated entanglement to different parameters, such as the dipole orientations of the qubits, the pumping rate, and the inherent presence of dephasing mechanisms in the system. In all cases, it has been found that the dissipation-driven generation of entanglement is robust enough to be observed experimentally by using plasmonic waveguides that are currently available.

Finally, some experimental alternatives to characterize entanglement have been proposed. The measurement of the cross-term second order coherence function appears a solid candidate to characterize entanglement due to its connection with low values of concurrence.

Chapter 8

Entanglement of many qubits mediated by one-dimensional electromagnetic modes

8.1 Introduction.

During the first part of this Thesis, we have focused in physical systems where artificially designed atoms in solid-state setups, like quantum dots or nitrogen vacancy centers (NV), coupled deterministically to photonic cavities [28–30]. An important application of those systems is quantum information processing in solid devices [15], where artificial atoms acting as qubits are placed within the e.m. field confined in a microcavity. Typically, the realization of those ideas requires unitary qubit- field evolutions and a natural candidate is to consider collective couplings to a single mode in a cavity.

To conclude this Thesis, we are going to focus on a generalization of the idea of the previous Chapter where we showed how interesting applications can be found relying not in coherent unitary evolution but rather in the dissipative effects coming from the bath. The general idea relies in the fact that if one is able to tailor the interaction with the environment wisely one can induce quantum correlations in the steady-state [20] which has been experimentally proved to be a powerful tool to generate entanglement between atomic ensembles [23].

We upgrade the discussion of the previous Chapter in three ways:

- Firstly, we do not focus on a particular realization of waveguides like in the previous Chapter were a special emphasis was made on a particular configuration of plasmonc waveguides. We only assume the one-dimensional character of the modes.
- We consider a situation with more than two-emitters, so that it exists the possibility of generation many-qubit entanglement.
- Finally, apart from the simple 2LS configuration for the qubit, we consider a more elaborate scheme involving a four-level scheme. This scheme leaves us the possibility to further control the effective quantum state of the system by using with additional laser fields, being able to achieve a higher degree of entanglement than with simple 2LS.

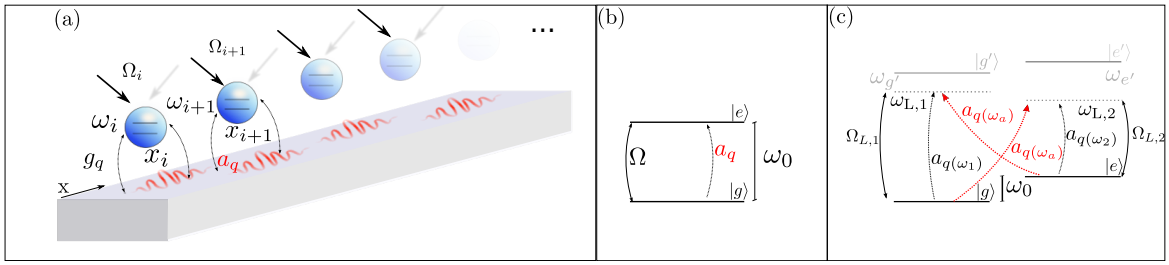

Figure 8.1: (a): Experimental scheme of the system: ensemble of equally-spaced qubits placed in the vicinity of a one-dimensional waveguide. (b): Two-level system configuration with resonant excitation. Panel (c): Four-level system configuration with two-additional lasers, where we impose the condition: $\omega_{\mathrm{L},1} - \omega_0 = \omega_{\mathrm{L},2} + \omega_0 = \omega_a$ and define $\omega_1 = \omega_{\mathrm{L},1}$, $\omega_2 = \omega_{\mathrm{L},2} - \omega_0$.

The structure of the Chapter is the following: first, we briefly introduce the scheme of the system in Section 8.2. Then, we show the results where the quantum emitters are simple 2LS, in Section 8.3, and four-level systems in Section 8.4. Finally, we explore the experimental feasibility with the current state-of-art parameters in Section 8.5 and conclude in Section 8.6.

8.2 System configuration.

The general scheme of the system studied within this Chapter is depicted in Fig, 8.1: an ensemble of identical qubits is placed in front of a one-dimensional waveguide, which contains a continuum of EM field. Even in the absence of direct coupling between the qubits, the coupling to a common bath induces a controllable dissipative (and coherent) coupling between the qubits.

In this Chapter we study in detail two possible configurations for the qubits. Firstly, the qubits will be simple 2LS as sketched in Fig. 8.1(b). The possibility of deterministically position the artificial atoms or qubits allows us to engineer the paradigm for quantum optical collective effects, i.e. the Dicke model of superradiance [281] in its pure form. The observation of the latter in optical systems is hindered due to dephasing caused by dipole-dipole interactions [81, 282]. In my scheme, those interactions can be switched off by an appropriate choice of the inter-qubit distance, similarly to what we showed in the previous Chapter. Adding a classical drive to the pure Dicke model one obtains a dissipative system with a phase diagram of steady states showing mesoscopic spin squeezing and entanglement. Even though this model has been theoretically investigated in the past [283–285], the experimental realizations have been scarce.

Finally, we study a more complicated and flexible configuration for the qubits as shown in 8.1(c). Here, we consider that the two-level system needed to describe qubits are the lowest level of a 4-level emitter scheme, reminiscent to atomic system, which has been recently proposed in the solid state context [286, 287]. Then. we show that again by a judicious choice of couplings to the waveguide and dispersion relations may lead to a variety of many-body dissipative models which show entangled steady-states.

8.3 Entanglement generation for two level systems.

In this Section, the qubits are modeled by simple 2LS. We consider the set of N 2LS, $\{|g\rangle_n, |e\rangle_n\}_{n=1...N}$, placed at positions x_n and coupled to a one dimensional field (Fig. 8.1(a)) with photon annihilation operators a_q, described by the Hamiltonian $H = H_0 + H_{\rm I}$. The free term is $H_0 = H_{\rm qb} + H_{\rm field}$,

$$H_{\rm qb} = \frac{\omega_0}{2}\sum_{n=1}^{N}\sigma_n^z, \qquad H_{\rm field} = \sum_q \omega_q a_q^\dagger a_q, \tag{8.1}$$

where ω_0 is the qubit energy (Fig. 8.1(b)) and ω_q is the field dispersion relation. The Pauli matrices are defined as $\sigma_n^z = |e\rangle_n\langle e| - |g\rangle_n\langle g|$, $\sigma_n^+ = |e\rangle_n\langle g|$, $\sigma_n^- = |g\rangle_n\langle e|$. The photon polarization is neglected to focus on the most relevant physics of our work. We consider a dipolar coupling of the form

$$H_{\rm I} = \sum_n \left(\sigma_n E(x_n) + \text{H.c.}\right), \tag{8.2}$$

with $E(x) = \sum_q g_q(a_q e^{iqx} + a_q^\dagger e^{-iqx})$, and g_q is a dipolar qubit-field coupling. In the weak coupling limit, the evolution of ρ, the reduced density matrix for the qubits, can be described by a markovian master equation of the form $d\rho/dt = \mathcal{L}(\rho)$, with the superoperator

$$\mathcal{L}(\rho) = \sum_{n,m} J_{n,m}\left(\sigma_n^-\rho\sigma_m^+ - \rho\sigma_m^+\sigma_n^-\right) + \text{H.c.}. \tag{8.3}$$

A detailed derivation is given in Appendix II following the description in dimensions higher than one presented in previous works [81]. Special care must be paid to the counter rotating terms in (8.3), which have to be included to get the following result for the collective decay rates

$$J_{n,m} \;=\; \frac{\Gamma}{2}e^{iq(\omega_0)|x_n - x_m|}. \tag{8.4}$$

We define $\Gamma = \gamma(\omega_0)$, with the function $\gamma(\omega) = g_{q(\omega)}^2 D(\omega)/\pi$, where $q(\omega)$ is the resonant wavevector at ω, and we have defined the e.m. density of states, $D(\omega) = (2\pi/L)|dq(\omega)/d\omega|$, with L the quantization length. A crucial observation for this work, is that couplings $J_{n,m}$ do not decay with the distance [1], a situation that is singular of one dimensional waveguides. On the contrary in free space collective couplings decay like $1/r$ or $1/r^3$, depending on the relative dipole orientation [81]. For completeness in Section 8.5, we make a thorough study of the effect the possible experimental imperfections on the results obtained.

Homogeneous couplings $J_{n,m} = \Gamma/2$ can be obtained from Eq. (8.4) by the choice $x_n = n\lambda_0$, with $\lambda_0 = 2\pi/q_0$, and $n \in \mathbb{Z}$. This condition cancels coherent dipole-dipole interactions and we get the pure Dicke superradiant decay described by

$$\mathcal{L}_{\rm D}(\rho) = \frac{\Gamma}{2}\left(S^-\rho S^+ - S^+S^-\rho\right) + \text{H.c.}, \tag{8.5}$$

[1] Eventually, couplings decay due to the finite propagation length of the modes caused by experimental imperfections and/or ohmic losses. However, in principle these difficulties can be overcome with suitable engineering. State of art propagation lengths are already of the order of several times the wavelength of the guided mode

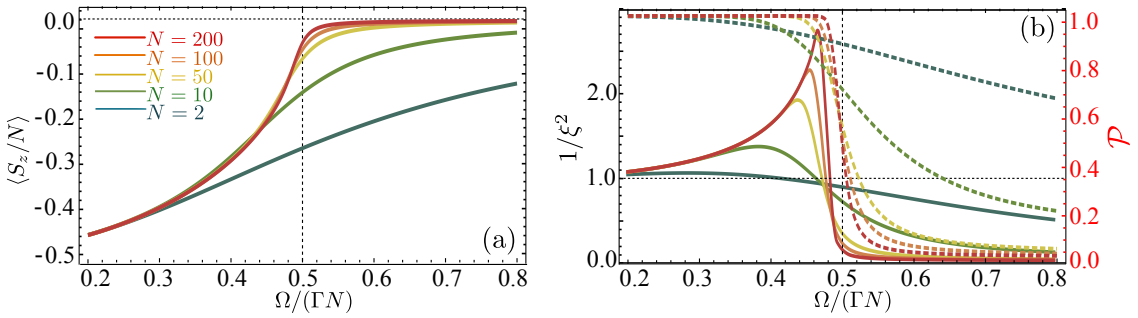

Figure 8.2: Numerical results for the coherently pumped Dicke model (8.6). Different colors represent different number of qubits from $N = 2$ (blue) to $N = 200$ (red) as shown in the legend. (a) Population inversion $\langle S_z\rangle/N$. (b) Purity $\mathcal{P}$ (dashed) and spin-squeezing parameter $1/\xi^2$(solid).

with $S^- = \sum_n \sigma_n^-$, $S^+ = \sum_n \sigma_n^+$. We also define $S_\alpha = \sum_n \sigma_n^\alpha/2$ ($\alpha = x, y, z$), and the basis $\{|J, M\rangle\}$ of eigenstates of $\vec{S}^2$, S_z. Assuming an initial state like $|\Psi_0\rangle = \otimes_n |e\rangle_n = |N/2, N/2\rangle$ the system evolves within the sector $J = N/2$. We stress that as an important point: Dicke superradiant decay is achieved in one dimension without the restriction that the whole atomic ensemble is confined within a region of length λ_0.

In this work we focus on the qubit steady-state, ρ_s, which for a given Liouvillian fulfills $\mathcal{L}(\rho_s) = 0$. To achieve controllability on ρ_s, we add a pump term which physically can be implemented by the interaction of qubits with a resonant field with Rabi frequency Ω,

$$\mathcal{L}_{D,p}(\rho) = \mathcal{L}_D(\rho) - i\frac{\Omega}{2}[S_x, \rho]. \tag{8.6}$$

Competition between the collective decay and the pumping leads to a non-equilibrium phase transition in the steady-state of the model at a critical pumping rate $\Omega_c = N\Gamma/2$ [283], manifested in a kink in the population inversion observable $\langle S_z\rangle$, see Fig. 8.2(a). Let us first give a brief description of the two limiting cases:

- *Coherent steady state regime*, $\Omega \ll N\Gamma/2$. Since $\mathcal{L}_{D,p}$ can be obtained from $\mathcal{L}_D$ by the substitution $S^- \to S^- + i\Omega/(2\Gamma)$, one can easily show that $\rho_s = |\Psi_c\rangle\langle\Psi_c| + \mathcal{O}^2(\frac{\Omega}{\Gamma})$, where $|\Psi_c\rangle = e^{i\frac{\Omega}{\Gamma}S_x}|N/2, -N/2\rangle$ is a spin coherent state.

- *Mixed state phase*, $\Omega \gg N\Gamma/2$. Here we get an infinite temperature state. To show this, it is convenient to write $\mathcal{L}_D$ in the interaction picture with respect to $\Omega S_x/2$. This accounts to replace $S^- \to S_x + (1/2)(\cos(t)S_y + \sin(t)S_z)$. Averaging over time, leads to

$$\mathcal{L}_{D,p} \approx \frac{\Gamma}{2}\left(S_x\rho S_x - S_x^2\rho + \frac{1}{2}\sum_{\alpha=y,z}\left(S_\alpha\rho S_\alpha - S_\alpha^2\rho\right)\right) + \text{H.c.}. \tag{8.7}$$

  which has the infinite temperature state $\rho_s = \mathbf{1}$ as steady-state.

For calculations in the intermediate regime we use the full solution in the $|J, M\rangle$ basis. To quantify many-particle entanglement we use spin-squeezing ξ as a figure of merit,

$$\xi^2 = \frac{N(\Delta S_x)^2}{\langle S_y\rangle^2 + \langle S_z\rangle^2}\,. \tag{8.8}$$

ξ is both an entanglement witness and it is also linked to applications in quantum metrology [288–290]. Values $\xi < 1$ are spin-squeezed states which can be proved to be entangled [289]. Note that the above mentioned (i) and (ii) phases lead to $\xi = 1$ and $\xi = \infty$, respectively. Another theoretical tool to be used is the purity, defined by $\mathcal{P}(\rho) = \mathrm{Tr}(\rho^2)$. Both magnitudes are plotted for different number of qubits N in Fig. 8.2. We find a range of pumping fields ($\Omega \leq \Omega_c$) at the on-set of the phase transition which combine entanglement and high purity. This result may lead to the generation of entanglement between many qubits in mesoscopic samples of artificial atoms.

8.4 Entanglement generation with four-level systems.

In order to get a more stable and flexible situation, in this Section, the simple 2LS is upgraded into a 4-level system (4LS) configuration (see Fig. 8.1(c)). This scheme, inspired in atomic system, can now be realized in the solid-state context with quantum dots or nitrogen vacancy centers [286, 287] and describes a variety of possible configurations in which a set of low-level states are coupled to excited states by lasers with different polarizations. Two low energy states ($|g\rangle_n, |e\rangle_n$) are coupled to high energy states ($|g'\rangle_n$, $|e'\rangle_n$). The qubit part of the free Hamiltonian becomes now;

$$H_{\mathrm{qb}} = \sum_n (\omega_{g'} |g'\rangle_n\langle g'| + \omega_{e'} |e'\rangle_n\langle e'| + \omega_g |g\rangle_n\langle g|)\,. \tag{8.9}$$

Two weak non-resonant fields with amplitudes $\Omega_{\mathrm{L},1(2)}$ and frequencies $\omega_{\mathrm{L},1(2)}$, induce transitions described by a Hamiltonian term:

$$H_{\mathrm{L}} = \sum_n ((\Omega_{\mathrm{L},1}/2)|e'\rangle_n\langle e|e^{-i\omega_{\mathrm{L},1}t} + (\Omega_{\mathrm{L},2}/2)|g'\rangle_n\langle g|e^{-i\omega_{\mathrm{L},2}t} + \mathrm{H.c.})\,. \tag{8.10}$$

8.4.1 Adiabatic elimination of the excited state.

The complete hamiltonian that describes the time-dependent laser fields of the four-level system coupled to the continuum of modes of panel (c) in Fig. 8.1 can be written in the *Schrödinger picture* as follows:

$$\begin{aligned} H &= \sum_q \omega_q a_q^\dagger a_q + \omega_{g'}|g'\rangle\langle g'| + \omega_{e'}|e'\rangle\langle e'| + \omega_0|e\rangle\langle e| \\ &+ \frac{\Omega_{L,1}}{2}\left(|g\rangle\langle g'|e^{i\omega_{\mathrm{L},1}t} + H.c.\right) + \frac{\Omega_{L,2}}{2}\left(|e\rangle\langle e'|e^{i\omega_{\mathrm{L},2}t} + H.c.\right) \\ &+ \sum_q g_q\left((|g'\rangle\langle e| + |e\rangle\langle g'|)a_q + H.c.\right) + \sum_q g_q\left((|e'\rangle\langle g| + |g\rangle\langle e'|)a_q + H.c.\right) \\ &+ \sum_q g_q\left((|g'\rangle\langle g| + |g\rangle\langle g'|)a_q + H.c.\right) + \sum_q g_q\left((|e'\rangle\langle e| + |e\rangle\langle e'|)a_q + H.c.\right) \end{aligned}$$

We impose the condition

$$\omega_{\mathrm{L},1} - \omega_0 = \omega_{\mathrm{L},2} + \omega_0 = \omega_a, \tag{8.11}$$

so that the two decay channels in red into modes a_q, correspond to photon emission with the same energy ω_a. Obviously, there are two non-desirable extra decay channels with mode

energy $\omega_{\mathrm{L},1}$ and $\omega_{\mathrm{L},2}-\omega_0$ that creates a dephasing term in the dynamics as we show afterwards. Now, one can go to a rotating frame where the classical fields are not oscillating in time just by the following unitary operation,

$$U = e^{i(\omega_1|g'\rangle\langle g'|+\omega_2|e'\rangle\langle e'|)t}. \tag{8.12}$$

The resulting Hamiltonian after the transformation, $H \to UHU^\dagger + iU^\dagger\dot{U}$, has the following form:

$$\begin{aligned} H &= \sum_k \omega_q a_q^\dagger a_q + \Delta_1|g'\rangle\langle g'| + \Delta_2|e'\rangle\langle e'| + \omega_0|e\rangle\langle e| \\ &+ \frac{\Omega_{L,1}}{2}\left(|g\rangle\langle g'| + H.c.\right) + \frac{\Omega_{L,2}}{2}\left(|e\rangle\langle e'| + H.c.\right) \\ &+ \sum_q g_q\left((|g'\rangle\langle e|e^{i\omega_{\mathrm{L},1}t} + |e\rangle\langle g'|e^{-i\omega_{\mathrm{L},1}t})a_q + H.c.\right) \\ &+ \sum_q g_q\left((|e'\rangle\langle g|e^{i\omega_{\mathrm{L},2}t} + |g\rangle\langle e'|e^{-i\omega_{\mathrm{L},2}t})a_q + H.c.\right) \\ &+ \sum_q g_q\left((|g'\rangle\langle g|e^{i\omega_{\mathrm{L},1}t} + |g\rangle\langle g'|e^{-i\omega_{\mathrm{L},1}t})a_q + H.c.\right) \\ &+ \sum_q g_q\left((|e'\rangle\langle e|e^{i\omega_{\mathrm{L},2}t} + |e\rangle\langle e'|e^{-i\omega_{\mathrm{L},2}t})a_q + H.c.\right)\,, \end{aligned} \tag{8.13}$$

where we have defined:

$$\Delta_{1,2} = \omega_{g',(e')} - \omega_{\mathrm{L}.1(2)}\,. \tag{8.14}$$

This Hamiltonian is still time-dependent but it is still possible to do an adiabatic elimination of the excited states as long as $\Omega_{\mathrm{L},1(2)} << \Delta_{1(2)}$ by applying the following canonical transformation $U = e^{-S}$, where:

$$S = \frac{\omega_{\mathrm{L},1}}{2\Delta_1}(|g'\rangle\langle g| - |g\rangle\langle g'|) + \frac{\omega_{\mathrm{L},2}}{2\Delta_2}(|e'\rangle\langle e| - |e\rangle\langle e'|)\,. \tag{8.15}$$

The transformed Hamiltonian, $H \to e^S H e^{-S}$, up to order $O(\frac{\Omega^2_{\mathrm{L},1,2}}{2\Delta_{1,2}})$ and neglecting the terms which are proportional to the excited state populations, can be cast

$$H = \sum_q \omega_q a_q^\dagger a_q + \omega_0|e\rangle\langle e| + H_{\mathrm{I}}^{sq}(t) + H_{\mathrm{I}}^{z}(t)\,, \tag{8.16}$$

where $H_{\mathrm{I}}^{sq}(t)$ is given, in the *interaction picture*, by

$$H_{\mathrm{I}}^{\mathrm{sq}}(t) = \kappa E(x_0,t)(D^\dagger e^{i\omega_a t} + De^{-i\omega_a t})\,, \tag{8.17}$$

where $\kappa^2 = (\Omega_{\mathrm{L},1}/2\Delta_1)^2 - (\Omega_{\mathrm{L},2}/2\Delta_2)^2$ is a normalization constant. $D = u\sigma^- + v\sigma^+$ is a jump operator resulting from the cross radiative decay, with $u = \kappa^{-1}\Omega_{\mathrm{L},1}/2\Delta_1$, $v = \kappa^{-1}\Omega_{\mathrm{L},2}/2\Delta_2$, fulfilling $u^2 - v^2 = 1$. The latter condition will be useful in the discussion below, and allows us to characterize the degree of squeezing by a single parameter r, with $u = \cosh(r)$ and $v = \sinh(r)$.

The last term contains the contribution from the direct radiative process (non-diagonal processes in the scheme of Fig. 8.1(c)) and can be written in the *interaction picture*,

$$H_{\rm I}^{z}(t) = \kappa E(x_0,t)(u\sigma^z e^{i\omega_1 t} + v\sigma^z e^{-i\omega_2 t} + \text{H.c.})\,. \tag{8.18}$$

Then, the generalization to the situation where one has N quantum emitters is straightforward:

$$H_{\rm I}^{\rm sq}(t) = \sum_n \kappa E(x_n,t)(D_n^\dagger e^{i\omega_a t} + D_n e^{-i\omega_a t})\,, \tag{8.19}$$

$$H_{\rm I}^{z}(t) = \kappa \sum_n E(x_n,t)(u\sigma_n^z e^{i\omega_1 t} + v\sigma_n^z e^{-i\omega_2 t} + \text{H.c.}), \tag{8.20}$$

8.4.2 Squeezing and entanglement generation.

After an adiabatic elimination of the excited states one gets an effective qubit-field interaction $H_{\rm I}(t) = H_{\rm I}^{\rm sq}(t) + H_{\rm I}^{z}(t)$, as shown in Eq. 1, written in the interaction picture with respect to H_0. After eliminating the EM field degrees of freedom the Liouvillian for the reduced density matrix of the ensemble of qubits reads:

$$\mathcal{L}_{\rm sq}(\rho) = \sum_{n,m} J_{n,m}^{\rm sq}\left(D_n^- \rho D_m^+ - \rho D_m^+ D_n^-\right) + \text{H.c.}. \tag{8.21}$$

with $J_{n,m}^{\rm sq} = \Gamma_{\rm sq} e^{iq(\omega_a)|x_n - x_m|}$ and $\Gamma_{\rm sq} = \kappa^2\gamma(\omega_a)$. The second term in the effective qubit-field interaction, $H_{\rm I}^{z}(t)$, describes longitudinal decay processes and leads to

$$\mathcal{L}_z(\rho) = \sum_{n,m} J_{n,m}^{z}\left(\sigma_n^z \rho \sigma_m^z - \rho \sigma_m^z \sigma_n^z\right) + \text{H.c.}, \tag{8.22}$$

with $J_{n,m}^{z} = \kappa^2(\gamma(\omega_1)u^2 e^{iq(\omega_1)|x_n - x_m|} + \gamma(\omega_2)v^2 e^{iq(\omega_2)|x_n - x_m|})$ where $\omega_1 = \omega_{\rm L,1}$ and $\omega_2 = \omega_{\rm L,2} - \omega_0$. The term $\mathcal{L}_z$ induces a dephasing mechanism that competes with the spontaneous coherence build up induced by $\mathcal{L}_{\rm sq}$. The relative importance of those contributions depends on the photon density of states at frequencies $\omega_{\rm a}$ and $\omega_{1,2}$. We consider two limiting cases:

- *Small photonic bandwidth*: This is the most favorable configuration. If one assumes that the density of states in the waveguide is peaked around $\omega_{\rm a}$, with a bandwidth $\Delta\omega \ll |\omega_1 - \omega_{\rm a}|, |\omega_2 - \omega_{\rm a}|$ such that $\gamma(\omega_{1,2}) \approx 0$ and therefore $J_{n,m}^{z} \approx 0$. For example, this can be the case of one dimensional waveguides consisting of coupled cavities forming a one-dimensional photonic crystal.

  Defining $q(\omega_a) = 2\pi/\lambda_a$ and choosing $x_n = n\lambda_a$, one arrives to a spin-squeezing version of the Dicke superradiant model,

  $$\mathcal{L}_{\rm sq,D}(\rho) \;=\; \frac{\Gamma_{\rm sq}}{2}\left(D^-\rho D^+ - D^+D^-\rho + \text{H.c.}\right), \tag{8.23}$$

  where we have introduced collective squeezed spin operators $D^{+/-} = \sum_n D_n^{-/+}$. In Fig. 8.3(a), we show a calculation of the spin-squeezing in the steady-state as function of the squeezing parameter, r. Remarkably, an enhancement of the maximum value of entanglement of several orders of magnitude compared to the case of an ensemble of 2LS's is observed.

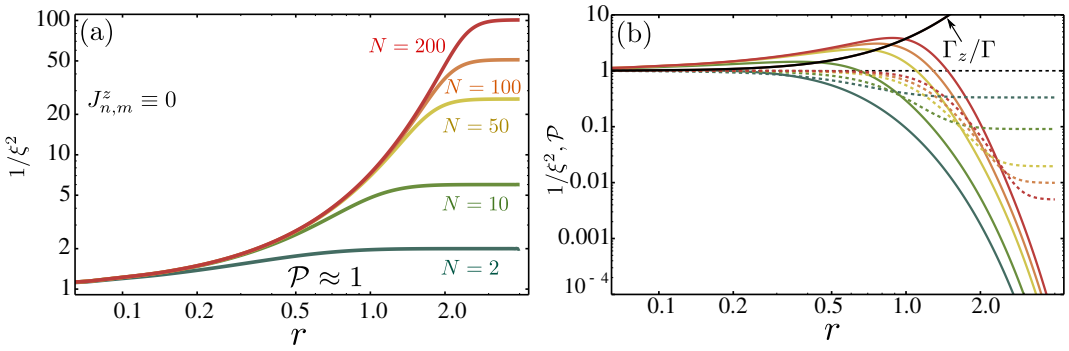

Figure 8.3: Same as Fig. 8.2 for the 4LS scheme. (a) Entanglement witness ($1/\xi^2$,solid) as a function of the squeezing parameter, r, for increasing number of qubits ($N = 2, 10, 50, 100, 200$) in the limit of *small photonic bandwidth* limit, where $J^z_{m,n} \equiv 0$. In all the cases, the purity of the system is $\mathcal{P} \approx 1$. (b) Entanglement witness ($1/\xi^2$, solid) and purity ($\mathcal{P}$, dashed) as a function of the parameter r for increasing number of qubits ($N = 2, 10, 50, 100, 200$) in the limit of *large bandwidth* limit. The evolution of the collective dephasing mechanism, Γ_z, with the squeezing parameter is also plotted in solid black.

- *Large photonic bandwidth*: In the opposite limit we have considered a broadband waveguide ($|\omega_{\mathrm{L},1} - \omega_{\mathrm{L},2}| \ll \Delta\omega$) such that the density of states at the frequencies considered here is comparable $\gamma(\omega_1) \approx \gamma(\omega_2)$. In experiments with optical transitions, for example with quantum dots in optical or plasmonic waveguides, condition $\omega_1, \omega_2, \omega_a \gg \omega_0$ is found, since transition energies are in the eV and meV for high energy and low energy transitions, respectively [286, 287]. Thus, one can safely assume $q(\omega_a) \approx q(\omega_1) \approx q(\omega_2) = 2\pi/\lambda_a$, and consider that quantum dots can be placed at the same relative optical path with respect to all frequencies. To give a more quantitative argument for this approximation, one can define the group velocity of the modes of the waveguide $v_g(\omega) = |\partial_q \omega_q|$, and consider the limit $|\omega_1 - \omega_{\mathrm{a}}| v_g(\omega_{\mathrm{a}}), |\omega_2 - \omega_{\mathrm{a}}| v_g(\omega_{\mathrm{b}}) \ll q(\omega_{\mathrm{a}})$, which corresponds to small wavevector differences. In the case of constant v_g and optical transitions, this condition leads to differences of 10^{-3} in $q(\omega_{\mathrm{a}})$, $q(\omega_{1,2})$. We neglect for the moment those differences, which may lead to inhomogeneous broadening effects that are discussed later in this work. Thus, the condition $x_n = n\lambda_a$ leads to a collective dephasing term of the form

$$\mathcal{L}_{\mathrm{z,D}}(\rho) \;=\; \frac{\Gamma_z}{2}\left(S^z \rho S^z - S^z \rho + \mathrm{H.c.}\right), \tag{8.24}$$

where we have introduced the rate $\Gamma_z = J^z_{n,n}$. In the large photonic bandwidth limit one gets thus two competing terms $\mathcal{L} = \mathcal{L}_{\mathrm{sq,D}} + \mathcal{L}_{\mathrm{z,D}}$. Collective dephasing increases with the squeezing parameter r, as depicted in solid black in Fig. 8.3(b). The competition between dephasing and squeezing mechanisms determines an optimal r to generate maximal entanglement. The latter can be higher than the one generated by $\mathcal{L}_{\mathrm{D,p}}$ considered above. The purity of the system is also affected by the dephasing term, however one can still find a region that combine high purity and high values of entanglement as

shown in Fig. 8.3 (b).

8.5 Experimental feasibility.

In this Section, we discuss about the experimental feasibility of the proposal: firstly, reviewing the key requirements needed and how far the current experimental state-of-art is from them. Then, we show theoretical calculations to study the robustness to these possible experimental imperfections. The main requirements of our scheme are:

- *One-dimensional waveguides.-* It is required long propagation lengths and efficient coupling to the qubits. Significant coupling to the guided modes of more than $85-89\%$ have already been reported for photonic [247, 248] and plasmonic [56, 61] waveguides. Theoretical predictions of even higher efficiencies has also been pointed out [254, 291] at expense of increasing the losses and reducing the propagation length. Limitations in the propagation length limits the number of qubits one can entangle. Besides, the precise location of the qubits is also needed, which is possible for solid-state emitters using, e.g. by lithographic methods which nowadays have precision better than $50nm$ [31].

- *Lambda-transitions in solid-state qubits.-* It is assumed a degree of manipulation of electronic levels similar to the one achieved in atomic physics, specially the 4LS scheme. Applications in quantum information processing [15, 292] typically require controlling optical transitions for spin-pumping and initialization. Recent experimental results [286, 287] show level schemes in quantum dots similar to those required in our work.

- *Markovian approximation.-* We require $\Gamma N \ll \omega_0$ in the 2LS scheme and $\Gamma N \ll \omega_{\mathrm{L}1,2}, \omega_{\mathrm{a}}$ in the 4LS case, such that the cooperative decay rate is much smaller than the transition frequencies, the latter determine the photonic bath memory time [25]. This condition is well satisfied in the case of optical transitions of quantum dots.

- *Independent decay channels on each transition frequency.-* This is required for the 4LS's scheme in the large bandwidth limit, to get Eqs. (8.21, 8.22), and it is justified as long as $\Gamma N \ll |\omega_{\mathrm{L},1}-\omega_{\mathrm{a}}|, |\omega_{\mathrm{L},2}-\omega_{\mathrm{a}}|$. Since differences in transition energies are of the order of meV, this condition imposes a restriction on the achievable rates for entanglement generation in our scheme.

- *Homogeneous couplings.-* This scheme neglects inhomogeneous couplings which may take the steady state out of the collective basis $|J, M\rangle$. This may be the most important restriction since spectral dispersion of energies is a limitation of quantum optical solid-state devices. The dispersion in energies in solid-state setups, like QDs, is still of the order of meV [31] due to the inherent randomness in the process of fabrication (explained in Chapter 1). Other alternatives, like NV centers, seem more attractive as the spreading of energies here is much smaller (of the order of μeV [293]) which is mainly coming from the presence of different isotopes of C or in relative orientations relative to the waveguide. In both cases, the feasibility of our proposal benefits from current experimental efforts in this direction in the field.

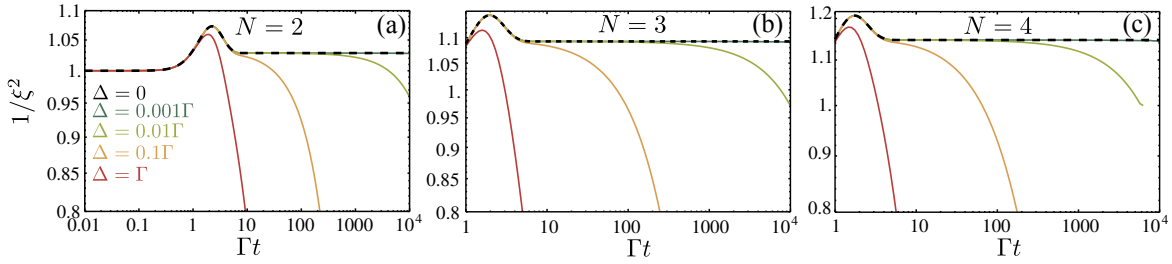

Figure 8.4: Entanglement witness, $1/\xi^2$, for the simple 2LS scheme with $\Omega/N = 0.4\Gamma$, for $N = 2$ (a), $N = 3$ (b) and $N = 4$ (c). The different colors represent different energy dispersions $\Delta = 0$ (dashed black) and $\Delta = 0.001\Gamma$, 0.01Γ, 0.1Γ, Γ in the colors indicated in the legend.

Now, we show the effect of the possible experimental imperfections appearing in the experiments, paying special attention to spectral dispersion of energies which is possible the main drawback for the application of the proposal in solid-state systems. The theoretical problem of dealing with inhomogeneous systems is numerically very demanding. So far, we have taken advantage of the perfect collective behavior of the system which allows to work with a collective basis $|J, M\rangle$ whose computational complexity grows only quadratically with the number of qubits. However, if one wants to consider the effect of inhomogeneities, i.e., a random dispersion of energies in the qubit energies, it is not possible then to work with the collective basis. Thus, the computational complexity of the problem grows exponentially with the number of qubits (2^{2N}), which unfortunately limits us to work with a very reduced number of qubits as it quickly transforms into an intractable problem [1].

Firstly, we start by considering the effect of a dispersion of energies for the simple 2LS case. Assuming a random variation of energies induced by a term $H_{\rm inh} = \Delta\omega_j S_j^z$, with $\Delta\omega_j \in [-\Delta, \Delta]$, we have done the calculation for $N = 2, 3$ and 4 qubits for different dispersions Δ's and the results are shown in Fig. 8.4. Due to the randomness of the spread of energies, we repeat the calculation n_t times (i.e. 20 for Fig. 8.4), and then calculate the average of the observables. As expected, the effect of this inhomogeneity in the energies is to create a dephasing time $1/\tau_{\rm d} \propto \Delta$, such that entanglement is destroyed for times $t > \tau_{\rm d}$ as shown in Fig. 8.4. This can be a severe limitation, especially for QDs, where the variation of energies is still large due to the randomness in the fabrication. However, due to the computational limitations, it is difficult to argue about the scaling with the number of qubits.

The alternative proposal with 4LS is more advantageous than the simple 2LS case in two ways: firstly, as we show in Fig. 8.5 with an exact calculation, it is more robust to inhomogeneities than the simple 2LS scheme. Secondly, one can find non-negligible entanglement ($1/\xi^2 > 1$) for squeezing parameters r which are still "small", in the sense that the associated occupation $\langle S\rangle_z \approx -0,5$ (see Fig. 8.3). This justifies to do a Holstein-Primakoff approxmation [108] to the σ_n's operators yielding to a linear scaling of the computational. The bosonization of operators has already been used in this Thesis (see Chapter 3 or 6) and basically consist in substituting $\sigma_n \to a_n$, with a_n being a bosonic operator.

[1] This is a typical example where the limitations of classical computers to simulate quantum systems. Quantum computers are expected to overcome these limitations.

The exact calculation is done as explained for the simple 2LS case. One considers a random distribution of energies such that $\Delta\omega_j \in [-\Delta, \Delta]$ and repeats the calculation for a number of times to perform an average. The results are shown in Fig. 8.5 for $N = 2, 3, 4$ qubit ensembles for different Δ's. From these results it is clear that this scheme is more robust to these inhomogeneities than the simple 2LS. The inhomogeneities leads to a degradation of the steady-state value of $1/\xi^2$ but still steady-state entanglement can be found. Only for very big Δ, the inhomogeneity yields a complete destruction of the the steady-state entanglement.

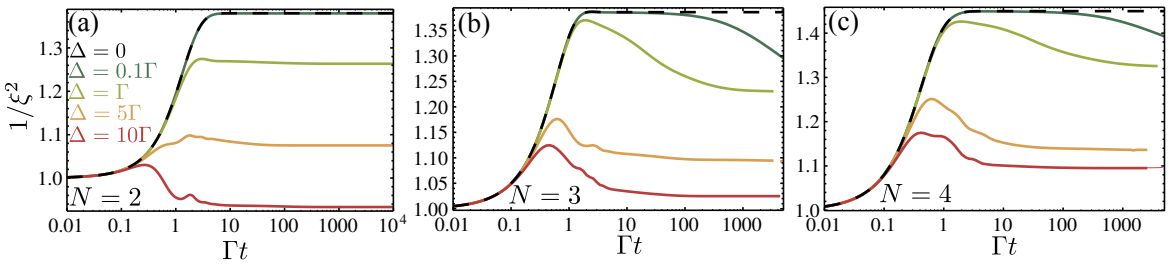

Figure 8.5: Entanglement witness, $1/\xi^2$, for the 4LS scheme with $r = 0.2$, for $N = 2$ (a), $N = 3$ (b) and $N = 4$ (c). The different colors represent different energy dispersions $\Delta = 0$ (dashed black) and $\Delta = 0.1\Gamma$, Γ, 5Γ, 10Γ in the colors indicated in the legend.

Other common experimental imperfection is the imperfect coupling of the QE to the modes of the waveguides. It is usually characterized by β-factor smaller than one. The robustness against this imperfection is studied in Fig. 8.6 for a small number of QEs. One can see that the maximum entanglement that can be achieved with a perfect coupling is degraded as β decreases, however some steady-state entanglement remains in the steady state, except for very bad coupling efficiencies as in the case $\beta = 0.1$.

Regarding, the scalability with the number of qubits not much can be inferred from these figures as the number of qubits is not big enough. However, in both cases the tendency is positive as it points to a higher robustness of the scheme as the number of qubits increases.

Fortunately, the Holstein-Primakoff approximation allows us to study more systematically the robustness of the 4LS scheme against random spread of the energies of the qubit, together with other typical experimental imperfections. Before getting into details, in Fig. 8.7 we

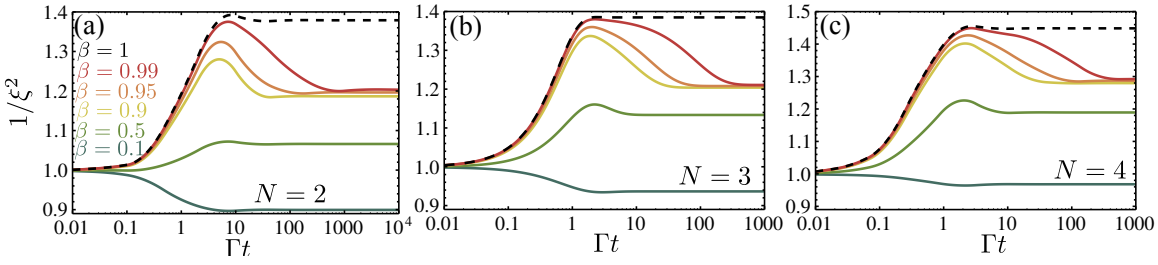

Figure 8.6: Entanglement witness, $1/\xi^2$, for the 4LS scheme with $r = 0.2$, for $N = 2$ (a), $N = 3$ (b) and $N = 4$ (c). The different colors represent different energy dispersions $\Delta = 0$ (dashed black) and $\beta = 1$, 0.99, 0.95, 0.9, 0.5, 0.1 in the colors indicated in the legend.

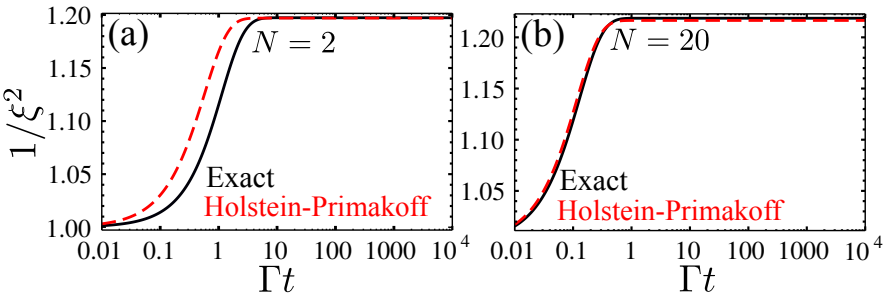

Figure 8.7: Comparison of entanglement witness between the exact calculation (solid black) and the Holstein-Primakoff approximations (dashed red) for an homogeneous system with squeezing parameter $r = 0.2$ for $N = 2$ (Panel (a)) and $N = 20$ (Panel (b)).

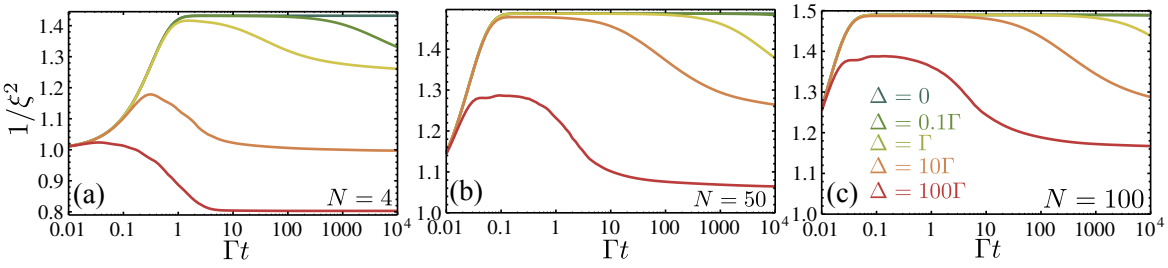

Figure 8.8: Entanglement witness, $1/\xi^2$, for the 4LS scheme calculated within the Holstein-Primakoff approximation with $r = 0.2$, for $N = 4$ (a), $N = 50$ (b) and $N = 100$ (c). The different colors represent different energy dispersions $\Delta = 0, 0.1\Gamma$, Γ, 10Γ and 100Γ in the colors indicated in the legend.

have plotted, for a fixed squeezing parameter r, the comparison between the exact and the approximated calculations for a number of qubits $N = 2$ and $N = 20$. In both cases $\langle S_z \rangle \approx -0.5$ (not shown) so the bosonization of the σ_n operators is justified and this is why both results (exact and approximated) compare so well. The only limitation of the approximation is that one can not go to higher values of r which leads to higher degrees of entanglement, however, within this values one can still study the robustness of the proposal to the different imperfections.

Once the validity of the approximation has been settled, we start by showing in Fig. 8.8 a calculation similar to the one of Fig. 8.5, but for a higher number of qubits. It can be seen the robustness of the entanglement compared to the 2LS case, as entanglement survives for greater dispersions in the energies. The scaling with N is also positive as the tendency of the system is to being more stable for bigger number of qubits.

The dynamics of the entanglement achieves a maximum entanglement and then degrades until a constant value of $1/\xi^2$ that can be $\lesssim 1$ depending on the magnitude of the spread of the energies. This is more clearly seen in Fig. 8.9, where we have plotted the dynamics for a fixed $\Delta = 10\Gamma$, for different number of qubits. This behavior allows us to define a *dephasing time*, t_d, by considering the time where the entanglement has degraded to a certain value from its maximum, i.e. 95%. This is plotted in the inset of Fig. 8.9(a) for different number of qubits. Here, the tendency here is also positive as dephasing time is bigger as the number

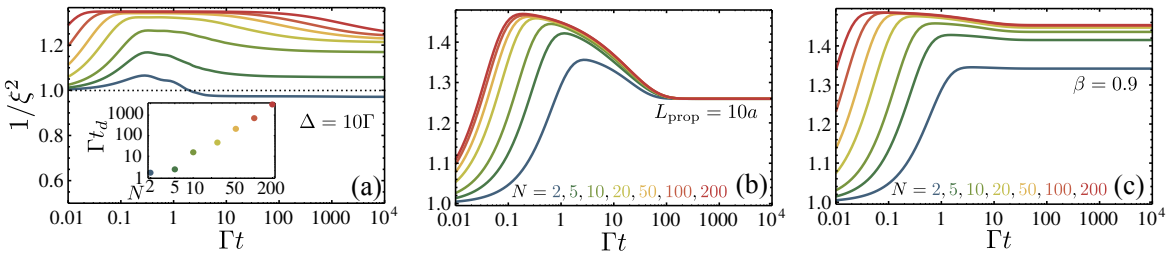

Figure 8.9: Entanglement witness, $1/\xi^2$, for the 4LS scheme calculated within the Holstein-Primakoff approximation with $r = 0.2$ for different number of qubits $N = 2, 5, 10, 20, 50, 100, 200$ indicated by the colors in the legend. Panel (a): Robustness of $1/\xi^2$ for a fixed dispersion of energies, $\Delta = 10\Gamma$, with different number of qubits. Inset: Dephasing time, t_d (see definition in the main text) as a function of the number of qubit N. Panel (b): Robustness of $1/\xi^2$ for waveguide with finite propagation length $L_{\text{prop}} = 10a$, where a is the interqubit distance, with different number of qubits. Panel (c): Robustness of $1/\xi^2$ for β-factor of 0.9 with different number of qubits.

of qubits coupled to the waveguide increases.

The advantage of the Holstein-Primakoff approximation is that it allows very naturally to extend the study of other experimental imperfections, such as the finite propagation length of the modes of the waveguide or the imperfect coupling to them, reflected in β-factor smaller than one. The finite propagation length arises due to fabrication imperfections and/or ohmic dissipation in the metal in the case of plasmonic waveguides. In the latter, this limits considerable the range that the interactions can extend. In Fig. 8.9(b), we have plotted the results for a finite propagation length of $L_{\text{prop}} = 10a$, begin a the separation between the qubits, for different number of qubits. In this case, the inhomogeneity of the system is caused by the fact that Γ_{ij} decays with the distance exponentially. The effect is that the maximum of entanglement achieved increases with the number of qubits, but after a certain time, they collapse to a steady-state value. The scaling with the number of qubits is not so relevant as the finite propagation length of the interaction makes that only a finite number qubits are connected through the waveguides modes due to the finite range of the interaction. Thus, in the case of the Fig. 8.9(b) no matter how many QEs are placed in front of the waveguide that if $L_{\text{prop}} = 10a$, no more than approximately 10 emitters are effectively coupled.

As a last result, in Fig. 8.9(c), we have studied the consequences of an imperfect coupling to the modes of the waveguide, reflected in the so-called β-factor. In this figure, we have considered a fixed $\beta = 0.9$ and study its scaling with the number of qubits (N). One can see how increasing N leads to a degradation of the entanglement that can be achieved if the coupling was perfect, but still being entangled ($1/\xi^2$) at finite time. The scaling with the number qubits benefits from the collective effect: it is more robust as N increases, as it happened with he inhomogeneous broadening.

8.6 Conclusions.

In conclusion, we have proved that one-dimensional plasmonic [56, 61] or photonic [247, 248, 294–296] waveguides are excellent candidates to correlate a large number of qubits by collective radiative decay. By exploiting the site-controllability of solid state emitters [31],

one gets an exciting playground to study non-equilibrium dissipative dynamics.

We have presented two different schemes with both two and four level systems which are ideally suited to achieve mesoscopic entanglement in controllable solid-state devices currently under investigation for quantum information processing. The latter appears to be more robust under typical experimental imperfections. Furthermore, a thorough analysis on the experimental challenges has been done. These ideas can be easily translated to circuit QED by generating of sidebands in the qubit-field coupling [297].

Chapter 9

Conclusions

English

In this Thesis, we have studied the interplay between coherence and dissipation in a different plethora of systems which are candidates to develop future quantum information applications. We have paid special attention to semiconductor optical systems which are promising due to the possibility of controlling optically their quantum state and for their prospects for scalability in the near future technology. In these systems, decoherence stems from the unavoidable coupling to the environment, which consists of several elements such as the bath of vacuum radiative modes or the vibrational bath present in the solid-state matrix where the system is embedded. Throughout this Thesis, we have reviewed examples which highlight the importance of studying decoherence not only to control or limit its detrimental effect, but also to turn it into an resource for applications.

During the first part the Thesis, our system under study has been the interaction between the excitons –bound states composed of an electron and a hole- in quantum dots, and the photonic modes confined in microcavities. When the quantum dots are grown inside microcavities they interact with the photon modes supported by the them. When this interaction overcomes the intrinsic losses of the exciton and cavity, a new type of particles is formed: *polaritons*. They are composite particles of light and matter and whose characteristics make them very attractive for quantum information applications.

Apart from the intrinsic losses of the exciton and cavity system, the semiconductor environment introduces new elements which can be harnessing for the coherence of the polaritons. With the model developed in this Thesis, we are able to address all the specificities of the semiconductor environment, namely the incoherent nature of the pumping and the effect of the coupling to the vibrational modes. Thanks to the careful modeling of both elements, we have been able to identify the effect of the vibrational modes in the observation of strong-coupling through the study of the light emitted from the system. We have shown that the non-linear behaviour induced by the strong-coupling has a robust tendency to display triplet structures in the photoluminescence spectra, rather than the expected JC multiplets of paired doublets with lack of emission at the cavity (central) mode. This is a non-trivial observation that allows us to explain some experimental reports showing these triplet structures, but which lacked of a clear explanation. To strength our argument, we have also presented a

global fitting within the non-linear regime.

The previous mechanism is a paradigmatic example where decoherence acts as a detrimental element. On the other hand, the light emitted from the systems, that is another source of decoherence, can be used to learn about the systems. In fact the study of the properties of these photons leaking out of the systems is the only way the experimentalists have to characterize these systems. In this context, we have also developed a new theory to efficiently compute correlations between an arbitrary number of photons of any given frequencies and time delays. Even though they were becoming increasingly popular in the experimental setups, the theoretical efforts were devoted solely to very specific examples due to an intrinsic computational complexity. The new method presented here, simulate the effect of frequency-dependent sensors by introducing these *sensors* into the whole dynamics. The approach is independent of the details of the particular quantum system that emits the photons. This makes it a highly versatile tool for the description and analysis of photo-detection in various technological platforms. Our method is an important theoretical milestone as it paves the way for the interpretation of experiments which are routinely implemented in the laboratory but which lacked hitherto an adequate and tractable theoretical support. We have applied the method to a plethora of single and coupled quantum systems, putting special emphasis in the Jaynes-Cummings model due its paramount importance in quantum optics. During the characterization of their two-photon spectra, we have shown striking multiphoton features related to virtual states, e.g. strongly enhanced two-photon virtual processes, due to the indeterminacy in frequency and time imposed by the finite resolution detectors.

The excitonic description can be upgraded from the simplified two-level system picture by considering their spin degrees of freedom. In this case, the level scheme is built up with 4 different levels, whose upper level is the so-called biexcitonic state. This state is formed when there are two excitons of opposite spins in the quantum dot. Due to the Coulomb interaction, the biexciton has a certain binding energy which detunes it from the one-photon resonances. In cavity QED systems, we have made use of this property and presented a scheme where the biexciton is in two-photon resonance with a microcavity mode, as an efficient two-photon source both in terms of the purity of the two-photon state and of its emission efficiency. By considering all the coherent and decoherent elements, we have been able to demonstrate quantum character of the two-photon emission by a detailed analysis of all the processes involved in the biexciton de-excitation, which also allows us to find analytically the optimum conditions for its realization. We have shown that the two-photons are emitted simultaneously with no delay in the autocorrelation time. In the case of continuous excitation, we have studied the impact of both kind of excitations. Remarkably, we are able to characterize the regions for optimally generating the 2P states thanks to the analytical understanding of the problem.

In the second part of the Thesis, the role of the electromagnetic field has been moved from photonic cavity systems to metallic structures that support the propagation of surface plasmons polaritons. As a first result, by using a proper open quantum system formalism we identified the key elements that are preventing the observation of strong-coupling between single emitters and surface plasmons in two-dimensional systems. With this understanding, we have proposed alternatives to increase the visibility of reversibility, e.g. the use of a high index dielectric host for the quantum emitter. In the typical experimental configuration, however, the strong-coupling is observed when many emitters are placed in front of these

surfaces. For this situation, we have developed a self-consistent quantum treatment for metallic systems adopting a open-quantum system perspective. Our new framework takes into account all the experimental ingredients allowing us to reproduce the experimental state-of art observations and predict the optimal conditions for maximizing the strong- coupling. Moreover, we have gone a step further predicting the conditions where these systems can be operating in a purely quantum regime and how to characterize them experimentally.

Due to the difficulties of achieving the strong-coupling regime in plasmonic systems, one is tempted to think that they are not suitable for quantum information and computation applications. However, in this Thesis we have just shown the opposite by turning dissipation into a powerful resource for quantum computation. Firstly, we have proved the possibility of generating entanglement in two-qubit systems coupled through a common plasmonic one-dimensional waveguide. We have seen that these plasmonic waveguides induce a controllable coherent and incoherent coupling between the emitters, which combined with some continuous excitation can lead to useful steady-state entanglement. A thorough analysis of the robustness of the proposal against experimental imperfections has been done, proving that the scheme can work by using plasmonic waveguides that are currently available.

Finally, we have upgraded this system to a more general configuration which offers a very exciting playground to study non-equilibrium dissipative physics. By assuming only the one-dimensional character of the waveguides and exploiting the site-controllability of solid state emitters, we have presented two different schemes with both two and four level systems. We have proved that they are ideally suited to achieve mesoscopic entanglement in controllable solid-state devices currently under investigation for quantum information processing. The latter scheme with four level systems appears to be more robust under typical experimental imperfections, even the unavoidable dispersion of transition energies in solid-state emitters like quantum dots.

Español

En esta Tesis hemos estudiado la competencia entre coherencia y disipación en una serie de sistemas candidatos para desarrollar aplicaciones en información y computación cuántica. El foco principal se ha puesto en sistemas ópticos semiconductores. Estos sistemas son especialmente prometedores debido a la posibilidad de modificar su estado cuántico a través de la luz y a su posible fabricación escalable, un requisito imprescindible para el desarrollo de una tecnología. En estos sistemas la decoherencia del sistema viene dada fundamentalmente por la invevitable interacción con su entorno. Los principales elementos son el baño de modos electromagnéticos de vacio y los modos vibracionales de la matrix dielectrica en la que se encuentran embebidos los sistemas. En esta Tesis hemos resaltado la importancia de estudiar adecuadamente estos fenomenos de decoherencia no solo para controlar y limitar su efecto, sino también para transformarlos en un elemento útil para nuestros objetivos.

La primera parte de la Tesis se ha dedicado al estudio de la interacción entre los excitones –particulas compuestas de un par electrón-hueco– confinados en puntos cuánticos y los modos fotónicos de las cavidades en las que estan embebidos. Al poner los puntos cuánticos dentro de las microcavidades, éstos elementos ópticamente activos interaccionan con los fotones confinados en la cavidad. Cuando esta interacción es más fuerte que las perdidas intrinsicas de ambos sistemas, dan lugar a nuevas particulas híbridas llamadas *polaritones*. Su caracter compuesto las convierte en elementos atractivos para la información cuantica.

Estos sistemas semiconductores contienen otros elementos que tienden a destruir la coherencia de los polaritones. En esta Tesis, hemos realizado un estudio detallados de estos elementos especificos de los semiconductores, en especial, la naturaleza incoherente de su excitación asi como la presencia de un baño de modos vibracionales que pueden crear un nuevo canal de pérdida de coherenecia conocido como *pure dephasing*. Uno de los resultados principales de esta Tesis ha consistido en estudiar como afecta este último mecanismo a la observación del acoplo fuerte en estos sistemas cuando es estudiado a traves del espectro de la luz de la cavidad. Hemos probado la combinación de acoplo fuerte y *pure dephasing* puede dar lugar estructura de triplete en la emisión de cavidad, cuyo pico central proviene de la no-linearidad intrinseca del sistema. Esta indicación no es un resultado trivial, pues tal y como hemos enseñado, este tipo de estructuras ya habían sido observadas en ciertos experimentos pero eran atribuidas a una combinación entre acoplo debil y fuerte. Para corroborar nuestra teoría, hemos hecho un ajuste a uno de esos experimentos dando fuerza a nuestra explicación.

El mecanismo anterior es un ejemplo claro donde la decoherencia inducida por los baños tiene un efecto perjucial para observar la coherencia de los sistemas. Sin embargo, en esta Tesis hemos visto como aprovechar en ciertos casos esa decoherencia para nuestro interés. Por ejemplo, la luz emitida por estos sistemas a través de la cavidad, que también es una fuente decoherencia, es sin embargo la forma más directa de estudiar el estado cuántico de los sistemas sin necesidad de alterarlos. A traves de ella podemos estudiar su estructura de niveles, estadistica, etc. A lo largo de esta Tesis, hemos desarrollado un nuevo formalismo teórico para calcular funciones de correlación que cada vez es más populares en los experimentos. La teoría desarrollada permite calcular las correlaciones entre fotones de distintas frecuencias y con un retraso arbitrario entre ellos, lo que da información muy valiosa sobre la estructura interna del sistema y su dinámica. Computacionalmente la teoría clásica estaba muy limitida y solo era capaz de calcular casos muy simples. Con nuestro método hemos

sido capaces de calcular esta nueva magnitud en un gran conjunto de sistemas cuánticos, individuales y acoplados, sentando las bases de todo un nuevo tipo experimentos. El estudio de esta nueva magnitud nos ha permitido predecir la observación de una serie de procesos que pasan desapercibidos en la espectroscopía usual. Este es un hito importante ya que allana el camino para la interpretación de los experimentos que carecían hasta ahora un soporte teórico adecuado.

Para cerrar esta parte de la Tesis, hemos considerado una imagen más compleja para los excitones en puntos cuánticos. Si se considera el posible espín de los excitones, es necesario amplicar la descripción a cuatro niveles, en la que el nivel más excitado se debe a la posibilidad de alojar dos excitones, de espín opuesto en el mismo punto cuántico. Debido la interacción electrostática entre la pareja de excitones, la energía de este estado excitado está desplazada respecto a la suma de las energías de los excitones individuales. Gracias a eso, es posible situar el modo de cavidad de modo que esté en resonancia con el estado de biexciton, pero muy alejado de la resonancia de un fotón. Haciendo uso de esta propiedad, hemos estudiado las posibilidades de este sistema para emitir parejas de fotones, bien dejando al sistema decaer libremente desde el estado de biexcitón o bien por excitación continua. Teniendo en cuenta todos los elementos, incluida los mecanismos de decoherencia, somos capaces the predecir analíticamente las condiciones óptimas para la emisión de parejas de fotones y caracterizar su estado cuántico a traves de las funciones de correlación. La importancia de este resultado reside en que la emisión de parejas de fotones es un requisito necesario para muchos protocolos de información cuántica.

En la segunda parte hemos cambiado los sistemas de cavidades fotónicas por sistemas metálicos. Estos últimos son capaces de albergar otro tipo de excitaciones de superficie del campo electromagnético llamadas plasmones de superficie. Los plasmones son especialmente prometedores ya que son capaces de confinar el campo electromagnetico en dimensiones por debajo de su longitud de onda, lo cual incrementa su interacción con los sistemas ópticos semiconductores. Sin embargo, estos modos tambien tienen mayores perdidas debido a que los metales son medios fuertemente absorbentes. Por esta razón, empezamos por dedicar atención a la posibilidad de observar acoplo fuerte entre los plasmones y los excitones en los límites en los que hay uno o más emisores. En particular, nos hemos restringido al caso de estructuras bidimensionales debido a que son las más sencillas de fabricar. Tanto en el caso de uno como de muchos emisores hemos estudiado los mecanismos que condicionan la observación de una dinámica coherente haciendo predicciones sobre cuales son las situaciones más óptimas para ello.

En el caso de que uno (o pocos) emisores esten interactuando con los plasmones, en la mayoria de los casos el aumento de la interacción no es suficiente para compensar las pérdidas introducidas por el medio metálico. Gracias a un análisis adecuado, hemos dado algunas indicaciones de como mejorar las posibilidades de observación de acoplo fuerte, p.e. con la introducción de una matrix dielectrica de un indice de refracción elevado. Sin embargo podemos concluir que la observación de acoplo fuerte en estos sistemas es un gran reto experimental. La otra configuración, donde son muchos emisores los que interactuan con los modos plasmónicos, si que es favorable para la observación de acoplo fuerte. En este caso, hemos desarrollo un formalismo teórico dentro del marco de la teoría de sistemas cuánticos abiertos para tratar los mecanismos de coherencia y decoherencia en sistemas metálicos de forma sencilla. Con él, somos capaces de reproducir la fenomenología ya encontrada en los

experimentos y predecir un régimen de parámetros donde estos sistemas se comporten de una manera puramente cuántica. La importancia del desarrollo de este formalismo no es solo la de poder dar esas predicciones, sino la de establecer un marco teórico adecuada para estudiar aplicaciones cuánticas en sistemas plasmónicos que se han venido tratando (casi) siempre dentro de un contexto semiclásico.

Por último, debido a las dificultades para alcanzar el régimen de acoplo fuerte en sistemas plasmónicos, la última parte de la Tesis ha estado enfocada a buscar aplicaciones que no dependan de ese régimen. En particular, nos hemos centrado en una aplicación en la que la decoherencia en lugar de ser perjudicial, se convierte en un elemento clave para la generación de estados entrelazados. La importancia de este tipo de estados radica en que son la base de muchos protocolos de informaci'on cuántica. En primer lugar, hemos presentado un estudio sistemático y detallado de la posibilidad de generar entrelazamiento en dos emisores cuánticos semiconductores que están acoplados a una guía de onda plasmónica unidimensional. Se ha probado que con el diseño adecuado de la guía y escogiendo adecuadamente las posiciones de los emisores es posible inducir acoplamiento controlable entre los emisores. Incluyendo una fuente de excitación coherente, este acoplo da lugar a la generación de estados entrelazados estacionarios. Además, se ha hecho un análisis concienzudo de las posibles limitaciones experimentales que pueden presentar estos sistemas, probando la robustez del mismo con parámetros dentro del rango de los experimentos actuales.

Dado que cada vez están apareciendo un mayor número de sistemas de guias de onda electromagneticas unidimensionales, ya sean de naturaleza plasmonica o fotónica, hemos generalizado el resultados anterior de tres maneras. Primero, hemos considerado una situación para un número arbitrario de qubits. Segunda, hemos generalizado los resultados para guías de onda unidimensionales de cualquier naturaleza. Y por último hemos considerado varios tipos de emisores, desde aquellos que pueden ser descritos como sistemas de dos niveles a esquemas más complicados de cuatro niveles. En ambos casos, hemos probado como la capacidad de fijar la posición de estos emisores y las caracteristicas introducidas por la dimensionalidad reducida ofrece un campo de estudio interesante para estudiar la física de sistemas cuánticos disipativos fuera del equilibrio. Desde el punto de vista más práctico, hemos demostrado las capacidades de estos sistemas para generar estados entrelazados controlables y robustos frente a posibles imperfecciones.

Appendix I: Equivalence of the sensing method and standard theory of frequency and time-resolved N-photon correlations.

In this Appendix, we will show the equivalence of the sensing method used in Chapter 4 and the standard theory introduced in Chapter 2. To set the notations let us assume a quantum system described by a set of operators a, b, etc., in a Hilbert space $\mathcal{H}$. In second quantization, these operators define annihilation operators in the Heisenberg picture. All single-time quantities can be obtained from correlators of the type $\langle a^{\dagger\mu} a^{\nu} b^{\dagger\eta} b^{\theta} \ldots \rangle$ with μ, ν, η, θ, etc., integers. Let us call $\mathcal{O}$ the set of operators which averages correspond to the correlators required to describe the system, i.e., $\mathcal{O}$ includes all the sought observables as well as operators which couple to them through the equations of motion. In the following, we assume, without loss of generality, that a is the mode of interest, which correlations in time and frequencies are to be computed.

We will start by proving the case for $N = 1$, which corresponds to the power spectrum, and the for $N = 2$ which is the most important correlation function that we have used extensively in Chapter 4 of this Thesis. The generalization to higher N is tedious, but straightforward. The proof proceeds by computing separately the integral expressions on the one hand and the intensity correlations on the other hand, and showing that they are equal to leading order in the couplings. We assume the steady state case for simplicity, with little loss of generality.

$N = 1$, power spectrum

Standard theory: Integral method

For any two operators X and $Y \in \mathcal{H}$, we define the vector $\mathbf{v}_{X,Y}(\tau)$ as:

$$\mathbf{v}_{X,Y}(\tau) = \begin{pmatrix} \langle X(0)Y(0)\rangle \\ \langle X(0)a(\tau)Y(0)\rangle \\ \langle X(0)a^\dagger(\tau)Y(0)\rangle \\ \langle X(0)(a^\dagger a)(\tau)Y(0)\rangle \\ \vdots \end{pmatrix} . \tag{1}$$

where X and Y in the steady state sandwich the operators of $\mathcal{O}$ taken in some order, which will be kept for the remainder of the text as starting with the sequence $\mathcal{O} = \{a, a^\dagger, a^\dagger a, \dots\}$.

From the quantum regression theorem, one can define for $\mathcal{O}$ a matrix M which rules the dynamical evolution of $\mathbf{v}$:

$$\partial_\tau \mathbf{v}_{X,Y}(\tau) = M\mathbf{v}_{X,Y}(\tau)\,, \tag{2}$$

with solution $\mathbf{v}_{X,Y}(\tau) = e^{M\tau}\mathbf{v}_{X,Y}(0)$. The steady state of the system is then given by:

$$\mathbf{v}^{\text{ss}} = \lim_{\tau\to\infty} \mathbf{v}_{\mathbf{1},\mathbf{1}}(\tau) = \lim_{\tau\to\infty} e^{M\tau} \begin{pmatrix} 1 \\ 0 \\ \vdots \end{pmatrix} , \tag{3}$$

since $\mathcal{O}$ contains all the sought observables of the system. Here we have chosen the vacuum as the initial condition (the steady state being unique, the initial state doesn't matter and the information is encoded in $e^{M\tau}$).

We now define two matrices, $T_\pm$, which, when acting on $\mathbf{v}_{X,Y}(\tau)$, introduce an extra $a^\dagger$ for T_+ and an a for T_- between X and Y, keeping normal ordering:

$$T_+\mathbf{v}_{X,Y}(\tau) = \begin{pmatrix} \langle X(0)a^\dagger(\tau)Y(0)\rangle \\ \langle X(0)(a^\dagger a)(\tau)Y(0)\rangle \\ \langle X(0)a^{\dagger 2}(\tau)Y(0)\rangle \\ \langle X(0)(a^{\dagger 2}a)(\tau)Y(0)\rangle \\ \vdots \end{pmatrix} , \tag{4}$$

and

$$T_-\mathbf{v}_{X,Y}(\tau) = \begin{pmatrix} \langle X(0)a(\tau)Y(0)\rangle \\ \langle X(0)a^2(\tau)Y(0)\rangle \\ \langle X(0)(a^\dagger a)(\tau)Y(0)\rangle \\ \langle X(0)(a^\dagger a^2)(\tau)Y(0)\rangle \\ \vdots \end{pmatrix} . \tag{5}$$

Appendix I: Equivalence of sensing method and standard theory

These matrices always exist, in infinite or within truncated Hilbert spaces (where, if truncation is to order n, a^n is an operator in $\mathcal{O}$ but $a^{n+1}=0$). For instance, if the mode a is a two-level system, the vector $\mathbf{v}_{X,Y}(\tau)$ consists of the first four entries in Eq. (1) only, since $a^{\dagger\mu}a^{\nu}=0$ if μ or $\nu>1$. Then, these matrices read

$$T_+=\begin{pmatrix}0&0&1&0\\0&0&0&1\\0&0&0&0\\0&0&0&0\end{pmatrix}\quad\text{and}\quad T_-=\begin{pmatrix}0&1&0&0\\0&0&0&0\\0&0&0&1\\0&0&0&0\end{pmatrix}. \tag{6}$$

With these definitions, the correlator $\langle a^\dagger(t_1)a(t_1-\tau_1)\rangle$ with $\tau_1>0$ is the first element of $T_+\mathbf{v}_{1,a}(\tau_1)$:

$$\langle a^\dagger(t_1)a(t_1-\tau_1)\rangle=\left[T_+e^{M\tau_1}T_-\mathbf{v}^{\rm ss}\right]_1. \tag{7}$$

where we have used $[\cdots]_i$ to denote the ith element of a vector. The power spectrum in its integral form is given by:

$$S^{(1)}_{\Gamma_1}(\omega_1)=\frac{1}{\pi}\Re\int_0^\infty d\tau_1 e^{-\frac{\Gamma_1}{2}\tau_1}e^{-i\omega_1\tau_1}\langle a^\dagger(t_1)a(t_1-\tau_1)\rangle=\frac{1}{\pi}\Re\left[T_+\frac{-1}{M+(-i\omega_1-\frac{\Gamma_1}{2})\mathbf{1}}T_-\mathbf{v}^{\rm ss}\right]_1. \tag{8}$$

Sensing method

We now consider two sensors σ_i, $i=1,2$ with linewidths Γ_i coupled to the system with strength ε_i, as explained in the text, and introduce a sensing vector $\mathbf{w}$ of steady state correlators, by multiplying $\sigma_1^{\dagger\mu_1}\sigma_1^{\nu_1}\sigma_2^{\dagger\mu_2}\sigma_2^{\nu_2}$ with the operators in $\mathcal{O}$:

$$\mathbf{w}[\mu_1\nu_1,\mu_2\nu_2]=\begin{pmatrix}\langle\sigma_1^{\dagger\mu_1}\sigma_1^{\nu_1}\sigma_2^{\dagger\mu_2}\sigma_2^{\nu_2}\rangle\\ \langle\sigma_1^{\dagger\mu_1}\sigma_1^{\nu_1}\sigma_2^{\dagger\mu_2}\sigma_2^{\nu_2}a\rangle\\ \langle\sigma_1^{\dagger\mu_1}\sigma_1^{\nu_1}\sigma_2^{\dagger\mu_2}\sigma_2^{\nu_2}a^\dagger\rangle\\ \langle\sigma_1^{\dagger\mu_1}\sigma_1^{\nu_1}\sigma_2^{\dagger\mu_2}\sigma_2^{\nu_2}a^\dagger a\rangle\\ \vdots\end{pmatrix}, \tag{9}$$

where μ_i and ν_i take the values 0 or 1. Its equation of motion, to leading order in ε, reads:

$$\begin{aligned}\partial_t\mathbf{w}[\mu_1\nu_1,\mu_2\nu_2]=&\{M+[(\mu_1-\nu_1)i\omega_1-(\mu_1+\nu_1)\Gamma_1+(\mu_2-\nu_2)i\omega_2-(\mu_2+\nu_2)\Gamma_2]\mathbf{1}\}\mathbf{w}[\mu_1\nu_1,\mu_2\nu_2]\\&+\mu_1(i\varepsilon_1T_+)\mathbf{w}[0\nu_1,\mu_2\nu_2]+\nu_1(-i\varepsilon_1T_-)\mathbf{w}[\mu_1 0,\mu_2\nu_2]+\\&\mu_2(i\varepsilon_2T_+)\mathbf{w}[\mu_1\nu_1,0\nu_2]+\nu_2(-i\varepsilon_2T_-)\mathbf{w}[\mu_1\nu_1,\mu_2 0]\,,\end{aligned} \tag{10}$$

which can be solved recursively:

$$\mathbf{w}[\mu_1\nu_1,\mu_2\nu_2] = \frac{-1}{M+[(\mu_1-\nu_1)i\omega_1-(\mu_1+\nu_1)\Gamma_1+(\mu_2-\nu_2)i\omega_2-(\mu_2+\nu_2)\Gamma_2]\mathbf{1}} \times\Big\{\mu_1(i\varepsilon_1 T_+)\mathbf{w}[0\nu_1,\mu_2\nu_2]+\nu_1(-i\varepsilon_1 T_-)\mathbf{w}[\mu_1 0,\mu_2\nu_2]+ \mu_2(i\varepsilon_2 T_+)\mathbf{w}[\mu_1\nu_1,0\nu_2]+\nu_2(-i\varepsilon_2 T_-)\mathbf{w}[\mu_1\nu_1,\mu_2 0]\Big\}. \quad (11)$$

The spectrum of emission of a is given by the average population, in the steady state, of only one of them, say, sensor 1: $\langle n_1\rangle = \langle\sigma_1^\dagger\sigma_1\rangle$. Its equation of motion reads $\partial_t\langle n_1\rangle = -\Gamma_1\langle n_1\rangle + 2\Re(i\varepsilon_1\langle\sigma_1 a^\dagger\rangle)$, and with the above notations, is therefore given in the steady state by:

$$\langle n_1\rangle = \frac{2}{\Gamma_1}\Re\Big[i\varepsilon_1 T_+\mathbf{w}[01,00]\Big]_1 . \quad (12)$$

Using the solution Eq. (11), the correlator of interest for the spectrum reads:

$$\mathbf{w}[01,0,0] = \frac{-1}{M+[-i\omega_1-\frac{\Gamma_1}{2}]\mathbf{1}}(-i\varepsilon_1 T_-)\mathbf{v}^{\rm ss} . \quad (13)$$

Equality of the integral and sensing methods

The proof is now complete since, to leading order, we find that Eq. (8) and Eqs. (12-13) provide the claimed identity:

$$\langle n_1\rangle = \frac{2\varepsilon_1^2}{\Gamma_1}\Re\left[T_+\frac{-1}{M+[-i\omega_1-\frac{\Gamma_1}{2}]\mathbf{1}}T_-\mathbf{v}^{\rm ss}\right]_1 = \frac{\varepsilon_1^2}{\Gamma_1}(2\pi)S^{(1)}_{\Gamma_1}(\omega_1) . \quad (14)$$

$N=2$, two-photon correlations

Standard Theory: Integral method

Let us separate the $\tau = T_2 - T_1$ contributions to the two-photon correlation function between its $\tau = 0$ and $\tau > 0$ terms:

$$S^{(2)}_{\Gamma_1,\Gamma_2}(\omega_1;\omega_2,\tau) = e^{-\Gamma_2\tau}S^{(2)}_{\Gamma_1,\Gamma_2}(\omega_1;\omega_2) + \Delta S^{(2)}_{\Gamma_1,\Gamma_2}(\omega_1;\omega_2,\tau) , \quad (15)$$

with

$$S^{(2)}_{\Gamma_1,\Gamma_2}(\omega_1;\omega_2) = \Gamma_1\Gamma_2\int_{-\infty}^{T_1}dt_2\int_{-\infty}^{t_2}dt_1\times e^{-\Gamma_1(T_1-t_1)}e^{-\Gamma_2(T_1-t_2)}\Sigma^{(2)}_{\Gamma_1,\Gamma_2}(\omega_1,t_1;\omega_2,t_2)+[1\leftrightarrow 2] , \quad (16)$$

and

$$\Delta S^{(2)}_{\Gamma_1,\Gamma_2}(\omega_1;\omega_2,\tau) = \Gamma_1\Gamma_2 \int_{T_1}^{T_2} dt_2 \int_{-\infty}^{T_1} dt_1 \times e^{-\Gamma_1(T_1-t_1)} e^{-\Gamma_2(T_2-t_2)} \Sigma^{(2)}_{\Gamma_1,\Gamma_2}(\omega_1,t_1;\omega_2,t_2)\,, \quad (17)$$

where $[1 \leftrightarrow 2]$ means the interchange of indices 1 and 2, that is, permuting $\omega_1 \leftrightarrow \omega_2$ and $\Gamma_1 \leftrightarrow \Gamma_2$.

To compute these quantities, it is enough to consider $\Sigma^{(2)}_{\Gamma_1,\Gamma_2}(\omega_1,t_1;\omega_2,t_2)$ for $t = t_2 - t_1 > 0$ since the inverse order is given by the exchange $[1 \leftrightarrow 2]$. Therefore, we restrict the integration to ordering of the time variables where $t_1 - \tau_1 < t_1 < t_2$. The fourth variable yields three different domains of integration:

(1) $t_2 - \tau_2 < t_1 - \tau_1 < t_1 < t_2$,

(2) $t_1 - \tau_1 < t_2 - \tau_2 < t_1 < t_2$,

(3) $t_1 - \tau_1 < t_1 < t_2 - \tau_2 < t_2$.

For each of them, there are two different correlators appearing in $\Sigma^{(2)}$: one with the factor $e^{-i\omega_2\tau_2}e^{i\omega_1\tau_1}$, the other with $e^{-i\omega_2\tau_2}e^{-i\omega_1\tau_1}$. They will be respectively referred to as $\mathcal{C}_{(ia)}$ and $\mathcal{C}_{(ib)}$, with $i = 1, 2, 3$ depending on their domains of integration. This gives rise to six integrals which we shall denote $\mathcal{I}_{(ia)}$ and $\mathcal{I}_{(ib)}$.

From this discussion, we can find a general expression for the complexity of the integration method in terms of the various domains of integration and the different correlators to be considered. The number of independent time ordering is $(2N-1)!!$ and the number of independent terms in $\Sigma^{(N)}$ is $2^N/2$ (we divide by 2 because half are complex conjugates of the other half). The total number of independent time integrals and correlators is therefore $(2N-1)!!2^{N-1}$.

The first correlator we need, $\mathcal{C}_{(1a)} = \langle a^\dagger(t_1-\tau_1)a^\dagger(t_2)a(t_1)a(t_2-\tau_2)\rangle$, is the first element of the vector $T_+\mathbf{v}_{X_1,Y_1}(t)$ with $X_1 = a^\dagger(t_1-\tau_1)$ and $Y_1 = a(t_1)a(t_2-\tau_2)$. We obtain $\mathbf{v}_{X_1,Y_1}(t) = e^{Mt}\mathbf{v}_{X_1,Y_1}(0) = e^{Mt}T_-\mathbf{v}_{X_1,Y_2}(\tau_1)$ with $Y_2 = a(t_2-\tau_2)$. In turn, $\mathbf{v}_{X_1,Y_2}(\tau_1) = e^{M\tau_1}\mathbf{v}_{X_1,Y_2}(0) = e^{M\tau_1}T_+\mathbf{v}_{1,Y_2}(t')$ is obtained with $Y_2 = a(t_2-\tau_2)$ and $t' = \tau_2 - \tau_1 - t$. Finally, we get $\mathbf{v}_{1,Y_2}(t') = e^{Mt'}\mathbf{v}_{1,Y_2}(0) = e^{Mt'}T_-\mathbf{v}^{\rm ss}$. Putting everything together, we get:

$$\mathcal{C}_{\substack{(1a)\\(1b)}} = \left[T_+ e^{Mt} T_\mp e^{M\tau_1} T_\pm e^{Mt'} T_- \mathbf{v}^{\rm ss}\right]_1\,, \quad (18)$$

with correspondence between upper and lower indices with the sign. Repeating this procedure for the other domains of integration, we also get:

$$\mathcal{C}_{\substack{(2a)\\(2b)}} = \left[T_+ e^{Mt} T_\mp e^{-Mt} e^{M\tau_2} T_- e^{Mt''} T_\pm \mathbf{v}^{\rm ss}\right]_1\,, \quad (19)$$

where we defined $t'' = t + \tau_1 - \tau_2$ (going from 0 to ∞), and

$$\mathcal{C}_{\substack{(3a)\\(3b)}} = \left[T_+ e^{M\tau_2} T_- e^{Mt} e^{-M\tau_2} T_\mp e^{M\tau_1} T_\pm \mathbf{v}^{\rm ss}\right]_1\,. \quad (20)$$

Integral method at $\tau = 0$

We now turn to the zero time delay contribution $S^{(2)}_{\Gamma_1,\Gamma_2}(\omega_1;\omega_2)$, which, according to Eq. (16), is given by integrating the correlators (Eqs. (18–20)) over their corresponding domains, changing variables as needed. For instance, the integrals of correlators $\mathcal{C}_{(1i)}$ require the change of variables $t_1 \to t$ and $\tau_2 \to t'$ (both extending from 0 to ∞). The final expressions for the two integrals (a) and (b) read:

$$\mathcal{I}_{\substack{(1a)\\(1b)}} = \frac{\Gamma_1\Gamma_2}{\Gamma_1+\Gamma_2}\frac{1}{(2\pi)^2}\Big[T_+\frac{-1}{M+(-i\omega_2-\Gamma_1-\frac{\Gamma_2}{2})\mathbf{1}}\times T_\mp\frac{-1}{M+(\pm i\omega_1-i\omega_2-\frac{\Gamma_1+\Gamma_2}{2})\mathbf{1}} \times T_\pm\frac{-1}{M+(-i\omega_2-\frac{\Gamma_2}{2})\mathbf{1}}T_-\mathbf{v}^{\rm ss}\Big]_1 . \quad (21)$$

The second correlators $\mathcal{C}_{(2i)}$ lead to:

$$\mathcal{I}_{\substack{(2a)\\(2b)}} = \frac{\Gamma_1\Gamma_2}{\Gamma_1+\Gamma_2}\frac{1}{(2\pi)^2}\Big[T_+\frac{-1}{M+(-i\omega_2-\Gamma_1-\frac{\Gamma_2}{2})\mathbf{1}}\times T_\mp\frac{-1}{M+(\pm i\omega_1-i\omega_2-\frac{\Gamma_1+\Gamma_2}{2})\mathbf{1}} \times T_-\frac{-1}{M+(\pm i\omega_1-\frac{\Gamma_1}{2})\mathbf{1}}T_\pm\mathbf{v}^{\rm ss}\Big]_1 . \quad (22)$$

And the third correlators $\mathcal{C}_{(3i)}$ lead to:

$$\mathcal{I}_{\substack{(3a)\\(3b)}} = \frac{\Gamma_1\Gamma_2}{\Gamma_1+\Gamma_2}\frac{1}{(2\pi)^2}\Big[T_+\frac{-1}{M+(-i\omega_2-\Gamma_1-\frac{\Gamma_2}{2})\mathbf{1}}\times T_-\frac{-1}{M-\Gamma_1\mathbf{1}} \times T_\mp\frac{-1}{M+(\pm i\omega_1-\frac{\Gamma_1}{2})\mathbf{1}}T_\pm\mathbf{v}^{\rm ss}\Big]_1 . \quad (23)$$

The total correlation function follows from twice the real part of the six previous integrals summed over and exchanging photons:

$$S^{(2)}_{\Gamma_1,\Gamma_2}(\omega_1;\omega_2) = 2\Re\sum_{i=1,2,3}\Big[\mathcal{I}_{(ia)}+\mathcal{I}_{(ib)}\Big] + [1\leftrightarrow 2] . \quad (24)$$

The finite time delay contribution $\Delta S^{(2)}_{\Gamma_1,\Gamma_2}(\omega_1;\omega_2,\tau)$ requires different domains of integration only for the variables t_2, now ranging from T_1 to T_2, and $t = t_2 - t_1$ now ranging from $t_2 - T_1$ to ∞. As a result, the integrals in Eq. (17) depend on τ. The integrals on the correlators $\mathcal{C}_{\substack{(1a)\\(1b)}}$ and $\mathcal{C}_{\substack{(2a)\\(2b)}}$, that we note $\Delta\mathcal{I}_{\substack{(1a)\\(1b)}}$ and $\Delta\mathcal{I}_{\substack{(2a)\\(2b)}}$ give similar results as the corresponding $\mathcal{I}_{\substack{(ia)\\(ib)}}$, but they acquire the τ-dependence in the form of a factor $(\Gamma_1+\Gamma_2)\mathcal{F}(\tau)$,

Appendix I: Equivalence of sensing method and standard theory

with

$$\mathcal{F}(\tau) = e^{-\Gamma_2\tau}\frac{e^{[M+(-i\omega_2+\frac{\Gamma_2}{2})\mathbf{1}]\tau}-1}{M+(-i\omega_2+\frac{\Gamma_2}{2})\mathbf{1}}\,, \tag{25}$$

that is to be inserted in Eqs. (21), (22) after the first matrix T_+. The integrals on $\mathcal{C}_{\substack{(3a)\\(3b)}}$, on the other hand, are not so straightforward. They are to be separated into two parts: one where $t_2-\tau_2 < T_1$, the other one $t_2-\tau_2 > T_1$. The first part, with integrals $\int_{T_1}^{T_2} dt_2 \int_{\tau_2}^{\infty} dt \int_{t_2-T_1}^{\infty} d\tau_2 \int_0^{\infty} d\tau_1(\ldots)$, gives rise to a quantity similar to $\Delta\mathcal{I}_{\substack{(ia)\\(ib)}}(\tau)$ with $i=1,2$, in that its τ-dependence also consists in the factor $(\Gamma_1+\Gamma_2)\mathcal{F}(\tau)$ inserted after the first matrix T_+ in Eq. (23). For this reason we note it $\Delta\mathcal{I}_{\substack{(3a)\\(3b)}}(\tau)$. The second part, with integrals $\int_{T_1}^{T_2} dt_2 \int_{t_2-T_1}^{\infty} dt \int_0^{t_2-T_1} d\tau_2 \int_0^{\infty} d\tau_1(\ldots)$, yields two more contributions:

$$\Delta\mathcal{I}_{\substack{(3\alpha)\\(3\beta)}}(\tau) = \frac{\Gamma_1\Gamma_2}{(2\pi)^2}\Big[T_+\mathcal{Z}(\tau)\times\frac{-1}{M-\Gamma_1\mathbf{1}}T_\mp\frac{-1}{M+(\pm i\omega_1-\frac{\Gamma_1}{2})\mathbf{1}}T_\pm\mathbf{v}^{\rm ss}\Big]_1\,, \tag{26}$$

where we introduced the τ-dependent matrix

$$\mathcal{Z}(\tau) = \int_{T_1}^{T_2} dt_2 \int_0^{t_2-T_1} d\tau_2 e^{-\Gamma_2(T_2-t_2)}\times e^{\left(M+(-i\omega_2-\frac{\Gamma_2}{2})\mathbf{1}\right)\tau_2}T_- e^{M(t_2-T_1-\tau_2)}\,. \tag{27}$$

$\mathcal{Z}(\tau)$ can be calculated for each element $T_-^{kl}\in\{0,1\}$ of the matrix T_-:

$$\mathcal{Z}_{i,j}(\tau) = e^{-\Gamma_2\tau}\sum_{p,k,l,q}\frac{E_{ip}E^{-1}_{pk}T_-^{kl}E_{lq}E^{-1}_{qj}}{m_p-m_q-i\omega_2-\frac{\Gamma_2}{2}}\times\Big\{\frac{e^{(m_p-i\omega_2+\frac{\Gamma_2}{2})\tau}-1}{m_p-i\omega_2+\frac{\Gamma_2}{2}}-\frac{e^{(m_q+\Gamma_2)\tau}-1}{m_q+\Gamma_2}\Big\}, \tag{28}$$

where E is the matrix of eigenvectors of M, that diagonalises it: $M_{ik}=\sum_p E_{ip}m_pE^{-1}_{pk}$, with m_p the eigenvalues.

Gathering terms with the same τ dependence defines $\Delta\mathcal{I}(\tau) = \sum_{i=1,2,3}\Big[\Delta\mathcal{I}_{(ia)}(\tau)+\Delta\mathcal{I}_{(ib)}(\tau)\Big]$ which enters in the final result:

$$\Delta S^{(2)}_{\Gamma_1,\Gamma_2}(\omega_1;\omega_2,\tau) = 2\Re\Big[\Delta\mathcal{I}(\tau)+\Delta\mathcal{I}_{(3\alpha)}(\tau)+\Delta\mathcal{I}_{(3\beta)}(\tau)\Big]\,. \tag{29}$$

Sensing method at $\tau = 0$

The intensity correlations between two sensors, $\langle n_1n_2\rangle = \langle\sigma_1^\dagger\sigma_1\sigma_2^\dagger\sigma_2\rangle$, have the equation of motion:

$$\partial_t\langle n_1n_2\rangle = -(\Gamma_1+\Gamma_2)\langle n_1n_2\rangle + 2\Re\Big[i\varepsilon_2\langle\sigma_1^\dagger\sigma_1\sigma_2a^\dagger\rangle + i\varepsilon_1\langle\sigma_1\sigma_2^\dagger\sigma_2a^\dagger\rangle\Big]\,. \tag{30}$$

This leads to the steady state solution:

$$\langle n_1 n_2 \rangle = \frac{2}{\Gamma_1 + \Gamma_2} \Re\Big[i\varepsilon_1 T_+ \mathbf{w}[11,01] \Big]_1 + [1 \leftrightarrow 2]\,. \tag{31}$$

This solution relies on $\mathbf{w}[11,01]$ which can be expressed in terms of three lower order correlators:

$$\mathbf{w}[11,01] = \frac{-1}{M + (-i\omega_2 - \Gamma_1 - \frac{\Gamma_2}{2})\mathbf{1}} \times \Big\{ -i\varepsilon_2 T_- \mathbf{w}[11,00] - i\varepsilon_1 T_- \mathbf{w}[10,01] + i\varepsilon_1 T_+ \mathbf{w}[01,01] \Big\}\,, \tag{32}$$

each of which is given by:

$$\mathbf{w}[11,00] = \frac{-1}{M - \Gamma_1 \mathbf{1}} \times \Big\{ i\varepsilon_1 T_+ \mathbf{w}[01,00] - i\varepsilon_1 T_- \mathbf{w}[10,00] \Big\}\,, \tag{33}$$

$$\mathbf{w}[10,01] = \frac{-1}{M + (i\omega_1 - i\omega_2 - \frac{\Gamma_1 + \Gamma_2}{2})\mathbf{1}} \times \Big\{ -i\varepsilon_2 T_- \mathbf{w}[10,00] + i\varepsilon_1 T_+ \mathbf{w}[00,01] \Big\}\,, \tag{34}$$

and

$$\mathbf{w}[01,01] = \frac{-1}{M + (-i\omega_1 - i\omega_2 - \frac{\Gamma_1 + \Gamma_2}{2})\mathbf{1}} \times \Big\{ -i\varepsilon_1 T_- \mathbf{w}[00,01] - i\varepsilon_2 T_- \mathbf{w}[01,00] \Big\}\,. \tag{35}$$

Finally, we apply a last time the recursive relation Eq. (11) to find the three different correlators involved in the previous expressions:

$$\mathbf{w}[10,00] = \frac{-1}{M + (i\omega_1 - \frac{\Gamma_1}{2})\mathbf{1}} i\varepsilon_1 T_+ \mathbf{v}^{\rm ss}\,, \tag{36a}$$

$$\mathbf{w}[00,01] = \frac{-1}{M + (-i\omega_2 - \frac{\Gamma_2}{2})\mathbf{1}} (-i\varepsilon_2 T_-) \mathbf{v}^{\rm ss}\,, \tag{36b}$$

$$\mathbf{w}[01,00] = \frac{-1}{M + (-i\omega_1 - \frac{\Gamma_1}{2})\mathbf{1}} (-i\varepsilon_1 T_-) \mathbf{v}^{\rm ss}\,. \tag{36c}$$

Sensing method at $\tau > 0$

We now consider the case where the second photon is absorbed by sensor 2 with some delay $\tau > 0$ after a first photon is absorbed by sensor 1. The correlator of interest is $\langle n_1(0) n_2(\tau) \rangle$,

with equation of motion:

$$\partial_\tau \langle n_1(0) n_2(\tau)\rangle = -\Gamma_2 \langle n_1(0) n_2(\tau)\rangle + 2\Re\Big[i\varepsilon_2 \langle n_1(0)(\sigma_2 a^\dagger)(\tau)\rangle\Big]\,, \tag{37}$$

with the initial condition in the steady state $\langle n_1(0) n_2(0)\rangle = \langle n_1 n_2\rangle$. This solution relies on $\langle n_1(0)(\sigma_2 a^\dagger)(\tau)\rangle$. To compute it, we introduce a vector analogous to Eq. (38) but now consisting of two-time correlators:

$$\mathbf{w}'[11,\mu_2\nu_2](\tau) = \begin{pmatrix} \langle n_1(0)(\sigma_2^{\dagger\mu_2}\sigma_2^{\nu_2})(\tau)\rangle \\ \langle n_1(0)(\sigma_2^{\dagger\mu_2}\sigma_2^{\nu_2} a)(\tau)\rangle \\ \langle n_1(0)(\sigma_2^{\dagger\mu_2}\sigma_2^{\nu_2} a^\dagger)(\tau)\rangle \\ \langle n_1(0)(\sigma_2^{\dagger\mu_2}\sigma_2^{\nu_2} a^\dagger a)(\tau)\rangle \\ \vdots \end{pmatrix}. \tag{38}$$

With this definition, $\langle n_1(0)(\sigma_2 a^\dagger)(\tau)\rangle$ is the first element of the vector $T_+\mathbf{w}'[11,01](\tau)$. The τ-equation for $\mathbf{w}'[11,01](\tau)$ reads:

$$\partial_\tau \mathbf{w}'[11,01](\tau) = \Big[M + (-i\omega_2 - \frac{\Gamma_2}{2})\mathbf{1}\Big]\mathbf{w}'[11,01](\tau) - i\varepsilon_2 T_-\mathbf{w}'[11,00](\tau)\,, \tag{39}$$

with $\mathbf{w}'[11,00](\tau) = e^{M\tau}\mathbf{w}[11,00]$ with initial condition $\mathbf{w}'[11,01](0) = \mathbf{w}[11,01]$ in the steady state. After some algebra, one arrives to the solution:

$$\mathbf{w}'[11,01](\tau) = e^{\left[M+(-i\omega_2-\frac{\Gamma_2}{2})\mathbf{1}\right]\tau}\mathbf{w}[11,01] - (-i\varepsilon_2)\mathcal{Y}(\tau)\mathbf{w}[11,00]\,, \tag{40}$$

in terms of a matrix $\mathcal{Y}(\tau)$ defined elementwise as:

$$\mathcal{Y}_{ij}(\tau) = \sum_{p,k,l,q} \frac{E_{ip}E^{-1}_{pk}T^{kl}_- E_{lq}E^{-1}_{qj}}{m_p - m_q - i\omega_2 - \frac{\Gamma_2}{2}}\Big\{e^{(m_p - i\omega_2 - \frac{\Gamma_2}{2})\tau} - e^{m_q\tau}\Big\}\,. \tag{41}$$

Substituting this expression into Eq. (37) and solving it, we obtain:

$$\langle n_1(0) n_2(\tau)\rangle = e^{-\Gamma_2\tau}\langle n_1 n_2\rangle + 2\Re\Big[i\varepsilon_2 T_+\mathcal{F}(\tau)\mathbf{w}[11,01]\Big]_1 + 2\Re\Big[\varepsilon_2^2 T_+\mathcal{Z}(\tau)\mathbf{w}[11,00]\Big]_1\,, \tag{42}$$

where the matrices $\mathcal{F}(\tau)$ and $\mathcal{Z}(\tau)$ are those introduced in the previous section, namely, Eqs. (25) and (28), respectively.

Equality of the integral and sensing methods

We complete the proof by showing that the results from the integration and the sensing methods are the same to leading order in the coupling ε.

First, the case $\tau = 0$. The final expression for $\langle n_1 n_2 \rangle$ is obtained by inserting the solutions for the correlators (33–35) into Eq. (31). This leads to the same results as Eq. (24), with the integrals appearing precisely in the following order:

$$\langle n_1 n_2 \rangle = \frac{\varepsilon_1^2 \varepsilon_2^2}{\Gamma_1 \Gamma_2} (2\pi)^2 \times 2\Re\Big\{ \mathcal{I}_{(3b)} + \mathcal{I}_{(3a)} + \mathcal{I}_{(2a)} + \mathcal{I}_{(1a)} + \mathcal{I}_{(1b)} + \mathcal{I}_{(2b)} \Big\} + [1 \leftrightarrow 2] = \\ = \frac{\varepsilon_1^2 \varepsilon_2^2}{\Gamma_1 \Gamma_2} (2\pi)^2 S^{(2)}_{\Gamma_1,\Gamma_2}(\omega_1;\omega_2)\,. \quad (43)$$

Second, the case $\tau > 0$. For ease of comparison, we rewrite the term $\Delta\mathcal{I}$ in term of the vector $\mathbf{w}[11,01]$ as:

$$\Delta\mathcal{I}(\tau) = \frac{\Gamma_1\Gamma_2}{(2\pi)^2} \Big[T_+ \mathcal{F}(\tau) \frac{1}{\varepsilon_1^2(-i\varepsilon_2)} \mathbf{w}[11,01] \Big]_1 . \quad (44)$$

It is then clear that this expression is equal, up to a constant, to the second line in the expression for $\langle n_1(0) n_2(\tau) \rangle$, Eq. (42). Similarly, the term $\Delta\mathcal{I}_{(3\alpha)}(\tau) + \Delta\mathcal{I}_{(3\beta)}(\tau)$ in Eq. (26) can be rewritten as:

$$\Delta\mathcal{I}_{(3\alpha)}(\tau) + \Delta\mathcal{I}_{(3\beta)}(\tau) = \frac{\Gamma_1\Gamma_2}{(2\pi)^2} \Big[T_+ \mathcal{Z}(\tau) \frac{1}{\varepsilon_1^2} \mathbf{w}[11,00] \Big]_1 , \quad (45)$$

and related to the third line in Eq. (42). All together, we can therefore conclude that, to leading order in the couplings:

$$\langle n_1(0) n_2(\tau) \rangle = \frac{\varepsilon_1^2 \varepsilon_2^2}{\Gamma_1 \Gamma_2} (2\pi)^2 S^{(2)}_{\Gamma_1,\Gamma_2}(\omega_1;\omega_2,\tau)\,. \quad (46)$$

This proof can be generalised to N-photon correlations and/or for finite T_1-time dynamics (instead of a steady state) by repeating these procedures linearly in the number of sensors and integrals. There is no conceptual difference brought by the higher number of variables, but notations become heavy and for the sake of clarity, we have illustrated the proof in the simplest, as well as most relevant cases, of $N = 1$ and 2. Also, nothing in the proof relies on the choice of sensors as two-level systems, which has been made for convenience. As we always examine crossed correlations between them, they could also be, e.g., harmonic oscillators, and provide identical results.

Appendix II: Master equation for qubits coupled to a common 1D EM modes.

In Chapters 7 and 8, we have studied the situation where many emitters are coupled to a common one-dimensional reservoir. In this Appendix, we will obtain the master equation which describes this situation. When a collection of N emitters, placed at positions x_n and described by operators $\mathcal{O}_n$, are interacting with common EM one-dimensional reservoir, the general interaction Hamiltonian in the interaction picture can be written as follows:

$$H_I(t) = \sum_{n=1}^{N} (e^{i\omega_0 t}\mathcal{O}_n^\dagger E(x_n,t) + \text{H.c.}), \tag{1}$$

with $E(x_n,t)$ given by the one-dimensional quantized electromagnetic (EM) field:

$$E(x_n,t) = \sum_q g_q \Big(a_q e^{-i(\omega_q t - q x_n)} + a_q^\dagger e^{i(\omega_q t - q x_n)} \Big). \tag{2}$$

In order to trace out the degrees of freedom of the waveguides, a_q, we will assume the Born-Markov approximation which is justified as long as the radiation reservoir has a memory time which is much shorter than the inverse system-bath coupling. As we have shown in Chapter 6, this will be generally the case. Similar discussions as the one presented here can be found in several text-books (see for example [25]), however it is interesting to review here the main steps since a detailed derivation is required to understand, for example, the role of counter-rotating terms in the atom-field coupling to get the effective dipole-dipole interactions and the specificities introduced by the one-dimensional character. The reduced density matrix for the quantum emitters is defined $\rho_{\rm S} = {\rm Tr}_{\rm B}\{\rho\}$, where ${\rm Tr}_{\rm B}\{\bullet\}$ represents the trace over the field degrees of freedom. Within the Born-Markov approximation one finds the following

equation for the dynamics of $\rho_{\rm S}$,

$$\frac{d\rho_{\rm S}}{dt} = -\int_0^\infty ds {\rm Tr}_B\Big\{\big[H_I(t),[H_I(t-s),\rho_{\rm S}\otimes\rho_B\big]\Big\}. \tag{3}$$

Tracing out the electromagnetic degrees of freedom one arrives to the following Lindblad form for the master equation

$$\mathcal{L}(\rho_{\rm S}) = \sum_{n,m} J_{n,m}\left(\mathcal{O}_n^-\rho_{\rm S}\mathcal{O}_m^+ - \rho_{\rm S}\mathcal{O}_m^+\mathcal{O}_n^-\right) + {\rm H.c.}. \tag{4}$$

With collective couplings $J_{n,m}$ given by

$$J_{n,m} = \int_0^\infty ds(e^{-i\omega_0 s} + e^{i\omega_0 s})\langle E(x_n,t)E(x_m,t-s)\rangle\,. \tag{5}$$

One should keep the counter-rotating terms since they will be crucial to get the right expression for dipole-dipole forces. One needs to compute the bath correlator,

$$\langle E(x_n,t)E(x_m,t-s)\rangle = \sum_q |g_q|^2 e^{-i\omega_q s}e^{iqx_{n,m}}\,, \tag{6}$$

obtained under the assumption that the radiation field is in the vacuum, $\langle a_q^\dagger a_q\rangle = 0$ and where $x_{n,m} = x_n - x_m$. Note that this assumption holds for most of the physical situations considered in this work, in particular experiments at optical frequencies at room temperature. To get explicit expressions, we assume a general light-matter coupling $g_q = \mu^2\sqrt{\frac{2\pi\omega_q}{L}} = \frac{\bar{g}_q}{\sqrt{L}}$, with L being the quantization length and μ the dipolar coupling strength. Using (5), one can carry out the calculation of $J_{n,m}$

$$J_{n,m} = \frac{1}{L}\sum_q \bar{g}_q^2\int_0^\infty ds e^{iqx_{n,m}}\left(e^{i(\omega_0-\omega_q)s} + e^{-i(\omega_0+\omega_q)s}\right). \tag{7}$$

The next step consists of performing the continuum limit and transform into an ω integral by making use of the dispersion relationship $q(\omega)$:

$$\frac{1}{L}\sum_q \to \int_{-\infty}^\infty \frac{dq}{2\pi}\,, \tag{8}$$

arriving to

$$J_{n,m} = \int_{-\infty}^{\infty} \frac{dq}{2\pi} |\bar{g}_q|^2 \int_0^{\infty} ds e^{iqx_{n,m}} \left(e^{i(\omega_0 - \omega_q)s} + e^{-i(\omega_0 + \omega_q)s} \right). \tag{9}$$

Then, it is convenient to separate the negative and positive intervals of the q-integral:

$$J_{n,m} = \int_0^{\infty} \frac{dq}{\pi} |\bar{g}_q|^2 \cos(qx_{m,n}) \int_0^{\infty} ds \left(e^{i(\omega_0 - \omega_q)s} + e^{-i(\omega_0 + \omega_q)s} \right). \tag{10}$$

Making use of the dispersion relationship ω_q, one can transform the q integral into an energy integral:

$$J_{n,m} = \int_0^{\infty} \frac{d\omega}{\pi} |\partial_\omega q(\omega)| |\bar{g}_{q(\omega)}|^2 \cos(qx_{m,n}) \int_0^{\infty} ds (e^{i(\omega_0 - \omega)s} + e^{-i(\omega_0 + \omega)s}), \tag{11}$$

where $q = q(\omega)$ is the inverse function of the dispersion relationship ω_q of the one-dimensional waveguide modes. In the case of a light-like dispersion relationship $\omega_q = cq$, then $|\partial_\omega q(\omega)| = c^{-1}$. However, we will keep as general as possible to be able to generalize the results to other modes, i.e, plasmons. Now I use the following formula:

$$\int_0^{\infty} ds e^{ias} = \pi\delta(a) + i\text{P.V.}\frac{1}{a}. \tag{12}$$

Inserting this relationship into (11) one arrives to

$$J_{n,m} = \int_0^{\infty} \frac{d\omega}{\pi} |\partial_\omega q(\omega)| |\bar{g}_{q(\omega)}|^2 \cos(qx_{m,n}) \Big(\pi\delta(\omega_0 - \omega) + \pi\delta(\omega + \omega_0) + i\text{P.V.}\frac{1}{\omega_0 - \omega} - i\text{P.V.}\frac{1}{\omega + \omega_0} \Big), \tag{13}$$

where P.V. is denoting that the Cauchy *principal value* integral should be computed. The contribution coming from the δ function can be computed straightforwardly, whereas the one of the principal value can be grouped into a single term

$$\begin{aligned} J_{n,m} &= |\partial_\omega q(\omega_0)| |\bar{g}_{q(\omega_0)}|^2 \cos(q(\omega_0)x_{m,n}) + \\ \text{P.V.}\frac{i}{\pi} \int_0^{\infty} d\omega \text{Re}\Big[|\partial_\omega q(\omega)| |\bar{g}_{q(\omega)}|^2 e^{iq(\omega)x_{m,n}} \Big] \Big(\frac{1}{\omega_0 - \omega} - \frac{1}{\omega_0 + \omega} \Big) &= \\ &= |\partial_\omega q(\omega_0)| |\bar{g}_{q(\omega_0)}|^2 \cos(q(\omega_0)x_{m,n}) - \\ \text{P.V.}\frac{i}{\pi} \int_{-\infty}^{\infty} d\omega \frac{\text{Re}\Big[|\partial_\omega q(\omega)| |\bar{g}_{q(\omega)}|^2 e^{iq(\omega)x_{m,n}} \Big]}{\omega - \omega_0}, \end{aligned} \tag{14}$$

by using that $q(-\omega) = q(\omega)$. Making use of the well-known *Kramers-Kroning* relationships:

$$\mathrm{Im}[f(\omega_0)] = -\frac{1}{\pi}\int_{-\infty}^{\infty}\frac{\mathrm{Re}[f(\omega)]}{\omega-\omega_0}\,, \tag{15}$$

the coupling can be written as:

$$J_{n,m} \;=\; \frac{\Gamma}{2}\left(\cos(q(\omega_0)(x_n-x_m)) + i\sin(q(\omega_0)|x_n-x_m|)\right),\,, \tag{16}$$

where $\Gamma = \gamma(\omega_0)$, with the function $\gamma(\omega) = 2|\partial_\omega q(\omega)||\bar{g}_{q(\omega)}|^2 = |g_{q(\omega)}|^2 D(\omega)/\pi$, where $q(\omega)$ is the resonant wavevector at ω and $D(\omega) = (2\pi/L)|\partial_\omega q(\omega)|$ is the e.m. density of states. This is the expression that will be used for the coupling in the Thesis, i.e. in Chapter 8.

List of publications

Regular Journals.

1. *Two-photon lasing by a single quantum dot in a high-Q microcavity.* E. del Valle, S. Zippilli, F. P. Laussy, **A. Gonzalez-Tudela**, G. Morigi and C. Tejedor. Phys. Rev. B **81**, 035302 (2010)

2. *Effect of pure dephasing on the Jaynes-Cummings nonlinearities.* **A. Gonzalez-Tudela**, E. del Valle, E. Cancellieri, C. Tejedor, D. Sanvitto and F.P. Laussy. Optics Express **18**, 7002-7009 (2010).

3. *Dissipative dynamics of a solid-state qubit coupled to surface plasmons: From Markov to non-Markov regimes.* **A. Gonzalez-Tudela**, F. J. Rodriguez, L. Quiroga and C. Tejedor. Phys. Rev. B **82**, 115334 (2010)

4. *Entanglement of two qubits mediated by one-dimensional plasmonic waveguides.* . **A. Gonzalez-Tudela**, D. Martin-Cano, L. Martin-Moreno, E. Moreno, C. Tejedor and F. J. Garcia-Vidal. Phys. Rev. Let. **106**, 205201 (2011). (Highlighted in *Physics*).

5. *Generation of a two-photon state from a quantum dot in a microcavity.* E. del Valle, **A. Gonzalez-Tudela**, E. Cancellieri, F. P. Laussy and C. Tejedor. New Journal of Physics **13**, 113014 (2011)

6. *Dissipation-driven generation of two-qubit entanglement mediated by one-dimensional plasmonic waveguides* . D. Martin-Cano, **A. Gonzalez-Tudela**, L. Martin-Moreno, C. Tejedor, F. J. Garcia-Vidal and E. Moreno. Phys. Rev. B **84**, 235306 (2011).

7. *Plasmon-Polariton emission from a coherently p-excited quantum dot near a metal interface.* C. Sanchez-Munoz, **A. Gonzalez-Tudela** and C. Tejedor. Phys. Rev. B **85**, 125301 (2012)

8. *Theory of frequency-filtered and time-resolved N-photon correlations.* E. del Valle, **A. Gonzalez-Tudela**, F. P. Laussy, C. Tejedor and M. J. Hartmann. Phys. Rev. Let. **109**, 183601 (2012)

Book Chapters.

9. *Luminescence spectra of quantum dots in Microcavities.* F.P. Laussy, E. del Valle, A. Laucht, **A. Gonzalez-Tudela**, M. Kaniber, J. J. Finley and, C. Tejedor. Book Chapter in Woodhead Publishing Series in Electronic and Optical Materials No **28** (2012).

Conference proceedings with peer review.

10. *Dephasing of strong-coupling in the non-linear regime.* **A. Gonzalez-Tudela**, E. del Valle, E. Cancellieri, C. Tejedor, D. Sanvitto and F. P. Laussy. AIP Conference Proceedings ICPS 30, **1399**, 1015 (2010).

11. *Linear and non-linear coupling of quantum dots in microcavities.* F.P. Laussy, E. del Valle, **A. Gonzalez-Tudela**, D. Sanvitto and C. Tejedor. 18th Int. Symp. "Nanostructures: Physics and Technology" **298** (2010).

12. *Anticrossing in the PL spectrum of light-matter coupling under incoherent continuous pumping.* **A. Gonzalez-Tudela**, E. del Valle, C. Tejedor and F.P. Laussy. Superlattices and Microstructures **47**, 16-18 (Proceedings of PLMCN9) (2010).

13. *Quantum dot coupled to metal-semiconductor interface plasmons..* **A. Gonzalez-Tudela**, F. J. Rodriguez, L. Quiroga and C. Tejedor. AIP Conference Proceedings ICPS30 **1399**, 1015 (2011)

14. *Exploring qubit-qubit entanglement mediated by one-dimensional plasmonic nanowaveguides.* **A. Gonzalez-Tudela**, D. Martin-Cano, L. Martin-Moreno, E. Moreno, F. J. Garcia-Vidal and C. Tejedor. Phys. Status Solidi C **9**, 1303-1308 (2012).

15. *Generation of a two-photon state from a quantum dot in a microcavity under incoherent and coherent continous excitation.* E. del Valle, **A. Gonzalez-Tudela**, F. P. Laussy. Proceedings of SPIE **8255**, 825505 (2012)

Pre-prints.

16. *Theory of Strong-Coupling between quantum emitters and propagating surface Plasmon Polaritons.* **A. Gonzalez-Tudela**, P. A. Huidobro, L. Martin-Moreno, C. Tejedor and F. J. Garcia-Vidal. arXiv: 1203-6016 (2012) (Submitted to Phys. Rev. Let.).

17. *Mesoscopic Entanglement Induced by Spontaneous Emission in Solid-State Quantum Optics* . **A. Gonzalez-Tudela** and D. Porras. arXiv:1209.4730 (2012) (Submitted to Phys. Rev. Let.).

18. *Two-photon spectra of quantum emitters.* **A. Gonzalez-Tudela**, F. P. Laussy, C. Tejedor, M. J. Hartmann and E. del Valle.arXiv:1211.5592 (2012) (Submitted to New Journal of Physics)

19. *Reversible dynamics between quantum emitters and propagating surface Plasmon Polaritons.* **A. Gonzalez-Tudela**, P. A. Huidobro, L. Martin-Moreno, C. Tejedor and F. J. Garcia-Vidal. (*in preparation*)

Bibliography

[1] A. Einstein, "Die Grundlage der allgemeinen Relativitätstheorie," *Annalen der Physik*, vol. 49, p. 549, 1916. 1

[2] A. Einstein, B. Podolsky, and N. Rosen, "Can Quantum-Mechanical Description of Physical Reality Be Considered Complete?," *Phys. Rev.*, vol. 47, p. 777, 1935. 1

[3] M. F. Pusey, J. Barrett, and T. Rudolph, "On the reality of the quantum state," *Nature Physics*, vol. 8, no. 476–479, 2012. 1

[4] J. Bardeen and W. H. Brattain, "Physical Principles Involved in Transistor Action," *Phys. Rev.*, vol. 75, pp. 1208–1225, Apr 1949. 1

[5] A. L. Schawlow and C. H. Townes, "Infrared and Optical Masers," *Phys. Rev.*, vol. 112, p. 1940, 1958. 1

[6] C. H. Townes, "Production of coherent radiation by atoms—and molecules," *Nobel Lecture*, 1964. 1

[7] M. A. Nielsen and I. L. Chuang, *Quantum computation and quantum information*. Cambridge University Press, 2000. 2, 13, 119

[8] N. Gisin, G. Ribordy, W. Tittel, and H. Zbinden, "Quantum cryptography," *Rev. Mod. Phys.*, vol. 74, p. 145, 2002. 2

[9] T. D. Ladd, F. Jelezko, R. Laflamme, Y. Nakamura, C. Monroe, and J. L. O'Brien, "Quantum computers," *Nature*, vol. 464, p. 45, 2010. 2

[10] J. I. Cirac and P. Zoller, "Quantum Computations with Cold Trapped Ions," *Phys. Rev. Lett.*, vol. 74, pp. 4091–4094, May 1995. 2

[11] T. Monz, P. Schindler, J. T. Barreiro, M. Chwalla, D. Nigg, W. A. Coish, M. Harlander, W. Hänsel, M. Hennrich, and R. Blatt, "14-Qubit Entanglement: Creation and Coherence," *Phys. Rev. Lett.*, vol. 106, p. 130506, Mar 2011. 2

[12] I. Bloch, "Quantum coherence and entanglement with ultracold atoms in optical lattices," *Nature*, vol. 453, p. 1016, 2008. 2

[13] S. Haroche and D. Kleppner, "Cavity Quantum Electrodynamics," *Physics Today*, vol. 42, p. 24, 1989. 2, 29

[14] D. Loss and D. P. DiVincenzo, "Quantum computation with quantum dots," *Phys. Rev. A*, vol. 57, pp. 120–126, Jan 1998. 2, 5, 6

[15] A. Ĭmamoḡlu, D. D. Awschalom, G. Burkard, D. P. DiVincenzo, D. Loss, M. Sherwin, and A. Small, "Quantum Information Processing Using Quantum Dot Spins and Cavity QED," *Phys. Rev. Lett.*, vol. 83, p. 4204, 1999. 2, 5, 6, 13, 119, 143, 151

[16] W. Weisskopf and E. Wigner, "Calculation of the Natural Line Width on the Basis of Dirac's Theory of Light (as translated by J. B. Sykes)," *Zeitschrift für Physik*, vol. 63, p. 54, 1930. 2

[17] G. Khitrova, H. M. Gibbs, M. Kira, S. W. Koch, and A. Scherer, "Vacuum Rabi splitting in semiconductors," *Nat. Phys.*, vol. 2, p. 81, 2006. 3, 7

[18] W. L. Barnes, A. Dereux, and T. W. Ebbesen, "Surface plasmon wavelength optics," *Nature*, vol. 424, p. 824, 2003. 3, 9, 94

[19] S. A. Maier, *Plasmonics: fundamentals and applications.* Springer, 2007. 3, 9

[20] F. Verstraete, M. M. Wolf, and J. I. Cirac, "Quantum computation and quantum-state engineering driven by dissipation," *Nature Phys.*, vol. 5, p. 633, 2009. 3, 119, 143

[21] M. B. Plenio, S. F. Huelga, A. Beige, and P. L. Knight, "Cavity-loss-induced generation of entangled atoms," *Phys. Rev. A*, vol. 59, p. 2468, 1999. 3

[22] B. Kraus, H. P. Büchler, S. Diehl, A. Kantian, A. Micheli, and P. Zoller, "Preparation of entangled states by quantum Markov processes," *Phys. Rev. A*, vol. 78, p. 042307, Oct 2008. 3

[23] H. Krauter, C. A. Muschik, K. Jensen, W. Wasilewski, J. M. Petersen, J. I. Cirac, and E. S. Polzik, "Entanglement Generated by Dissipation and Steady State Entanglement of Two Macroscopic Objects," *Phys. Rev. Lett.*, vol. 107, p. 080503, Aug 2011. 3, 119, 143

[24] C. A. Muschik, E. S. Polzik, and J. I. Cirac, "Dissipatively driven entanglement of two macroscopic atomic ensembles," *Phys. Rev. A*, vol. 83, p. 052312, May 2011. 3

[25] H.-P. Breuer and F. Petruccione, *The Theory of Open Quantum Systems.* Oxford, 2002. 4, 13, 98, 100, 101, 151, 173

[26] G. W. Gardiner and P. Zoller, *Quantum Noise.* Springer-Verlag, Berlin, 2nd ed., 2000.

[27] H. J. Carmichael, *Statistical methods in quantum optics 1.* Springer, 2 ed., 2002. 4, 13, 21, 24

[28] A. Badolato, K. Hennessy, M. Atature, J. Dreyser, E. Hu, P. M. Petroff, and A. Ĭmamoḡlu, "Deterministic Coupling of Single Quantum Dots to Single Nanocavity Modes," *Science*, vol. 308, p. 1158, 2005. 5, 7, 143

[29] K. Hennessy, A. Badolato, M. Winger, D. Gerace, M. Atature, S. Gulde, S. Fält, E. L. Hu, and A. Ĭmamoḡlu, "Quantum nature of a strongly coupled single quantum dot–cavity system," *Nature*, vol. 445, p. 896, 2007. 7, 10, 29, 38, 39, 41, 43, 51, 59

[30] D. Englund, A. Majumdar, A. Faraon, M. Toishi, N. Stoltz, P. Petroff, and J. Vuckovic, "Resonant Excitation of a Quantum Dot Strongly Coupled to a Photonic Crystal Nanocavity," *Phys. Rev. Lett.*, vol. 104, p. 073904, 2010. 5, 143

[31] A. Mohan, P. Gallo, M. Felici, B. Dwir, A. Rudra, J. Faist, and E. Kapon, "Record-Low Inhomogeneous Broadening of Site-Controlled Quantum Dots for Nanophotonics," *Small*, vol. 6, no. 12, pp. 1268–1272, 2010. 5, 6, 151, 155

[32] J. M. Elzerman, R. Hanson, L. H. Willems van Beveren, B. Witkamp, L. M. K. Vandersypen, and L. P. Kouwenhoven, "Single-shot read-out of an individual electron spin in a quantum dot," *Nature*, vol. 430, pp. 431–435, July 2004. 6

[33] J. R. Petta, A. C. Johnson, J. M. Taylor, E. A. Laird, A. Yacoby, M. D. Lukin, C. M. Marcus, M. P. Hanson, and A. C. Gossard, "Coherent Manipulation of Coupled Electron Spins in Semiconductor Quantum Dots," *Science*, vol. 309, no. 5744, pp. 2180–2184, 2005. 6

[34] S. Haroche and J.-M. Raimond, *Exploring the Quantum: Atoms, Cavities, and Photons*. Oxford University Press, 2006. 6, 13

[35] E. M. Purcell, H. C. Torrey, and R. V. Pound, "Resonance Absorption by Nuclear Magnetic Moments in a Solid," *Phys. Rev.*, vol. 69, p. 37, 1946. 7

[36] E. Fermi, "Quantum Theory of Radiation," *Rev. Mod. Phys.*, vol. 4, p. 87, 1932. 7, 17, 94, 95

[37] J. P. Reithmaier, G. Sek, A. Löffler, C. Hofmann, S. Kuhn, S. Reitzenstein, L. V. Keldysh, V. D. Kulakovskii, T. L. Reinecker, and A. Forchel, "Strong coupling in a single quantum dot–semiconductor microcavity system," *Nature*, vol. 432, p. 197, 2004. 7, 50

[38] C. Weisbuch, M. Nishioka, A. Ishikawa, and Y. Arakawa, "Observation of the coupled exciton-photon mode splitting in a semiconductor quantum microcavity," *Phys. Rev. Lett.*, vol. 69, p. 3314, 1992. 7, 10

[39] K. Brunner, U. Bockelmann, G. Abstreiter, M. Walther, G. Böhm, G. Tränkle, and G. Weimann, "Photoluminescence from a single GaAs/AlGaAs quantum dot," *Phys. Rev. Lett.*, vol. 69, p. 3216, 1992. 7

[40] J.-Y. Marzin, J.-M. Gérard, A. Izraël, D. Barrier, and G. Bastard, "Photoluminescence of Single InAs Quantum Dots Obtained by Self-Organized Growth on GaAs," *Phys. Rev. Lett.*, vol. 73, p. 716, 1994. 7

[41] D. Sanvitto, A. Daraei, A. Tahraoui, M. Hopkinson, P. W. Fry, D. M. Whittaker, and M. S. Skolnick, "Observation of ultrahigh quality factor in a semiconductor microcavity," *Appl. Phys. Lett.*, vol. 86, p. 191109, 2005. 7

[42] E. Yablonovitch, "Inhibited Spontaneous Emission in Solid-State Physics and Electronics," *Phys. Rev. Lett.*, vol. 58, p. 2059, 1987. 7

[43] S. John, "Strong localization of photons in certain disordered dielectric superlattices," *Phys. Rev. Lett.*, vol. 58, p. 2486, 1987.

[44] E. Yablonovitch, T. J. Gmitter, and K. M. Leung, "Photonic band structure: The face-centered-cubic case employing nonspherical atoms," *Phys. Rev. Lett.*, vol. 67, p. 2295, 1991. 7

[45] A. I. Nosich, E. I. Smotrova, S. V. Boriskina, T. M. Benson, and P. Sewell, "Trends in microdisk laser research and linear optical modelling," *Opt. Quant. Electron.*, vol. 39, p. 1253, 2007. 7

[46] T. Yoshie, A. Scherer, J. Heindrickson, G. Khitrova, H. M. Gibbs, G. Rupper, C. Ell, O. B. Shchekin, and D. G. Deppe, "Vacuum Rabi splitting with a single quantum dot in a photonic crystal nanocavity," *Nature*, vol. 432, p. 200, 2004. 7

[47] E. Peter, P. Senellart, D. Martrou, A. Lemaître, J. Hours, J. M. Gérard, and J. Bloch, "Exciton-Photon Strong-Coupling Regime for a Single Quantum Dot Embedded in a Microcavity," *Phys. Rev. Lett.*, vol. 95, p. 067401, 2005. 7

[48] A. Laucht, F. Hofbauer, N. Hauke, J. Angele, S. Stobbe, M. Kaniber, G. Böhm, P. Lodahl, M.-C. Amann, and J. J. Finley, "Electrical control of spontaneous emission and strong coupling for a single quantum dot," *New J. Phys.*, vol. 11, p. 023034, 2009. 7, 8, 29, 30, 36, 40

[49] H. Haug and S. W. Koch, *Quantum theory of the optical and electronic properties of semiconductors*. World Scientific, 1990. 8

[50] M. Kira and S. W. Koch, "Cluster-expansion representation in quantum optics," *Phys. Rev. A*, vol. 78, p. 022102, 2008. 8

[51] C. Gies, J. Wiersig, M. Lorke, and F. Jahnke, "Semiconductor model for quantum-dot-based microcavity lasers," *Phys. Rev. A*, vol. 75, p. 013803, 2007. 8

[52] M. Richter, A. Carmele, A. Sitek, and A. Knorr, "Few-Photon Model of the Optical Emission of Semiconductor Quantum Dots," *Phys. Rev. Lett.*, vol. 103, p. 087407, 2009. 8

[53] A. Carmele, M. Richter, W. W. Chow, and A. Knorr, "Antibunching of Thermal Radiation by a Room-Temperature Phonon Bath: A Numerically Solvable Model for a Strongly Interacting Light-Matter-Reservoir System," *Phys. Rev. Lett.*, vol. 104, p. 156801, 2010. 8

[54] J. Wiersig, "Microscopic theory of first-order coherence in microcavity lasers based on semiconductor quantum dots," *Phys. Rev. B*, vol. 82, p. 155320, 2010. 8

[55] F. P. Laussy, E. del Valle, A. Gonzalez-Tudela, E. Cancellieri, D. Sanvitto, and C. Tejedor, "Linear and nonlinear coupling of quantum dots in microcavities," *Int. Symp. "Nanostructures: Physics and Technology"*, vol. 18, p. 298, 2010. 8

[56] A. V. Akimov, A. Mukherjee, C. L. Yu, D. E. Chang, A. S. Zibrov, P. R. Hemmer, H. Park, and M. D. Lukin, "Generation of single optical plasmons in metallic nanowires coupled to quantum dots," *Nature*, vol. 450, Nov 2007. 8, 10, 89, 120, 121, 151, 155

[57] T. W. Ebbesen, C. Genet, and S. I. Bozhevolnyi, "Surface-plasmon circuitry," *Physics Today*, vol. 5, pp. 44–50, 2008. 9

[58] L. Novotny and B. Hecht, *Principles of Nano-Optics*. Cambridge, 2006. 9, 17, 89, 91, 94, 95, 96, 123, 126

[59] A. Trügler and U. Hohenester, "Strong coupling between a metallic nanoparticle and a single molecule," *Phys. Rev. B*, vol. 77, p. 115403, Mar 2008. 104

[60] T. Lund-Hansen, S. Stobbe, B. Julsgaard, H. Thyrrestrup, T. Sünner, M. Kamp, A. Forchel, and P. Lodahl, "Experimental Realization of Highly Efficient Broadband Coupling of Single Quantum Dots to a Photonic Crystal Waveguide," *Phys. Rev. Lett.*, vol. 101, p. 113903, Sep 2008. 9, 89

[61] A. Huck, S. Kumar, A. Shakoor, and U. L. Andersen, "Controlled Coupling of a Single Nitrogen-Vacancy Center to a Silver Nanowire," *Phys. Rev. Lett.*, vol. 106, p. 096801, Feb 2011. 10, 89, 120, 121, 129, 138, 151, 155

[62] A. Cuche, O. Mollet, A. Drezet, and S. Huant, ""Deterministic" Quantum Plasmonics," *Nano Letters*, vol. 10, no. 11, pp. 4566–4570, 2010. 10, 89

[63] D. E. Chang, A. S. Sørensen, P. R. Hemmer, and M. D. Lukin, "Strong coupling of single emitters to surface plasmons," *Phys. Rev. B*, vol. 76, p. 035420, Jul 2007. 10, 95, 101, 120

[64] A. Gonzalez-Tudela, D. Martin-Cano, E. Moreno, L. Martin-Moreno, C. Tejedor, and F. J. Garcia-Vidal, "Entanglement of Two Qubits Mediated by One-Dimensional Plasmonic Waveguides," *Phys. Rev. Lett.*, vol. 106, p. 020501, Jan 2011. 10, 89, 120, 125, 128, 134

[65] D. Dzsotjan, J. Kästel, and M. Fleischhauer, "Dipole-dipole shift of quantum emitters coupled to surface plasmons of a nanowire," *Phys. Rev. B*, vol. 84, p. 075419, Aug 2011. 123, 129

[66] D. Martín-Cano, A. González-Tudela, L. Martín-Moreno, F. J. García-Vidal, C. Tejedor, and E. Moreno, "Dissipation-driven generation of two-qubit entanglement mediated by plasmonic waveguides," *Phys. Rev. B*, vol. 84, p. 235306, Dec 2011. 10, 89, 120, 126, 134

[67] J. Bellessa, C. Bonnand, J. C. Plenet, and J. Mugnier, "Strong Coupling between Surface Plasmons and Excitons in an Organic Semiconductor," *Phys. Rev. Lett.*, vol. 93, p. 036404, Jul 2004. 10, 89, 104, 108

[68] J. Dintinger, S. Klein, F. Bustos, W. L. Barnes, and T. W. Ebbesen, "Strong coupling between surface plasmon-polaritons and organic molecules in subwavelength hole arrays," *Phys. Rev. B*, vol. 71, p. 035424, Jan 2005.

[69] T. K. Hakala, J. J. Toppari, A. Kuzyk, M. Pettersson, H. Tikkanen, H. Kunttu, and P. Törmä, "Vacuum Rabi Splitting and Strong-Coupling Dynamics for Surface-Plasmon Polaritons and Rhodamine 6G Molecules," *Phys. Rev. Lett.*, vol. 103, p. 053602, Jul 2009. 115

[70] S. Aberra Guebrou, C. Symonds, E. Homeyer, J. C. Plenet, Y. N. Gartstein, V. M. Agranovich, and J. Bellessa, "Coherent Emission from a Disordered Organic Semiconductor Induced by Strong Coupling with Surface Plasmons," *Phys. Rev. Lett.*, vol. 108, p. 066401, Feb 2012. 10, 89

[71] P. Vasa, R. Pomraenke, S. Schwieger, Y. I. Mazur, V. Kunets, P. Srinivasan, E. Johnson, J. E. Kihm, D. S. Kim, E. Runge, G. Salamo, and C. Lienau, "Coherent Exciton–Surface-Plasmon-Polariton Interaction in Hybrid Metal-Semiconductor Nanostructures," *Phys. Rev. Lett.*, vol. 101, p. 116801, Sep 2008. 10, 89

[72] J. Bellessa, C. Symonds, C. Meynaud, J. C. Plenet, E. Cambril, A. Miard, L. Ferlazzo, and A. Lemaitre, "Exciton/plasmon polaritons in GaAs/Al_0.93Ga_0.07As heterostructures near a metallic layer," *Phys. Rev. B*, vol. 78, p. 205326, Nov 2008.

[73] D. Gomez, K. Vernon, P. Mulvaney, and T. Davis, "Surface Plasmon Mediated Strong ExcitonPhoton Coupling in Semiconductor Nanocrystals," *Nano Letters*, vol. 10, pp. 274–278, 2010. 10, 89, 104, 108

[74] Y. Ota, N. Kumagai, S. Ohkouchi, M. Shirane, M. Nomura, S. Ishida, S. Iwamoto, S. Yorozu, and Y. Arakawa, "Investigation of the Spectral Triplet in Strongly Coupled Quantum Dot–Nanocavity System," *Appl. Phys. Express*, vol. 2, p. 122301, 2009. 10, 35, 38, 40, 41, 59

[75] D. Sanvitto, F. P. Laussy, F. Bello, D. M. Whittaker, A. M. Fox, M. S. Skolnick, A. Tahraoui, P. W. Fry, and M. Hopkinson, "Single-photon nonlinearity of a semiconductor quantum dot in a cavity," *arXiv:cond-mat/0612034*, 2006. 10, 39, 40, 41

[76] C. C. Gerry and P. L. Knight, *Introductory Quantum Optics*. Cambridge University Press, 2005. 13

[77] M. O. Scully and M. S. Zubairy, *Quantum optics*. Cambridge University Press, 2002. 13, 14, 17, 125, 139

[78] Y. Yamamoto and A. Ĭmamoḡlu, *Mesoscopic Quantum Optics*. John Wiley & Sons, inc., 1999. 13

[79] A. Kavokin, J. J. Baumberg, G. Malpuech, and F. P. Laussy, *Microcavities*. Oxford University Press, 2007. 13

[80] C. Cohen-Tannoudji, J. Dupont-Roc, and G. Grynberg, *Photons et atomes*. EDP Sciences, 2001. 15

[81] R. H. Lehmberg, "Radiation from an N-Atom System. I. General Formalism," *Phys. Rev. A*, vol. 2, pp. 883–888, Sep 1970. 21, 144, 145

[82] G. S. Agarwal and S. Dutta Gupta, "Steady states in cavity QED due to incoherent pumping," *Phys. Rev. A*, vol. 42, p. 1737, 1990. 21, 35

[83] J. Eberly and K. Wódkiewicz, "The time-dependent physical spectrum of light," *J. Opt. Soc. Am.*, vol. 67, p. 1252, 1977. 23, 47, 65, 74

[84] G. Nienhuis, "Time-dependent spectra of colliding atoms in an intense radiation field," *J. phys. B.: At. Mol. Phys.*, vol. 16, p. 2677, 1983. 23

[85] D. G. Lampard, "Generalization of the Wiener-Khintchine Theorem to Nonstationary Processes," *J. Appl. Phys.*, vol. 25, p. 802, 1954. 24

[86] M. Lax, "Formal Theory of Quantum Fluctuations from a Driven State," *Phys. Rev.*, vol. 129, p. 2342, 1963. 24

[87] E. del Valle, *Microcavity Quantum Electrodynamics*. VDM Verlag, 2010. 24, 33, 36, 48, 50, 55

[88] Y. Mu and C. M. Savage, "One-atom lasers," *Phys. Rev. A*, vol. 46, p. 5944, 1992. 24, 59

[89] J. P. Clemens and P. R. Rice, "Nonclassical effects of a driven atoms-cavity system in the presence of an arbitrary driving field and dephasing," *Phys. Rev. A*, vol. 61, p. 063810, 2000.

[90] J. I. Perea, D. Porras, and C. Tejedor, "Dynamics of the excitations of a quantum dot in a microcavity," *Phys. Rev. B*, vol. 70, p. 115304, 2004. 24

[91] H. F. Arnoldus and G. Nienhuis, "Photon correlations between the lines in the spectrum of resonance fluorescence," *J. phys. B.: At. Mol. Phys.*, vol. 17, p. 963, 1984. 25, 27, 60

[92] J. D. Cresser, "Intensity correlations of frequency-filtered light fields," *J. phys. B.: At. Mol. Phys.*, vol. 20, p. 4915, 1987. 25

[93] L. Knoll and G. Weber, "Theory of n-fold time-resolved correlation spectroscopy and its application to resonance fluorescence radiation," *J. phys. B.: At. Mol. Phys.*, vol. 19, p. 2817, 1986. 26, 44, 60

[94] J. Wiersig, C. Gies, F. Jahnke, M. Aßmann, T. Berstermann, M. Bayer, C. Kistner, S. Reitzenstein, C. Schneider, S. Höfling, A. Forchel, C. Kruse, J. Kalden, and D. Homme, "Direct observation of correlations between individual photon emission events of a microcavity laser," *Nature*, vol. 460, p. 245, 2009. 27, 74

[95] K. Joosten and G. Nienhuis, "Influence of spectral filtering on the quantum nature of light," *J. phys. B.: At. Mol. Phys.*, vol. 2, p. 158, 2000. 27, 60

[96] G. Bel and F. L. H. Brown, "Theory for Wavelength-Resolved Photon Emission Statistics in Single-Molecule Fluorescence Spectroscopy," *Phys. Rev. Lett.*, vol. 102, p. 018303, 2009. 27, 44, 57, 60

[97] D. Press, S. Götzinger, S. Reitzenstein, C. Hofmann, A. Löffler, M. Kamp, A. Forchel, and Y. Yamamoto, "Photon Antibunching from a Single Quantum Dot-Microcavity System in the Strong Coupling Regime," *Phys. Rev. Lett.*, vol. 98, p. 117402, 2007. 29, 43

[98] M. Nomura, Y. Ota, N. Kumagai, S. Iwamoto, and Y. Arakawa, "Large Vacuum Rabi Splitting in Single Self-Assembled Quantum Dot-Nanocavity System," *Appl. Phys. Express*, vol. 1, p. 072102, 2008. 78

[99] C. Kistner, T. Heindel, C. Schneider, A. Rahimi-Iman, S. Reitzenstein, S. Höfling, and A. Forchel, "Demonstration of strong coupling via electro-optical tuning in high-quality QD-micropillar systems," *Opt. Express*, vol. 16, p. 15006, 2008.

[100] A. Dousse, J. Suffczyński, R. Braive, A. Miard, A. Lemaître, I. Sagnes, L. Lanco, J. Bloch, P. Voisin, and P. Senellart, "Scalable implementation of strongly coupled cavity-quantum dot devices," *Appl. Phys. Lett.*, vol. 94, p. 121102, 2009. 29

[101] A. Wallraff, D. I. Schuster, A. Blais, L. Frunzio, R.-S. Huang, J. Majer, S. Kumar, S. M. Girvin, and R. J. Schoelkopf, "Strong coupling of a single photon to a superconducting qubit using circuit quantum electrodynamics," *Nature*, vol. 431, p. 162, 2004. 29, 35

[102] Y. Zhu, D. J. Gauthier, S. E. Morin, Q. Wu, H. J. Carmichael, and T. W. Mossberg, "Vacuum Rabi splitting as a feature of linear-dispersion theory: Analysis and experimental observations," *Phys. Rev. Lett.*, vol. 64, p. 2499, 1990. 29

[103] E. Jaynes and F. Cummings, "Comparison of Quantum and Semiclassical Radiation Theory with Application to the Beam Maser," *Proc. IEEE*, vol. 51, p. 89, 1963. 29, 30

[104] M. Brune, F. Schmidt-Kaler, A. Maali, J. Dreyer, E. Hagley, J. M. Raimond, and S. Haroche, "Quantum Rabi Oscillation: A Direct Test of Field Quantization in a Cavity," *Phys. Rev. Lett.*, vol. 76, p. 1800, 1996. 29

[105] J. M. Fink, M. Göppl, M. Baur, R. Bianchetti, P. J. Leek, A. Blais, and A. Wallraff, "Climbing the Jaynes–Cummings ladder and observing its $\sqrt{n}$ nonlinearity in a cavity QED system," *Nature*, vol. 454, p. 315, 2008. 29

[106] P. Borri, W. Langbein, U. Woggon, V. Stavarache, D. Reuter, and A. D. Wieck, "Exciton dephasing via phonon interactions in InAs quantum dots: Dependence on quantum confinement," *Phys. Rev. B*, vol. 71, p. 115328, 2005. 29

[107] I. Favero, A. Berthelot, G. Cassabois, C. Voisin, C. Delalande, P. Roussignol, R. Ferreira, and J. M. Gérard, "Temperature dependence of the zero-phonon linewidth in quantum dots: An effect of the fluctuating environment," *Phys. Rev. B*, vol. 75, p. 073308, 2007. 29

[108] T. Holstein and H. Primakoff, "Field Dependence of the Intrinsic Domain Magnetization of a Ferromagnet," *Phys. Rev.*, vol. 58, pp. 1098–1113, Dec 1940. 31, 113, 152

[109] F. P. Laussy, E. del Valle, and C. Tejedor, "Strong Coupling of Quantum Dots in Microcavities," *Phys. Rev. Lett.*, vol. 101, p. 083601, 2008. 32, 37, 40, 99

[110] F. P. Laussy, E. del Valle, and C. Tejedor, "Luminescence Spectra of Quantum Dots in Microcavities. I. Bosons," *Phys. Rev. B*, vol. 79, p. 235325, 2009. 32, 53, 72

[111] T. R. Nielsen, P. Gartner, and F. Jahnke, "Many-body theory of carrier capture and relaxation in semiconductor quantum-dot lasers," *Phys. Rev. B*, vol. 69, p. 235314, 2004. 32

[112] N. Averkiev, M. Glazov, and A. Poddubny, "Collective modes of quantum dot ensembles in microcavities," *Sov. Phys. JETP*, vol. 135, p. 959, 2009. 32

[113] L. V. Keldysh, V. D. Kulakovskii, S. Reitzenstein, M. N. Makhonin, and A. Forchel, "Interference effects in the emission spectra of QD's in high quality cavities," *Pis'ma ZhETF*, vol. 84, p. 584, 2006. 32

[114] E. del Valle and F. P. Laussy, "Effective cavity pumping from weakly coupled quantum dots," *Superlatt. Microstruct.*, vol. 49, p. 241, 2010. 32

[115] E. del Valle and F. P. Laussy, "Regimes of strong light-matter coupling under incoherent excitation," *Phys. Rev. A*, vol. 84, p. 043816, 2011. 33, 58, 59, 139

[116] A. N. Poddubny, M. M. Glazov, and N. S. Averkiev, "Nonlinear emission spectra of quantum dots strongly coupled to a photonic mode," *Phys. Rev. B*, vol. 82, p. 205330, 2010. 33, 59

[117] Y. Ota, M. Shirane, M. Nomura, N. Kumagai, S. Ishida, S. Iwamoto, S. Yorozu, and Y. Arakawa, "Vacuum Rabi splitting with a single quantum dot embedded in a H1 photonic crystal nanocavity," *Appl. Phys. Lett.*, vol. 94, p. 033102, 2009. 35

[118] J. Kasprzak, S. Reitzenstein, E. A. Muljarov, C. Kistner, C. Schneider, M. Strauss, S. Höfling, A. Forchel, and W. Langbein, "Up on the Jaynes-Cummings ladder of a quantum-dot/microcavity system," *Nat. Mater.*, vol. 9, p. 304, 2010. 35

[119] F. P. Laussy and E. del Valle, "Optical Spectra of the Jaynes-Cummings Ladder," *AIP Conference Proceedings*, vol. 1147, p. 46, 2009. 37

[120] E. del Valle, F. P. Laussy, and C. Tejedor, "Luminescence spectra of quantum dots in microcavities. II. Fermions," *Phys. Rev. B*, vol. 79, p. 235326, 2009. 37, 39, 40, 41, 46, 55, 75

[121] M. Nomura, N. Kumagai, S. Iwamoto, Y. Ota, and Y. Arakawa, "Laser oscillation in a strongly coupled single-quantum-dot–nanocavity system," *Nat. Phys.*, vol. 6, p. 279, 2010. 37, 51

[122] S. Hughes and P. Yao, "Theory of quantum light emission from a strongly-coupled single quantum dot photonic-crystal cavity system," *Opt. Express*, vol. 17, p. 3322, 2009. 38

[123] B. R. Mollow, "Power Spectrum of Light Scattered by Two-Level Systems," *Phys. Rev.*, vol. 188, p. 1969, 1969. 38, 59

[124] A. Auffèves, J.-M. Gérard, and J.-P. Poizat, "Pure emitter dephasing: A resource for advanced solid-state single-photon sources," *Phys. Rev. A*, vol. 79, p. 053838, 2009. 38, 50

[125] A. Gonzalez-Tudela, E. del Valle, C. Tejedor, and F. Laussy, "Anticrossing in the PL spectrum of light–matter coupling under incoherent continuous pumping," *Superlatt. Microstruct.*, vol. 47, p. 16, 2010. 40, 41

[126] Z. Michalewicz, *Genetic Algorithms + Data Structures= Evolutionary Programming.* Springe-Verlagr, 1992. 40

[127] A. Aspect, G. Roger, S. Reynaud, J. Dalibard, and C. Cohen-Tannoudji, "Time Correlations between the Two Sidebands of the Resonance Fluorescence Triplet," *Phys. Rev. Lett.*, vol. 45, p. 617, 1980. 43, 60

[128] C. A. Schrama, G. Nienhuis, H. A. Dijkerman, C. Steijsiger, and H. G. M. Heideman, "Destructive interference between opposite time orders of photon emission," *Phys. Rev. Lett.*, vol. 67, 1991. 62

[129] A. Ulhaq, S. Weiler, S. M. Ulrich, R. Roßbach, M. Jetter, and P. Michler, "Cascaded single-photon emission from the Mollow triplet sidebands of a quantum dot," *Nat. Photon.*, 2012. 43, 60, 62, 65

[130] M. Kaniber, A. Laucht, A. Neumann, J. M. Villas-Bôas, M. Bichler, M.-C. Amann, and J. J. Finley, "Investigation of the nonresonant dot-cavity coupling in two-dimensional photonic crystal nanocavities," *Phys. Rev. B*, vol. 77, p. 161303(R), 2008. 43, 69

[131] N. Akopian, N. H. Lindner, E. Poem, Y. Berlatzky, J. Avron, D. Gershoni, B. D. Gerardot, and P. M. Petroff, "Entangled Photon Pairs from Semiconductor Quantum Dots," *Phys. Rev. Lett.*, vol. 96, p. 130501, 2006. 43, 69

[132] E. Moreau, I. Robert, L. Manin, V. Thierry-Mieg, J. M. Gérard, and I. Abram, "Quantum Cascade of Photons in Semiconductor Quantum Dots," *Phys. Rev. Lett.*, vol. 87, p. 183601, 2001. 43, 59

[133] C. Cohen-Tannoudji and S. Reynaud, "Atoms in Strong Light-Fields: Photon Antibunching in Single Atom Fluorescence," vol. 293, p. 223, 1979. 44, 60, 64

[134] J. Dalibard and S. Reynaud, "Correlation signals in resonance fluorescence : interpretation via photon scattering amplitudes," vol. 44, p. 1337, 1983. 62, 64

[135] G. Nienhuis, "Spectral correlations in resonance fluorescence," *Phys. Rev. A*, vol. 47, p. 510, 1993. 44, 60

[136] R. Centeno Neelen, D. M. Boersma, M. P. van Exter, G. Nienhuis, and J. P. Woerdman, "Spectral filtering within the Schawlow–Townes linewidth as a diagnostic tool for studying laser phase noise," *Opt. Commun.*, vol. 100, p. 289, 1993. 48

[137] G. Sallen, A. Tribu, T. Aichele, R. André, L. Besombes, C. Bougerol, S. T. M. Richard, K. Khen, and J.-P. Poizat, "Subnanosecond spectral diffusion measurement using photon correlation," *Nat. Photon.*, vol. 4, p. 696, 2010. 50

[138] A. Laucht, N. Hauke, J. M. Villas-Bôas, F. Hofbauer, G. Böhm, M. Kaniber, and J. J. Finley, "Dephasing of Exciton Polaritons in Photoexcited InGaAs Quantum Dots in GaAs Nanocavities," *Phys. Rev. Lett.*, vol. 103, p. 087405, 2009. 50

[139] A. Gonzalez-Tudela, E. del Valle, E. Cancellieri, C. Tejedor, D. Sanvitto, and F. P. Laussy, "Effect of pure dephasing on the Jaynes-Cummings nonlinearities," *Opt. Express*, vol. 18, p. 7002, 2010. 50, 59, 139

[140] A. Auffèves, D. Gerace, J.-M. Gérard, M. F. Santos, L. C. Andreani, and J.-P. Poizat, "Controlling the dynamics of a coupled atom-cavity system by pure dephasing," *Phys. Rev. B*, vol. 81, p. 245419, 2010. 50

[141] A. Kavokin, J. J. Baumberg, G. Malpuech, and F. P. Laussy, *Microcavities*. Oxford University Press, 2 ed., 2011. 50

[142] J. B. Majer, F. G. Paauw, A. C. J. ter Haar, C. J. P. M. Harmans, and J. E. Mooij, "Spectroscopy on Two Coupled Superconducting Flux Qubits," *Phys. Rev. Lett.*, vol. 94, p. 090501, 2005. 50

[143] E. Gallardo, L. J. Martinez, A. K. Nowak, D. Sarkar, H. P. van der Meulen, J. M. Calleja, C. Tejedor, I. Prieto, D. Granados, A. G. Taboada, J. M. García, and P. A. Postigo, "Optical coupling of two distant InAs/GaAs quantum dots by a photonic-crystal microcavity," *Phys. Rev. B*, vol. 81, p. 193301, 2010. 119

[144] A. Laucht, J. Villas-Bôas, S. Stobbe, N. Hauke, F. Hofbauer, G. Böhm, P. Lodahl, M.-C. Amannand, M. Kaniber, and J. J. Finley, "Mutual coupling of two semiconductor quantum dots via an optical nanocavity," *Phys. Rev. B*, vol. 82, p. 075305, 2010. 119

[145] K. Mueller, A. Bechtold, C. Ruppert, M. Zecherle, G. Reithmaier, M. Bichler, H. Krenner, G. Abstreiter, A. Holleitner, J. M. Villas-Boas, and J. Finley, "Electrical Control of Interdot Electron Tunneling in a Double InGaAs Quantum-Dot Nanostructure," *Phys. Rev. Lett.*, vol. 108, p. 197402, 2012. 50

[146] K. Birnbaum, A. Boca, R. Miller, A. Boozer, T. Northup, and H. Kimble, "Photon blockade in an optical cavity with one trapped atom," *Nature*, vol. 436, p. 87, 2005. 51

[147] C. Lang, D. Bozyigit, C. Eichler, L. Steffen, J. M. Fink, A. A. A. Jr., M. Baur, S. Filipp, M. P. da Silva, A. Blais, and A. Wallraff, "Observation of Resonant Photon Blockade at Microwave Frequencies Using Correlation Function Measurements," *Phys. Rev. Lett.*, vol. 106, p. 243601, 2011.

[148] M. Koch, C. Sames, M. Balbach, H. Chibani, A. Kubanek, K. Murr, T. Wilk, and G. Rempe, "Three-Photon Correlations in a Strongly Driven Atom-Cavity System," *Phys. Rev. Lett.*, vol. 107, p. 023601, 2011. 51

[149] E. del Valle, S. Zippilli, F. P. Laussy, A. Gonzalez-Tudela, G. Morigi, and C. Tejedor, "Two-photon lasing by a single quantum dot in a high-Q microcavity," *Phys. Rev. B*, vol. 81, p. 035302, 2010. 54, 69, 70, 71, 72, 74, 80, 86

[150] E. del Valle, A. Gonzalez-Tudela, E. Cancellieri, F. P. Laussy, and C. Tejedor, "Generation of a two-photon state from a quantum dot in a microcavity," *New J. Phys.*, vol. 13, p. 113014, 2011. 67, 69, 80, 83

[151] Y. Ota, S. Iwamoto, N. Kumagai, and Y. Arakawa, "Spontaneous Two-Photon Emission from a Single Quantum Dot," *Phys. Rev. Lett.*, vol. 107, p. 233602, 2011. 54, 70, 71, 74, 80

[152] E. del Valle, A. Gonzalez-Tudela, F. P. Laussy, C. Tejedor, and M. J. Hartmann, "Theory of Frequency-Filtered and Time-Resolved N-Photon Correlations," *Phys. Rev. Lett.*, vol. 109, p. 183601, Oct 2012. 55, 65, 87

[153] P. Gartner, "Two-level laser: Analytical results and the laser transition," *Phys. Rev. A*, vol. 84, p. 053804, 2011. 58

[154] E. del Valle and F. P. Laussy, "Mollow Triplet under Incoherent Pumping," *Phys. Rev. Lett.*, vol. 105, p. 233601, 2010. 59

[155] S. Reynaud, "La fluorescence de résonance: étude par la méthode de l'atome habillé," vol. 8, p. 315, 1983. 60

[156] L. Knöll, G. Weber, and T. Schafer, "Theory of time-resolved correlation spectroscopy and its application to resonance fluorescence radiation," *J. phys. B.: At. Mol. Phys.*, vol. 17, p. 4861, 1984. 60

[157] G. Nienhuis, "Spectral Correlations within the Fluorescence Triplet," *Europhys. Lett.*, vol. 21, p. 285, 1993. 62

[158] H. J. Kimble and L. Mandel, "Resonance fluorescence with excitation of finite bandwidth," *Phys. Rev. A*, vol. 15, p. 689, 1977. 63

[159] H. F. Arnoldus and G. Nienhuis, "Atomic fluorescence in a mode-hopping laser field," *Journal of Physics B: Atomic and Molecular Physics*, vol. 19, no. 16, p. 2421, 1986. 63

[160] G. S. Agarwal, "Exact Solution for the Influence of Laser Temporal Fluctuations on Resonance Fluorescence," *Phys. Rev. Lett.*, vol. 37, p. 1383, 1976. 63

[161] K. Wódkiewicz, "Laser linewidth effects in intensity correlations in resonance fluorescence," *Physics Letters A*, vol. 77, no. 5, pp. 315–317, 1980. 63

[162] H. M. Gibbs and T. N. C. Venkatesan, "Direct observation of fluorescence narrower than the natural linewidth," *Opt. Commun.*, 1976. 64

[163] J. T. Höffges, H. W. Baldauf, T. Eichler, S. R. Helmfrid, and H. Walther, "Heterodyne measurement of the fluorescent radiation of a single trapped ion," *Opt. Commun.*, vol. 133, p. 170, 1997.

[164] J. Volz, M. Weber, D. Schlenk, W. Rosenfeld, C. Kurtsiefer, and H. Weinfurter, "An atom and a photon," *Laser Phys.*, vol. 17, p. 1007, 2007.

[165] H. S. Nguyen, G. Sallen, C. Voisin, P. Roussignol, C. Diederichs, and G. Cassabois, "Ultra-coherent single photon source," *Appl. Phys. Lett.*, vol. 99, p. 261904, 2011.

[166] C. Matthiesen, A. N. Vamivakas, and M. Atatüre, "Subnatural linewidth single photons from a quantum dot," *Phys. Rev. Lett.*, vol. 108, p. 093602, 2012. 64

[167] A. Gonzalez-Tudela, F. P. Laussy, C. Tejedor, M. J. Hartmann, and E. del Valle, "Two-photon spectra of quantum emitters," *ArXiv e-prints*, Nov. 2012. 65

[168] E. del Valle, "Distilling one, two and entangled pairs of photons from a quantum dot with cavity QED effects and spectral filtering," *ArXiv e-prints*, Oct. 2012. 65, 67

[169] A. Ridolfo, M. Leib, S. Savasta, and M. J. Hartmann, "Photon blockade in the ultrastrong coupling regime," *Phys. Rev. Lett.*, vol. 109, p. 193602, 2012. 67

[170] P. Degenfeld-Schonburg, E. del Valle, and M. J. Hartmann, "Signatures of single site addressability in resonance fluorescence spectra," *Phys. Rev. A*, vol. 85, p. 013842, 2012. 67

[171] V. Ardizzone, M. Abbarchi, A. Lemaitre, I. Sagnes, P. Senellart, J. Bloch, C. Delalande, J. Tignon, and P. Roussignol, "Bunching visibility of optical parametric emission in a semiconductor microcavity," *Phys. Rev. B*, vol. 86, 2012. 67

[172] T. Nagata, R. Okamoto, J. L. O'Brien, K. Sasaki, and S. Takeuchi, "Beating the Standard Quantum Limit with Four-Entangled Photons," *Science*, vol. 316, p. 726, 2007. 69

[173] C. Simon, H. de Riedmatten, M. Afzelius, N. Sangouard, H. Zbinden, and N. Gisin, "Quantum Repeaters with Photon Pair Sources and Multimode Memories," *Phys. Rev. Lett.*, vol. 98, p. 190503, 2007. 69

[174] J. I. Cirac, P. Zoller, H. J. Kimble, and H. Mabuchi, "Quantum State Transfer and Entanglement Distribution among Distant Nodes in a Quantum Network," *Phys. Rev. Lett.*, vol. 78, p. 3221, 1997.

[175] L.-M. Duan, M. D. Lukin, J. I. Cirac, and P. Zoller, "Long-distance quantum communication with atomic ensembles and linear optics," *Nature*, vol. 414, p. 413, 2001. 69

[176] C. Santori, D. Fattal, J. Vukovick, G. S. Solomon, and Y. Yamamoto, "Indistinguishable photons from a single-photon device," *Nature*, vol. 419, p. 594, 2002. 69

[177] P. Kok, W. J. Munro, K. Nemoto, T. C. Ralph, J. P. Dowling, and G. J. Milburn, "Linear optical quantum computing with photonic qubits," *Rev. Mod. Phys.*, vol. 79, p. 135, 2007.

[178] B. P. Lanyon, T. J. Weinhold, N. K. Langford, J. L. O'Brien, K. J. Resch, A. Gilchrist, and A. G. White, "Manipulating Biphotonic Qutrits," *Phys. Rev. Lett.*, vol. 100, p. 060504, 2008. 69

[179] E. Cancellieri, F. Troiani, and G. Goldoni, "Optimal generation of indistinguishable photons from non-identical artificial molecules," *Opt. Express*, vol. 17, p. 17156, 2009.

[180] N. Sangouard, C. Simon, H. de Riedmatten, and N. Gisin, "Quantum repeaters based on atomic ensembles and linear optics," *Rev. Mod. Phys.*, vol. 83, p. 33, 2011. 69

[181] A. Aspect, P. Grangier, and G. Roger, "Experimental Realization of Einstein-Podolsky-Rosen-Bohm Gedankenexperiment: A New Violation of Bell's Inequalities," *Phys. Rev. Lett.*, vol. 49, p. 91, 1982. 69

[182] D. Collins, N. Gisin, N. Linden, S. Massar, and S. Popescu, "Bell Inequalities for Arbitrarily High-Dimensional Systems," *Phys. Rev. Lett.*, vol. 88, p. 040404, 2002. 69

[183] J. K. Thompson, J. Simon, H. Loh, and V. Vuletić, "A High-Brightness Source of Narrowband, Identical-Photon Pairs," *Science*, vol. 313, p. 74, 2006. 69

[184] V. Balić, D. A. Braje, P. Kolchin, G. Y. Yin, and S. E. Harris, "Generation of Paired Photons with Controllable Waveforms," *Phys. Rev. Lett.*, vol. 94, p. 183601, 2005.

[185] S. Du, P. Kolchin, C. Belthangady, G. Y. Yin, and S. E. Harris, "Subnatural Linewidth Biphotons with Controllable Temporal Length," *Phys. Rev. Lett.*, vol. 100, p. 183603, 2008. 69

[186] M. Scholz, L. Koch, and O. Benson, "Statistics of Narrow-Band Single Photons for Quantum Memories Generated by Ultrabright Cavity-Enhanced Parametric Down-Conversion," *Phys. Rev. Lett.*, vol. 102, p. 063603, 2009. 69

[187] K. Akiba, K. Kashiwagi, M. Arikawa, and M. Kozuma, "Storage and retrieval of non-classical photon pairs and conditional single photons generated by the parametric down-conversion process," *New J. Phys.*, vol. 11, p. 013049, 2009. 69

[188] R. Hafenbrak, S. M. Ulrich, P. Michler, L. Wang, A. Rastelli, and O. G. Schmidt, "Triggered polarization-entangled photon pairs from a single quantum dot up to 30K," *New J. Phys.*, vol. 9, p. 315, 2007. 69

[189] S. Ates, S. M. Ulrich, A. Ulhaq, S. Reitzenstein, A. Löoffler, S. Höfling, A. Forchel, and P. Michler, "Non-resonant dot-cavity coupling and its potential for resonant single-quantum-dot spectroscopy," *Nat. Photon.*, vol. 3, p. 724, 2009.

[190] S. Ates, S. M. Ulrich, S. Reitzenstein, A. Löffler, A. Forchel, and P. Michler, "Post-Selected Indistinguishable Photons from the Resonance Fluorescence of a Single Quantum Dot in a Microcavity," *Phys. Rev. Lett.*, vol. 103, p. 167402, 2009. 69

[191] M. Yamaguchi, T. Asano, K. Kojima, and S. Noda, "Quantum electrodynamics of a nanocavity coupled with exciton complexes in a quantum dot," *Phys. Rev. B*, vol. 80, p. 155326, 2009. 69

[192] M. Winger, T. Volz, G. Tarel, S. Portolan, A. Badolato, K. J. Hennessy, E. L. Hu, A. Beveratos, J. Finley, V. Savona, and A. Ĭmamoḡlu, "Explanation of Photon Correlations in the Far-Off-Resonance Optical Emission from a Quantum-Dot-Cavity System," *Phys. Rev. Lett.*, vol. 103, p. 207403, 2009. 69

[193] P. Machnikowski, "Theory of two-photon processes in quantum dots: Coherent evolution and phonon-induced dephasing," *Phys. Rev. B*, vol. 78, p. 195320, 2008. 71

[194] J.-M. Gérard, B. Sermage, B. Gayral, B. Legrand, E. Costard, and V. Thierry-Mieg, "Enhanced Spontaneous Emission by Quantum Boxes in a Monolithic Optical Microcavity," *Phys. Rev. Lett.*, vol. 81, p. 1110, 1998. 72

[195] T. Miyazawa1, T. Kodera, T. Nakaoka, K. Watanabe, N. Kumagai, N. Yokoyama, and Y. Arakawa, "Two-Photon Control of Biexciton Population in Telecommunication-Band Quantum Dot," *Appl. Phys. Express*, vol. 3, p. 064401, 2010. 73

[196] A. Dousse, J. Suffczyński, A. Beveratos, O. Krebs, A. Lemaître, I. Sagnes, J. Bloch, P. Voisin, and P. Senellart, "Ultrabright source of entangled photon pairs," *Nature*, vol. 466, p. 217, 2010. 73

[197] G. Chen, T. H. Stievater, E. T. Batteh, X. Li, D. G. Steel, D. Gammon, D. S. Katzer, D. Park, and L. J. Sham, "Biexciton Quantum Coherence in a Single Quantum Dot," *Phys. Rev. Lett.*, vol. 88, p. 117901, 2002. 73

[198] S. Boyle, A. Ramsay, A. Fox, and M. Skolnick, "Two-color two-photon Rabi oscillation of biexciton in single InAs/GaAs quantum dot," *Physica E*, vol. 42, p. 2485, 2010. 73

[199] S. Stufler, P. Machnikowski, P. Ester, M. Bichler, V. M. Axt, T. Kuhn, and A. Zrenner, "Two-photon Rabi oscillations in a single In_xGa_1 − xAs/GaAs quantum dot," *Phys. Rev. B*, vol. 73, p. 125304, 2006. 73, 79

[200] H. Y. Hui and R. B. Liu, "Proposal for geometric generation of a biexciton in a quantum dot using a chirped pulse," *Phys. Rev. B*, vol. 78, p. 155315, 2008. 73

[201] C. M. Simon, T. Belhadj, B. Chatel, T. Amand, P. Renucci, A. Lemaitre, O. Krebs, P. A. Dalgarno, R. J. Warburton, X. Marie, and B. Urbaszek, "Robust Quantum Dot Exciton Generation via Adiabatic Passage with Frequency-Swept Optical Pulses," *Phys. Rev. Lett.*, vol. 106, p. 166801, 2011. 73

[202] Y. Wu, I. M. Piper, M. Ediger, P. Brereton, E. R. Schmidgall, P. R. Eastham, M. Hugues, M. Hopkinson, and R. T. Phillips, "Population Inversion in a Single InGaAs Quantum Dot Using the Method of Adiabatic Rapid Passage," *Phys. Rev. Lett.*, vol. 106, p. 067401, 2011. 73

[203] A. J. Ramsay, "A review of the coherent optical control of the exciton and spin states of semiconductor quantum dots," *Semicond. Sci. Technol.*, vol. 25, p. 103001, 2010. 73

[204] T. Flissikowski, A. Betke, I. A. Akimov, and F. Henneberger, "Two-photon coherent control of a single quantum dot," *Phys. Rev. Lett.*, vol. 92, p. 227401, 2004. 73

[205] I. A. Akimov, J. T. Andrews, and F. Henneberger, "Stimulated Emission from the Biexciton in a Single Self-Assembled II-VI Quantum Dot," *Phys. Rev. Lett.*, vol. 96, p. 067401, 2006.

[206] S. J. Boyle, A. J. Ramsay, A. M. Fox, and M. S. Skolnick, "Beating of Exciton-Dressed States in a Single Semiconductor InGaAs/GaAs Quantum Dot," *Phys. Rev. Lett.*, vol. 102, p. 207401, 2009. 73

[207] A. Muller, W. Fang, J. Lawall, and G. S. Solomon, "Emission Spectrum of a Dressed Exciton-Biexciton Complex in a Semiconductor Quantum Dot," *Phys. Rev. Lett.*, vol. 101, p. 027401, 2008. 79

[208] E. D. Palik, *Handbook of Optical Constants of Solids.* Academic Press, 1985. 90

[209] P. A. Huidobro, A. Y. Nikitin, C. González-Ballestero, L. Martín-Moreno, and F. J. García-Vidal, "Superradiance mediated by graphene surface plasmons," *Phys. Rev. B*, vol. 85, p. 155438, Apr 2012. 93

[210] D. E. Chang, A. S. Sørensen, P. R. Hemmer, and M. D. Lukin, "Quantum Optics with Surface Plasmons," *Phys. Rev. Lett.*, vol. 97, p. 053002, Aug 2006. 95, 101, 120

[211] A. Archambault, T. V. Teperik, F. Marquier, and J. J. Greffet, "Surface plasmon Fourier optics," *Phys. Rev. B*, vol. 79, p. 195414, May 2009. 95, 107

[212] A. Archambault, F. Marquier, J.-J. Greffet, and C. Arnold, "Quantum theory of spontaneous and stimulated emission of surface plasmons," *Phys. Rev. B*, vol. 82, p. 035411, Jul 2010. 95, 107

[213] A. Gonzalez-Tudela, P. A. Huidobro, L. Martin-Moreno, C. Tejedor, and F. J. Garcia-Vidal, "Theory of the strong coupling between quantum emitters and propagating surface plasmons," *ArXiv e-prints*, May 2012. 96

[214] B. Huttner and S. M. Barnett, "Quantization of the electromagnetic field in dielectrics," *Phys. Rev. A*, vol. 46, pp. 4306–4322, Oct 1992. 96

[215] H. T. Dung, L. Knöll, and D.-G. Welsch, "Three-dimensional quantization of the electromagnetic field in dispersive and absorbing inhomogeneous dielectrics," *Phys. Rev. A*, vol. 57, pp. 3931–3942, May 1998. 96

[216] H. T. Dung, L. Knöll, and D.-G. Welsch, "Resonant dipole-dipole interaction in the presence of dispersing and absorbing surroundings," *Phys. Rev. A*, vol. 66, p. 063810, Dec 2002. 120, 122, 123

[217] S. Scheel and S. Y. Buhmann, "Macroscopic quantum electrodynamics-concepts and applications," *Acta Physica Slovaca*, vol. 58, pp. 675–809, October 2008. 96, 120, 122

[218] A. A. Anappara, S. D. Liberato, A. Tredicucci, C. Ciuti, G. Biasiol, L. Sorba, and F. Beltram, "Signatures of ultra-strong light–matter coupling regime," *Phys. Rev. B*, vol. 79, p. 201303(R), 2009. 100

[219] Y. N. Chen, G. Y. Chen, D. S. Chuu, and T. Brandes, "Quantum-dot exciton dynamics with a surface plasmon: Band-edge quantum optics," *Phys. Rev. A*, vol. 79, p. 033815, Mar 2009. 101

[220] A. Gonzalez-Tudela, F. J. Rodríguez, L. Quiroga, and C. Tejedor, "Dissipative dynamics of a solid-state qubit coupled to surface plasmons: From non-Markov to Markov regimes," *Phys. Rev. B*, vol. 82, p. 115334, Sep 2010. 101

[221] M. Kaliteevski, I. Iorsh, S. Brand, R. A. Abram, J. M. Chamberlain, A. V. Kavokin, and I. A. Shelykh, "Tamm plasmon-polaritons: Possible electromagnetic states at the interface of a metal and a dielectric Bragg mirror," *Phys. Rev. B*, vol. 76, p. 165415, Oct 2007. 104

[222] O. Gazzano, S. M. de Vasconcellos, K. Gauthron, C. Symonds, J. Bloch, P. Voisin, J. Bellessa, A. Lemaitre, and P. Senellart, "Evidence for Confined Tamm Plasmon Modes under Metallic Microdisks and Application to the Control of Spontaneous Optical Emission," *Phys. Rev. Lett.*, vol. 107, p. 247402, Dec 2011. 104

[223] T. Hümmer, F. J. García-Vidal, L. Martín-Moreno, and D. Zueco, "Weak and Strong coupling regimes in plasmonic-QED," *ArXiv e-prints*, Sept. 2012. 104, 115

[224] T. Schwartz, J. A. Hutchison, C. Genet, and T. W. Ebbesen, "Reversible Switching of Ultrastrong Light-Molecule Coupling," *Phys. Rev. Lett.*, vol. 106, p. 196405, May 2011. 104, 108

[225] W. Barnes, "Topical review: Fluorescence near interfaces: the role of photonic mode density," *J. Mod. Opt.*, vol. 45, p. 661, 1998. 106

[226] M. S. Tame, C. Lee, J. Lee, D. Ballester, M. Paternostro, A. V. Zayats, and M. S. Kim, "Single-Photon Excitation of Surface Plasmon Polaritons," *Phys. Rev. Lett.*, vol. 101, p. 190504, Nov 2008. 107, 111

[227] R. Houdré, R. P. Stanley, and M. Ilegems, "Vacuum-field Rabi splitting in the presence of inhomogeneous broadening: Resolution of a homogeneous linewidth in an inhomogeneously broadened system," *Phys. Rev. A*, vol. 53, pp. 2711–2715, Apr 1996. 112

[228] H. Fidder, J. Knoester, and D. A. Wiersma, "Superradiant emission and optical dephasing in J-aggregates," *Chemical Physics Letters*, vol. 171, no. 5–6, pp. 529–536, 1990. 113, 114, 115

[229] C. Ciuti, P. Schwendimann, and A. Quattropani, "Parametric luminescence of microcavity polaritons," *Phys. Rev. B*, vol. 63, p. 041303R, 2001. 114

[230] L. Mandel and E. Wolf, "Coherence Properties of Optical Fields," *Rev. Mod. Phys.*, vol. 37, p. 231, 1965. 116

[231] C. Ciuti, V. Savona, C. Piermarocchi, A. Quattropani, and P. Schwendimann, "Role of the exchange of carriers in elastic exciton-exciton scattering in quantum wells," *Phys. Rev. B*, vol. 58, p. 7926, 1998. 116

[232] K. Hammerer, A. S. Sørensen, and E. S. Polzik, "Quantum interface between light and atomic ensembles," *Rev. Mod. Phys.*, vol. 82, pp. 1041–1093, Apr 2010. 118

[233] J. Majer, J. M. Chow, J. M. Gambetta, J. Koch, B. R. Johnson, J. A. Schreier, L. Frunzio, D. I. Schuster, A. A. Houck, A. Wallraff, A. Blais, M. H. Devoret, S. M. Girvin, and R. J. Schoelkopf, "Coupling superconducting qubits via a cavity bus," *Nature*, vol. 449, p. 443, 2007. 119

[234] F. Le Kien, S. D. Gupta, K. P. Nayak, and K. Hakuta, "Nanofiber-mediated radiative transfer between two distant atoms," *Phys. Rev. A*, vol. 72, p. 063815, Dec 2005. 119

[235] P. Yao, V. M. Rao, and S. Hughes, "On-chip single photon sources using planar photonic crystals and single quantum dots," *Laser Photon. Rev.*, 2009. 119

[236] S. Diehl, A. Micheli, A. Kantian, B. Kraus, H. P. Buchler, and P. Zoller, "Quantum states and phases in driven open quantum systems with cold atoms," *Nature Phys.*, vol. 4, p. 878, 2008. 119

[237] Z. Ficek and R. Tanas, "Entangled states and collective nonclassical effects in two-atom systems," *Phys. Rep.*, vol. 372, p. 369, 2002. 119, 122, 123

[238] D. Braun, "Creation of Entanglement by Interaction with a Common Heat Bath," *Phys. Rev. Lett.*, vol. 89, p. 277901, 2002.

[239] M. S. Kim, J. Lee, D. Ahn, and P. L. Knight, "Entanglement induced by a single-mode heat environment," *Phys. Rev. A*, vol. 65, p. 040101R, 2002.

[240] F. Benatti, R. Floreanini, and M. Piani, "Environment Induced Entanglement in Markovian Dissipative Dynamics," *Phys. Rev. Lett.*, vol. 91, p. 070402, 2003.

[241] F. Benatti, R. Floreanini, and U. Marzolino, "Entangling two unequal atoms through a common bath," *Phys. Rev. A*, vol. 81, p. 012105, 2010.

[242] E. del Valle, F. P. Laussy, and C. Tejedor, "Electrostatic control of quantum dot entanglement induced by coupling to external reservoirs," *Europhys. Lett.*, vol. 80, p. 57001, 2007. 124

[243] E. del Valle, F. P. Laussy, F. Troiani, and C. Tejedor, "Entanglement and lasing with two quantum dots in a microcavity," *Phys. Rev. B*, vol. 76, p. 235317, 2007.

[244] E. del Valle, "Steady state entanglement of two coupled qubits," *J. Opt. Soc. Am. B*, vol. 28, p. 228, 2011. 119, 124

[245] J. T. Barreiro, P. Schindler, T. M. O. Guhne, M. Chwalla, C. F. Roos, M. Hennrich, and R. Blatt, "Quantum computation and quantum-state engineering driven by dissipation," *Nature Phys.*, vol. 6, p. 943, 2010. 119

[246] S. Hughes, "Modified Spontaneous Emission and Qubit Entanglement from Dipole-Coupled Quantum Dots in a Photonic Crystal Nanocavity," *Phys. Rev. Lett.*, vol. 94, p. 227402, Jun 2005. 119

[247] T. Lund-Hansen, S. Stobbe, B. Julsgaard, H. Thyrrestrup, T. Sünner, M. Kamp, A. Forchel, and P. Lodahl, "Experimental Realization of Highly Efficient Broadband Coupling of Single Quantum Dots to a Photonic Crystal Waveguide," *Phys. Rev. Lett.*, vol. 101, p. 113903, Sep 2008. 119, 151, 155

[248] A. Laucht, S. Pütz, T. Günthner, N. Hauke, R. Saive, S. Frédérick, M. Bichler, M.-C. Amann, A. W. Holleitner, M. Kaniber, and J. J. Finley, "A Waveguide-Coupled On-Chip Single-Photon Source," *Phys. Rev. X*, vol. 2, p. 011014, Mar 2012. 119, 151, 155

[249] J. Bleuse, J. Claudon, M. Creasey, N. S. Malik, J.-M. Gérard, I. Maksymov, J.-P. Hugonin, and P. Lalanne, "Inhibition, Enhancement, and Control of Spontaneous Emission in Photonic Nanowires," *Phys. Rev. Lett.*, vol. 106, p. 103601, Mar 2011. 119

[250] Q. Quan, I. Bulu, and M. Lončar, "Broadband waveguide QED system on a chip," *Phys. Rev. A*, vol. 80, p. 011810, Jul 2009. 119

[251] P. Anger, P. Bharadwaj, and L. Novotny, "Enhancement and Quenching of Single-Molecule Fluorescence," *Phys. Rev. Lett.*, vol. 96, p. 113002, Mar 2006. 120

[252] A. G. Curto, G. Volpe, T. H. Taminiau, M. P. Kreuzer, R. Quidant, and N. F. van Hulst, "Unidirectional Emission of a Quantum Dot Coupled to a Nanoantenna," *Science*, vol. 329, no. 5994, pp. 930–933, 2010. 120

[253] P. Andrew and W. L. Barnes, "Energy Transfer Across a Metal Film Mediated by Surface Plasmon Polaritons," *Science*, vol. 306, no. 5698, pp. 1002–1005, 2004. 120

[254] D. Martin-Cano, L. Martin-Moreno, F. J. Garcia-Vidal, and E. Moreno, "Resonance Energy Transfer and Superradiance Mediated by Plasmonic Nanowaveguides," *Nano Letters*, vol. 10, no. 8, pp. 3129–3134, 2010. 120, 126, 127, 128, 151

[255] A. L. Falk, F. H. L. Koppens, C. L. Yu, K. Kang, N. de Leon Snapp, A. V. Akimov, M.-H. Ho, M. D. Lukin, and H. Park, "Near-field electrical detection of optical plasmons and single-plasmon sources," *Nat. Phys.*, vol. 5, p. 475, 2009. 120, 139

[256] R. W. Heeres, S. N. Dorenbos, B. Koene, G. S. Solomon, L. P. Kouwenhoven, and V. Zwiller, "On-Chip Single Plasmon Detection," *Nano Letters*, vol. 10, no. 2, pp. 661–664, 2010. PMID: 20041700. 120, 139

[257] A. Gonzalez-Tudela, D. Martin-Cano, E. Moreno, L. Martin-Moreno, F. J. Garcia-Vidal, and C. Tejedor, "Exploring qubit-qubit entanglement mediated by one-dimensional plasmonic nanowaveguides," *physica status solidi (c)*, vol. 9, no. 5, pp. 1303–1308, 2012. 120, 125, 134

[258] M. L. Andersen, S. Stobbe, A. S. Sorensen, and P. Lodahl, "Strongly modified plasmon–matter interaction with mesoscopic quantum emitters," *Nat. Phys.*, vol. 7, p. 215, 2011. 121

[259] S. G. Rodrigo, F. J. García-Vidal, and L. Martín-Moreno, "Influence of material properties on extraordinary optical transmission through hole arrays," *Phys. Rev. B*, vol. 77, p. 075401, Feb 2008. 121

[260] L. Knoll, S. Scheel, and D.-G. Welsch, *Coherence and Statistics of Photons and Atoms*. Wiley, 2001. 122

[261] D. Dzsotjan, A. S. Sørensen, and M. Fleischhauer, "Quantum emitters coupled to surface plasmons of a nanowire: A Green's function approach," *Phys. Rev. B*, vol. 82, p. 075427, Aug 2010. 122, 123

[262] D. F. Walls and G. J. Milburn, *Quantum Optics*. Springer-Verlag, 1994. 125, 139

[263] R. Horodecki, P. Horodecki, M. Horodecki, and K. Horodecki, "Quantum entanglement," *Rev. Mod. Phys.*, vol. 81, p. 865, 2009. 125

[264] W. K. Wootters, "Entanglement of Formation of an Arbitrary State of Two Qubits," *Phys. Rev. Lett.*, vol. 80, p. 2245, 1998. 125

[265] T. Søndergaard and S. I. Bozhevolnyi, "Surface plasmon polariton scattering by a small particle placed near a metal surface: An analytical study," *Phys. Rev. B*, vol. 69, p. 045422, Jan 2004. 126

[266] T. Søndergaard and B. Tromborg, "General theory for spontaneous emission in active dielectric microstructures: Example of a fiber amplifier," *Phys. Rev. A*, vol. 64, p. 033812, Aug 2001. 126

[267] A. W. Snyder and J. Love, *Optical Waveguide Theory*. Springer, 1983. 127

[268] R. E. Collin, *Field theory of guided waves*. IEEE Press Series on Electromagnetic Wave Theory, 1990. 127

[269] Y. Chen, T. R. Nielsen, N. Gregersen, P. Lodahl, and J. Mørk, "Finite-element modeling of spontaneous emission of a quantum emitter at nanoscale proximity to plasmonic waveguides," *Phys. Rev. B*, vol. 81, p. 125431, Mar 2010. 127

[270] J. Jung, T. Søndergaard, and S. I. Bozhevolnyi, "Theoretical analysis of square surface plasmon-polariton waveguides for long-range polarization-independent waveguiding," *Phys. Rev. B*, vol. 76, p. 035434, Jul 2007. 127

[271] D. Englund, B. Shields, K. Rivoire, F. Hatami, J. Vučković, H. Park, and M. D. Lukin, "Deterministic Coupling of a Single Nitrogen Vacancy Center to a Photonic Crystal Cavity," *Nano Letters*, vol. 10, no. 10, pp. 3922–3926, 2010. 129

[272] C. E. López, G. Romero, F. Lastra, E. Solano, and J. C. Retamal, "Sudden Birth versus Sudden Death of Entanglement in Multipartite Systems," *Phys. Rev. Lett.*, vol. 101, p. 080503, Aug 2008. 134

[273] Z. Ficek and R. Tanaś, "Delayed sudden birth of entanglement," *Phys. Rev. A*, vol. 77, p. 054301, May 2008. 134

[274] Z. Ficek and R. Tanaś, "Dark periods and revivals of entanglement in a two-qubit system," *Phys. Rev. A*, vol. 74, p. 024304, Aug 2006. 134

[275] S. Bose and V. Vedral, "Mixedness and teleportation," *Phys. Rev. A*, vol. 61, p. 040101, Mar 2000. 137

[276] S. Bose and V. Vedral, "Mixedness and teleportation," *Phys. Rev. A*, vol. 61, p. 040101, Mar 2000. 137

[277] S. Ishizaka and T. Hiroshima, "Maximally entangled mixed states under nonlocal unitary operations in two qubits," *Phys. Rev. A*, vol. 62, p. 022310, Jul 2000. 137

[278] W. J. Munro, D. F. V. James, A. G. White, and P. G. Kwiat, "Maximizing the entanglement of two mixed qubits," *Phys. Rev. A*, vol. 64, p. 030302, 2001. 137

[279] F. Jelezko, T. Gaebel, I. Popa, A. Gruber, and J. Wrachtrup, "Observation of Coherent Oscillations in a Single Electron Spin," *Phys. Rev. Lett.*, vol. 92, p. 076401, Feb 2004. 139

[280] A. Batalov, C. Zierl, T. Gaebel, P. Neumann, I.-Y. Chan, G. Balasubramanian, P. R. Hemmer, F. Jelezko, and J. Wrachtrup, "Temporal Coherence of Photons Emitted by Single Nitrogen-Vacancy Defect Centers in Diamond Using Optical Rabi-Oscillations," *Phys. Rev. Lett.*, vol. 100, p. 077401, Feb 2008. 139

[281] R. H. Dicke, "Coherence in Spontaneous Radiation Processes," *Phys. Rev.*, vol. 93, p. 99, 1954. 144

[282] M. Gross and S. Haroche, "Superradiance: An essay on the theory of collective spontaneous emission," *Phys. Rep.*, vol. 93, p. 301, 1982. 144

[283] P. D. Drummond and C. H. J., "Volterra cycles and the cooperative fluorescence critical point," *Optics Communications*, vol. 27, p. 160, 1978. 144, 146

[284] P. D. Drummond, "Observables and moments in cooperative resonance fluorescence," *Phys. Rev. A*, vol. 22, p. 1179, 1980.

[285] S. Schneider and G. J. Milburn, "Entanglement in the steady state of a collective-angular-momentum (Dicke) model," *Phys. Rev. A*, vol. 65, p. 042107, Mar 2002. 144

[286] J. M. Elzerman, K. M. Weiss, J. Miguel-Sanchez, and A. Imamoğlu, "Optical Amplification Using Raman Transitions between Spin-Singlet and Spin-Triplet States of a Pair of Coupled In-GaAs Quantum Dots," *Phys. Rev. Lett.*, vol. 107, p. 017401, Jun 2011. 144, 147, 150, 151

[287] K. M. Weiss, J. M. Elzerman, Y. L. Delley, J. Miguel-Sanchez, and A. Imamoğlu, "Coherent Two-Electron Spin Qubits in an Optically Active Pair of Coupled InGaAs Quantum Dots," *Phys. Rev. Lett.*, vol. 109, p. 107401, Sep 2012. 144, 147, 150, 151

[288] D. J. Wineland, J. J. Bollinger, and I. W. M., "Squeezed atomic states and projection noise in spectroscopy," *Phys. Rev. A.*, vol. 50, p. 67, 1994. 147

[289] A. Sorensen, L.-M. Duan, J. I. Cirac, and P. Zoller, "Many-particle entanglement with Bose-Einstein condensates," *Nature*, vol. 409, p. 63, 2001. 147

[290] M. Kitagawa and M. Ueda, "Squeezed spin states," *Phys. Rev. A*, vol. 47, p. 5138, 1993. 147

[291] G. Lecamp, P. Lalanne, and J. P. Hugonin, "Very Large Spontaneous-Emission $\beta Factors in Photonic - Crystal Waveguides$," *Phys. Rev. Lett.*, vol. 99, p. 023902, Jul 2007. 151

[292] X. Xu, B. Sun, P. R. Berman, D. G. Steel, A. S. Bracker, D. Gammon, and L. J. Sham, "Coherent Optical Spectroscopy of a Strongly Driven Quantum Dot," *Science*, vol. 317, p. 929, 07. 151

[293] Y. Kubo, I. Diniz, A. Dewes, V. Jacques, A. Dréau, J.-F. Roch, A. Auffeves, D. Vion, D. Esteve, and P. Bertet, "Storage and retrieval of a microwave field in a spin ensemble," *Phys. Rev. A*, vol. 85, p. 012333, Jan 2012. 151

[294] M. Lončar, D. Nedeljković, T. Doll, J. Vučković, A. Scherer, and T. P. Pearsall, "Waveguiding in planar photonic crystals," *Applied Physics Letters*, vol. 77, no. 13, pp. 1937–1939, 2000. 155

[295] Y. Vlasov, M. O'Boyle, H. H. F., and S. J. McNab, "Active control of slow light on a chip with photonic crystal waveguides," *Nature*, vol. 438, p. 65, nov 2005.

[296] E. Viasnoff-Schwoob, C. Weisbuch, H. Benisty, S. Olivier, S. Varoutsis, I. Robert-Philip, R. Houdré, and C. J. M. Smith, "Spontaneous Emission Enhancement of Quantum Dots in a Photonic Crystal Wire," *Phys. Rev. Lett.*, vol. 95, p. 183901, Oct 2005. 155

[297] D. Porras and J. J. García-Ripoll, "Shaping an Itinerant Quantum Field into a Multimode Squeezed Vacuum by Dissipation," *Phys. Rev. Lett.*, vol. 108, p. 043602, Jan 2012. 156